NASA-TM-108221

PRELIMINARY

M75-144-0

AL 76-108

VIKING 75 PROJECT

(NASA-TM-108221) VIKING 75 PROJECT: VIKING DATA ANALYSIS TEAM REPORT (NASA) 297 p
N93-71559
Unclas
Z9/91 0149868

NASA
7N-91-TM
149868
P-297

VIKING DATA ANALYSIS TEAM REPORT

NASA LIBRARY
AMES RESEARCH CENTER
MOFFETT FIELD, CALIF
1976

COPY NO. 1

NATIONAL AERONAUTICS AND SPACE ADMINISTRATION

Langley Research Center

Viking Project Office

PRELIMINARY

M75-144-0

VIKING 75 PROJECT

VIKING DATA ANALYSIS TEAM REPORT

APPROVED

James S. Martin, Jr.
Viking Project Manager

Date ____________________

NATIONAL AERONAUTICS AND SPACE ADMINISTRATION
Langley Research Center
Viking Project Office

PUBLICATION RESTRICTIONS

This report was prepared utilizing the reduced data and results available from the Mars '71 Mission and various earth-based observations. The MM'71 Project and Investigators have made available to the Viking Project, the data from the MM'71 Mission. Similarly, observations and results from various earth-based observations have also been provided, and some of the data is from unpublished sources.

The intent of this report is to provide the Viking Project with the Mars data necessary for the mission planning, without violating the publishing rights of the principal investigators. The document is to be used for planning purposes and is not a document that can be referenced or used for publishing in the "open" literature.

CONTENTS

1.0 INTRODUCTION 1-1
1.1 GENERAL 1-1
1.2 ORGANIZATION AND OBJECTIVES 1-1
1.3 PURPOSE OF REPORT 1-2

2.0 VIKING DATA ANALYSIS TEAM ACTIVITIES AND PRODUCTS 2-1
2.1 PREPARATION AND VDAT PARTICIPATION 2-1
2.2 NEAL-REAL TIME ACTIVITIES 2-2
2.3 REFERENCES 2-4

3.0 MARINER MARS '71 PRELIMINARY RESULTS 3-1
3.1 INTRODUCTION 3-1
3.1.1 Infrared Interferometer Spectrometer (IRIS) 3-1
3.1.2 Ultraviolet Spectrometer (UVS) 3-4
3.1.3 Infrared Radiometer (IRR) 3-4
3.1.4 Television Subsystem 3-6
3.1.5 S-Band and Celestial Mechanics 3-8
3.2 SURFACE INVESTIGATIONS 3-9
3.2.1 Surface Imagery and Mapping 3-9
3.2.2 Terrain Mapping and Analysis at a Scale of 1:25,000,000 3-22
3.2.3 Terrain Mapping and Analysis at a Scale of 1:5,000,000 3-79
3.2.4 Topographic Mapping 3-81
3.2.5 Surface Physical Properties 3-100
3.3 ATMOSPHERIC STUDIES 3-108
3.3.1 Visual Phenomenon 3-108
3.3.2 Spectroscopic Investigations - Mariner 9 3-115
3.4 SYNOPSIS OF RESULTS 3-139
3.5 REFERENCES 3-142

4.0 EARTH-BASED DATA ANALYSIS 4-1
4.1 TERRESTRIAL RADAR DATA 4-1
4.1.1 Root Mean Square (rms) Slopes on Mars and Lunar Comparison 4-2
4.1.2 Dielectric Constants 4-3
4.1.3 Preliminary Slope-Frequency Distributions on Mars 4-5
4.2 TERRESTRIAL PHOTOGRAPHIC AND SPECTROSCOPIC OBSERVATIONS 4-20
4.2.1 Cloud Phenomena 4-20
4.2.2 Spectroscopic Studies 4-22
4.3 REFERENCES 4-27

5.0 MARINER 9 COVERAGE OF VIKING AREAS OF INTEREST . . . 5-1
5.1 INTRODUCTION 5-1
5.2 DEFINITION OF ACCESSIBLE AREAS 5-1
5.3 DEFINITIONS OF TARGET AREAS 5-2
5.4 TYPE AND EXTENT OF COVERAGE 5-9

CONTENTS (Contd)

6.0 CONCLUSIONS AND RECOMMENDATIONS 6-1
6.1 SUMMARY AND IMPLICATIONS FOR VIKING 6-1
6.2 RECOMMENDED FOLLOW-ON STUDIES AND ANALYSES 6-2

TABLES

3-1 Approximate percentages of Viking Zone covered by terrains delineated on the VDAT 1:25,000,000 Generalized Terrain Map . 3-28
3-2 Averaged dielectric constants/rms slopes for 1/500,000 Terrain Map units 3-83
4-1 Algebraic standard deviation of slope angles for four gross lunar terrain types 4-1
4-2 Martian terrain slope statistics 4-6
5-1 Summary of Viking target sites 5-5

FIGURES

3-1 Mariner 9 IRIS Spectra 3-3
3-2 UVS Spectrum, 1900-2500Å 3-5
3-3 UVS Spectrum, 1400-1800Å 3-5
3-4 UVS Reflectance Spectrum, 2600-3400Å 3-6
3-5 Comparison of IRR thermal scan with mean thermal model 3-7
3-6 Mariner 9 gravity model compared with Earth-based radar topography 3-9
3-7 S-Band occultation topography 3-10
3-8 Enhanced mosaic of Nix Olympica 3-12
3-9 Great Equatorial Chasm with UVS elevation scan 3-13
3-10 Plateau area in Phoenicis Lacus 3-14
3-11 Canyonlands in Noctis Lacus 3-15
3-12 South Polar Region Tableland 3-16
3-13 North Polar Retion Terrain 3-17
3-14 Extensive sinuous valley in Mare Erythraeum region 3-18
3-15 Small erosional channels in heavily cratered terrain 3-19
3-16 B Frame mosaic of crater interior showing dune field 3-20
3-17 Sequence showing degradation of South Polar Cap 3-21
3-18 Wind-blown dust phenomenon 3-23
3-19 Geologic Province map 3-24
3-20 Airbrush rendition of South Polar Mosaic 3-25
3-21 Panoramic mosaic of a section of Mars Equatorial region 3-26
3-22 A sketch map for the Viking Zone 3-29
3-23 Contact between Cratered Terrain and Plains 3-30
3-24 Smooth Tablelands, east of scarps in canyons 3-38
3-25 Smooth Tablelands 3-38
3-26 Smooth Tablelands, south of Canyonlands 3-40
3-27 Smooth Tablelands, south of Canyonlands 3-40
3-28 Cratered Tablelands 3-42
3-29 Ridged Tablelands 3-42
3-30 Ridged Tablelands 3-44
3-31 Patterned Tablelands 3-44
3-32 Patterned Tablelands 3-46
3-33 Contact between Smooth Plains and Cratered Plains 3-46

CONTENTS (Contd)

FIGURES (Contd)

3-34 Smooth Plains 3-48
3-35 Cratered Plains 3-48
3-36 Cratered Plains 3-50
3-37 Hummocky Plains 3-50
3-38 Hummocky Plains 3-52
3-39 Isolated knobs in Smooth Plains 3-52
3-40 Lineated Plains 3-54
3-41 Patterned Plains 3-54
3-42 Patterned Plains 3-56
3-43 Ridged Plains 3-56
3-44 Ridged Plains 3-58
3-45 Cratered Terrain 3-58
3-46 Cratered Terrain 3-60
3-47 Flat Cratered Terrain 3-60
3-48 Flat Cratered Terrain 3-62
3-49 Patterned Cratered Terrain 3-62
3-50 Patterned Cratered Terrain 3-64
3-51 Irregular Terrain 3-64
3-52 Irregular Terrain 3-66
3-53 Irregular Terrain 3-66
3-54 Canyonlands 3-68
3-55 Canyonlands 3-68
3-56 Canyonlands 3-70
3-57 Canyonlands 3-70
3-58 Volcanic dome 3-72
3-59 Northern edge of volcanic dome 3-72
3-60 Flow fronts in Smooth Plains unit 3-74
3-61 Apparent stratification in Canyonland walls 3-74
3-62 Sand dune structures in floor of a crater 3-76
3-63 Comparison of averaged rms slope and dielectric constant for Cratered Terrain 3-82
3-64 Comparison between Smooth Terrain and Cratered Terrains 3-85
3-65 Comparison between averaged dielectric constant and rms slopes for various terrain units 3-86
3-66 Locations of occultation profiles 3-89
3-67 Pressure vs altitude derived from occultation data 3-90
3-68 IRIS topography of Hellas area 3-92
3-69 IRIS topography of Amazonis-Tharsis region 3-93
3-70 UVS elevation map of mid-latitudes 3-95
3-71 UVS elevation map of south polar region 3-96
3-72 Comparison of UVS and IRIS elevation contours in Hellas . . . 3-97
3-73 Comparison of UVS and IRIS elevation contours in Amazonis-Tharsis 3-98
3-74 Comparison of elevation profiles in Hellas and Amazonis-Tharsis from UVS, IRIS, radar and occultations 3-99
3-75 Surface diurnal temperature map by IRIS 3-102
3-76 IRR thermal scan of volcanic crater in Elysium 3-103

CONTENTS (Contd)

FIGURES (Contd)

3-77 IRR thermal scan near Novus Mons 3-104
3-78 IRR thermal scans showing albedo variations 3-105
3-79 IRR thermal scans showing slope variations 3-106
3-80 IRR thermal scans illustrating possible compositional variations 3-107
3-81 TV limb photo showing haze structure 3-109
3-82 *Localized dust storm* 3-110
3-83 White cloud occurrence near calderas 3-111
3-84 White cloud occurrence near calderas 3-112
3-85 Wave pattern and discrete clouds 3-113
3-86 Wave pattern and discrete clouds 3-114
3-87 Wave front 3-116
3-88 IRIS water vapor spectrum 3-117
3-89 IRIS south polar region water vapor spectrum 3-118
3-90 UVS ozone absorption spectrum 3-119
3-91 IRIS temperature profiles in south polar region 3-122
3-92 IRIS thermal cross section over south polar area 3-123
3-93 Additional IRIS temperature profiles 3-124
3-94 Effects of dust settling on IRIS retrieved temperature profiles 3-126
3-95 Diurnal atmospheric heating in Noachis 3-127
3-96 Preliminary wind fields deduced by IRIS 3-128
3-97 Early S-band occultation temperature profiles 3-130
3-98 Later S-band occultation temperature profiles 3-131
3-99 Additional, later occultation temperature profiles 3-132
3-100 S-band occultation pressure profile 3-134
3-101 UVS CO emission profile 3-135
3-102 UVS O and H emission profiles 3-136
3-103 S-band occultation electron density distribution 3-138
3-104 Variation of S-band peak electron density with time 3-140
4-1 Histogram of algebraic slope angles 4-7
4-2 Probability distribution of algebraic slope angles 4-8
4-3 Histogram of absolute slope angles 4-9
4-4 Probability distribution of absolute slope angles 4-10
4-5 Histogram of algebraic slope angles 4-11
4-6 Probability distribution of algebraic slope angles 4-12
4-7 Histogram of absolute slope angles 4-13
4-8 Probability distribution of absolute slope angles 4-14
4-9 Histogram of algebraic slope angles 4-15
4-10 Probability distribution of algebraic slope angles 4-16
4-11 Histogram of absolute slope angles 4-17
4-12 Probability distribution of absolute slope angles 4-18
4-13 Comparison of lunar, terrestrial and Martian absolute slope angles as a function of baselength 4-19
4-14 White cloud frequency distribution on Mars 4-21
4-15 Oblique view of south spot through several air masses 4-22
4-16 Diurnal increase in blue contrast 4-23

CONTENTS (Contd)

FIGURES (Contd)

4-17 Earth-based observed seasonal distribution of Martian water vapor 4-25
4-18 Suggested vertical distribution of Martian atmospheric water vapor 4-26
5-1 Correlation of Mars radar dielectric constant values with the various Martian terrain units 5-3
5-2 Correlation of Mars radar rms slope with the various Martian terrain units 5-4

APPENDIX A

Products presently available from Mariner Mars 1971 and VDAT activities A-1

APPENDIX B

Maps prepared by the Viking Data Analysis Team B-1

ACKNOWLEDGEMENT

This Viking Data Analysis Team (VDAT) Report resulted from the efforts of a relatively small number of people to prepare a timely summary of the VDAT activities during the Mariner Mars 1971 Mission. The contributors and participants in preparing this report are acknowledged as follows: T. A. Mutch for his excellent analysis and interpretation of the imagery data; H. J. Moore similarly for his analysis and interpretation of the imagery data and extensive efforts at correlating the results with the radar data; A. B. Binder for successfully pursuing the difficult task of preparing an elevation map so necessary for Viking mission planning, utilizing the earth-based radar and S-band occultation data; W. A. Baum for his contributions on dust observations and observations of clouds and other dondensates; J. Gliozzi and F. Bartko for their extensive efforts on preparation and correlation of the infrared and ultraviolet results with the other data and C. B. Farmer for his review and helpful recommendations to improve the report; D. M. Anderson for his contributions on the soil-water relationship and permafrost; R. A. Schmitz for the introduction, general discussion of VDAT activities and Viking targeting activity in the extended mission. A special acknowledgement to Bobbie Rambeau for typing the manuscript of this report and John Creaser for preparing and assembling the many maps and figures included herein.

The authors with to express thanks to D. Schneiderman, E. Pounder, R. Steinbacher and the staff of the Mariner Mars '71 Project for the cooperation and help provided the Viking Project and Viking Data Analysis Team during the Mariner Mars '71 Mission. Also to T. Vrebalovich, A. B. Whitehead and E. Christensen for their cooperation with the VDAT members.

A special thanks to the Mariner Mars '71 Science Investigators, who were cooperative in sharing the data and results from the various Mariner 9 experiments.

1.0 INTRODUCTION

1.1 GENERAL

The Mariner 9 spacecraft went into orbit around Mars on November 13, 1971 and began a long and successful mission of transmitting scientific data back to Earth. This wealth of information on the atmosphere and surface environment of Mars is very important to the Viking missions, and invaluable in defining the scientifically interesting and accessible areas for Viking landings in 1976. To be of maximum benefit to Viking, early analysis and correlation of data is necessary. In an attempt to expedite and aid in this analysis activity, a Viking group was formed to participate in the Mariner Mars '71 (MM'71) Mission. A more detailed discussion of the group is presented later in this report.

This group has been participating in the Mariner 9 science activities by reviewing the results from the mission and periodically attending the Mariner Science Evaluations Team meetings and working group meetings on topography, physical properties, and atmospheres. A member of the group has also attended the Science Recommendation Team (SRT) meetings. The SRT, where each MM'71 investigation is represented, plans and defines the science operations for the mission. The Viking representative was an observer on this team during the prime Mariner 9 mission, and an equivalent member during the extended phase of the mission, beginning in June 1972. Viking's recommendations for special scientific measurements were made through this team.

As a result of this activity, the Viking MM'71 Participation Group has had access to early results to assess the effects of the findings to date on Viking, to identify areas of interest to Viking, and to gain valuable experience in mission planning and operations.

1.2 ORGANIZATION AND OBJECTIVES

A Viking Mariner Mars '71 Participation Group was formed to participate in the MM'71 Mission. The manager of the group was R. A. Schmitz and was assisted through the prime phase of the mission by R. R. Peterson. The Viking Data Analysis Team (VDAT), a major component of the group, was formed to evaluate and correlate the Mariner 9 results and to make recommendations based on these evaluations for consideration in the SRT. The VDAT, composed primarily of Viking scientists knowledgeable in both the scientific and engineering characteristics significant to site selection, participated through the prime phase of the mission. The objectives of the VDAT were to (1) utilize the MM'71 science data for selection and evaluation of potential landing areas, and (2) to present recommendations for better satisfying Viking needs in the MM'71 Mission for consideration in mission planning. A more detailed discussion of the VDAT organization, objectives and members are contained in the document Organization and Operation of Viking Data Analysis Team in MM'71

Mission Operations dated October 20, 1971. Copies of this document can be obtained from R. A. Schmitz. The major VDAT participants in the MM'71 Mission, and their areas of interest are as follows:

Terrain mapping and photo-analysis	T. A. Mutch, Brown University H. J. Moore, U.S.G.S.
Correlation of UV Spectrometer and IR Spectrometer results	J. Gliozzi, MMC F. Bartko, MMC
Topography map preparation	A. B. Binder, IIT Research Inst.
Analysis and correlation of condensates and dust in the atmosphere	W. A. Baum, Lowell Observatory
Analysis and interpretation of ground-based radar	H. J. Moore, U.S.G.S.
Soil properties; soil-water relationship and permafrost	D. M. Anderson, U.S. Army, Cold Regions Research Eng. Lab.
Infrared Radiometer results	R. W. Shorthill, Boeing

1.3 PURPOSE OF REPORT

The purpose of this report is to summarize the activities of the Viking Data Analysis Team, including the on-site participation, data correlation and analysis activity and the meaning of the preliminary results to the Viking mission planning. This report includes an assessment of the status of the analysis of the Mariner 9 data and identifies areas where problems still exist. Also included are some recommendations for follow-on analysis and studies that are considered important to the success of the Viking mission. The Mariner 9 results were compared and correlated with some of the earth-based data. In addition, some of the earth-based data were used in identifying target areas for the extended mission. However, there are many more earth-based results that are not included or discussed in this report that should be considered in the continuing and more detailed process of site selection.

This report includes the planning and preparation activities for the on-site activities. The near-real-time plotting and analysis are also discussed, including the many products prepared to support this activity, or resulting from the on-site activity. A list of these products is included in Appendix A.

An opportunity to obtain measurements of areas of interest to Viking was present during the extended phase of the Mariner 9 Mission; this activity is discussed in Section 5.

2.0 VIKING DATA ANALYSIS TEAM ACTIVITIES AND PRODUCTS

Viking Data Analysis Team (VDAT) activities and products included: (1) planning and setting up the physical layout of the VDAT trailers, (2) manning the facilities during the Mariner 9 operations, (3) preparing various grids and plots of Mariner 9 data, and (4) performing near-real-time analyses.

2.1 PREPARATION AND VDAT PARTICIPATION

Consistent with the VDAT's recommendations, two office trailers (approximately 900 square feet) were obtained and installed near the Spacecraft Assembly Facility (SAF) area at JPL. The trailers were furnished with drafting tables and support equipment, filing and storage facilities for the various data products, and office space.

The Mariner 9 Mission developed in such a manner that near-real-time inputs were not required, or possible, to effect the mission planning in a timely fashion. The less adaptive, and more systematic mission planning scheme, plus the fact that reduced data were not available for long periods of time, resulted in a more relaxed manning schedule. During the mission, at least one Viking Project representative (R. A. Schmitz, the manager of the group or his alternate, R. R. Peterson) was present to participate in the mission operations and SRT meetings. The secretary and the draftsman were on duty during each week of the mission. U.S. Geological Survey personnel were on duty nearly continuously from the beginning of the mission to the end of Cycle 4 (November 23, 1971 to March 17, 1972). USGS personnel participation, in order of time spent on VDAT, are M. Grolier, H. Moore, B. Lucchitta, D. Stuart-Alexander, C. Hodges and R. Lugn. The major participants of the VDAT members were H. Moore, T. Mutch, J. Gliozzi, F. Bartko, A. Binder, W. Baum, R. Hutton, D. Anderson, and R. Shorthill.

Grids at scales of 1:25, 000, 000 and 1:5, 000, 000 were prepared on transparent scale-stable bases using a Mercator Projection (Ref. 1) tangent to the Martian equator, and equatorial radius of 3393.4 km, and a flattening of 1/192. Grid coverage at a scale of 1:25, 000, 000 included 360° of longitude and 130° of latitudes (65°N to 65°S). Grid coverage at a scale of 1:5, 000, 000 included 45° of longitude and 35° of latitude for terrain maps, and 45° of longitude and 45° of latitude for plotting grids. The following grids were produced by the USGS and made available to VDAT:

Grid Type	Number
1:25, 000, 000 Grids	50
1:5, 000, 000 Mapping Grids	48
1:5, 000, 000 Plotting Grids	32

Plots at a scale of 1:25, 000, 000 and 1:5, 000, 000 were prepared by the USGS. Pre-mission contour maps of elevation, radar cross-section, rms slopes, and pressure obtained by Haystack Observatory (Lincoln Laboratory, 1970) at a scale of 1:25, 000, 000 were available in the VDAT trailer. Additionally, radar occultation data and elevation estimates were plotted at the same scale along with generalized Haystack Radar elevation data obtained in 1971. Available elevation contour maps prepared by MM'71 UVS and IRIS teams were plotted at 1:25, 000, 000 near the end of the mission.

Plots at a scale of 1:5, 000, 000 were also prepared by the USGS. Haystack radar results from 1967 and 1969 were available pre-mission, and subsequently revised as a result of revisions made by Haystack. Haystack also furnished their 1971 data which was plotted at the same scale. Generalized Goldstone elevation data (1969 and 1971) furnished by D. A. O'Handley and detailed 1971 Goldstone elevation data furnished by R. M. Goldstein were also plotted at 1:5, 000, 000 (Refs. 2 and 3).

Mariner Mars 1969 IR and UV elevation data were plotted at 1:5, 000, 000 and available at VDAT pre-mission. Elevations furnished by UVS (MM'71) were plotted at 1:5, 000, 000.

2.2 NEAR-REAL TIME ACTIVITIES

Near-Real Time Plots made at a scale of 1:25, 000, 000 were: (1) Footprint plots and (2) detailed "Mini-Terrain" plots. The Footprint plots were used to assess image quality during the early dusty phases of the mission, as a base to prepare the "Mini-Terrain" map during the mapping phases of the mission, and to help locate images that were stereoscopic pairs during the final phases of the mission. Initial Footprint plots were prepared by hand but, during the middle part of the mapping mode, they were traced from computer plots. The "Mini-Terrain" map was prepared in near-real-time by sketching craters, lineaments, and other features in each frame of the Footprint plots. Since the plots were on matching transparent grids, this could be done readily. Later, the "Mini-Terrain" map was generalized to define terrain units. At a scale of 1:25, 000, 000, near-real-time plots were available to VDAT of the footprints, "Mini-Terrain" Map and Generalized Terrain Map.

A preliminary terrain map of Mars Chart 14 was prepared, at a scale of 1:5, 000, 000, using the footprint and imagery data. The photos were assembled in near-real-time to provide mosaics of the Viking zone. Several elevation contour plots at a scale of 1:25, 000, 000 were prepared using the earth-based radar and radio occultation data. The white cloud frequency occurrence was plotted at a scale of 1:25, 000, 000 for comparison with other data and the course of the global dust storm was also plotted.

Analyses performed in near-real-time are summarized below. During the earliest phase of the mission, surface obscuration, due to the dust storm, was studied by examination of the imagery and pre-mission data on the dust storm. Initially, only the South Polar region, Nix Olympica, North Spot, Middle Spot, and South Spot were visible. Evidence showed that the dust storm was clearing with time. This work was continued, and it was found that obscuration of the surface was (1) decreasing with time, (2) less in the more southerly latitudes, (3) less at higher elevations, and (4) also possibly a function of time of day. Additionally, image quality of the surface was dependent on the lighting angle and viewing angle. Small viewing angles of 0 to 5 degrees (nearly vertical) resulted in better imagery of the surface and lighting angles between 45 to 70 degrees (SEA angles of 45 to 30 degrees) produced better imagery of the surface. Reports on these results were furnished to the MM'71 TV team as the results were obtained prior to and during the first part of the first mapping cycle. Continued studies by VDAT, as late as the end of Cycle 3, showed that obscuration of the surface was still present near the North Pole, in some low areas, possibly around Nix Olympica, and areas mapped as "Smooth Plains".

Haystack dielectric constants, rms slopes, and elevations were analyzed. Initial analyses of the dielectric constants for 1967 and 1969 data showed they were incredibly small and averaged 1.74. At VDAT's request, Haystack Observatory reexamined the data, resulting in new values which averaged 2.1 for the 1967 data and 2.8 for the 1969 data. The Haystack 1971 data for average dielectric constant was 3.6. Dielectric constants were found to correlate weakly with rms slopes; detailed analysis showed that this was not true for many areas.

Mariner Mars '71 radar data were plotted at a scale of 1:25,000,000 and elevations calculated were compared with Haystack and Goldstone elevations. Discrepancies as large as 5 km were found. Two elevation contour maps were prepared at a scale of 1:25,000,000 using radar occultation data and Haystack data. From these analyses and efforts, discrepancies between the two sets of data (occultation and Haystack) were reduced to 3 km and less.

Using the 1:5,000,000 terrain map, a good correlation was found between the terrain units and Haystack radar data. In particular, the "Smooth-1" unit was found to have an average rms slope of 2.2 degrees while the "Rough-1" unit had an average rms slope of 4.3 degrees. The average dielectric constant for "Smooth-1" was 1.9 and for "Rough-1" was 3.7. The exceptionally low average dielectric constant of "Smooth-1" showed that roughness is not the only criteria for a landing site. Similar analyses of other terrain units yielded the same result.

The Mariner Mars '71 photos were scanned for stereopair imagery and the results were sent to photogrammetrists at the USGS Flagstaff Office.

VDAT also participated in Mariner '71 targeting for Cycle 4 and expressed a desire to see the following achieved during Cycle 4:

(1) Any image "gores" in the Viking zone should be filled during Cycle 4; (2) Additional imagery in low areas is desirable to see if dust settling continues; (3) Additional imagery using low sun elevation angle (SEA ≈ 15°) is needed in areas like Isidis Regio to see if there was any roughness that is lost using existing imagery with high sun elevation angles (SEA ≈ 60°), and; (4) Stereocoverage of areas where large amounts of relief are found. The imagery was studied and Mars Chart quadrangles were prioritized for potential Viking landing sites. Choices for first priority were: MC-8, MC-11, MC-16, MC-19, MC-20, MC-22, and MC-23; second priority were: MC-10, MC-12, MC-13, MC-14, MC-15, MC-18, and MC-21. Quadrangles MC-9 and -17 were eliminated because they were low pressure regions. Recommended Viking targets were listed with the criteria for selection. Unfortunately, due to a spacecraft anomaly, science data taking was suspended for a period of time when some of these targets were scheduled for coverage.

2.3 REFERENCES

1. Thomas, Paul D., 1952, Conformal Projections in Geodesy and Cartography: U.S. Dept. of Commerce Coast and Geodetic Survey Special Publication 251.

2. Goldstein, R. M., 1971 Mars Radar Data (unpublished).

3. O'Handley, D. A., 1971 Mars Radar Data (unpublished).

3.0 MARINER MARS '71 PRELIMINARY RESULTS

3.1 INTRODUCTION

The science payload of the Mariner 9 spacecraft was selected to include a complementary array of imaging, photometric, spectroscopic and communications experiments. This payload was intended to provide the most comprehensive investigation of the physical properties and structure of the atmosphere and surface of Mars to date. The original objectives and expectations have been met and, in some cases exceeded, in spite of the presence of a major global dust storm early in the mission. The results of this mission clearly have increased our knowledge of the planet by orders of magnitude and will have a major impact on the Viking mission planning.

Six carefully selected experiments comprise the scientific instrumentation on Mariner 9. All science instruments are mounted on a movable platform underneath the spacecraft. The scan platform and its control system provide the ability to target the instruments even though the spacecraft is inertially stabilized. All experiments are bore-sighted. Platform motions are permitted in clock and cone angles with a pointing accuracy of about one-fourth of a degree.

The six experiments consist of the IRIS and UVS spectrometers, the infrared radiometer (IRR), the TV cameras, and the Celestial Mechanics and S-Band occultation experiments which utilize the communication and navigation subsystems of the spacecraft.

The design and operation of all of these experiments have been adequately reported in the literature and the intent of this report is to only briefly describe each and summarize the early results and activities. A later section includes recommendations for follow-on analysis of the data.

3.1.1 Infrared Interferometer Spectrometer (IRIS)

The infrared spectroscopy experiment on Mariner 9 was designed to provide information on atmospheric and surface properties by recording a major portion of the thermal emission spectrum on Mars. The original objectives included derivation of vertical temperature profiles, surface temperatures, atmospheric pressure at the surface, and information related to the surface composition. The experiment also searched for minor atmospheric constituents, including water vapor and isotopic components of carbon dioxide.

The IRIS instrument is a Michelson infrared interferometer spectrometer which records the spectral interval from 200 cm^{-1} (50 μm) to about 2000 cm^{-1} (5 μm) with a nominal spectral resolution of 2.4 cm^{-1}. The field of view is almost circular with a half cone angle of 2.25°. At periapsis, the full angle projected field of view encompasses about 130 km on the surface. Wavenumber calibration is provided by a fringe control interferometer that uses the 0.6926-μm line of a neon discharge source as a standard. Intensity calibration is achieved by scaling Mars spectra to calibration spectra recorded periodically while alternately observing deep space and a 296°K onboard blackbody. After Fourier transformation and scaling of the raw spectra in an earth-based digital computer, the individual calibrated spectra are displayed in absolute radiometric units as a function of wavenumber.

The IRIS experiment was relatively less impaired by the presence of the dust storm early in the mission. In fact, the early data acquired by IRIS, in conjunction with later data, will be extremely useful in studies of the time dependence of the atmospheric structure under the influence of a major disturbance. Such studies will provide a greater physical understanding of the Martian atmosphere and its interaction with the surface.

Some typical results obtained by IRIS in the initial mission stages are shown in Figure 3-1. The spectra obtained are plotted in terms of radiance as a function of wavenumber. Part (a) shows a nominal mid-latitude spectrum while (b) illustrates values found over the South Polar Cap region. Major features common in these spectra are the two broad regions at 400 to 600 cm^{-1} and 850 to 1250 cm^{-1} which appear in absorption in the non-polar spectra and in emission in the polar spectra, and the molecular absorption by CO_2 in the range of 540 to 800 cm^{-1}. The difference in appearance of the spectra have been ascribed to differences in the atmospheric temperature profile, the underlying lower boundry surface, and the amount of dust in the atmosphere. In most of the non-polar spectra, all of the molecular bands of CO_2 appear in absorption, indicating that the atmospheric temperatures decrease with height on a gross scale. In the polar spectrum, the parts of the spectrum from 550 to 625 cm^{-1} and 700 to 800 cm^{-1} appear in emission, indicating that the lower atmospheric regions in which this radiation originates is at a warmer temperature than the underlying surface. The direct effect of the atmospheric dust on the emission spectra is most striking. The entire spectrum, with the exception of the strongly absorbing part of the 667 cm^{-1} (15 μm) CO_2 molecular band apparently is influenced to varying degrees by the opacity of the dust in the atmosphere.

The diffuse features shown near 470 and 1075 cm^{-1} have been attributed to dust particles in the atmosphere. The properties of these features are characteristic of SiO_2 bands in silicate-bearing minerals. Numerous investigators have shown that the spectral positions of absorption and reflection peaks depend on the silica content; acidic minerals (70 to 75% SiO_2) suspended in powder form, absorb most strongly at 1100 cm^{-1}, while ultra-basic materials (less than 45% SiO_2) show absorption peaks near 950 cm^{-1}. A preliminary comparison of the emission features measured over the south polar region with laboratory absorption spectra of fine dust shows generally good agreement with minerals and rocks whose SiO_2 content is in the intermediate range (55 to 65%). The silicates are also indicated in non-polar areas.

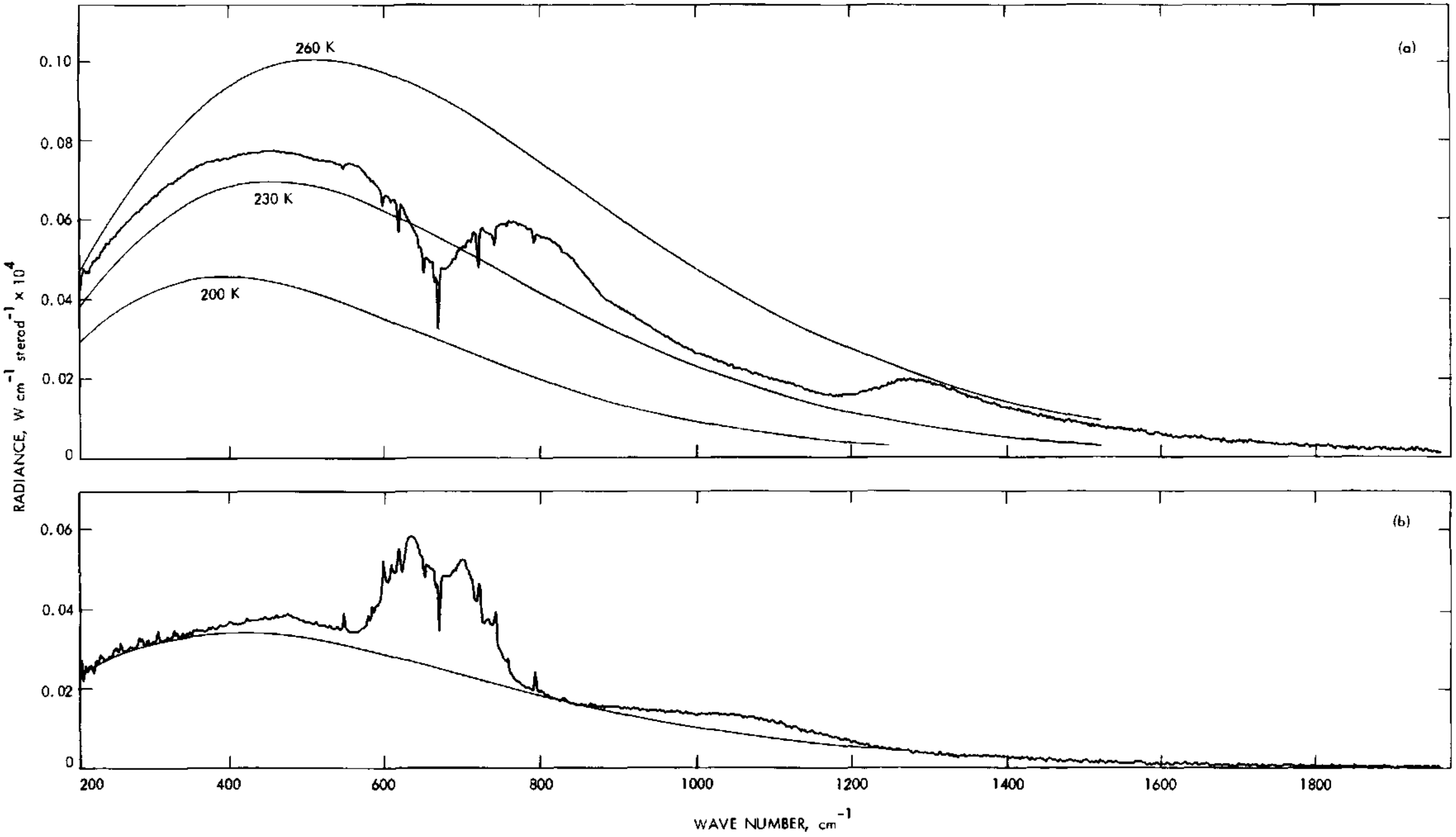

Figure 3-1. Mariner 9 IRIS Spectra

Spectra similar to these have been accumulated over much of the planet for the duration of the mission. These are presently under detailed investigation to yield results in fulfillment of the original experiment objectives.

3.1.2 Ultraviolet Spectrometer (UVS)

The UVS instrument is an Ebert-Fastie spectrometer sensitive in two channels, 1450-3500Å and 1100-1900Å. The field of view of the first channel is 0.20 by 0.55 degrees; channel 2 is 0.20 by 2.0 degrees, For channel 1, the effective field of view on the surface is ~ 20 km A single spectral scan is accomplished in 3 seconds. These two channels provide data for topographic mapping of the surface and lower atmosphere (channel 1), and data for aeronometric studies (channel 2).

The upper atmosphere measurements are performed by observing the sunlit limb of the planet as the spacecraft motion causes the field of view of the instrument to pass through successively lower levels of the atmosphere. Measurements of the lower atmosphere are obtained by pointing the instrument directly at the area of the planetary disk that is being mapped. The Mariner 9 spectrometer is similar to those used on Mariners 6 and 7 and OGO-4. (Ref. 24).

Some typical results of Martin limb spectra obtained by UVS on Mariner 9 are shown in Figures 3-2 and 3-3 (channels 1 and 2 respectively). Figure 3-2 illustrates bands of CO and CO+, as indicated (Ref. 1). Figure 3-3 shows bands of CO and lines of atomic carbon. The intensities of these spectral features are functions of altitude and the corresponding limb scans may be used to infer the scale heights of these emissions and the temperature of the upper atmosphere.

Figure 3-4 indicates some typical reflectance data obtained from channel one. The overall spectral shape is determined by the ratio of molecular to particulate scattering within the atmosphere. Although the early mission data of this type was hampered in inferring surface pressure mapping by the dust storm, subsequent results have been used for topographic mapping studies.

3.1.3 Infrared Radiometer (IRR)

The IRR instrument is a two-channel radiometer designed to measure equivalent black-body surface temperatures with high spatial resolution. Two spectral channels, 8-12μ and 18-25μ cover the range of temperature from 140°K to 325°K, with a temperature resolution of about 0.5°. Provisions are made for adequate in flight calibrations and calibration checks. The output of each channel is proportional to the difference in radiance between space and the planetary surface. The field of view is approximately 0.7° x 0.7° for each channel. At periapsis, the corresponding linear scale on the planet's surface is about 20 km.

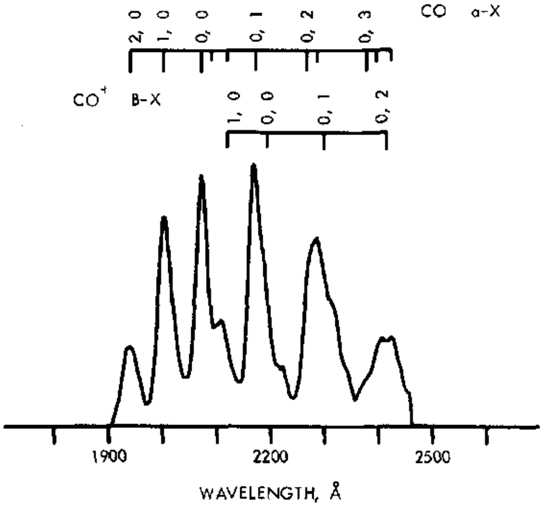

Figure 3-2. UVS Spectrum, 1900-2500Å

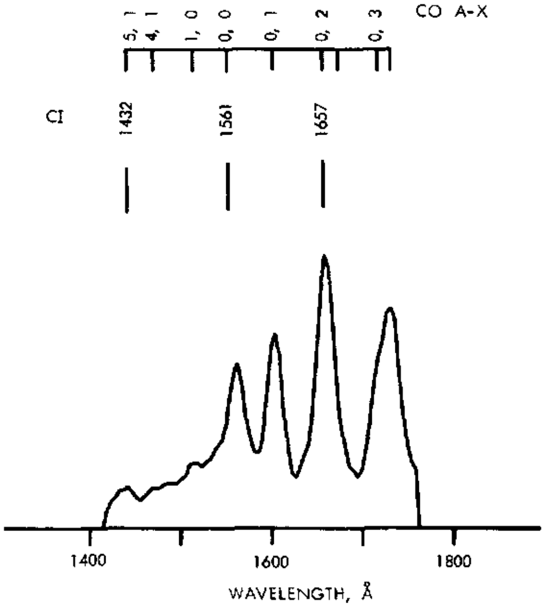

Figure 3-3. UVS Spectrum, 1400-1800Å

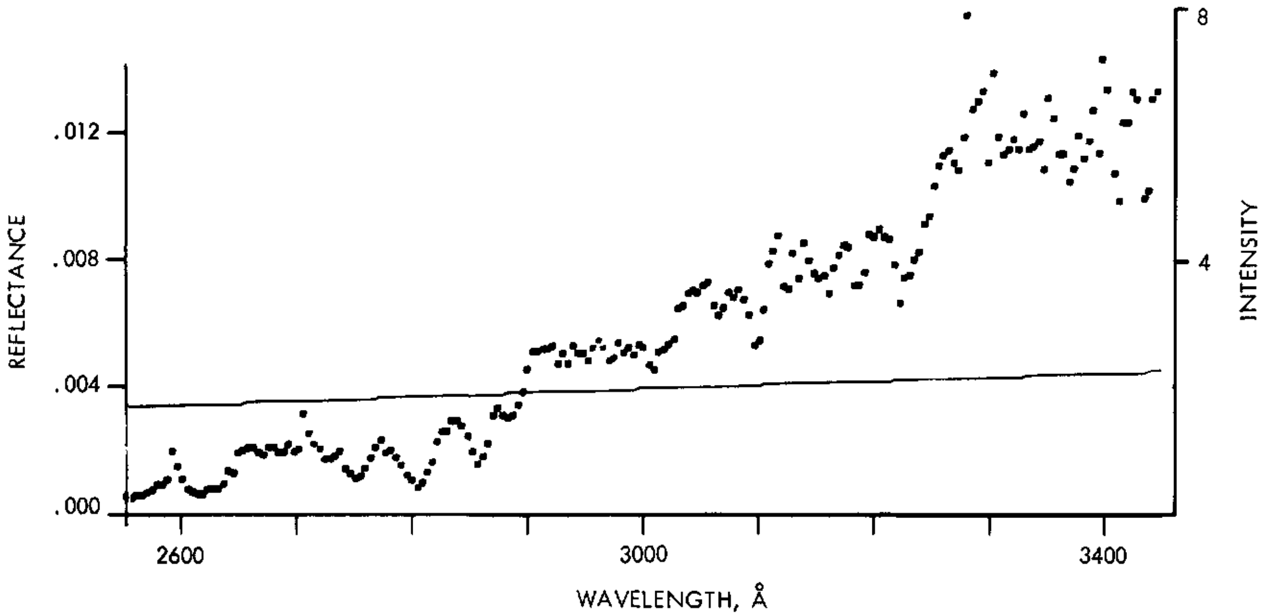

Figure 3-4. UVS Reflectance Spectrum, 2600-3400Å

Early IRR results were hampered by lack of adequate control data and, like the TV experiments, by the prevailing global dust storm. Early thermal scans could not be represented by the mean thermal model developed from the Mariner 1969 results (see Figure 3-5). After subsidence of the dust storm, good fit with the mean thermal model have been obtained and detailed investigations are in progress.

3.1.4 Television Subsystem

The television subsystem on Mariner 9 consists of two photometrically calibrated cameras mounted on the spacecraft planetary scan platform, with supporting electronics housed in the bus portion of the spacecraft. The wide- and narrow-angle optics and some portions of the electronics are identical to the Mariner 6 and 7 television subsystems. The wide-angle camera has a field of view of 11 by 14 degrees, utilizes a six-element lens and is equipped with a filter wheel that can be commanded to place any one of eight spectral and/or polarizing filters in the optical path. The narrow-angle camera has a field of view of 1.1 by 1.4 degrees, and utilizes a 200-mm-diameter Schmidt-Cassegrain telescope with a single fixed filter. The resolution of surface features in the field of view of each camera is dependent on the slant range from the cameras to the planetary surface. With the

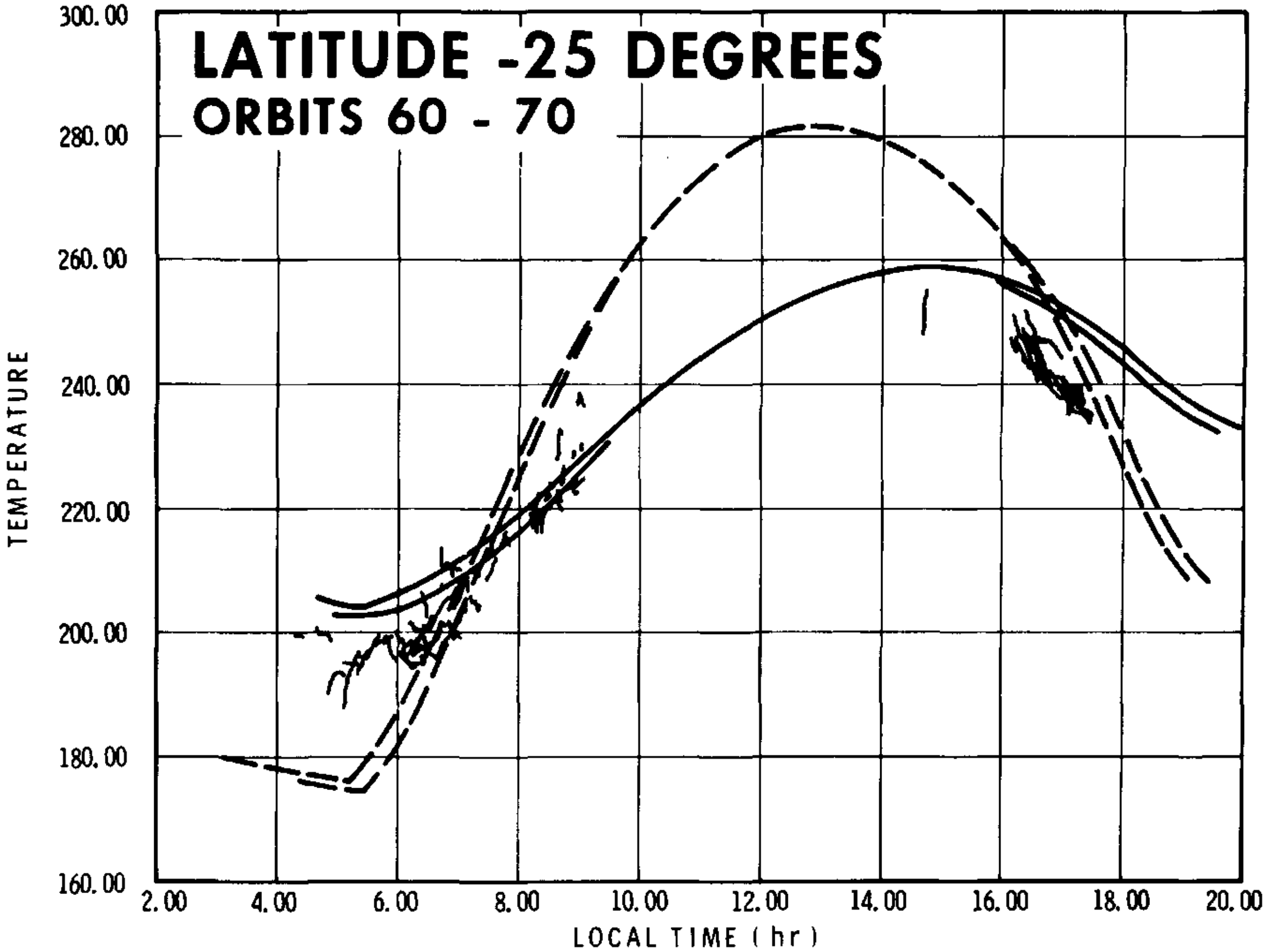

Figure 3-5. Comparison of IRR thermal scan with mean thermal model

cameras pointed in the nadir direction and the spacecraft at an altitude of 1600 km, surface resolution in the wide and narrow-angle cameras corresponds to about 1 and 0.1 km, respectively. Both cameras have focal-plane shutters, similar to the type used on the Mariner 1969 television cameras. After passing through the filter and shutter, the optical image is focused onto a slow scan vidicon.

The video signal is processed by a video amplifier, then bandpass filtered, amplified, and refiltered. The signal is then demodulated, synchronous with the vidicon cathode chopping input. The demodulated video signal is amplified and low-pass-filtered to produce baseband video reconstruction, which is converted to a digital signal that forms 832 nine-bit words for each of the 700 television lines. The digital signal is transmitted to the Data Automation Subsystem (DAS), where it is rate-buffered and formatted for input to the spacecraft's digital tape recorder. There it is stored until playback, at a lower bit rate, to the Deep Space Network to be recorded and reconstructed into a picture. Most picture playbacks used the 210-ft antenna at Goldstone, California. The cameras may be operated by either ground command or programmed in an automatic mode until the tape recorder is filled (approximately 32 pictures). Further details on this experiment are documented and available in the literature (Ref. 21). A number of examples taken from the vast collection of photographs acquired by the cameras on Mariner 9 are presented in following sections of this report.

3.1.5 S-Band and Celestial Mechanics

Both the S-Band occultation and the Celestial Mechanics experiment rely on the Mariner 9 spacecraft radio tracking and navigation system. The Celestial Mechanics experiment uses two-way Doppler and range data acquired through the Deep Space Network facilities. The accuracies achievable on these data, in conjunction with the Mariner orbital parameters, are sufficient to provide significant improvements in the Martian ephemeris and gravity field.

The S-Band occultation experiment consists of observing changes in the frequency, phase, and amplitude of the S-Band tracking and telemetry signal of the spacecraft immediately before and after occultation of the spacecraft by the planet. An important factor in the successful execution of this experiment is the selection of an orbit that achieves the maximum number of Earth occultations at different latitudes on Mars. The spacecraft signals are refracted by the ionosphere and the neutral atmosphere of Mars, both on its way to the spacecraft and on its return after being coherently retransmitted by the spacecraft transponder. The changes in frequency and phase introduced by this two-way passage through the atmosphere and ionosphere are accurately measured when the orbit of the spacecraft is known to a sufficient degree of precision. These changes are then used to infer the refractivity profile of the Martian ionosphere and atmosphere. In turn these data are reduced to a profile of electron density of the ionosphere and the number density of the atmosphere. To obtain the pressure and mass density, the composition and temperature are required. However, the refractivity profile provides a measure of the local scale height. This in turn yields the mean molecular weight when the temperature is known from other measurements. Also, the exact observation of the times of extinction and reappearance of the signal, when correlated with trajectory and atmospheric density information, yields the radius of the planet at the points of tangency with an accuracy of about 0.5 km. A precise measurement of the radius at many different latitudes then allows an accurate determination of its physical figure. Additional features and details regarding these experiments appear, for example, in Volume 12 of Icarus.

A careful analysis of the Martian gravity field and its irregularities by the Celestial Mechanics team, has provided significantly new basic information on the dynamical shape of the planet and additional results concerning surface topographic effects. The regional topographic effects incorporated in the gravitational potential model have been compared with earth-based radar data indicating surpirsingly good agreement (see Figure 3-6).

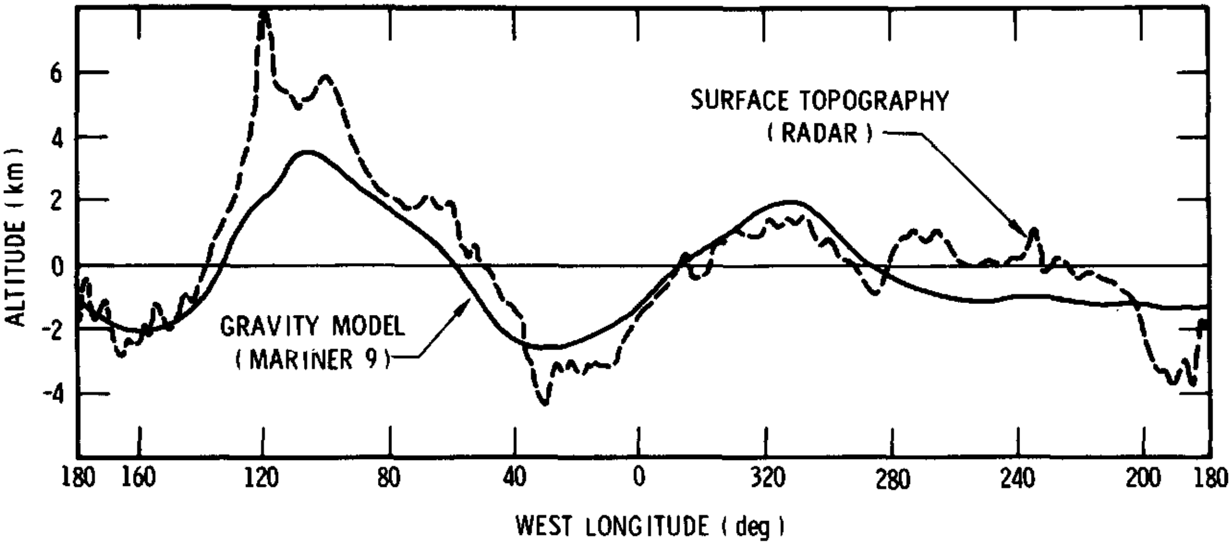

- RADAR FROM GOLDSTONE AND HAYSTACK TAKEN DURING SUMMER OF 1971.
- GRAVITY PROFILE FROM MARINER 9 DATA TAKEN BETWEEN 16 NOVEMBER AND 4 DECEMBER 1971.

Figure 3-6. Mariner 9 gravity model compared with Earth-based radar topography

Some of the early results from the S-Band occultation experiment have also centered on topographic analysis. Elevation differences of about 14 km have been indicated (see Figure 3-7). Further results from these and the other experiments on Mariner 9 are illustrated and discussed in subsequent sections.

3.2 SURFACE INVESTIGATIONS

3.2.1 Surface Imagery and Mapping

No attempt at a comprehensive summary of the TV mapping and specialized investigations will be attempted here. Justice cannot be done to the many photographs and associated interpretations acquired and supplied by the TV team. In this brief summary, we wish only to illustrate several examples of important surface features found during the fixed features, variable features and mapping investigations of the TV subsystem, that may have a special bearing on the Viking Mission.

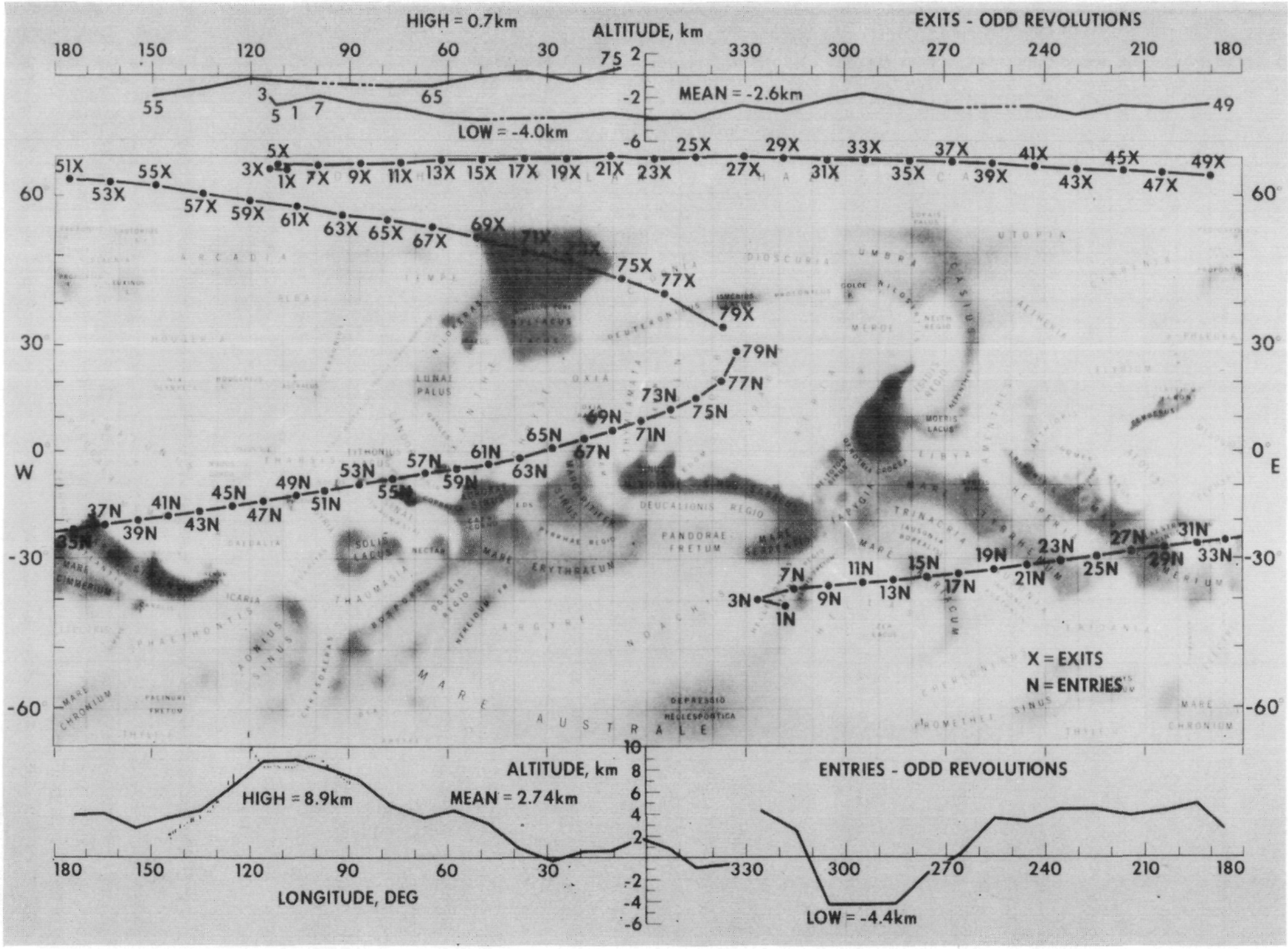
HIGH = 0.7km
ALTITUDE, km
EXITS - ODD REVOLUTIONS
MEAN = -2.6km
LOW = -4.0km
180
150
120
90
60
30
330
300
270
240
210
60
30
0
-30
-60
W
E
51X
53X
55X
57X
59X
61X
63X
65X
67X
69X
71X
73X
75X
77X
79X
1X
3X
5X
7X
9X
11X
13X
15X
17X
19X
21X
23X
25X
27X
29X
31X
33X
35X
37X
39X
41X
43X
45X
47X
49X
1N
3N
7N
9N
11N
13N
15N
17N
19N
21N
23N
25N
27N
29N
31N
33N
35N
37N
39N
41N
43N
45N
47N
49N
51N
53N
55N
57N
59N
61N
63N
65N
67N
69N
71N
73N
75N
77N
79N
X = EXITS
N = ENTRIES
ALTITUDE, km
ENTRIES - ODD REVOLUTIONS
HIGH = 8.9km
MEAN = 2.74km
LOW = -4.4km
LONGITUDE, DEG
10
8
6
4
2
-2
-4
-6

Figure 3-7. S-Band occultation topography

A brief, selected sample of photographs acquired during the fixed features, variable features, and mapping studies is presented here. This sample is by no means complete but is representative of the diverse surface features discovered during the course of the mission. No attempt is made at interpretation of these phenomena, but the samples shown are suggestive of the variety and complexity of surface phenomena and indicative of the potential hazards confronting the Viking lander. In that regard, they indicate the many compromises to be made due to restrictions imposed by lander capabilities and by the high degree of scientific interest and merit indicated for potential Viking locations.

Figure 3-8 illustrates a computer enhanced mosaic of Nix Olympica, whose summit was seen early in the mission above the dust clouds, and is representative of several large volcanic calderas found on the Martian surface. A great equatorial chasm, with branching canyons eroding the adjacent plateaulands, is shown in Figure 3-9, with a corresponding UVS elevation scan. This is a feature apparently unique to Mars in landform evolution, 120 km in width, 6 km deep, and 4000 km long.

A plateau area in Phoenicis Lacus is shown in Figure 3-10. This region illustrates the complex faulting zones cutting the surface into mosaic-like fragments. The presence of only a few craters suggests that this area is relatively young. Figure 3-11 presents a complex network of canyons on the fractured volcanic tablelands in Noctis Lacus, and is indicative of the erosional processes at work. A large oval tableland near the south pole appears in Figure 3-12. The light and dark contours are felt to represent layered deposits of dust or volcanic ash, and possibly CO_2 and H_2O ices. Figure 3-13, shows the north polar region. Here the older cratered terrain is apparently overlain by the younger glacial-aeolian layer rocks. The tilted, layered rocks suggest a depression of the Martian crust by overlying ice in this polar region.

An extensive sinuous valley is shown in Figure 3-14 and is suggestive of fluid flows and erosion. Other small but frequent erosional channels appear in Figure 3-15 in heavily cratered terrain.

Finally, Figure 3-16, a mosaic of high resolution camera photos of a dark area seen within a crater, demonstrates a pattern strongly suggestive of a sand dune field. More complete descriptions and interpretations of these features, and many more found during the Mariner 9 mission may be foun d in Reference 22.

Several results from variable features studies are included here. Again no attempt at completeness is made, and reference is made to the TV team publications for more extensive discussions. The gradual break-up and disappearance of the south polar cap is shown in the high resolution camera photo composite in Figure 3-17. The gradual degradation of the residual subliming frost cap is clearly seen in the time interval covered by the indicated orbits.

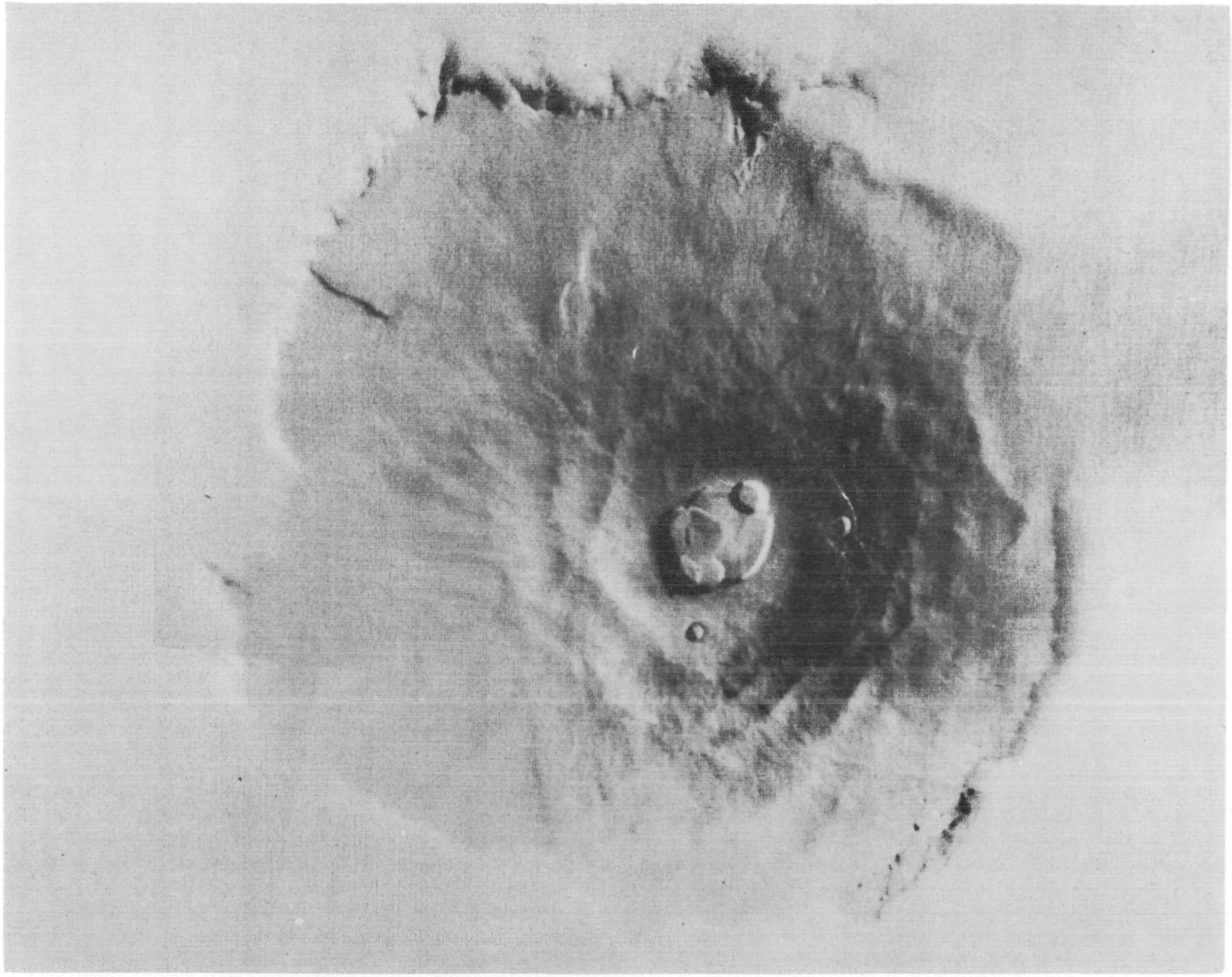

Figure 3-8. Enhanced mosaic of Nix Olympica

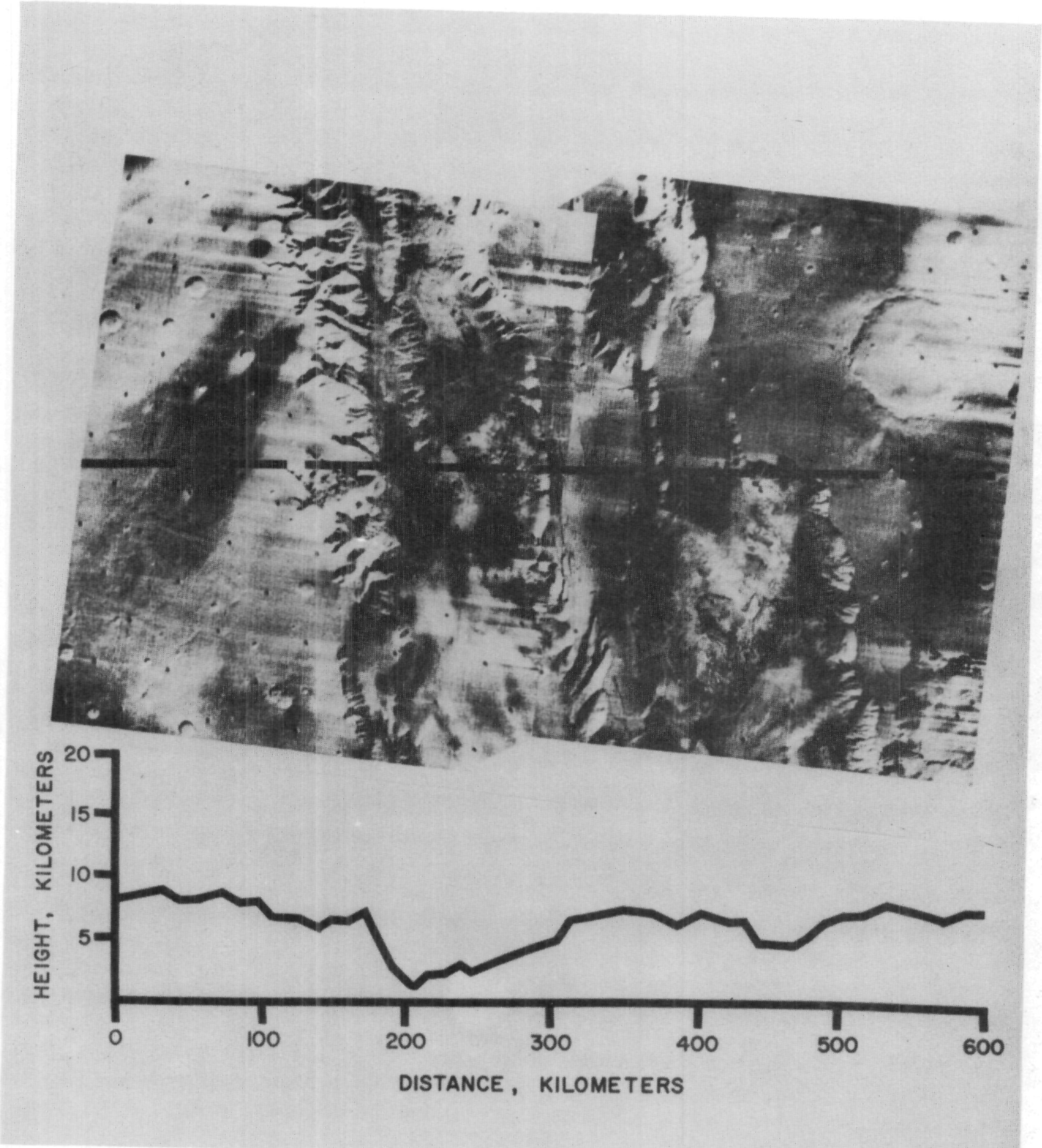

Figure 3-9. Great Equatorial Chasm with UVS elevation scan

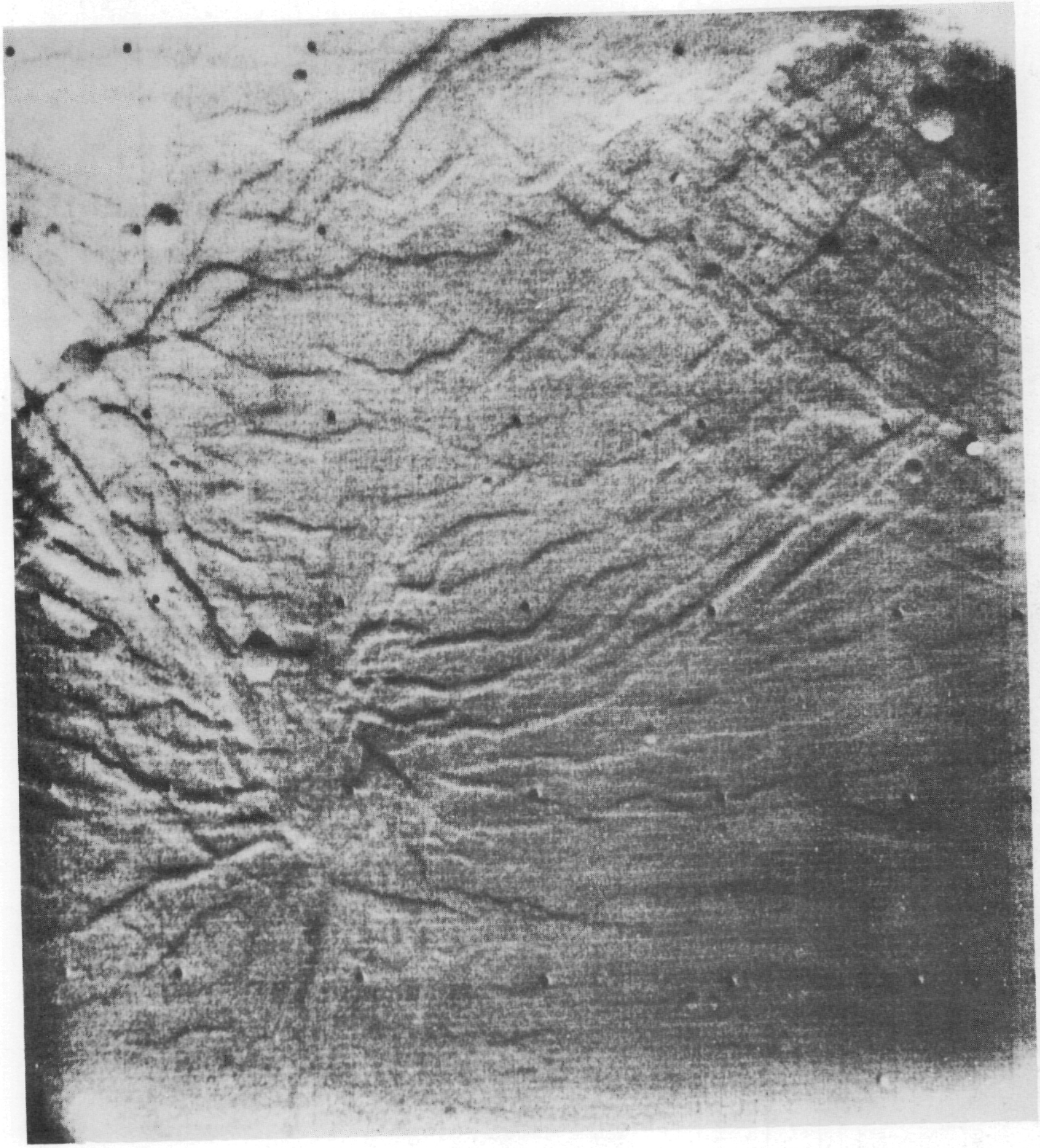

Figure 3-10. Plateau area in Phoenicis Lacus

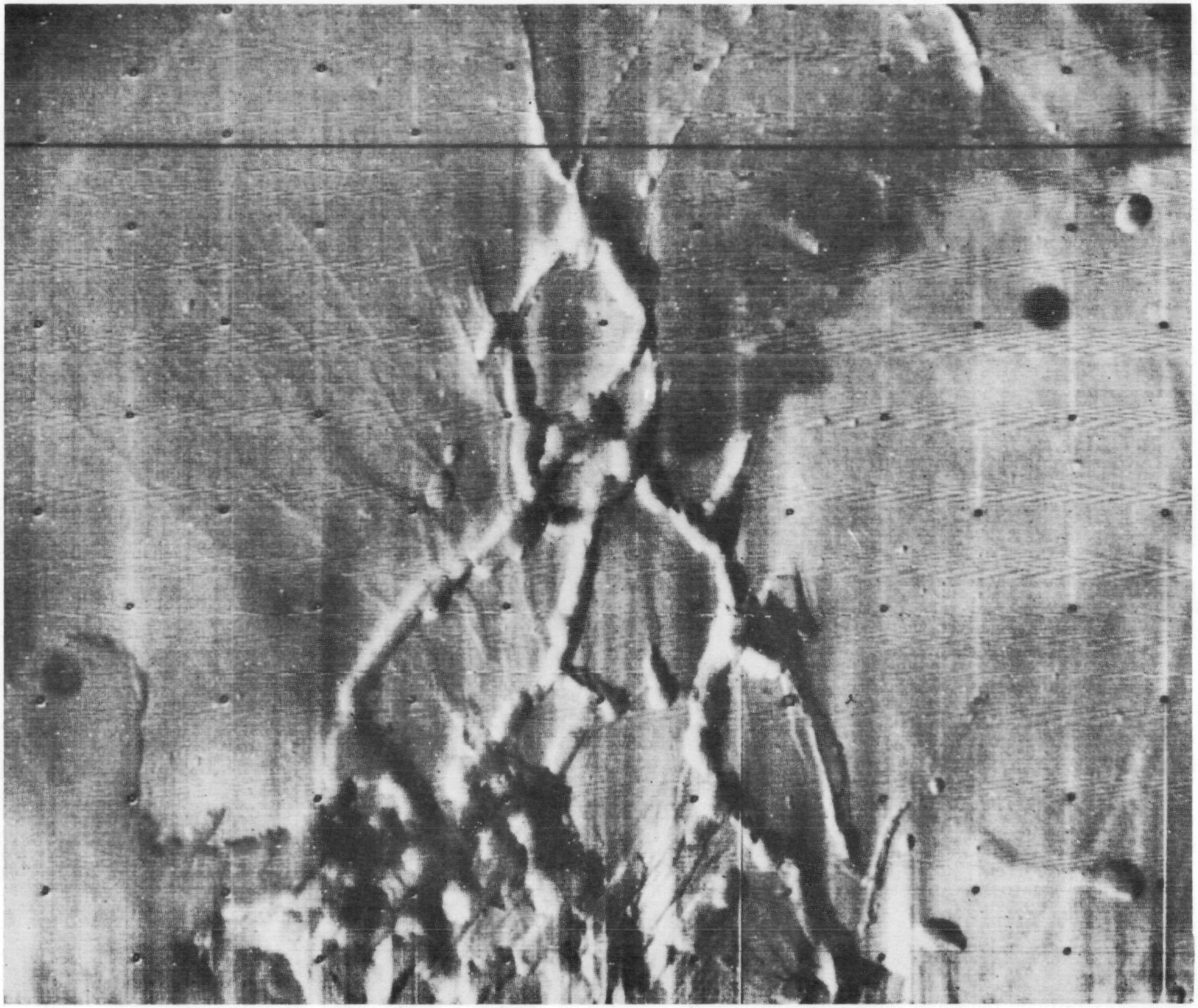

Figure 3-11. Canyonlands in Noctis Lacus

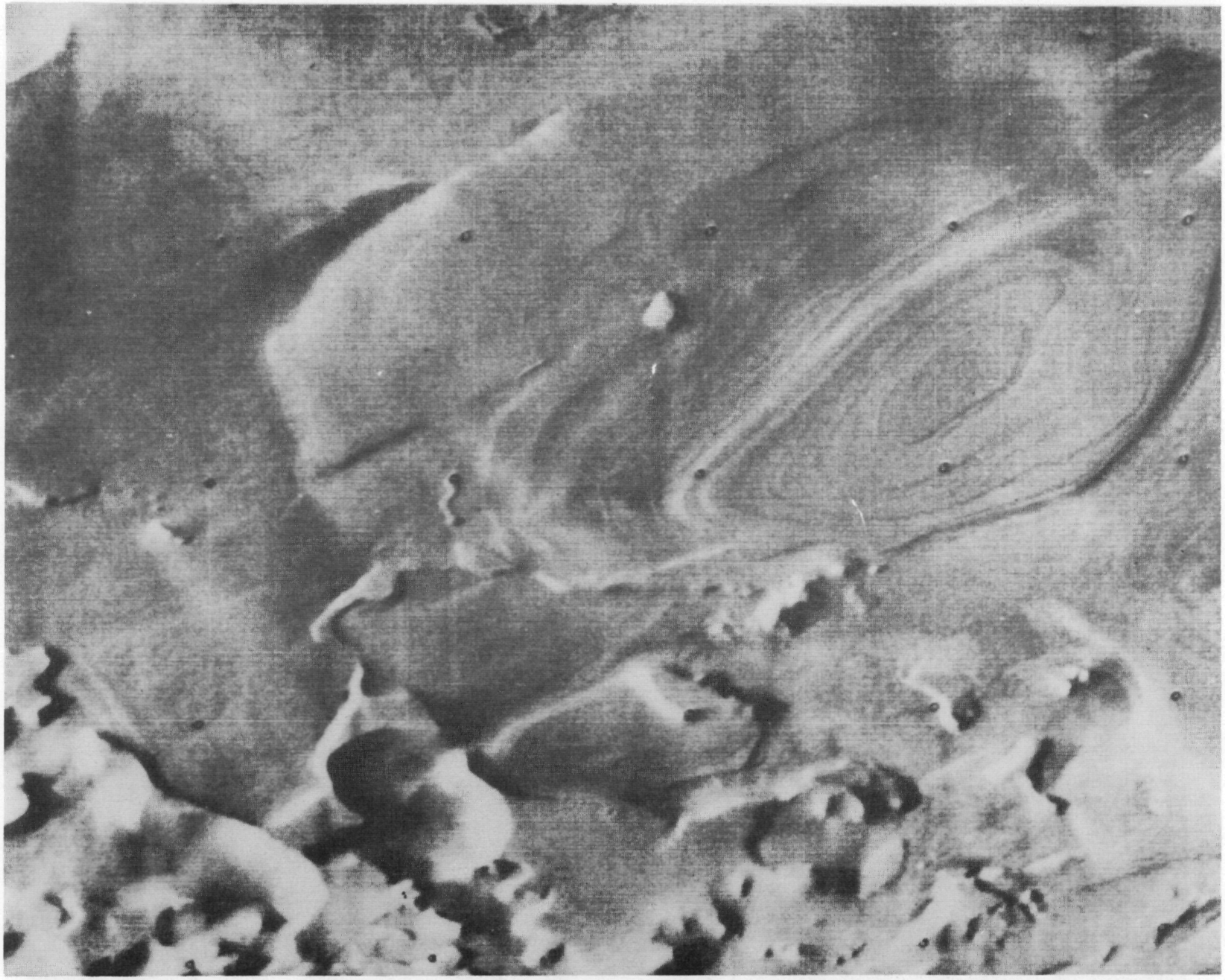

Figure 3-12. South Polar Region Tableland

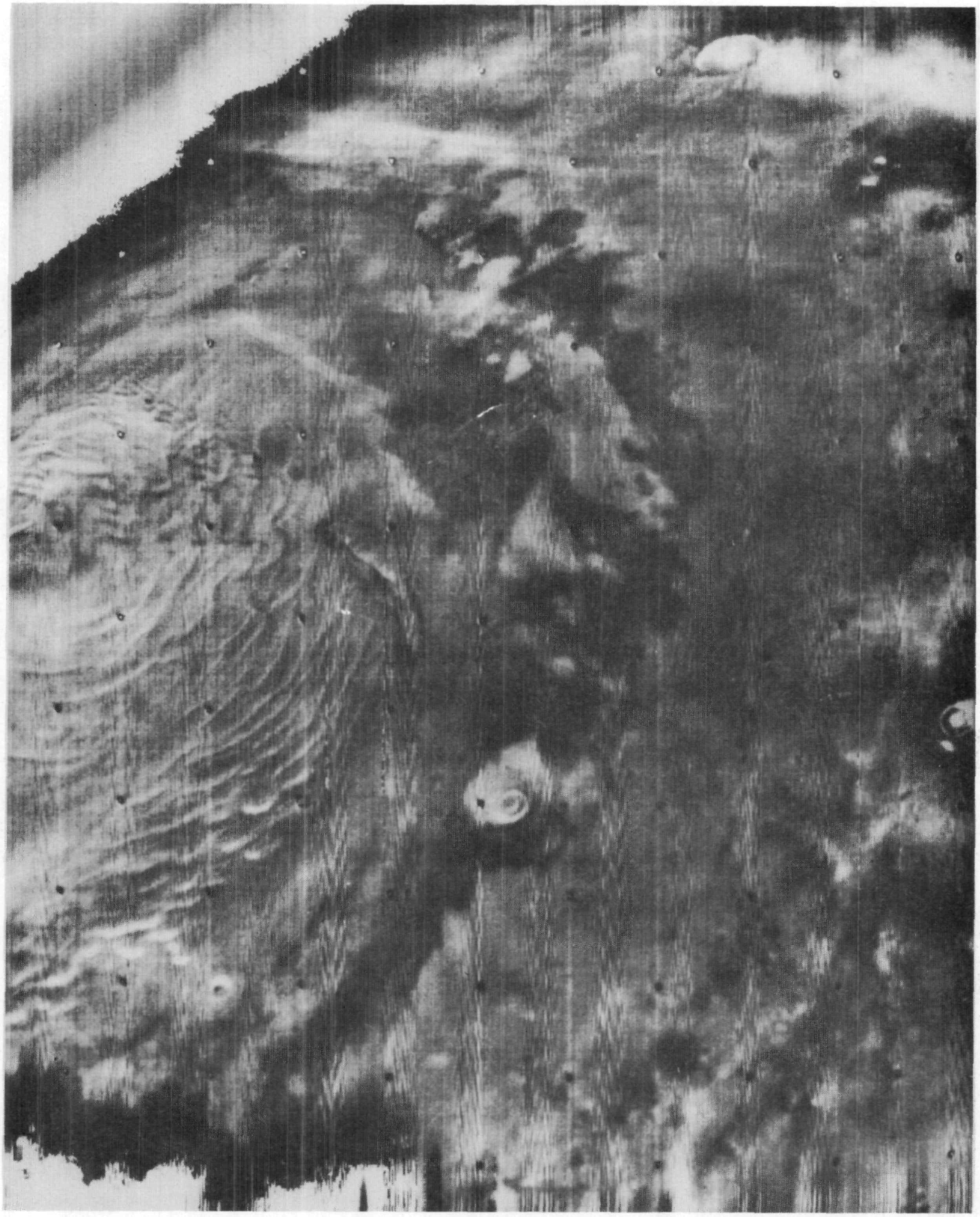

Figure 3-13. North Polar Region Terrain

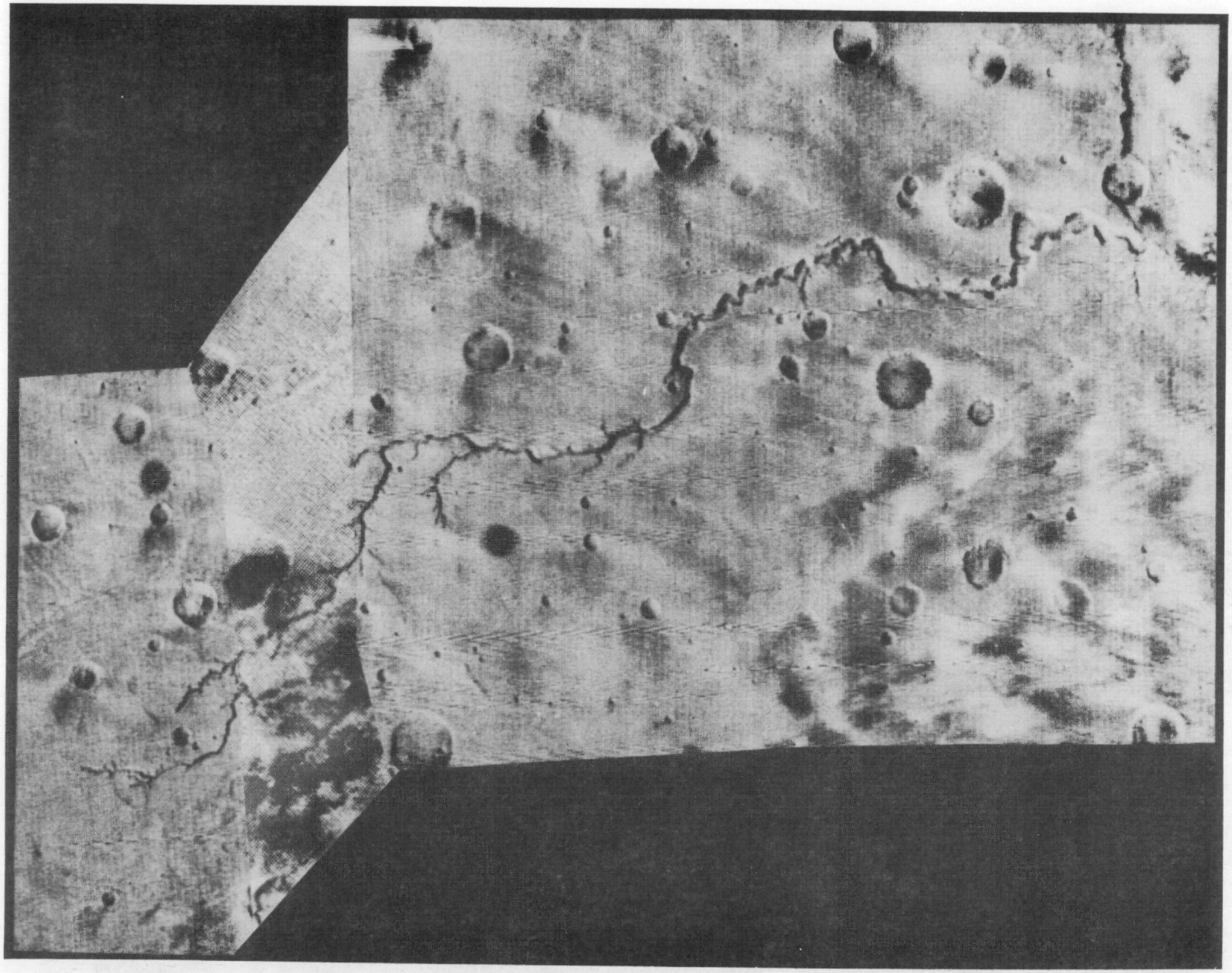

Figure 3-14. Extensive sinuous valley in Mare Erythraeum region

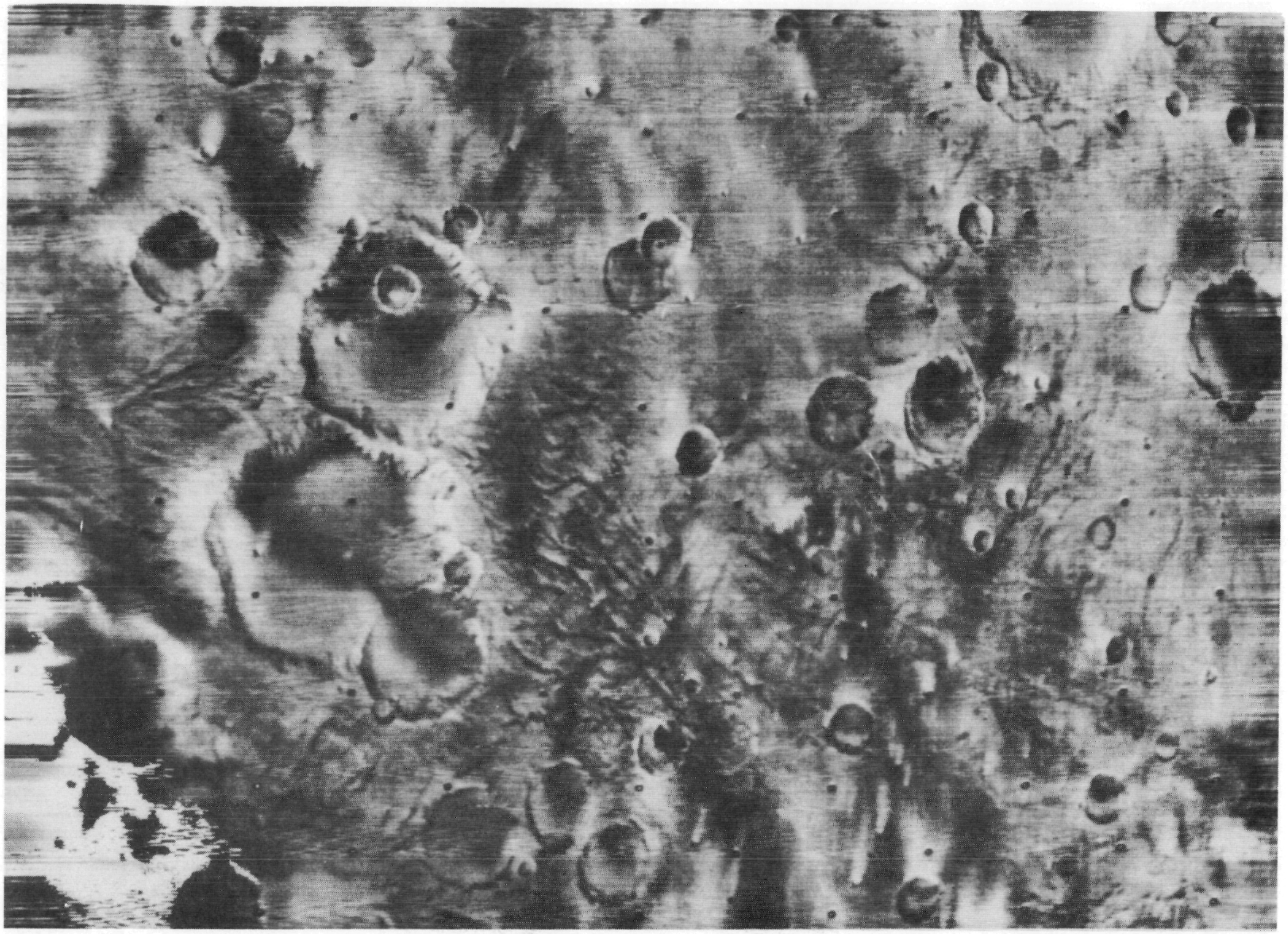

Figure 3-15. Small erosional channels in heavily cratered terrain

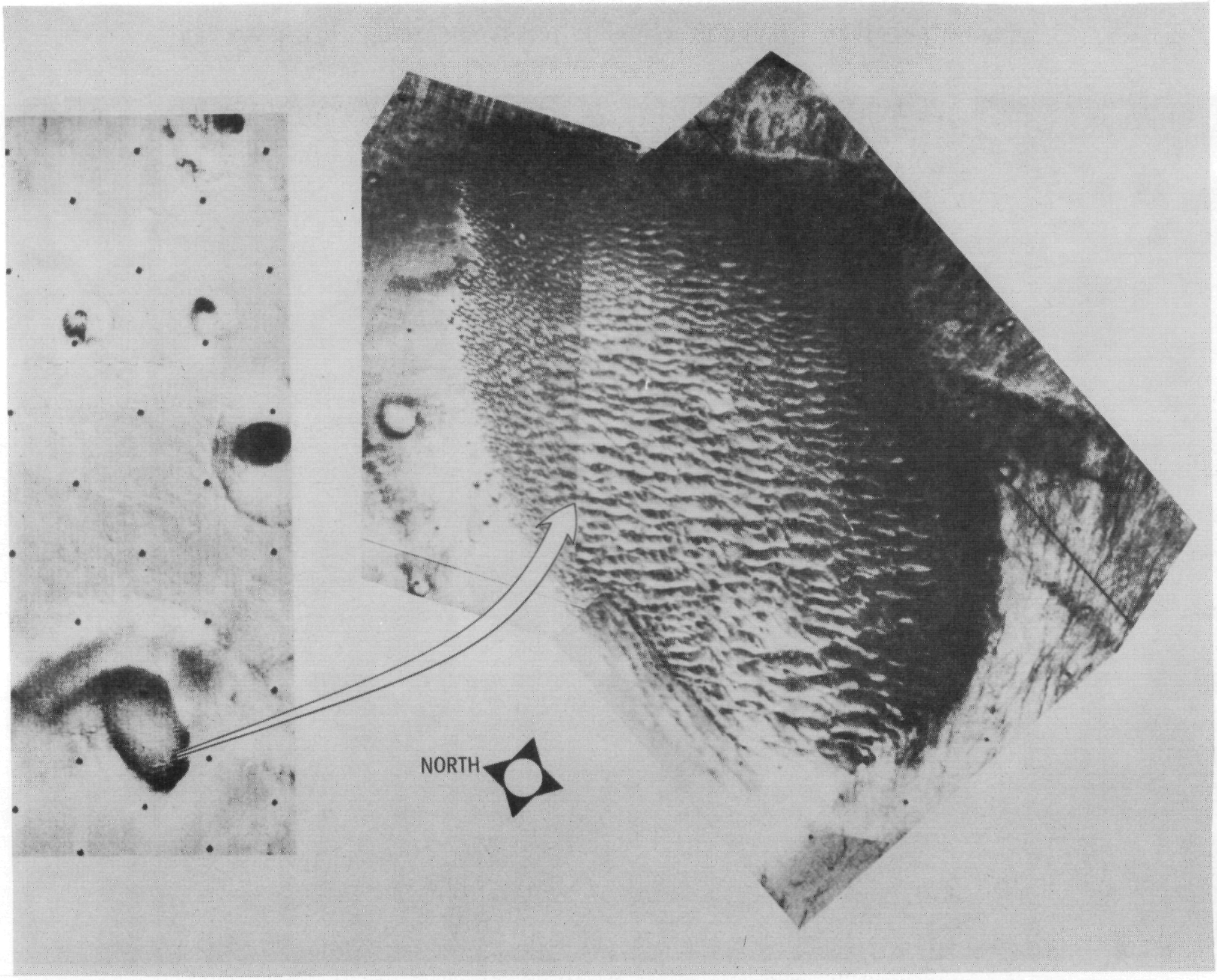

Figure 3-16. B Frame mosaic of crater interior showing dune field

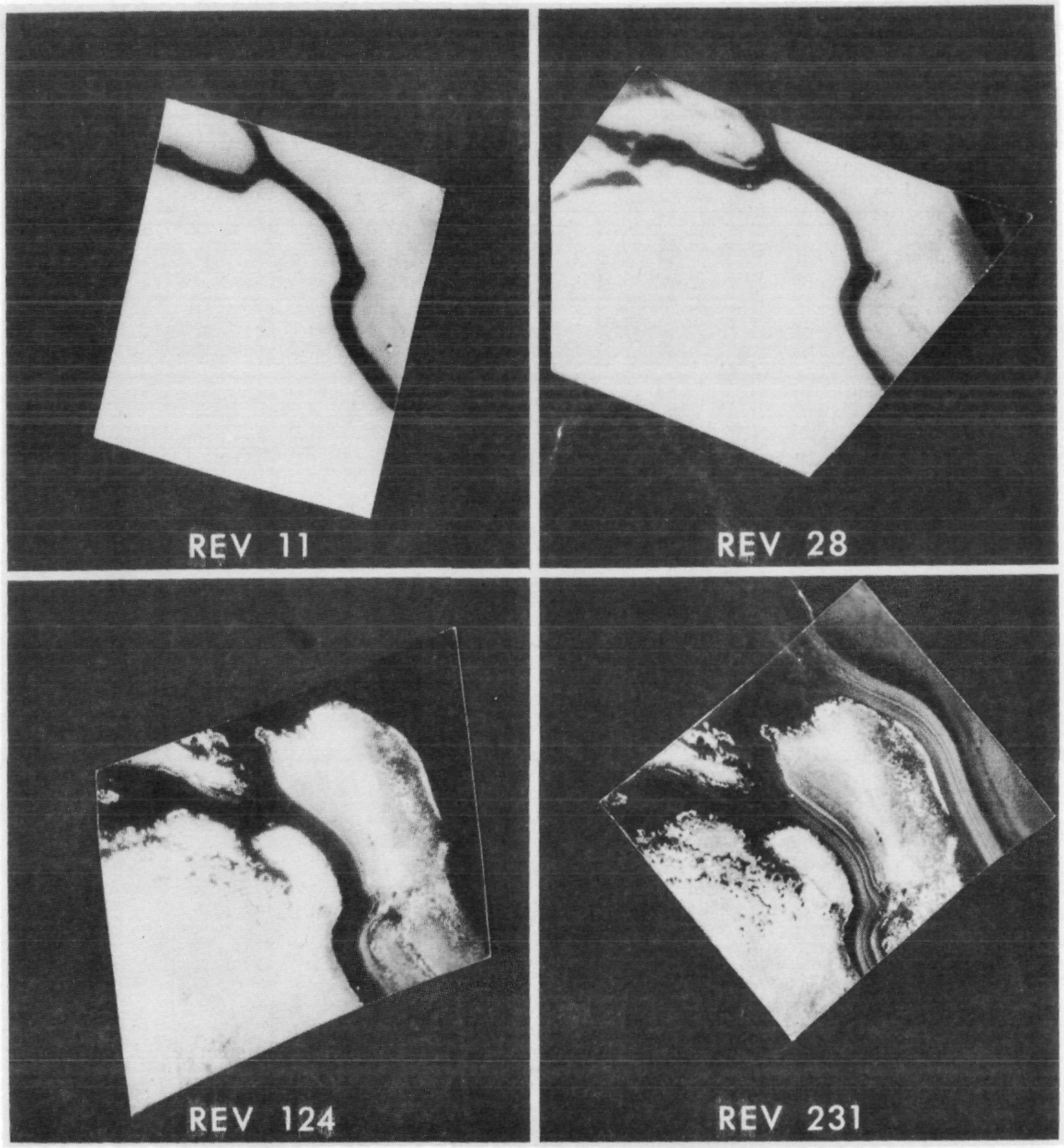
REV 11
REV 28
REV 124
REV 231

Figure 3-17. Sequence showing degradation of South Polar Cap

Wind blown dust phenomena appear in abundance on the Martian surface as indicated by the crater tails shown in Figure 3-18. Both light and dark materials comprise the tails seen. Extensive analysis by the TV team are underway regarding the extent of these tails, the particle sizes involved, and their expected relation to the craters and the prevailing wind field direction and velocities.

Other examples have been documented by the TV team, and variable features connected with atmospheric phenomenon exists. Some of these will be illustrated later in this report.

Several extensive and comprehensive mapping investigations have been completed by the TV team. Examples of these are presented in Figures 3-19, 3-20, and 3-21. These show, respectively, a geological province map with a superimposed elevation contour map; a rendition of a south polar region mosaic; and a panoramic mosaic of a portion of the equatorial region of Mars.

The results of analyses of these photographs, sampling virtually the complete surface of Mars, indicates a dynamically evolving planet. Many of the features discovered during the mission appear to be geologically young or fresh. Photographs of the fault zones show that the crust has been broken frequently. Coupled with results from the IRIS experiment, regarding surface composition and its implication for surface differentiations, the TV data suggest a chemically evolving planet as well. Moreover, significant erosional processes in the form of fluid motion, glaciation and wind transport are evident. Hence the selection of a suitable Viking landing site will have to be a reasonable compromise between the many scientifically interesting areas and the practical matter of achieving a successful landing.

3.2.2 Terrain Mapping and Analysis at a Scale of 1:25,000,000

Terrain mapping was conducted on a near-real-time basis to (1) establish general terrain types on the Martian surface; (2) develop a better understanding of Martian topography and geography; (3) continue to follow the dust storm and; (4) support the Viking Landing Site Working Group. Terrain mapping, analysis of imagery, and interpretation of imagery began on a near-real-time basis at a scale of 1:25,000,000, continued through the third mapping cycle, and into the fourth cycle of the Mariner Mars '71 mission. Efforts were concentrated in the Viking zone but extended about 40° to 45° south and northward to 40° to 50° north.

Mapping was accomplished by sketching features shown on the imagery with corresponding footprint outlines. Features mapped in near-real-time were chiefly craters, scarps, mountains, domes, and various surfaces ranging from smooth uncratered ones to cratered ones. Craters, hills, and other features down to about 60 km across were mapped. Thus, major features and terrain types were slowly delineated as the mission progressed. Selected features, such as Nix Olympica, were recognized early because the dust cleared from

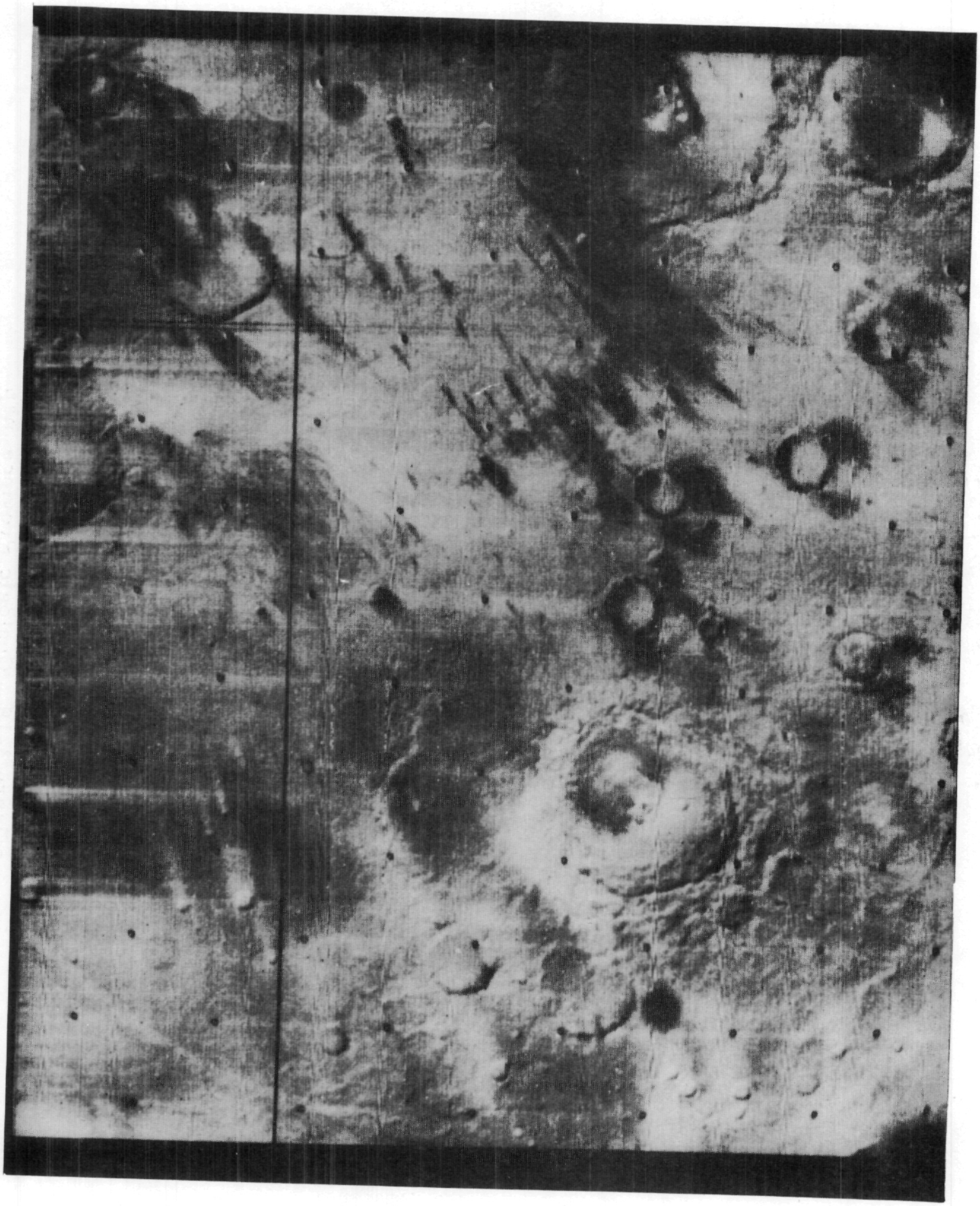

Figure 3-18. Wind-blown dust phenomenon

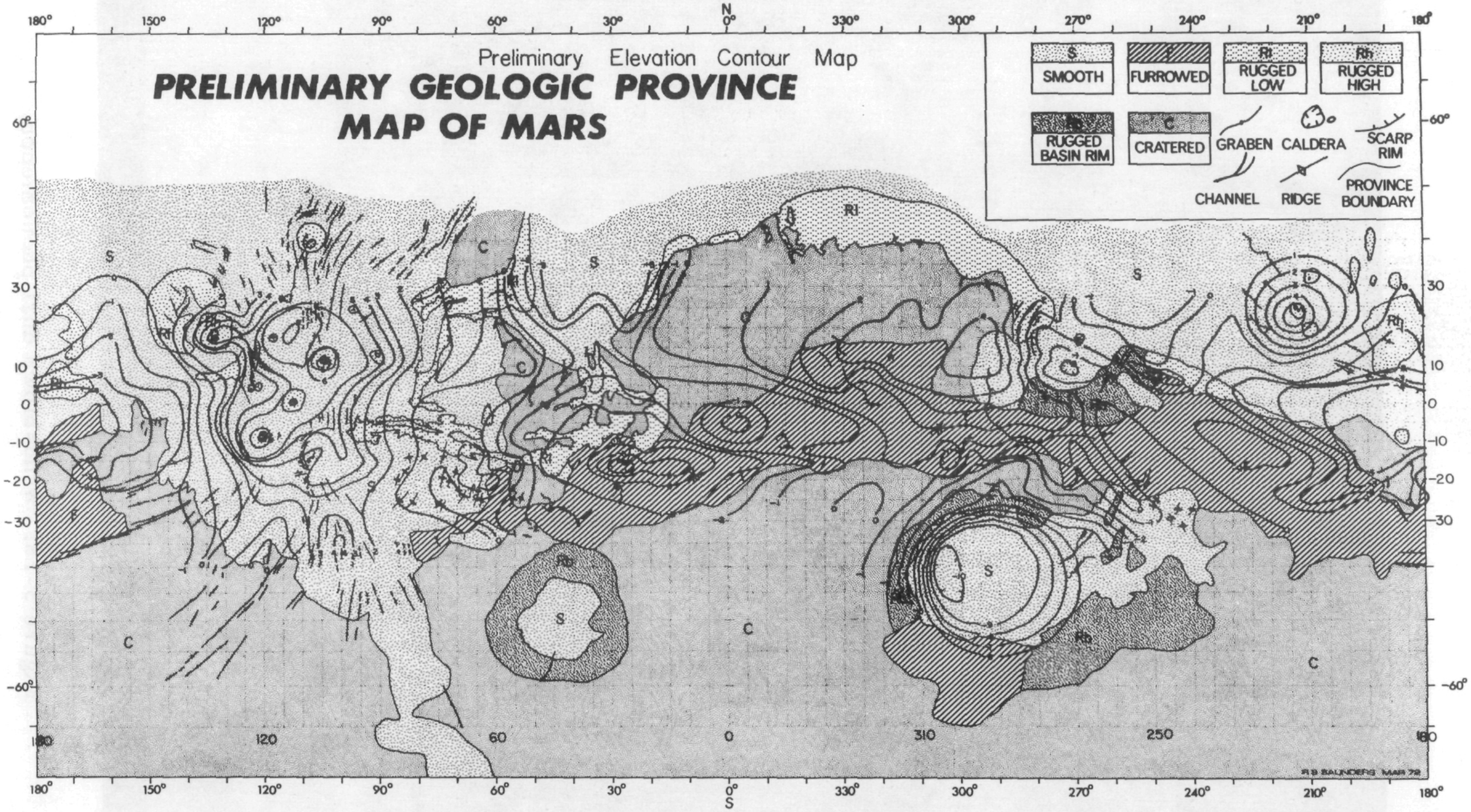
Preliminary Elevation Contour Map
PRELIMINARY GEOLOGIC PROVINCE MAP OF MARS
S SMOOTH
F FURROWED
Rl RUGGED LOW
Rh RUGGED HIGH
Rb RUGGED BASIN RIM
C CRATERED
GRABEN
CALDERA
SCARP RIM
CHANNEL
RIDGE
PROVINCE BOUNDARY
N
S
180°
150°
120°
90°
60°
30°
0°
330°
300°
270°
240°
210°
60°
30
10
0
-10
-20
-30
-60°
S
C
Rl
Rh
Rb
F
120
60
0
310
250
180
R B SAUNDERS MAR 72

Figure 3-19. Geologic Province map

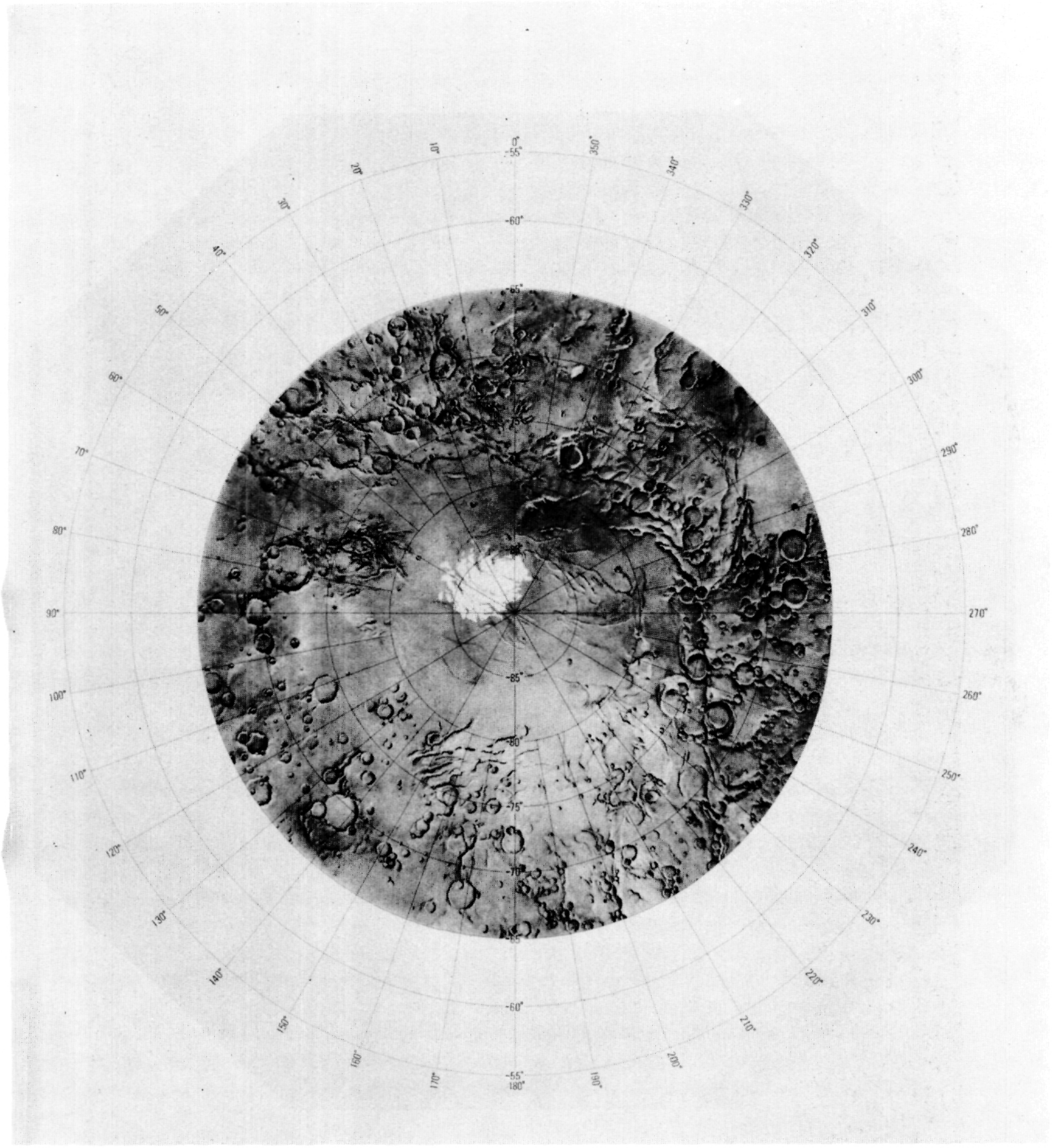
0°
-55°
10°
20°
30°
40°
50°
60°
70°
80°
90°
100°
110°
120°
130°
140°
150°
160°
170°
-55°
180°
190°
200°
210°
220°
230°
240°
250°
260°
270°
280°
290°
300°
310°
320°
330°
340°
350°
-60°
-65°
-70°
-75°
-80°
-85°
-60°

Figure 3-20. Airbrush rendition of South Polar Mosaic

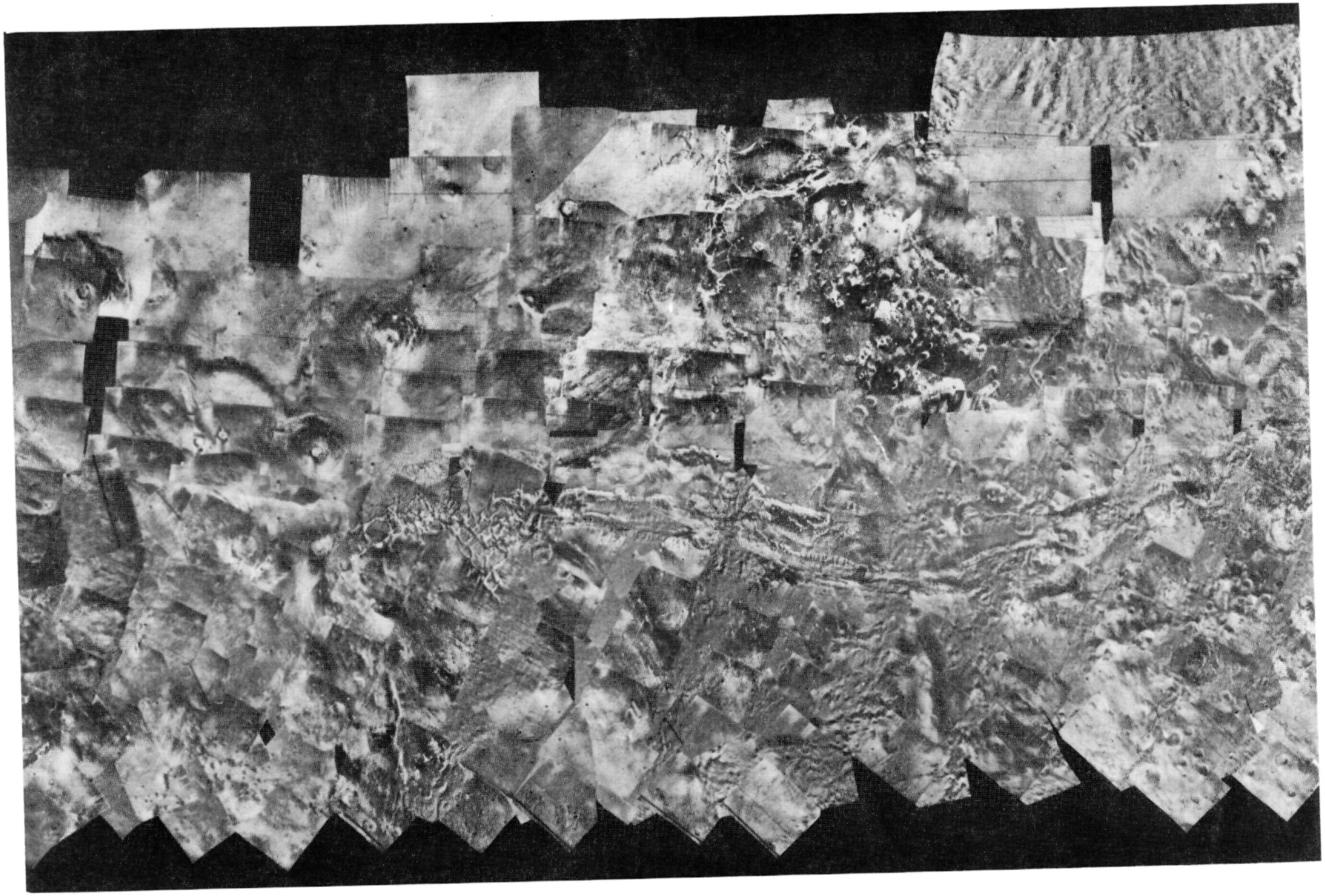

Figure 3-21. Panoramic mosaic of a section of Mars Equatorial Region

the higher elevations first. Cratered terrain, plains units, lineated terrain, canyonlands, and the north polar hood unfolded with time. Map-1, in the back of this report, shows the "mini-terrain" features observed.

Using mosaics, the near-real-time "mini-terrain" map (1:25,000,000 - scale), and previous observations, the terrain map was generalized and the Mars surface was classified into six types of terrain (see Map-2):

I. Tablelands which are plateaus and mesas, usually bounded along one edge by a steep escarpment. Tablelands grade at places with cratered terrain and Plains.

II. Plains which are broad, generally low areas with little or no apparent relief.

III. Cratered Terrain whose topography is dominated by craters 60 km in diameter and larger. Cratered Terrain grades into Plains and Tableland units.

IV. Irregular Terrain which has rugged, mountainous topography and which commonly occurs as islands within Plains units or along boundaries between Cratered Terrain and Plains units.

V. Canyonlands which are deep, wide linear depressions and closed depressions.

VI. Domes which are more or less circular features with summit craters.

Most major terrain units were divided into subunits and are discussed, first, in a general manner and then in more detail. The majority of the subunits are really unimportant. There are only four that comprise more than 10% of the Viking zone (Table 3-1). The six major terrains can be halved in terms of Viking considerations; the last three are so rugged as to present excessive engineering risk.

A very generalized sketch map of the relevant terrains, adapted from the 1:25,000,000 map, is shown in Figure 3-22. It is apparent that the overall physiography involves cratered terrain in the south and plains in the north. The contact between these two units is of special interest. It appears that the cratered terrain is being eroded to form plains which locally occur at lower elevations. A variety of erosional features, many of which may be structurally controlled, can all be fitted within one genetic scenario as shown in Figure 3-23. If water plays a part in surface erosion, then the gradational contact between cratered terrain and plains has been, at some previous time, a "water-rich" environment.

Table 3-1. Approximate percentages of Viking Zone covered by terrains delineated on the VDAT 1:25, 000, 000 Generalized Terrain Map

Terrain Unit	% Area in Viking Zone	
Tablelands		16
Smooth Tablelands (Ts)	8	
Lineated Tablelands (T_1)	1	
Cratered Tablelands (Tc)	5	
Ridged Tablelands (Tr)	1	
Patterned Tablelands (Tp)	1	
Plains		35
Smooth Plains (Ps)	28	
Hummocky Plains (Ph)	1	
Lineated Plains (Pl)	1	
Patterned Plains (Pp)	1	
Cratered Plains (Pc)	3	
Ridged Plains (Pr)	1	
Cratered Terrain		39
Cratered Terrain (CT)	12	
Flat Cratered Terrain (CTf)	15	
Patterned Cratered Terrain (CTp)	12	
Irregular Terrain (Ir)		6
Canyonlands (CL)		3
Volcanic Domes (Dc)		1

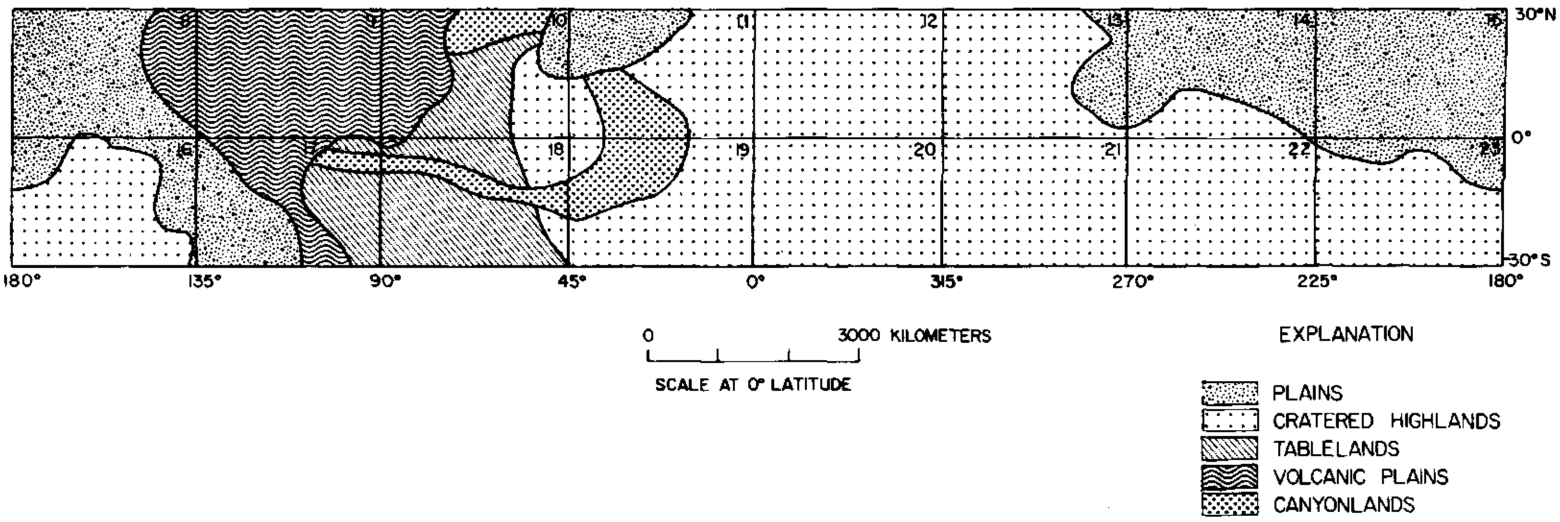
8
9
10
11
12
13
14
15
16
17
18
19
20
21
22
23
30°N
0°
30°S
180°
135°
90°
45°
0°
315°
270°
225°
180°
0
3000 KILOMETERS
SCALE AT 0° LATITUDE
EXPLANATION
PLAINS
CRATERED HIGHLANDS
TABLELANDS
VOLCANIC PLAINS
CANYONLANDS

Figure 3-22. A sketch map for the Viking Zone, generalized from the VDAT Generalized Terrain Map (i.e., doubly generalized). This map shows the location of the standard sixteen Mars charts in the Viking Zone (MC 8-MC 23). The intent is only to show disposition of major terrain types. For more specific information refer to the 1:25,000,000 or 1:5,000,000 VDAT Terrain Maps. The boundaries of the Volcanic Province are especially conjectural. The intent is to single out that region which contains large calderas and other features indicative of vulcanism.

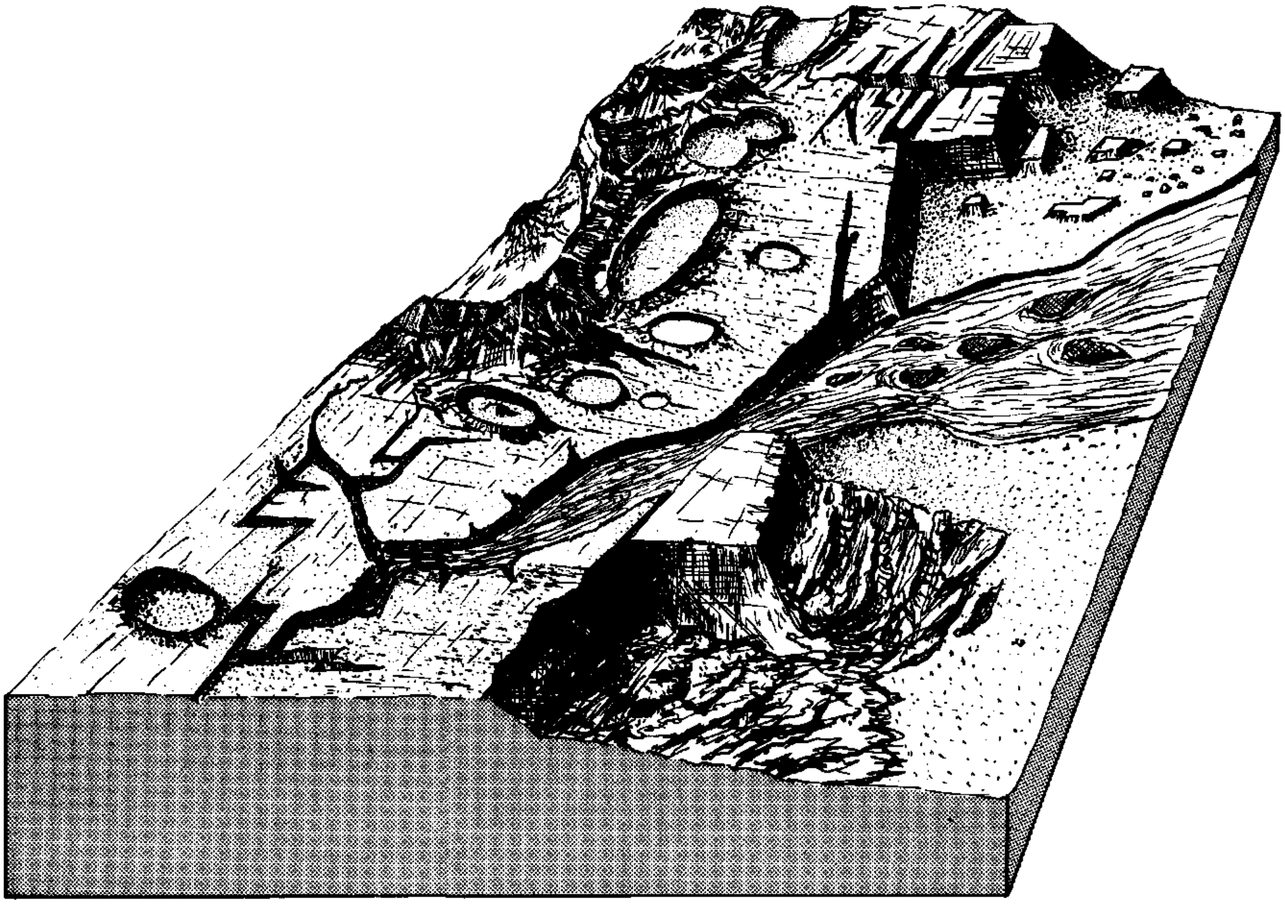

Figure 3-23. A highly idealized block diagram illustrating the array of features that can be found adjacent to the contact between Cratered Terrain and Plains. In the background, the Cratered Terrain is being eroded into large mesas, separated by channels. These mesas decrease in size and increase in spacing, moving away from the contact across the plains. In the foreground, a large channel cuts through the Cratered Terrain. Its tributaries have segmented linear plan view, indicating structural control of orthogonal joints or fractures. Close to its mouth, hydrodynamically shaped inliers occur within the channel. In the immediate foreground, the Cratered Terrain is being modified by collapse and slump to form a "chaotic" terrain.

It should be emphasized that this block diagram is a collage of features seen in pictures of different areas. Although the features tend to be situated as shown, there are numerous exceptions. For example, sinuous rilles occur throughout the equatorial zone. Some of the more prominent channels in Canyonland cut through Smooth Tablelands and parallel the contact between cratered and smooth terrains.

The twofold division of the Viking zone just described is complicated in the western hemisphere by the presence of a Volcanic Terrain, Tablelands and Canyonlands. The Volcanic Terrain includes the spectacular calderas identified early in the mission but is largely underlain by plains of possible volcanic origin.

The Tablelands closely resemble the Plains, as suggested by the fact the two units have five similar sub-units: Smooth, Lineated, Cratered, Ridged, and Patterned. Tablelands, as the name implies, are distinguished primarily by bounding scarps.

The Canyonlands contain many of the erosional features that elsewhere are associated with the Cratered Terrain-Plains contact. However, the Canyonlands do not occur along this contact but instead are emplaced in Tablelands. Alternately, one might say that the incision and erosion of plains materials has given rise to canyon-bounded tablelands. The major east-west trending canyon is almost certainly controlled by a large structural rift in the Martian crust.

3.2.2.1 Analysis and Interpretation of Imagery (1:25,000,000 - Scale)

The fundamental technique of terrain mapping, as distinguished from geologic mapping as it applies to the interpretation of Mariner 9 imagery for Viking requirements, should be briefly defined here. Ideally, terrain mapping takes into account only the shape, size, and distribution of landforms, without regard to their origin and age. Geologic mapping elucidates the physical attributes of surficial materials, their relative ages, and their probable origins. In this regard, an avoidance of generic nomenclature has been attempted. However, geologic mapping has a strong terrain or geomorphic bias since terrain information is the chief component of photographic data. With these limitations in mind, the following section describes the terrain types that may be mapped from preliminary photoanalysis of the Mariner 9 imagery.

Terrain mapping, analyses of imagery, and interpretation of imagery reveal that the surface of Mars is heterogeneous at all scales and that a wide range of topography and surface materials can be expected.

TABLELANDS

At a scale of 1:25,000,000, Tablelands can be divided into five subunits: (1) smooth (Ts); (2) lineated (Tl); (3) cratered (Tc); (4) ridged (Tr) and; (5) patterned (Tp).

Smooth Tablelands (Ts) are very smooth and essentially featureless, except for tonal contrasts and a few small craters. This subunit is found chiefly between 55° and 105°W and 30°S to 30°N and is bounded by scarps and graben on its westernmost boundaries. Canyonlands cut through this unit and, to the east, grade into cratered types of terrain. This terrain, which covers substantial parts of map quadrangles MC-10 and 18, (see Figure 3-22) resembles Smooth

Plains, although it appears to have a slightly higher crater density, better defined ridge-like texture, and--locally--more wind streaking associated with craters (Figure 3-26). However, the unit is distinguished from Smooth Plains principally by being on the upland side of a prominent scarp (Figures 3-24, 3-25), or by being bounded by the great clefts of the Canyonland (Figure 3-26). Smooth Tablelands not only appear to be smooth in Mariner A and B camera imagery, but also appear smooth to radar (average rms slopes 1° to 4°). Dielectric constants are rather high (averaging 2.8 to 3.8). This terrain is found at elevations between +7 and -4 km.

Lineated Tablelands (Tl) are characterized by conspicuous, narrow graben and closely spaced, subparallel fractures or faults. This unit is found chiefly between 70°W and 110°W and 0° to 40°S. It is mostly bounded by Smooth Tablelands, and Plains units. Limited sampling by Haystack radar indicates this unit is smooth (average rms slope 1.7°), although it appears rougher in parts where closely spaced graben occur. The average dielectric constant is near 4.0. Lineated Tablelands are found at elevations of +3 to +7 km except where one small patch occurs at 230°W and 2°S where it is near 0 km elevation. This terrain is identical in form to the Lineated Plains and occurs as a southern extension of the Volcanic Province (Figure 3-22).

Cratered Tablelands (Tc) are distinguished from Smooth Tablelands by a greater crater density (Figures 3-27, 3-28) and from Flat Cratered Terrain by more prominent broad, flat intercrater areas. The distinction between the first two is clear; between the latter two indistinct. In any event, the intercrater areas are significantly rougher than those in Smooth Tablelands (Compare Figures 3-25 and 3-28). This unit grades into Flat Cratered Terrain and is found along a band extending from 340°W, 40°N to 55°W, 10°S. In spite of broad flat intercrater areas, Haystack radar data indicate the unit is quite rough (average rms slopes 4.8° to 6.6°). The average dielectric constant is near 2.4 and is found at elevations of 0 to -4 km.

Ridged Tablelands (Tr) are similar to Smooth Tablelands except that they are characterized by "wrinkle ridges" similar to those found on the Moon, and closely resemble Ridged Plains (Figures 3-29, 3-30). Thus, this terrain appears smooth in both Mariner A and B camera imagery and is confined to a relatively small area centered on 20°S and 80°W. Limited sampling by Haystack radar indicates an average rms slope of 2° and a dielectric constant of 3.4. Ridged Tablelands occur at elevations of +3 to +4 km.

Patterned Tablelands (Tp) are characterized by irregular, commonly dendritic "patterned ground". At A-frame resolution (Figure 3-31), this terrain has an amoeboid or mottled texture and B-frames reveal an irregularly roughened surface (Figure 3-32). As in the case of Patterned Plains, the texture is subtle, but the Plains are more clearly incised by a network of discrete channels. These Tablelands occur in isolated patches at 20°S to 970°W, 28°S to 57°W, 20°S to 37°W, and 40°N to 323°W. Limited sampling by Haystack radar indicates an average rms slope of 4.4° and a dielectric constant near 5.0. The combination of a dendritic "patterned ground" and a large dielectric constant suggests either moist "soil-like" materials or rock. This terrain is found at varying elevations from +7 to -3 km.

PLAINS

The Plains may be subdivided into six subunits: (1) Smooth Plains (Ps); (2) Hummocky Plains (Ph); (3) Lineated Plains (Pl); (4) Patterned Plains (Pp); (5) Cratered Plains (Pc); and (6) Ridged Plains (Pr).

Smooth Plains (Ps) at A-frame resolution are essentially featureless and smooth except for tonal contrasts and a few small craters. This unit occurs extensively in the northern hemisphere between 70°W and 285°W. Smaller areas occurring at 0° to 35°S and 110° to 145°W, 0° to 10°S and 170° to 230°W, 15° to 45°N and 15° to 50°W. Additional patches are found in Argyre, the northwest flanks of Argyre, in Hellas and in smaller craters and local patches. The northern limits of these Plains during the mapping cycle were obscured by the North Polar Hood. B-frames demonstrate that very little of the Smooth Plains is, in fact, featureless. Expectedly, small craters are observed. Also present are scarps, ridges, hummocks, mesas, and depressions. The wide variety of features suggests a similarly wide variety of origin for Plains materials. Arcuate scarps observed in some B-frames (e.g., Figure 3-51) resemble scarps observed in Mare Imbrium on the Moon and are interpreted as volcanic flow fronts. Bead-like ridges in other B-frames suggest aeolian deposition (Figure 3-34).

Although this unit appears to be generally smooth in Mariner imagery, Haystack radar results indicate average rms slopes for different areas range between 2.5° and 6.1°. Averaged dielectric constants vary widely from place to place and range between 2.0 and 4.0. The apparent inconsistency between photoanalysis and radar results are puzzling. Additionally, the many mappers feel that, at least locally, this unit is obscured in the imagery, perhaps by low lying dust. Further study is required before assessing this unit as an optimum landing area on the basis of engineering constraints.

Smooth Plains are found at elevations between -7 and +6 km.

Hummocky Plains (Ph) are similar to Smooth Plains except that scattered hills, knobs, mesas and craters are found within it. Isolated patches are also found near 15°S to 20°N and 170°W to 190°W, 40°N and 195°W, and 300°W and 40°N. In addition to these small mapped areas on the 1:25,000,000 map, hummocks of similar form (and presumably, origin) occur at many places along the contact between plains and cratered terrains. The hummocky pattern is usually visible at both A and B-frame resolutions (Figures 3-37, 3-38).

There is complete gradation from closely spaced mesas separated by channels (Figure 3-38) to isolated hummocks rising above otherwise featureless plains (Figure 3-39).

Haystack radar data for this unit is meager. It is found to be at elevations between 0 and -4 km.

Lineated Plains (Pl) occur only within the Volcanic Province and are observable on both A and B-frames. Intricately braided depressions bounded by steep scarps, presumably faults, are emplaced in smooth plains materials (Figure 3-40). Lineated Plains are similar to Lineated Tablelands and rms slopes are similar and near 2° to 4°; dielectric constants are lower and near 2.5. It occurs at elevations of 0 to +2 km and in proximity to volcanic calderas suggesting a volcano-tectonic origin.

Patterned Plains (Pp) are characterized by irregular, meandering and/or dendritic patterned ground and scarps. It is found, chiefly, near 25°N and 230°W and 0° and 180°W. This subtly delineated terrain is generally decipherable only on B-frames (an exception is the area in the vicinity of 19°N to 235°W. Irregular, branching networks of small channels and scarps are present (Figure 3-41). Some broader channels have teardrop shaped inliers, suggesting hydro- or aerodynamic shaping (Figure 3-42). Limited sampling by Haystack radar yields an average dielectric constant near 2.0, rms slopes near 2.0°, and elevations of -3 to -4 km.

Ridged Plains (Pr) are similar to Ridged Tablelands in their appearance in Mariner Imagery. This unit occurs at 25°S and 245°W. A-frames reveal large-scale networks of linear ridges and rilles (Figure 3-43). Some of the ridges observable on B-frames resemble wrinkle ridges present on lunar maria (Figure 3-44). Haystack radar indicates the average rms slopes are near 4.0° at elevations of 0 to +2 km.

Cratered Plains (Pc) have a low to moderate crater density with broad intercrater areas and are found in an area centered on 7°N and 255°W. It is adjoined to the east by Smooth Plains, the boundary between the two approximately corresponding to the telescopically observed boundary between Syrtis Major and Isidis Regio (Figure 3-33). As the name implies, Cratered Plains have a greater crater density than Smooth Plains.

Figure 3-35 indicates that the Cratered Plains may have considerable relief: craters with substantial ejecta deposits and wrinkle ridges. Included in the same terrain unit is a region with remarkable albedo streaking. B-frames (Figure 3-36) demonstrate very little relief other than that associated with small cup-shaped craters. The flat surfaces may be a combination of aeolian-planed bedrock and windswept sand sheets. In agreement with its smooth appearance, Haystack radar indicates a rms slope near 2.8° but locally to 5.8°. The average dielectric constant is near 3.5 and it occurs at elevations of +1 to -1 km.

CRATERED TERRAIN

Cratered Terrain is the most densely cratered of all Martian surfaces (Figure 3-45) and may be subdivided into three subunits: (1) Flat Cratered Terrain (CTf); (2) Patterned Cratered Terrain (CTp) and; (3) Cratered Terrain (CT).

Cratered Terrain (CT) has a high density of craters with negligible intercrater flat areas. At B-frame resolution, these intercrater areas are commonly rough with prominent furrowed texture (Figure 3-46). This terrain is found chiefly between 145°W and 238°W and 10° to 40°S, with some patches near 25°S and 320°W. Average rms slopes range between 2.5° and 4.5° and dielectric constants between 3.25 and 4.5. An interesting geomorphological feature found in this terrain unit is sand dunes (Figure 3-62) which indicates transport of material by saltation and verifies one of the Mars Engineering Model (MEM) soil models. Cratered Terrain occurs at elevations between +2 and -4 km.

Flat Cratered Terrain (CTf) has a moderate density of craters with a wide range of diameters and apparent ages and prominent flat intercrater areas. This unit has a smaller crater density than Cratered Terrain (Figure 3-47). However, intercrater areas that are flat at A-frame resolution commonly show considerable roughness --craters, ejecta deposits, ridges, and rills at B-frame resolution (Figure 3-48). This unit occurs chiefly in a broad arcuate band from 48°S, 15°W to 20°N, 355°W to 25°N, 310°W. Haystack averaged rms slopes are between 2.0° and 2.5° and dielectric constants are between 2.25 and 4.7. Flat cratered terrain occurs at elevations ranging from -4 to 0 km.

Patterned Cratered Terrain (CTp) is characterized by obvious "patterned ground" superimposed on the terrain, particularly in intercrater areas and around rims of large craters. Patterns are commonly dendritic but they may also consist of closely spaced fine ridges arranged in irregular patterns or concentric patterns (Figure 3-49). They are particularly well expressed in certain B-frames (Figure 3-50). Averaged Haystack slopes range between 4.0° and 5.2° and dielectric constants between 2.5 to 4.5.

IRREGULAR TERRAIN

This unit, although not subdivided, easily could be. One sub-unit contains the highly cratered and mountainous terrain that surrounds ancient basins. It is mapped around Hellas (Figure 3-51) and south of Isidis Regio. A second sub-unit, closely resembling Hummocky Plains, occurs at the junction of plains and cratered terrains in the vicinity of 10°N, 245°W. A third sub-unit includes isolated peaks, occurs within the plains, and has a distinctive "pimply" appearance (Figures 3-52, 3-53).

Rugged Terrain (Ir) is characterized by high, sculptured ridges and peaks, commonly at margins of very large circular basins; dense concentrations of crenulate, arcuate mountain ranges. In part, it is also characterized by hummocky, rough, knobby surfaces of localized hills, hummocks, mesas, or crater remnants. This unit is scattered in patches across the Viking Zone. Such patches occur near 15°N and 180°W, 8°N and 245°W, 2°N and 270°W, 25°S and 295°W, 40°S and 40°W, 25°N and 140°W, and in other smaller patches. Averaged Haystack radar results are in general agreement with visual impressions of the imagery and averaged rms slopes are between 5° and 7°. Average dielectric constants are near 2.0 to 2.6.

CANYONLANDS

This exotic terrain contains a varied assortment of erosional features. In general, the western part of Canyonlands contains huge east-west trending clefts which are probably fault controlled (Figure 3-54). The walls of the canyons are fluted with evidence of headward erosion into the adjacent Tablelands (Figure 3-55). The eastern part of Canyonlands contains large regions with texture variously referred to as "wormy", "checkerboard", "slump", or "chaotic" (Figures 3-56, 3-57).

Canyonlands (CL) may be divided into four types of terrain: (1) a reticulate network of narrow intersecting canyons and small depressions that are apparently fracture controlled; (2) broad, deep branching channels and closed depressions with finer dendritic channels on steep walls and at the margin of the branching channels and smooth to hummocky floors; (3) chaotic patterns of low hummocks densely concentrated within channels and depressions and; (4) flat broad shallow channels with smooth or slightly grooved floors. The reticulate network is found near 5°S, 100°W at elevations near +6 to +7 km. Dendritic Canyonlands are found near 10°S, 72°W at elevations near +2 to +3 km. Chaotic Canyonlands are well developed near 30°W, 7°S at elevations near -2 km and the Flat Canyonlands are found near 45°W, 15°N and 60°W, 27°N at elevations near -2 to -5 km. Canyonlands, where sampled by Haystack radar, are rough (averaged rms slopes 7.5° - 8°). Because of the large rms slopes, dielectric constant estimates are more suspect, but values are near 2 to 3.

DOMES

Domes of unequivocal volcanic origin were among the first ground features to be photographed in the Viking Zone. The famous triad is North, Middle, and South Spots, but other domes occur in map quadrangles MC-9, -15, and -23. The domes have sloping flanks with lobate flow-like patterns topped by single or multiple coalescing calderas (Figures 3-58, 3-59).

Domes (Dc) are more or less circular hills with caldera-like summit craters. Flanks of Domes appear smooth to ridged and dissected in Mariner imagery. Summit craters are commonly a composite of arcuate segments with sheer walls. Total relief is small to very high. Best examples are at 17°N, 135°W, 0 km; 12°N, 105°W, +3 km; 0°N, 113°W, 0 km; 12°N, 105°W, +3 km; 0°N, 113°W, +8 km; 7°S, 122°W, +9 km; 32°N to 19°N, 210°W to 213°W, -1 to +2 km; and 20°S, 253°W, +2.5 km. For the Dome at 12°N, 105°W, Haystack rms slopes are 6.1° to 7.1°. Estimates of dielectric constants are again suspect, because of the larger rms slopes.

Figure 3-24. Smooth Tablelands situated just east (right) of scarps and canyons incised into the Tablelands. Footprint for Figure 3-25 is shown.

Figure 3-25. Smooth Tablelands. Headward terminus of canyon appears in upper right. Footprint of photo is shown in Figure 3-24.

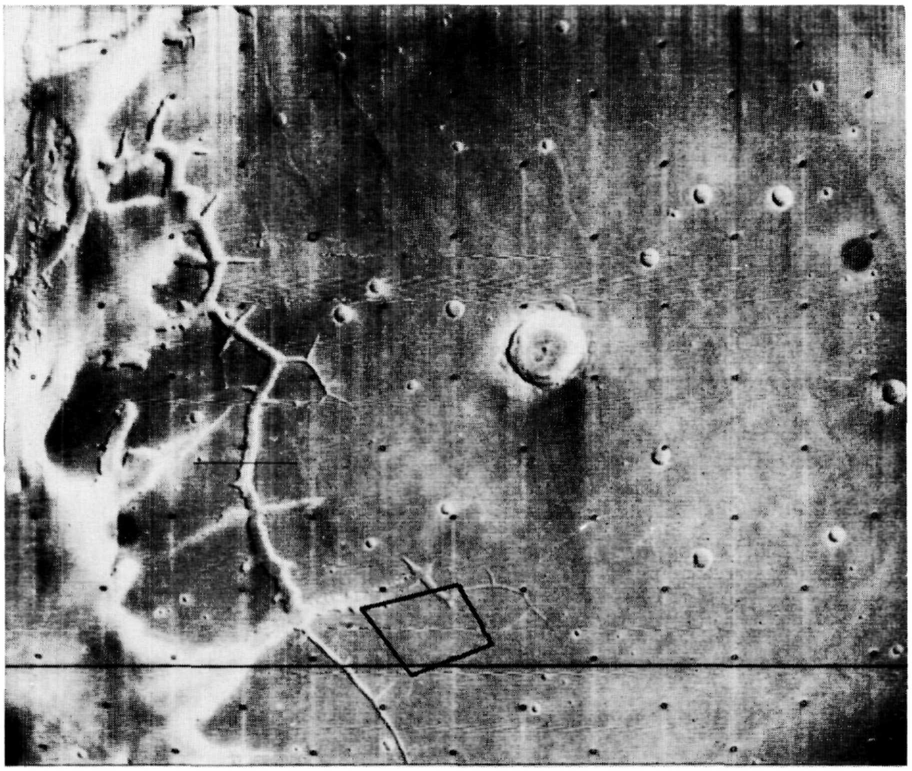

Frame A

Rev. 162

DAS 7399383

Center Point
16.9° 69.5°

MC 10

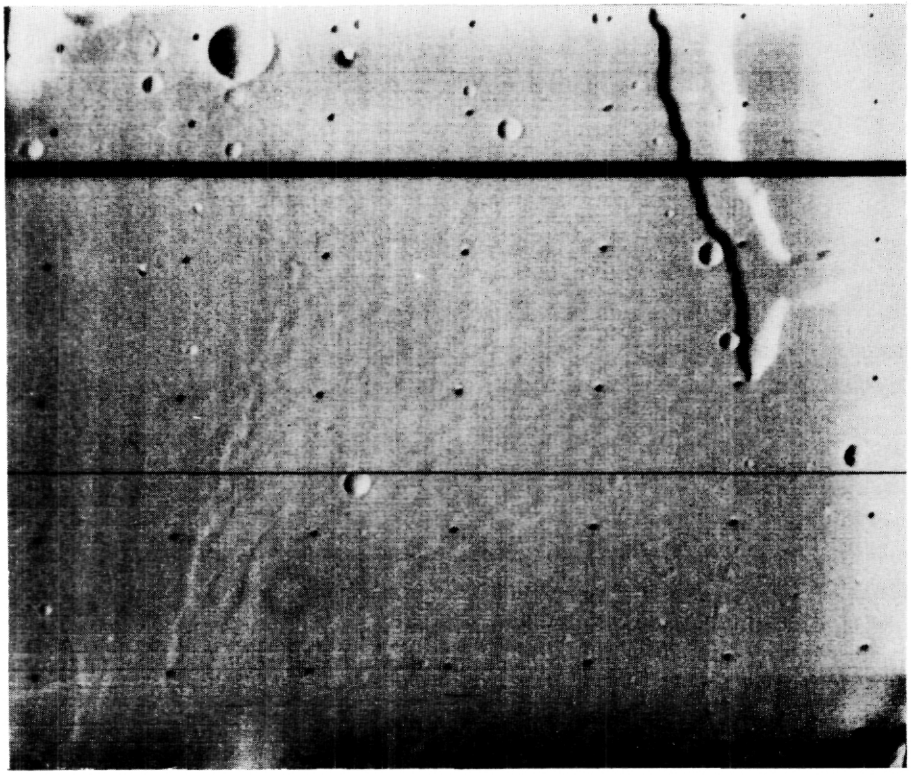

Frame B

Rev. 162

DAS 7399348

Center Point
14.6° 70.2°

MC 10

Figure 3-26. Smooth Tablelands south of a major east-west trending cleft within Canyonlands. Note wind streaking from upper left to lower right on Tablelands.

Figure 3-27. Smooth Tablelands appear in upper left, Cratered Tablelands in lower right.

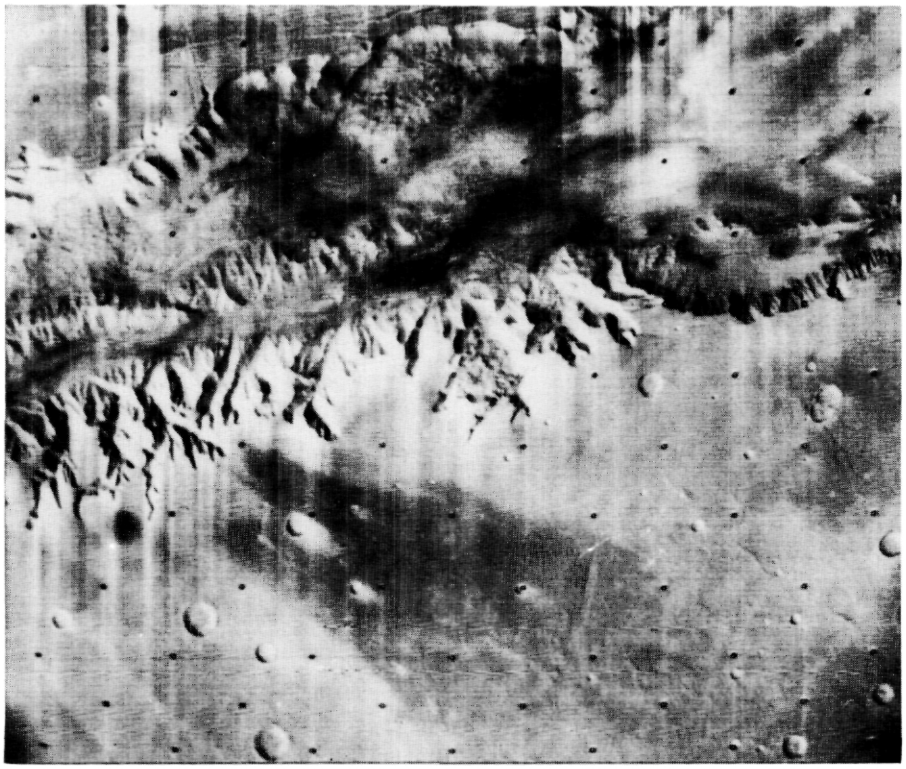

Frame A

Rev. 162

DAS 7398688

Center Point
-9.5° 79.0°

MC 18

100 km

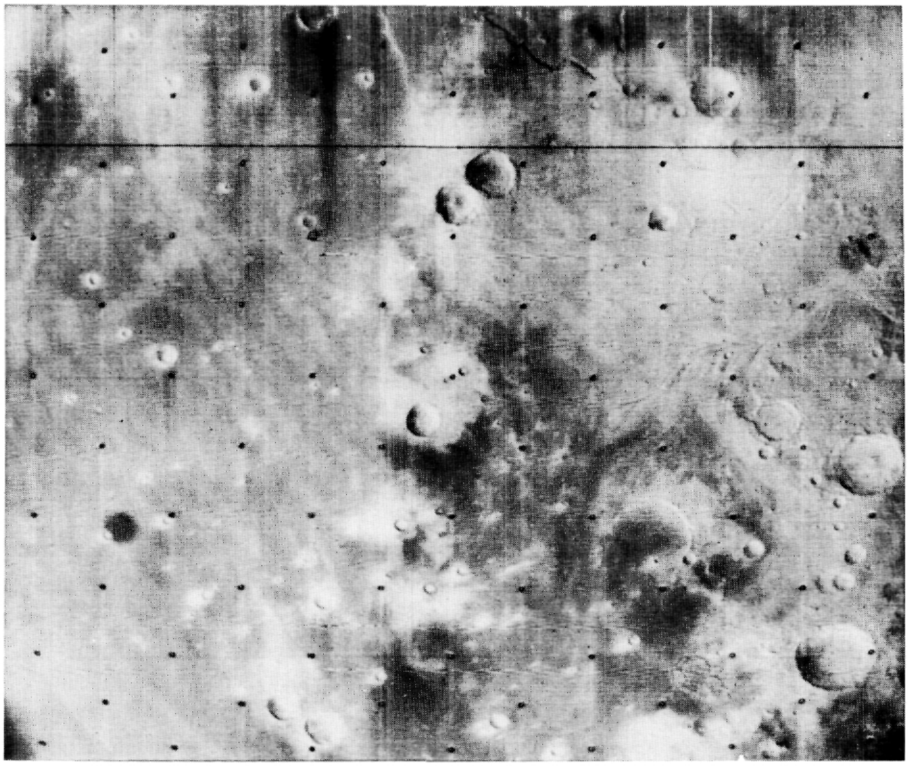

Frame A

Rev. 164

DAS 7471628

Center Point
16° 60°

MC 10

100 km

Figure 3-28. Cratered Tablelands, showing rough intercrater areas.

Figure 3-29. Ridged Tablelands. Wind streaking from upper left to lower right. Footprint of Figure 3-30 is shown.

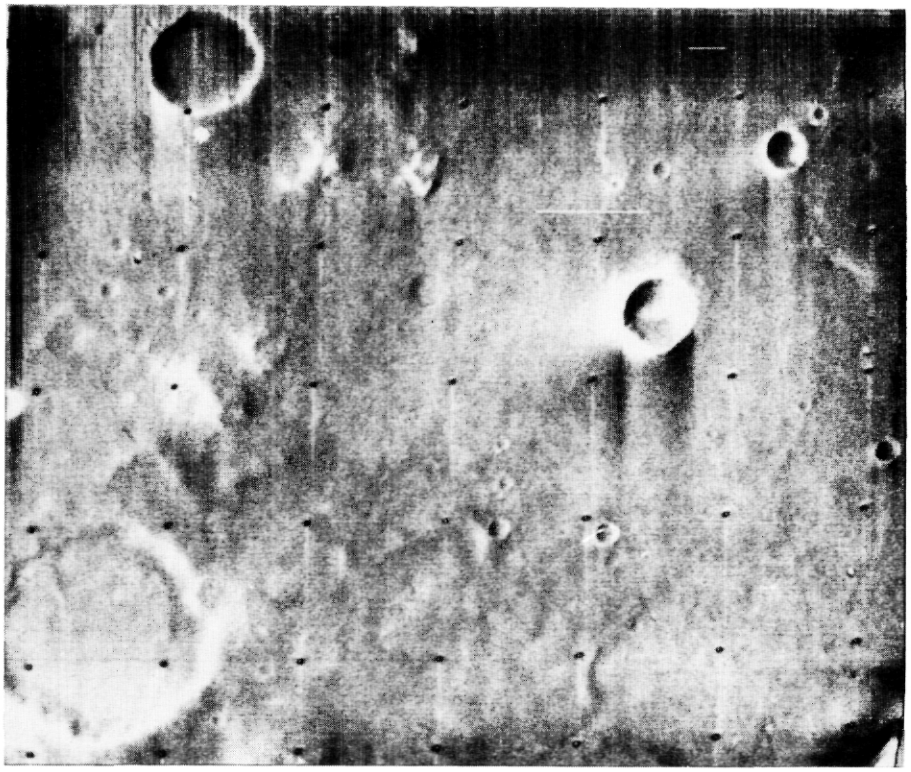

Frame B

Rev. 166

DAS 6543058

Center Point
5.8° 55.3°

MC 10

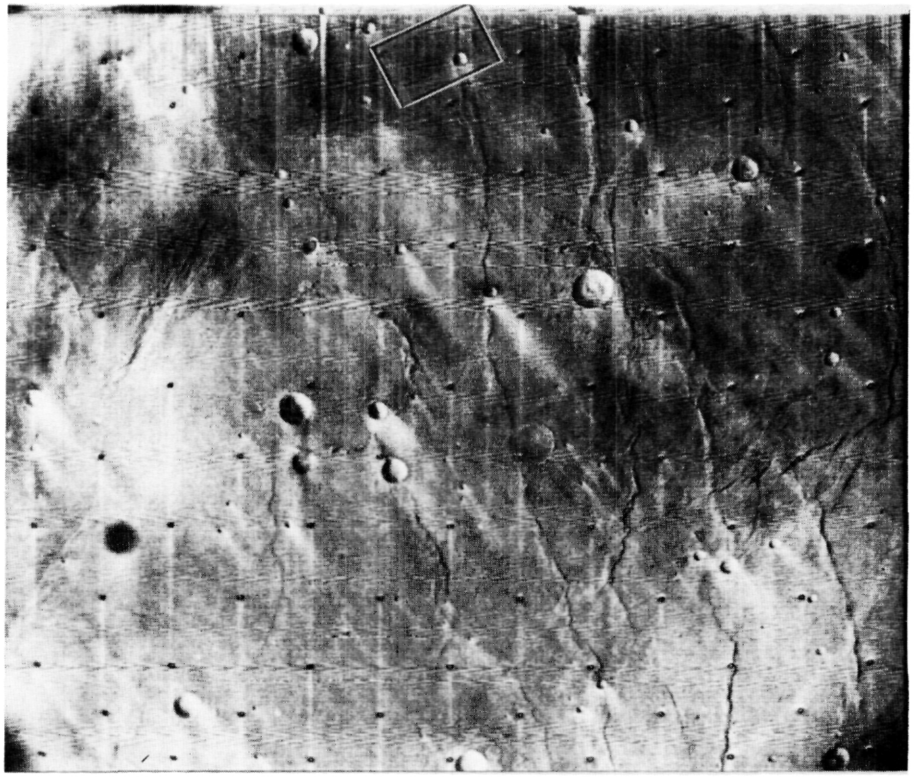

Frame A

Rev. 164

DAS 7470508

Center Point
-18.0° 73.6°

MC 18

Figure 3-30. Ridged Tablelands. Irregular flat-topped ridge trends from lower left to upper right. Footprint of photo is shown in Figure 3-29.

Figure 3-31. Patterned Tablelands. Mottled texture is evident in upper left. Wind streaking from lower left to upper right. Footprint for Figure 3-32 is shown.

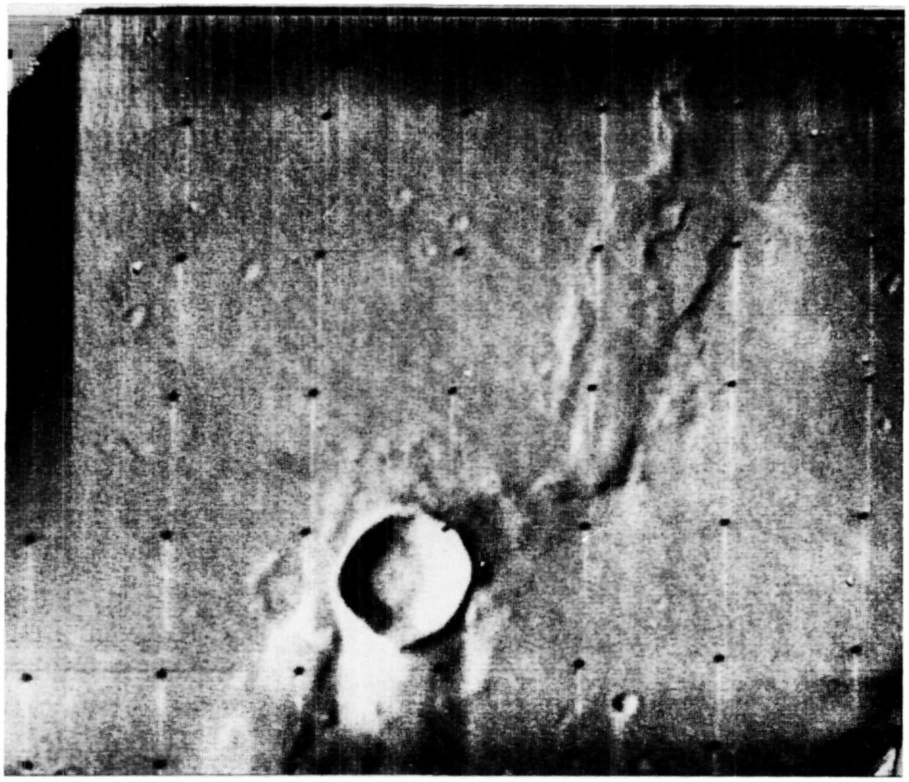

Frame B

Rev. 164

DAS 7470538

Center Point
-15.9° 72.4°

MC 18

10 km

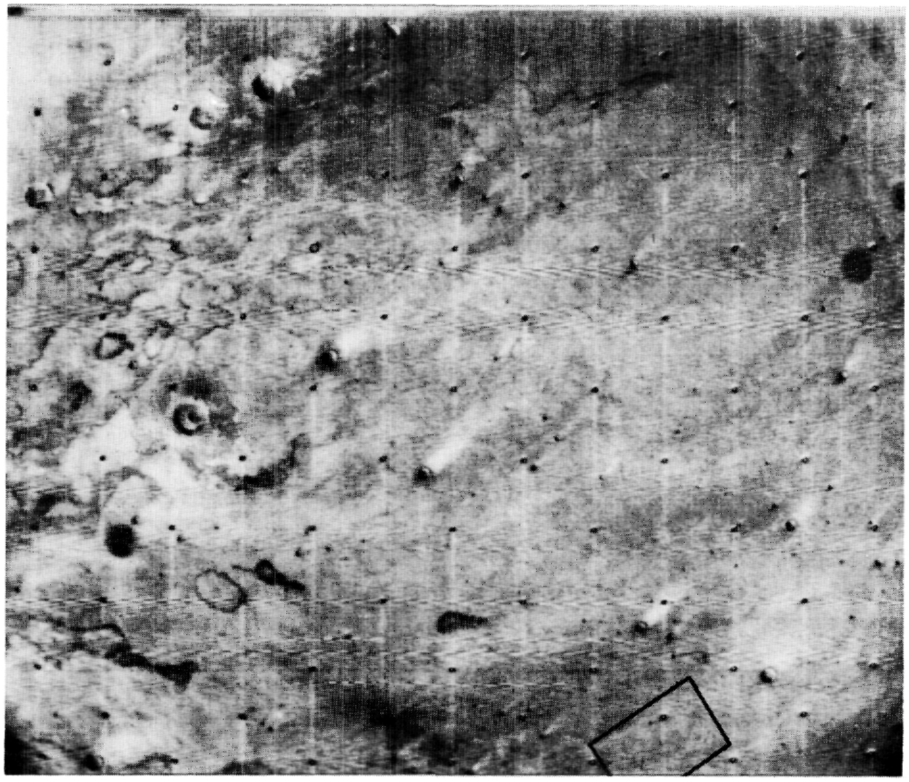

Frame A

Rev. 199

DAS 8729394

Center Point
-20.8° 97.2°

MC 17

100 km

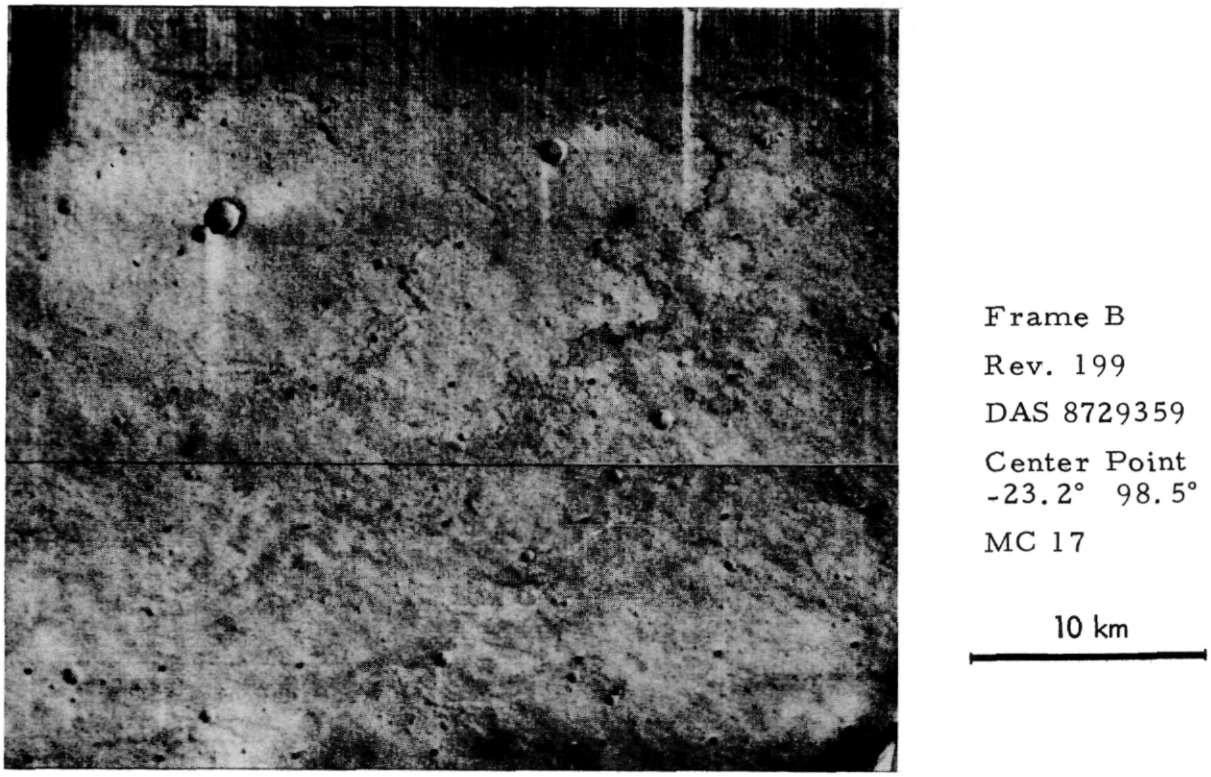
Frame B
Rev. 199
DAS 8729359
Center Point
-23.2° 98.5°
MC 17
10 km

Figure 3-32. Patterned Tablelands, showing irregular scarps and depressions. Footprint for photo is shown in Figure 3-31.

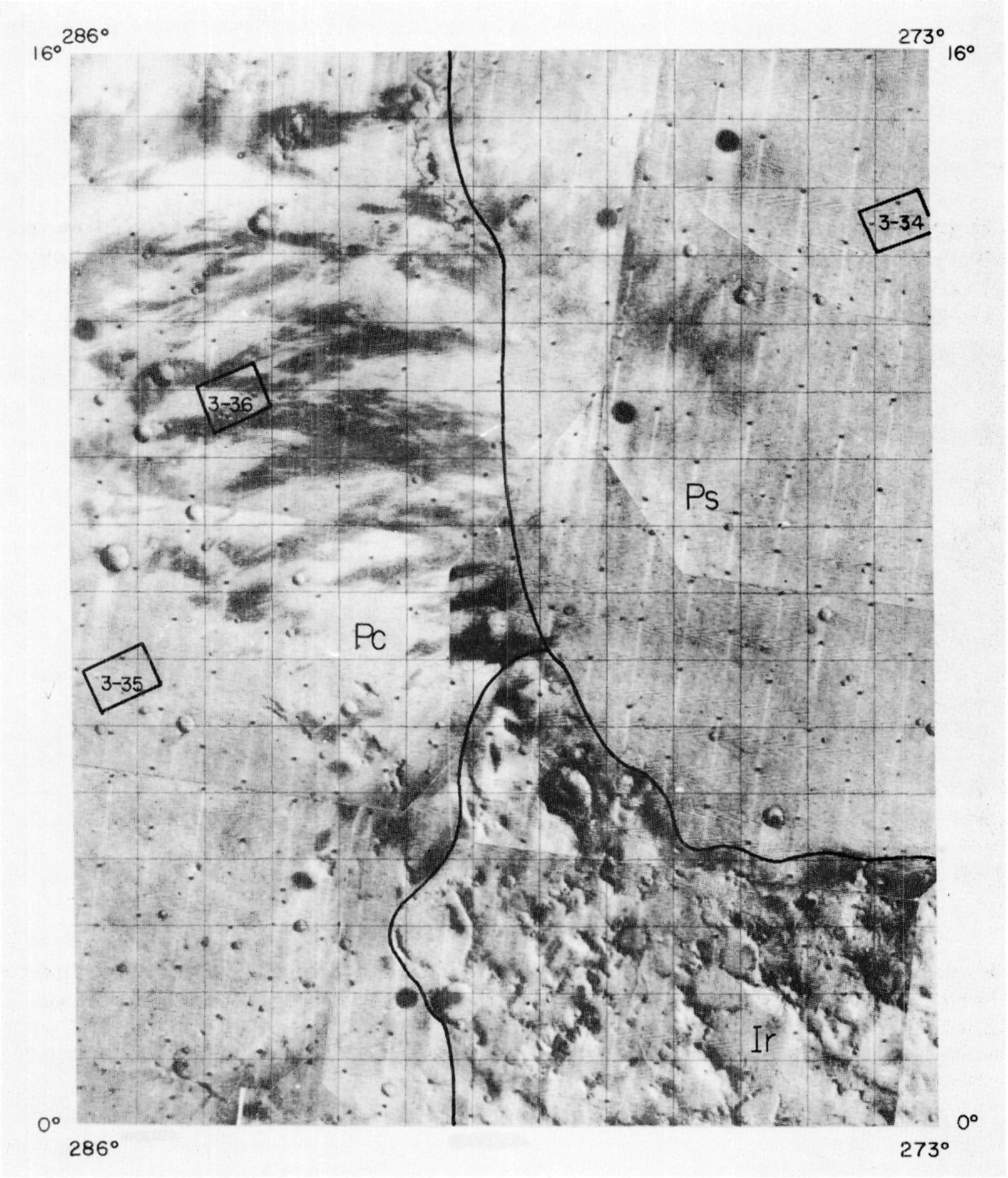
286°
16°
273°
16°
3-34
3-36
Ps
Pc
3-35
Ir
0°
286°
0°
273°

Figure 3-33. Mosaic of unrectified pictures showing contact between Smooth Plains and Cratered Plains, approximately corresponding to the telescopic contact between Syrtis Major and Isidris Regio. A small region of circum basin mountains (Ir) is in the lower right. Footprints for Figures 3-34, -35 and -36 are shown.

Figure 3-34. Smooth Plains. Bead-like ridges trending from lower left to upper right have possible aeolian origin. Footprint of photo shown in Figure 3-33.

Figure 3-35. Cratered Plains. Rough ejecta deposits surround the two larger craters. Low ridges trend toward upper right. Footprint of photo is shown in Figure 3-33.

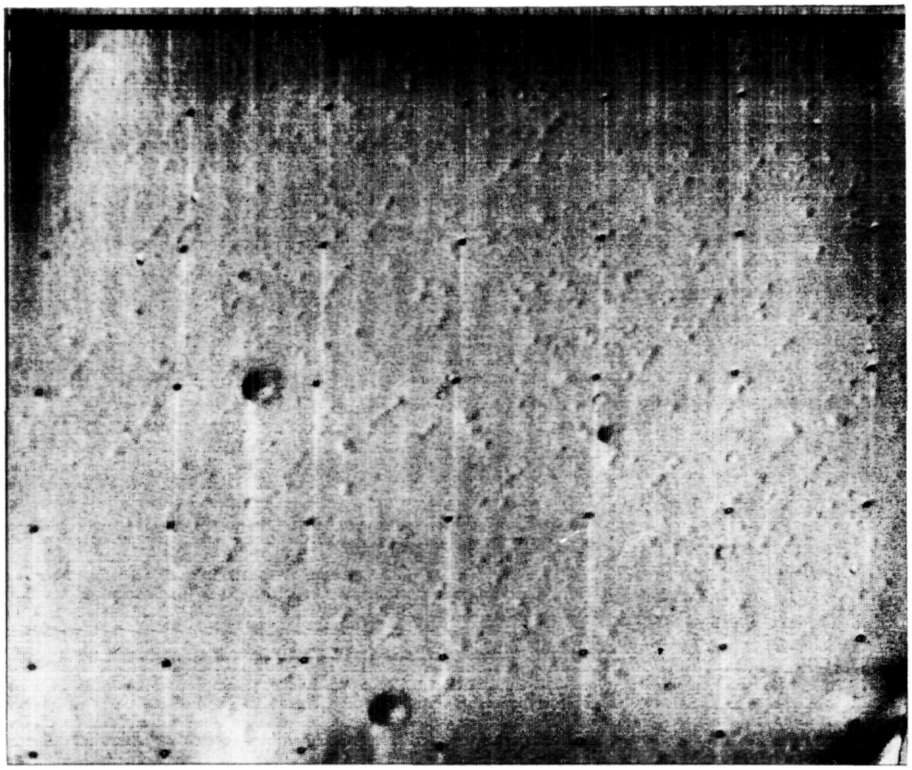

Frame B

Rev. 157

DAS 7219378

Center Point
13.5° 273.5°

MC 13

10 km

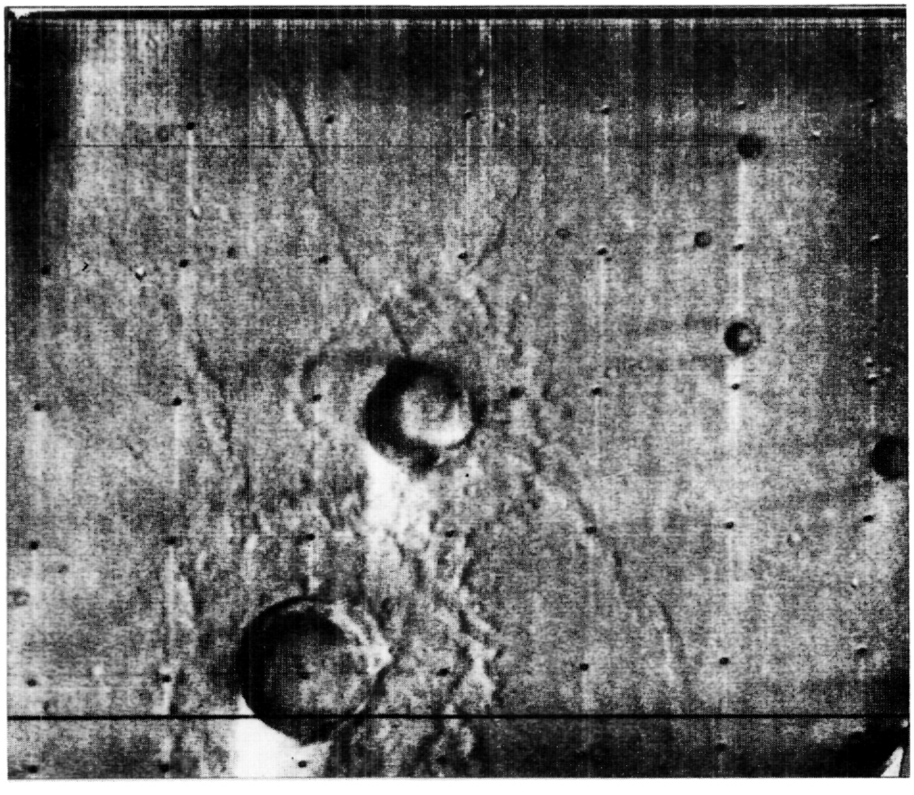

Frame B

Rev. 155

DAS 7147278

Center Point
6.6° 285.4°

MC 13

10 km

Figure 3-36. Cratered Plains. Wind streaking from left to right. Footprint of photo is shown in Figure 3-33.

Figure 3-37. Hummocky Plains occurring at junction of Cratered Terrain and Smooth Plains. Knobs and mesas are in lower right. A probable volcanic caldera with flanking furrowed deposits occurs in upper right. Footprint of Figure 3-38 is shown.

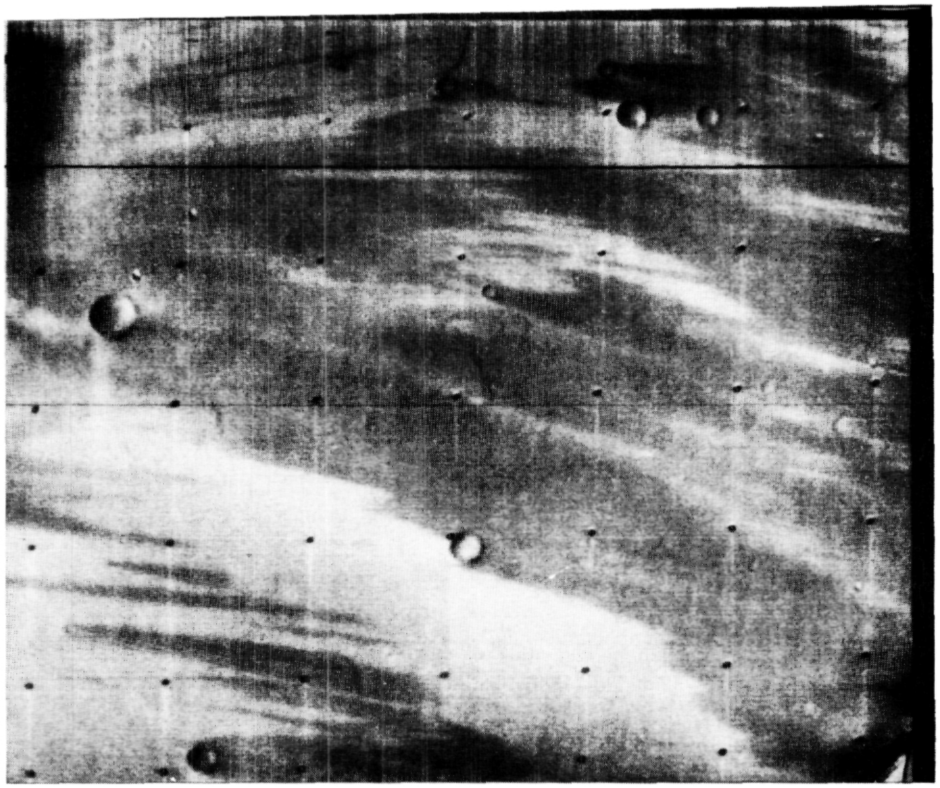

Frame B
Rev. 155
DAS 7147348
Center Point
10.7° 283.6°
MC 13

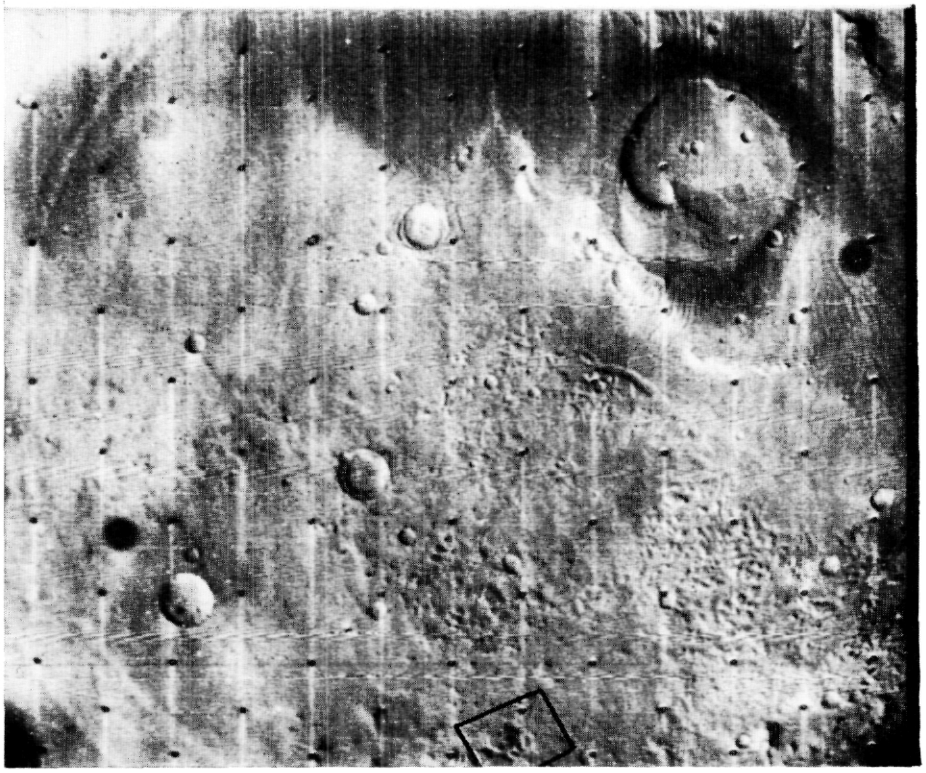

Frame A
Rev. 177
DAS 7937968
Center Point
-9.0° 188.1°

Figure 3-38. Hummocky Plains, showing closely-spaced mesas and knobs. Footprint for photo is shown in Figure 3-37.

Figure 3-39. Two isolated knobs, surrounded by Smooth Plains. Polygonal shape of knobs suggests structural control.

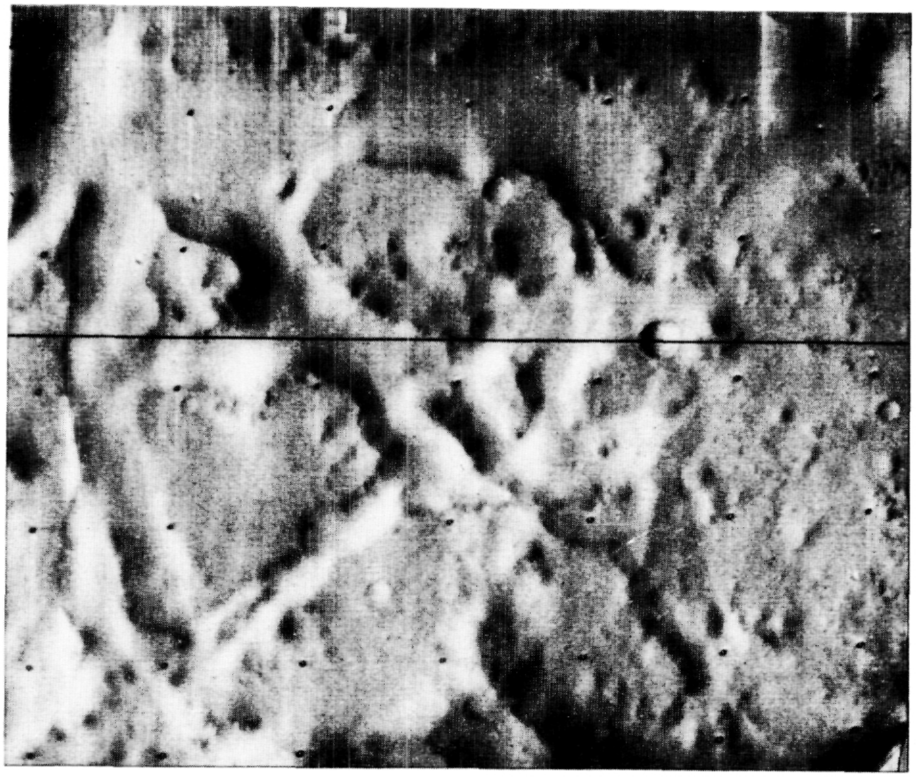

Frame B

Rev. 137

DAS 7937928

Center Point
-11.6° 189.1°

MC 23

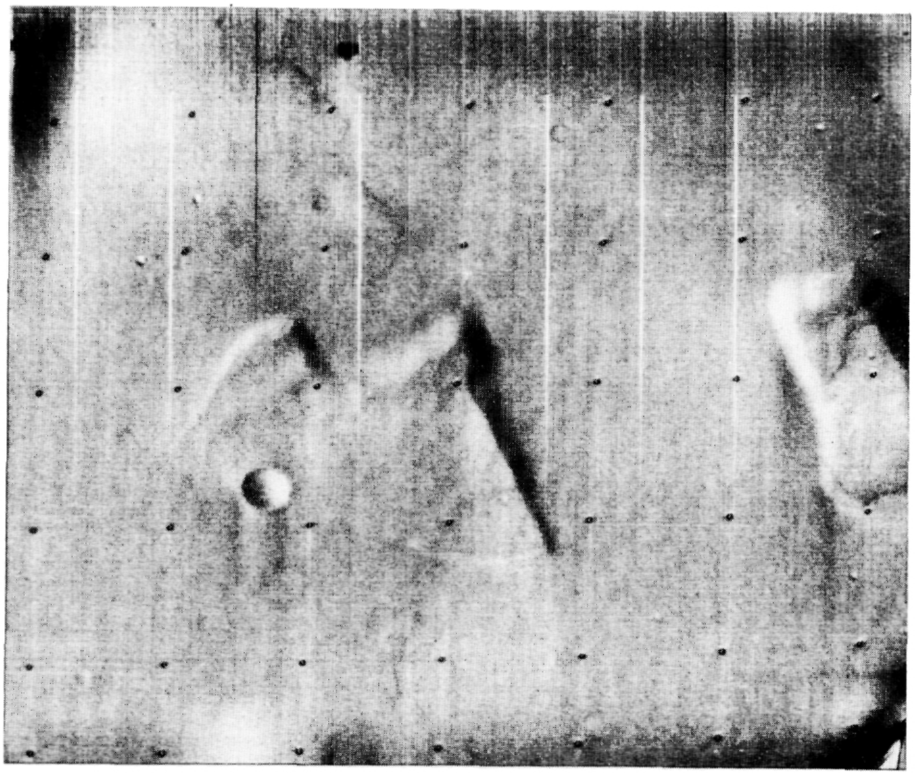

Frame B

Rev. 146

DAS 6823108

Center Point
-3.0° 149.3°

MC 16

Figure 3-40. Lineated Plains, showing braided, fault-bounded depressions and plateaus.

Figure 3-41. Patterned Plains, showing dendritic network of narrow depressions.

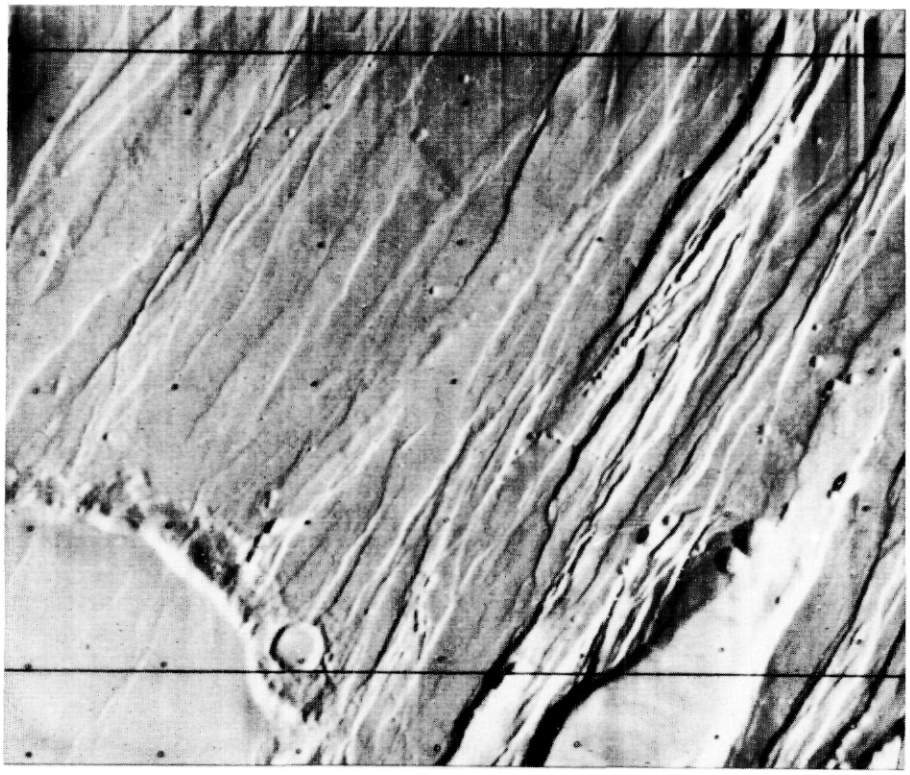

Frame B

Rev. 191

DAS 8442914

Center Point
31.2° 108.6°

MC 9

10 km

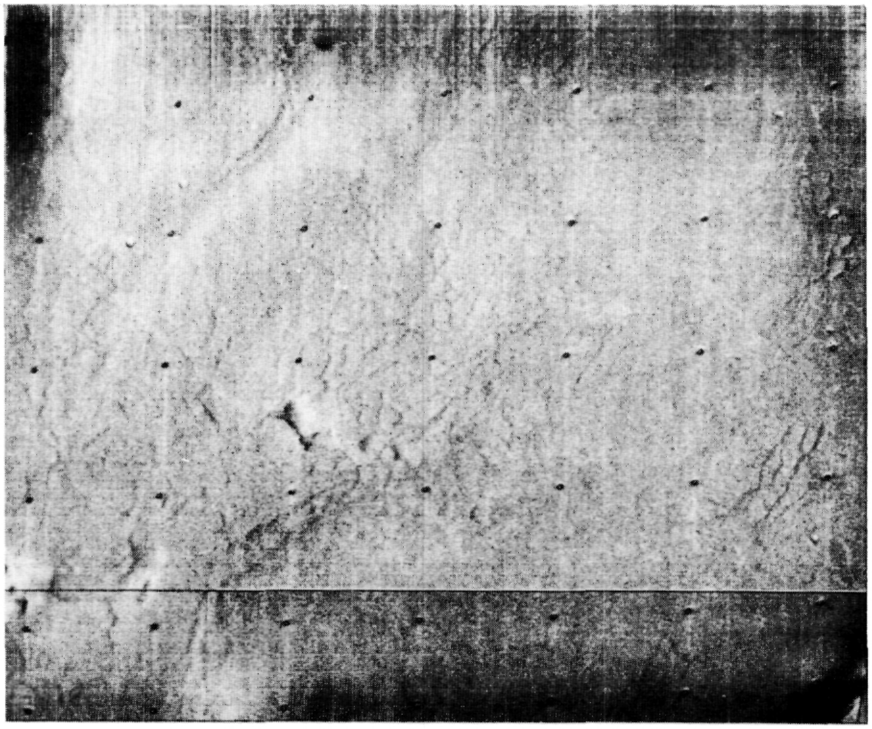

Frame B

Rev. 216

DAS 9341014

Center Point
-1.0° 186.1°

MC 23

10 km

Figure 3-42. Patterned Plains, showing broad channel trending from bottom to top and containing teardrop-shaped "islands" suggestive of hydrodynamic shaping.

Figure 3-43. Ridged Plains. Some of the ridges are associated with rilles. Note wind streaks emanating from craters.

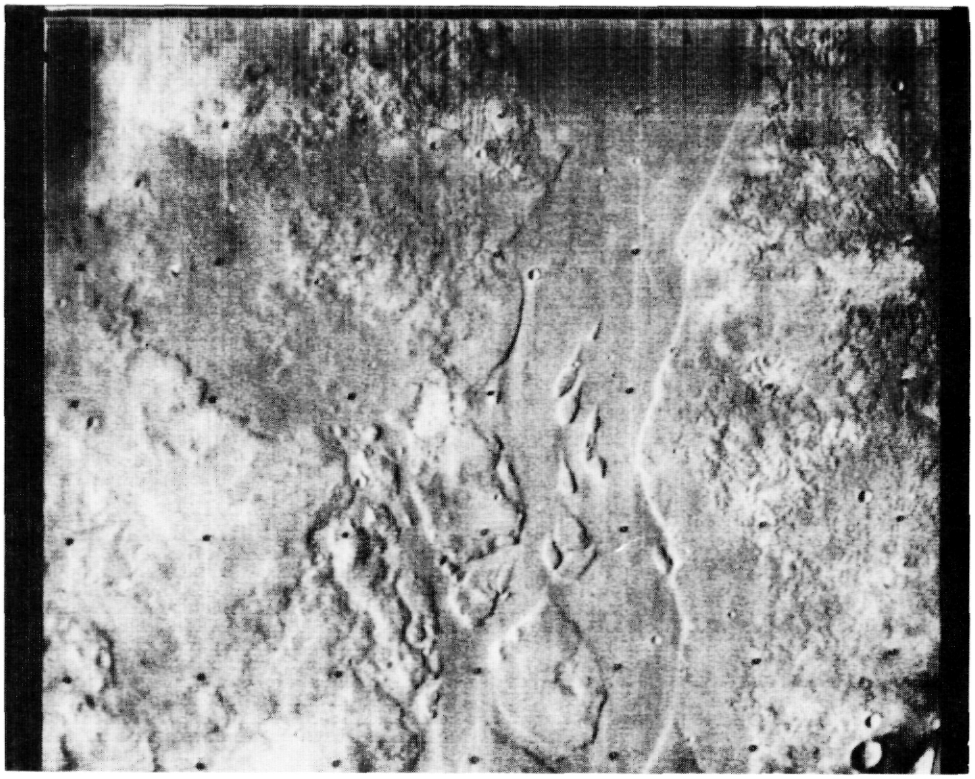

Frame B

Rev. 204

DAS 8910724

Center Point
31.1° 228.7°

MC 14

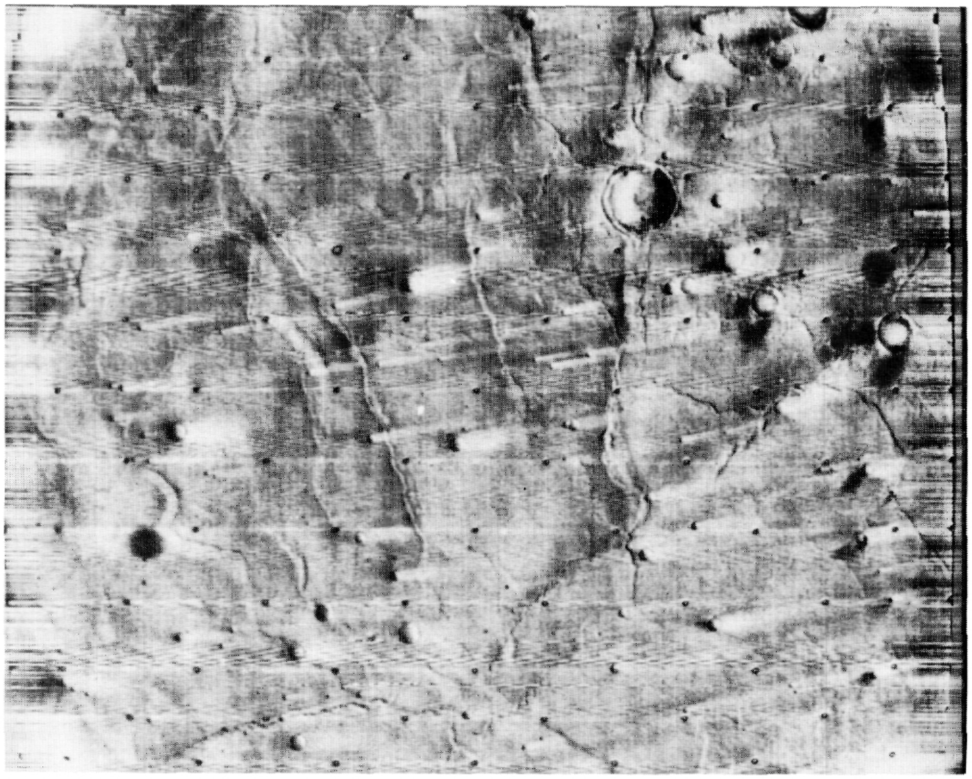

Frame A

Rev. 206

DAS 8981184

Center Point
-20.7° 245.2°

MC 22

Figure 3-44. Ridged Plains. Echelon ridges trend across top of picture. Note wind streaking from upper left to lower right.

Figure 3-45. Cratered Terrain. Smooth intercrater areas are neglibible.

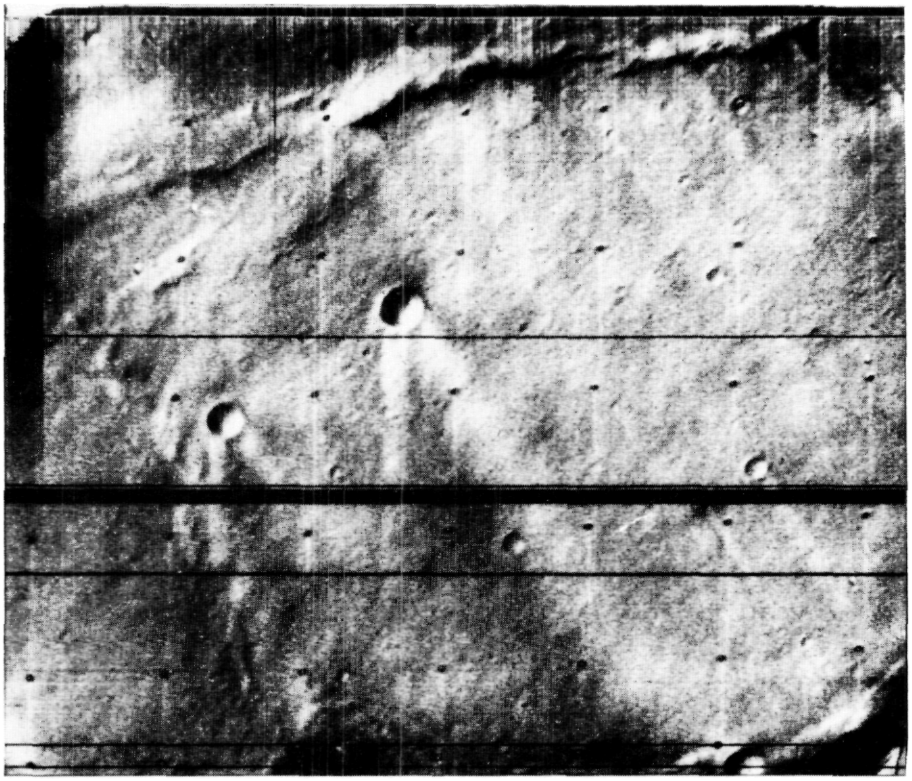

Frame B

Rev. 167

DAS 758338

Center Point
-20.8° 240.7°

MC 22

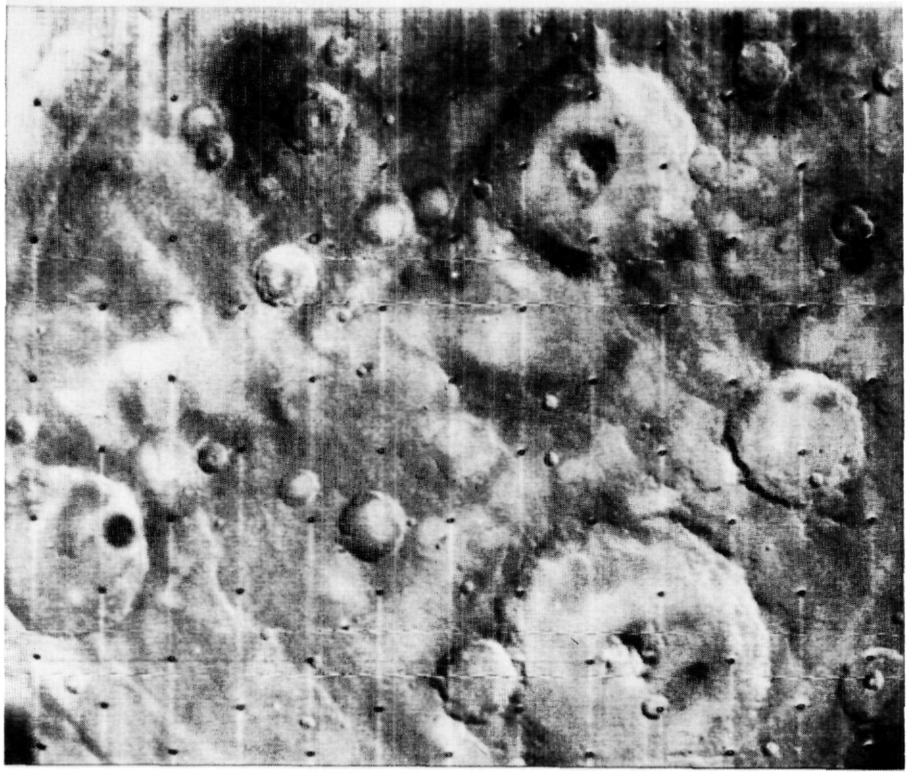

Frame A

Rev. 185

DAS 8225534

Center Point
-11.9° 155.6°

MC 16

Figure 3-46. Cratered Terrain. Furrowed texture characterizes large parts of cratered surfaces.

Figure 3-47. Flat Cratered Terrain, characterized by large intercrater areas generally featureless at A-frame resolution. Footprint of Figure 3-48 is shown.

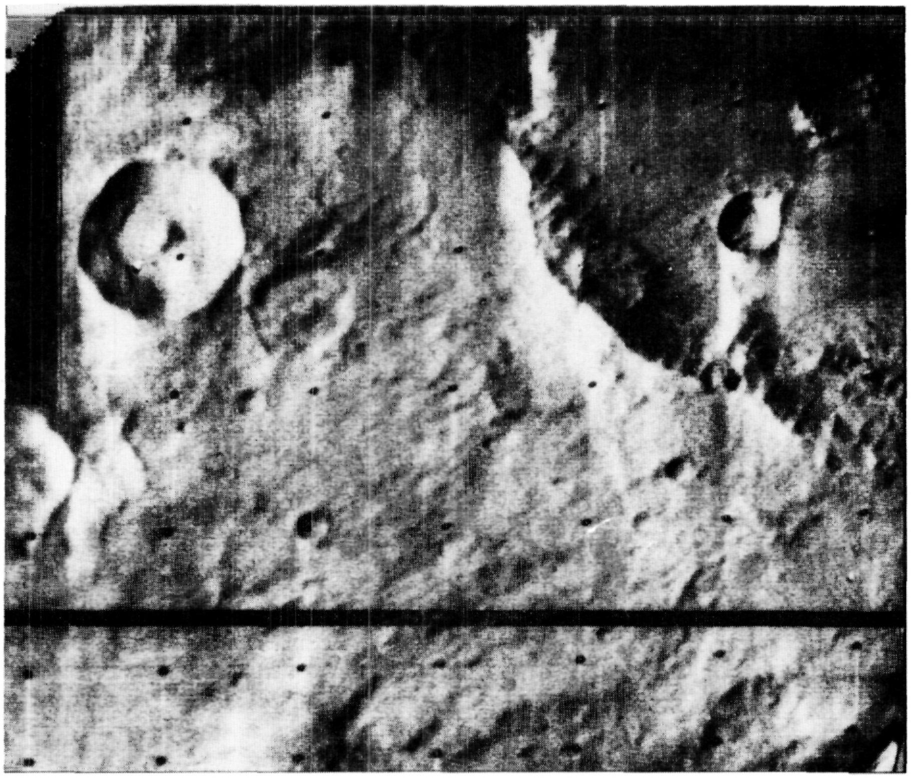

Frame B

Rev. 142

DAS 6678628

Center Point
-23.0° 175.2°

MC 16

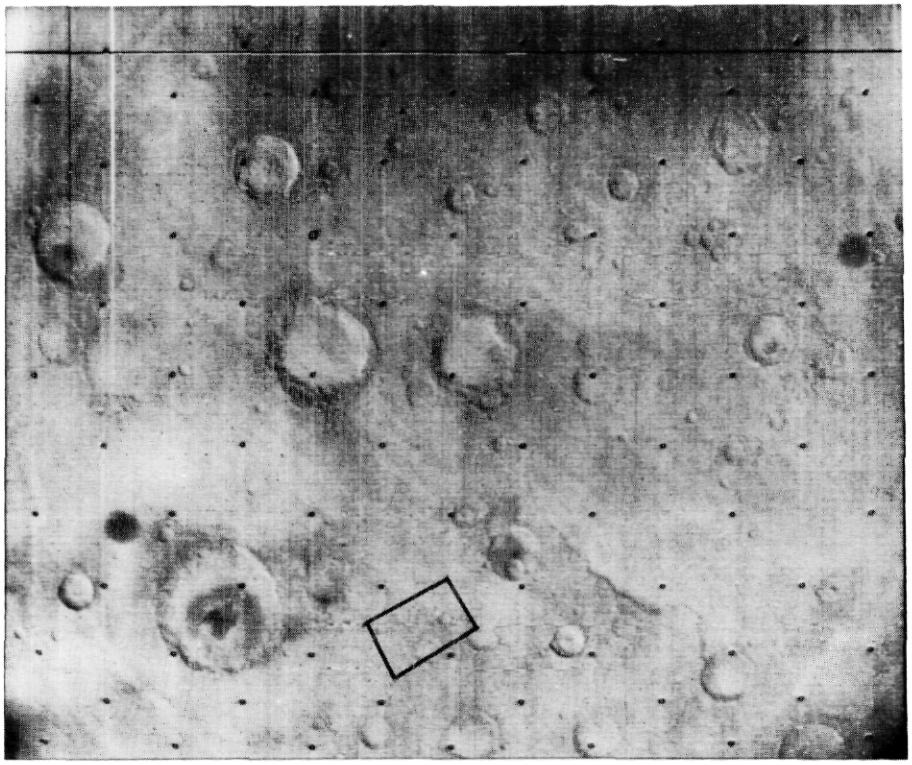

Frame A

Rev. 141

DAS 6643598

Center Point
17.4° 344.1°

MC 12

Figure 3-48. Flat Cratered Terrain. Intercrater areas have considerable relief, including scarps, ridges, and rough terrain around craters. Footprint of picture is shown in Figure 3-47.

Figure 3-49. Patterned Cratered Terrain. Intercrater areas contain irregular plateaus and depressions.

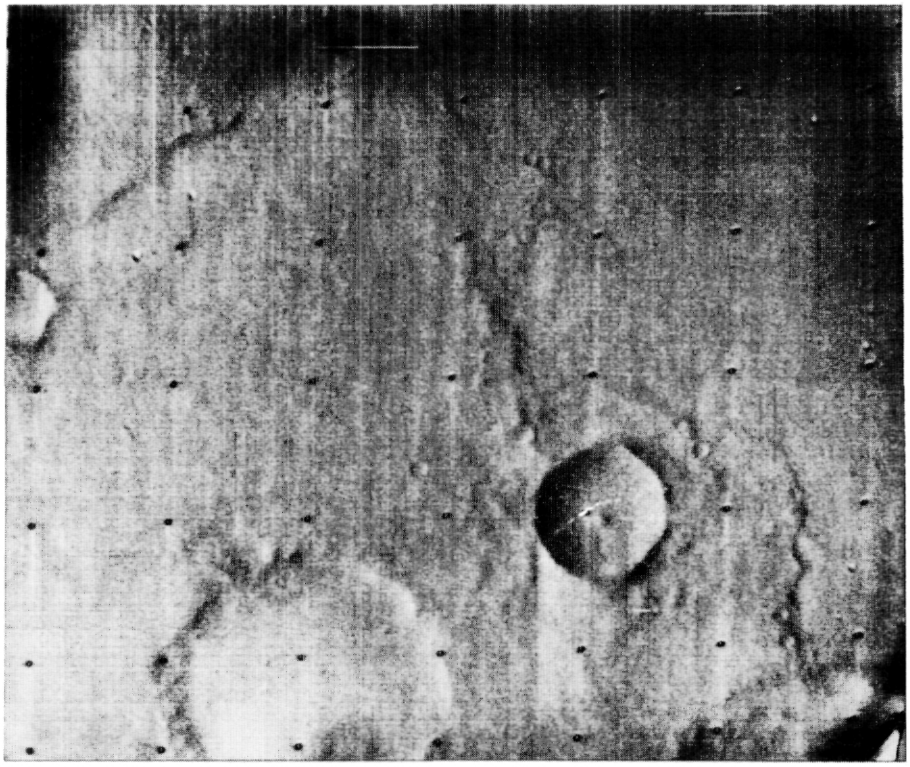

Frame B

Rev. 141

DAS 6643558

Center Point
15.1° 344.9°

MC 12

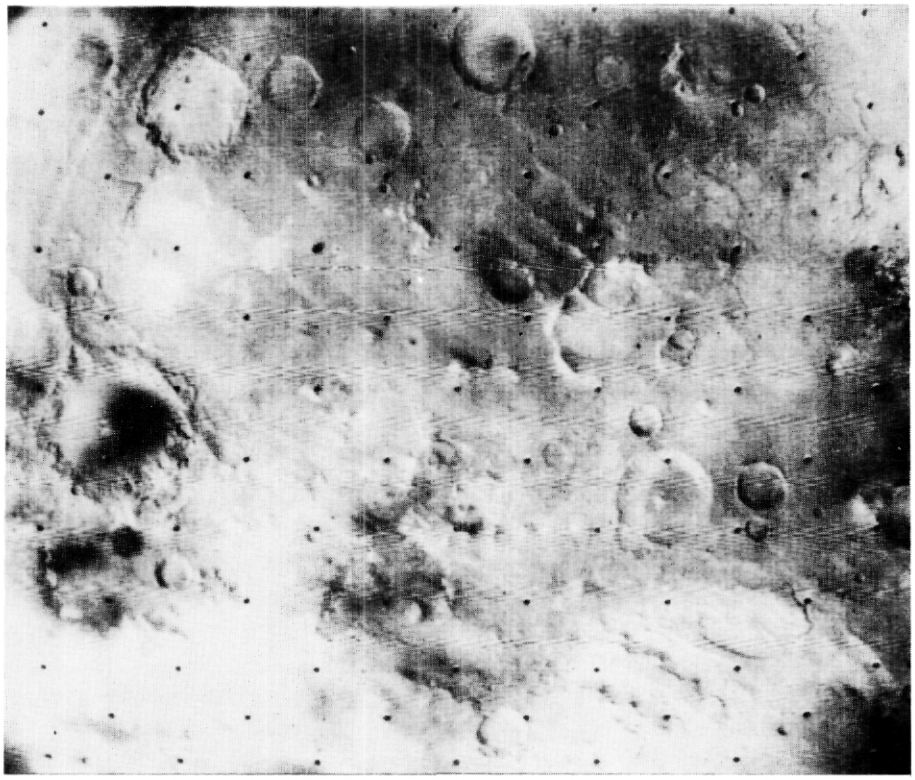

Frame A

Rev. 198

DAS 8693344

Center Point
-25.3° 284.3°

MC 21

Figure 3-50. Patterned Cratered Terrain. Intercrater areas have a rough, etched appearance.

Figure 3-51. Irregular Terrain. Prominent mountainous ridges occur in this rough terrain adjacent to the Hellas basin.

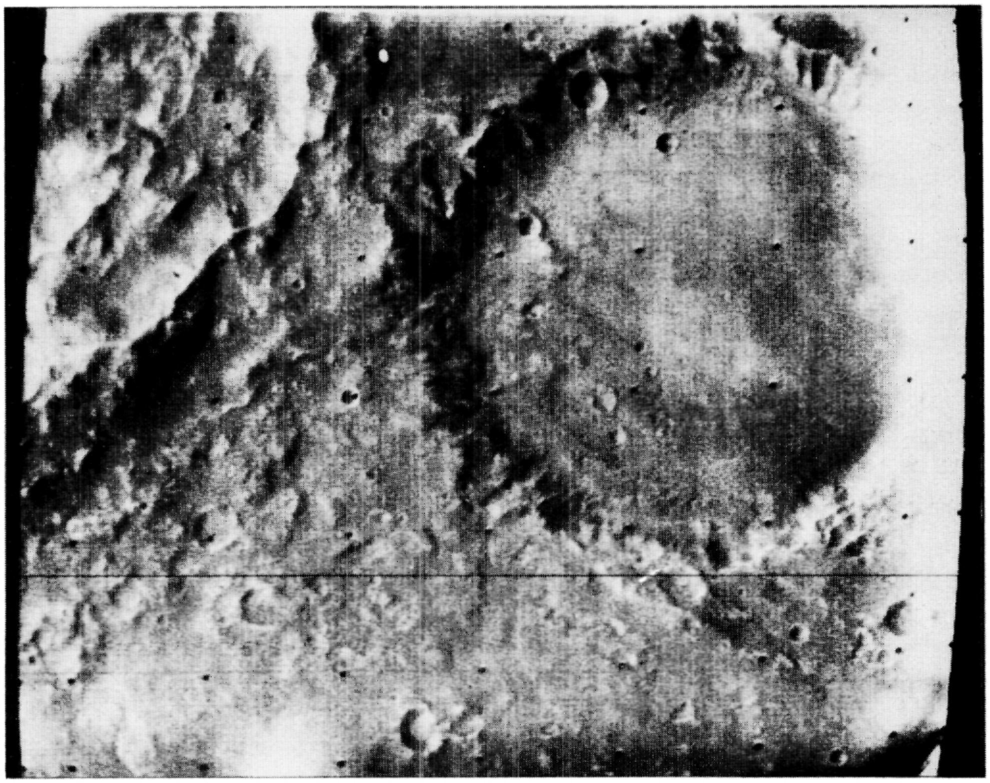

Frame B

Rev. 198

DAS 8693374

Center Point
-23.2° 283.0°

MC 21

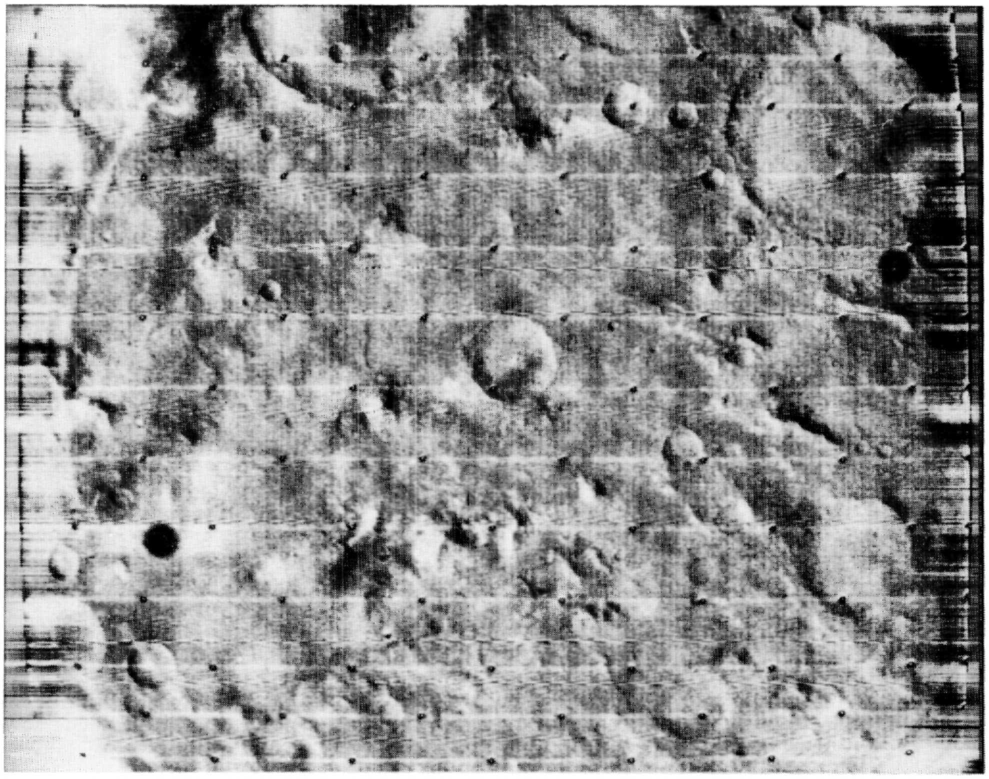

Frame A

Rev. 120

DAS 5887388

Center Point
-27.4° 280.3°

MC 21

Figure 3-52. Irregular Terrain, characterized by discreet equidimensional peaks, occurs within the plains. Note the wind streaking from upper right to lower left. Footprint of Figure 3-53 is shown.

Figure 3-53. Irregular Terrain. Isolated peaks protrude above plains. Note wind streaking from right to left. Footprint of picture is shown in Figure 3-52.

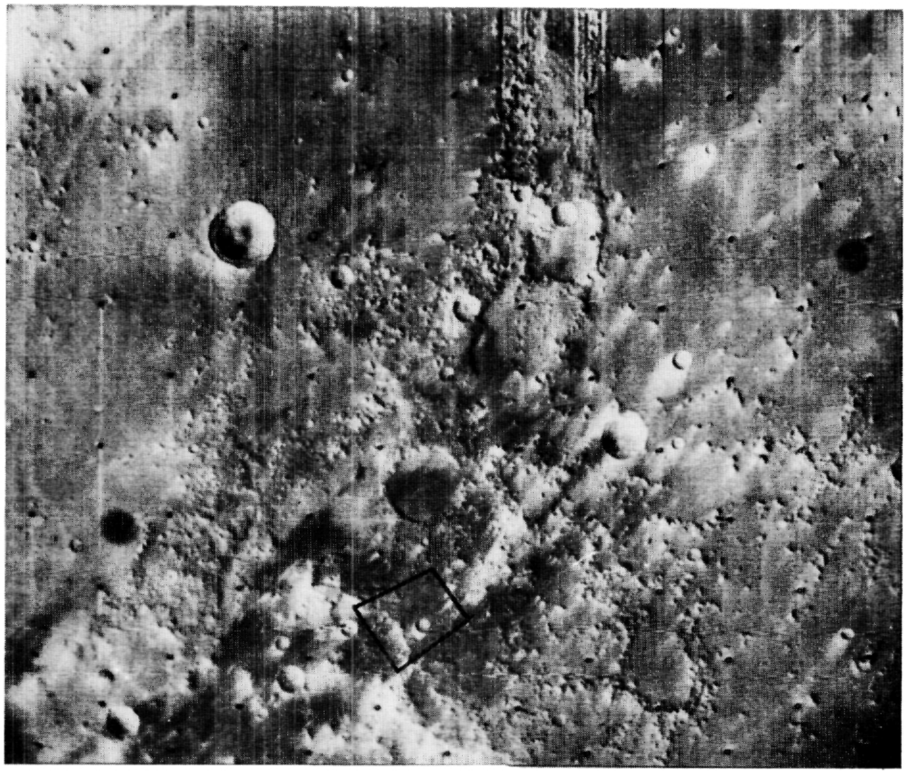

Frame A

Rev. 175

DAS 8766778

Center Point
17.4° 188.1°

MC 15

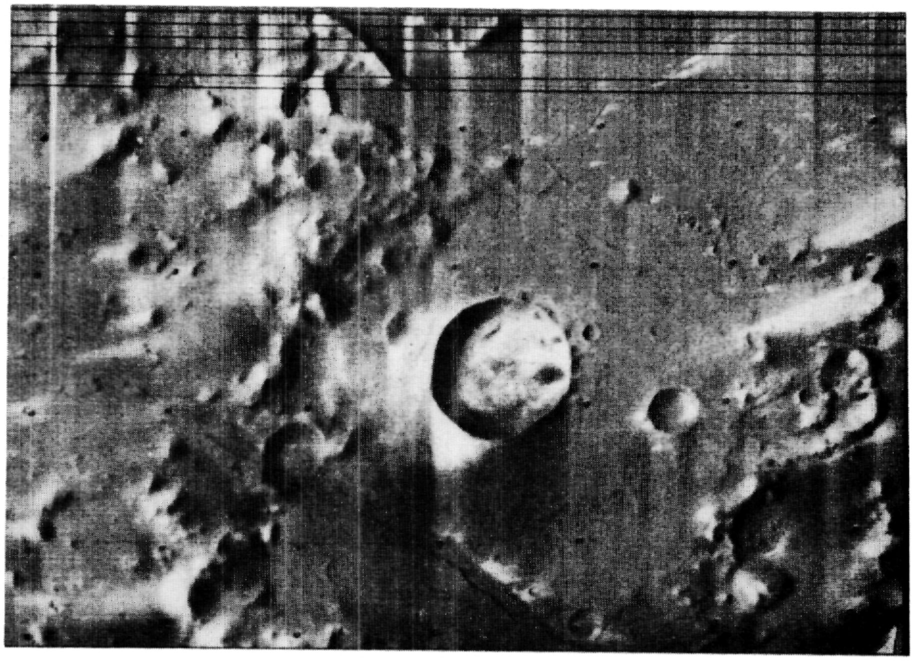

Frame B

Rev. 175

DAS 7866738

Center Point
15.1° 188.9°

MC 15

Figure 3-54. Canyonlands. This huge linear cleft is paralleled by straight crater chains, suggesting a structural control for both. Footprint of Figure 3-55 is shown.

Figure 3-55. Canyonlands. Ridged wall of great canyon shown in Figure 3-54. The slopes are encroaching on the flat Tablelands, visible at the top of the picture. Footprint of picture is shown in Figure 3-54.

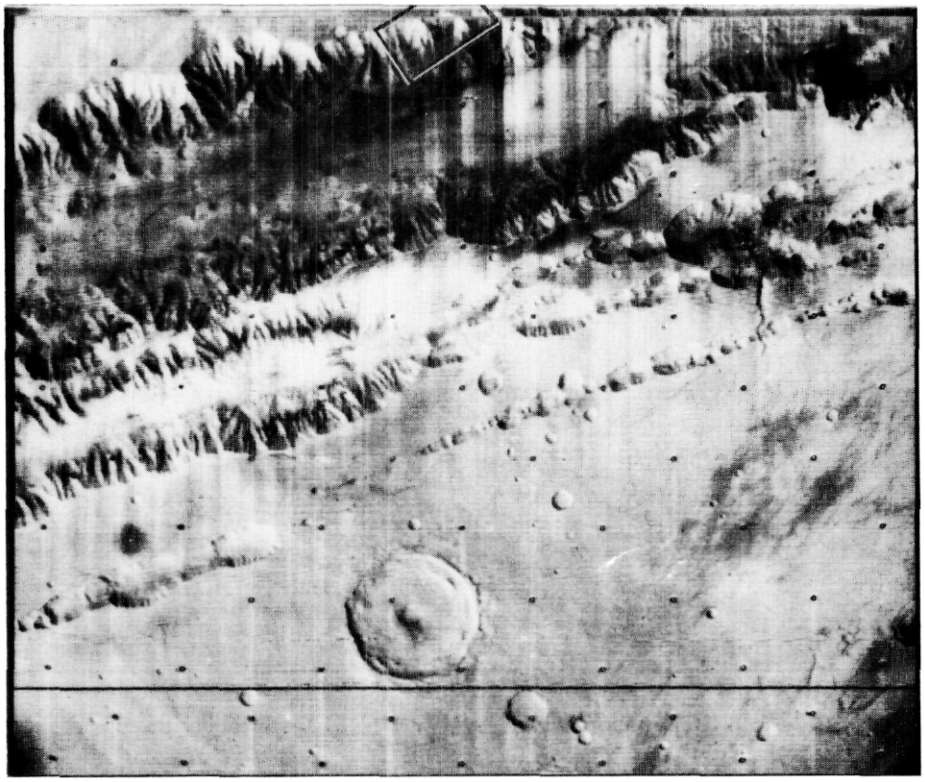

Frame A

Rev. 166

DAS 6542468

Center Point
-14.8° 62.7°

MC 18

100 km

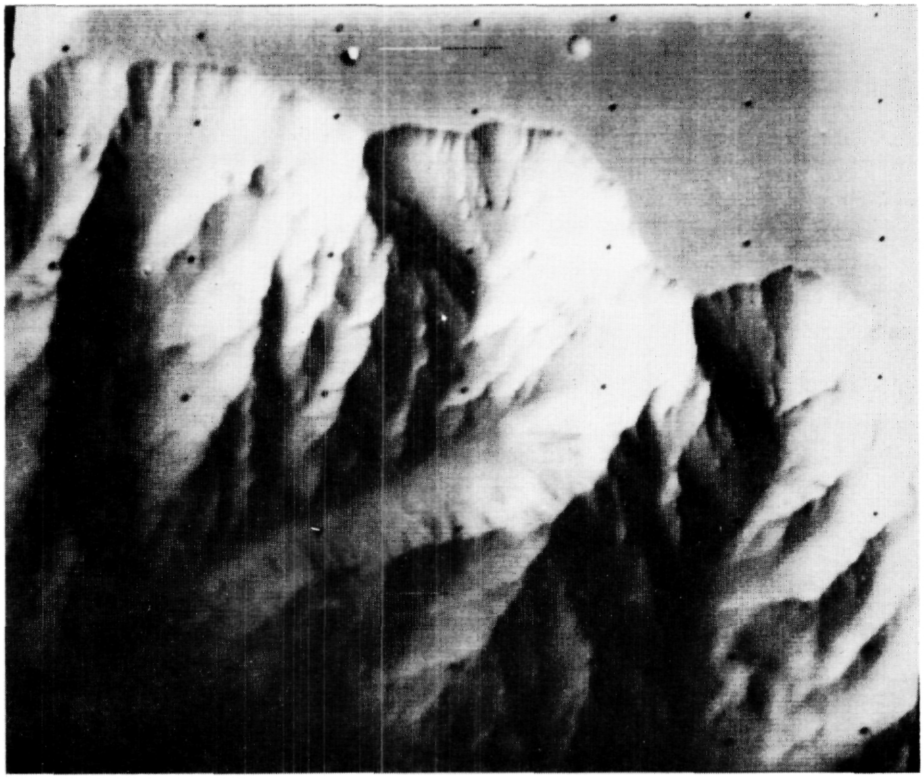

Frame B

Rev. 166

DAS 7542498

Center Point
-12.7° 61.6°

MC 18

10 km

Figure 3-56. Canyonlands. Chaotic unit. Tablelands are dissected and fragmented, probably by some combination of collapse and slumping. Footprint of Figure 3-57 is shown.

Figure 3-57. Canyonlands. Smooth Tablelands are fragmented to form a chaotic array of blocks. Footprint of picture is shown in Figure 3-56.

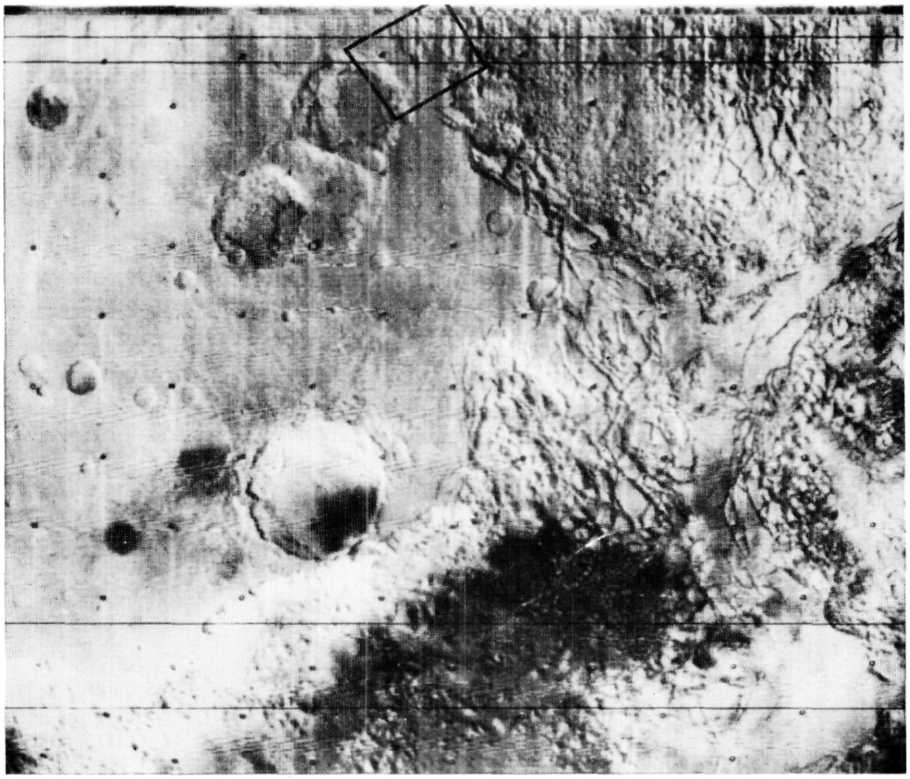

Frame A

Rev. 172

DAS 7758278

Center Point
-5.9° 30.4°

MC 19

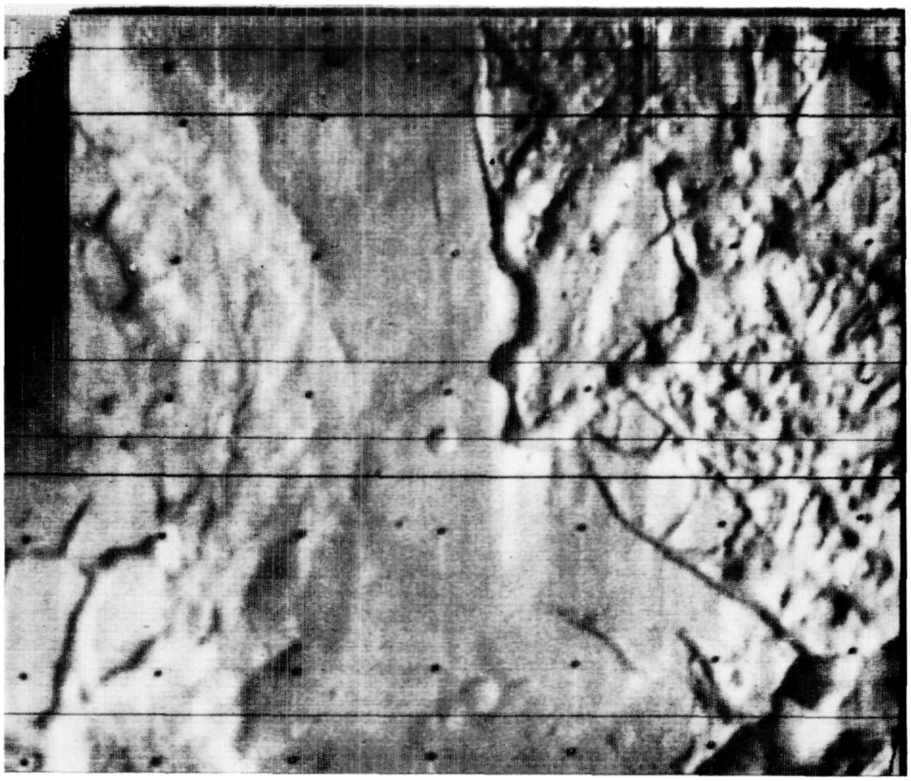

Frame A

Rev. 172

DAS 7758308

Center Point
-3.7° 29.4°

MC 19

Figure 3-58. Volcanic dome, "North Spot," showing cluster of summit calderas surrounded by flanks with lobate volcanic flow texture. Footprint of Figure 3-59 is shown.

Figure 3-59. Northern edge of volcanic dome, "North Spot." Fractures tend to be concentric around the central caldera.

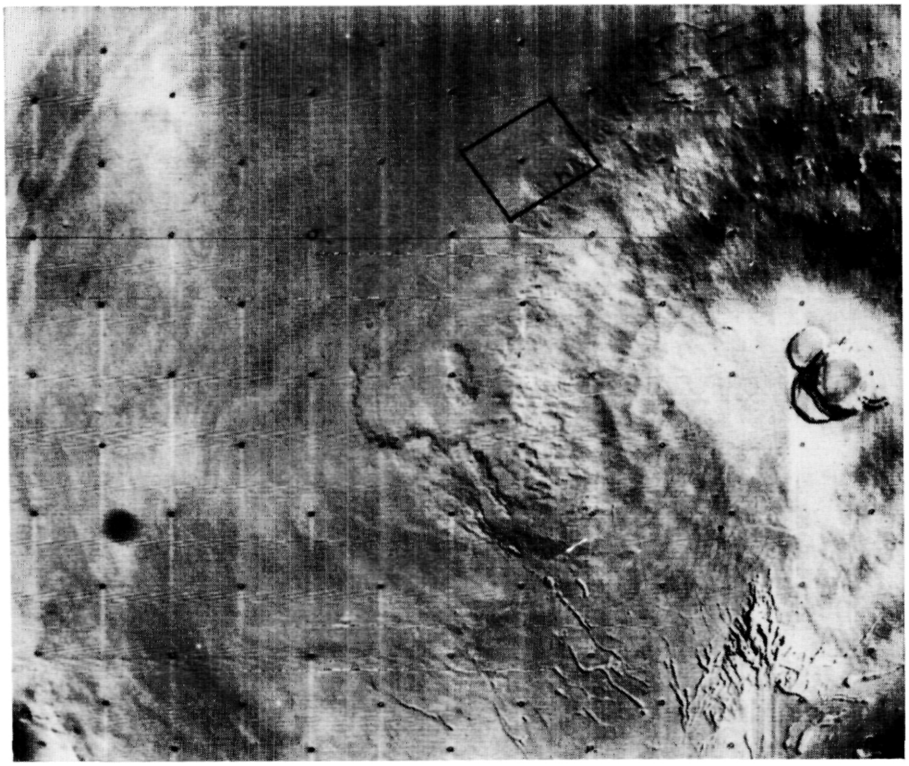

Frame A

Rev. 154

DAS 7111338

Center Point
11.4° 108.0°

MC 9

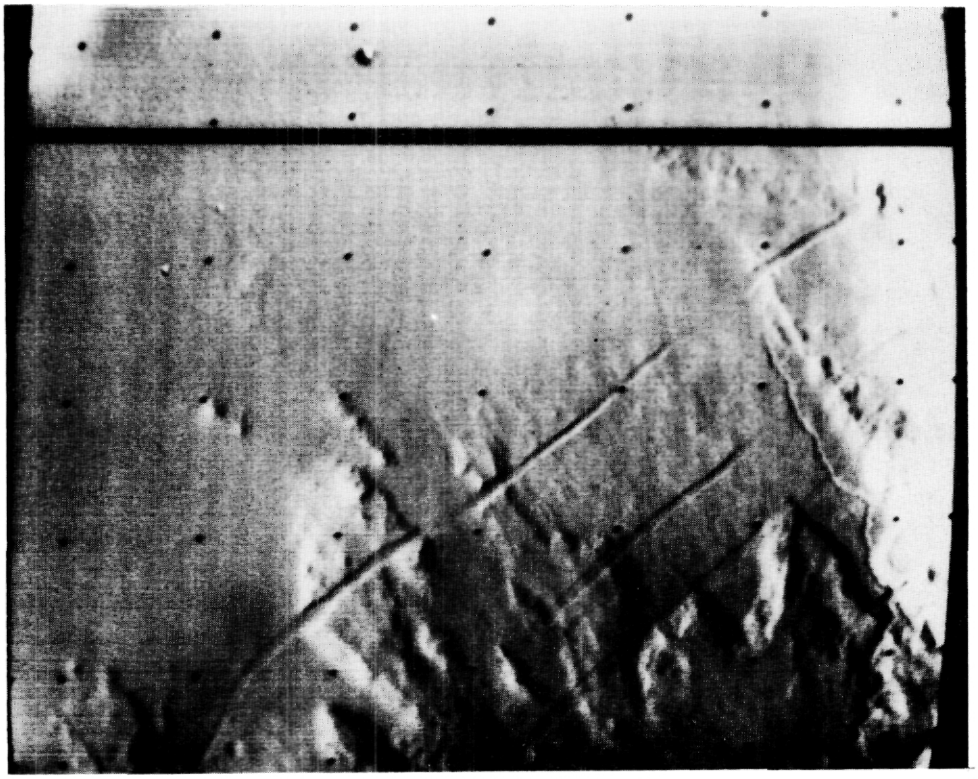

Frame B

Rev. 154

DAS 7111368

Center Point
13.2° 107.0°

MC 9

Figure 3-60. Flow fronts in Smooth Plains (Ps) unit.

Figure 3-61. Apparent stratification in Canyonlands walls.

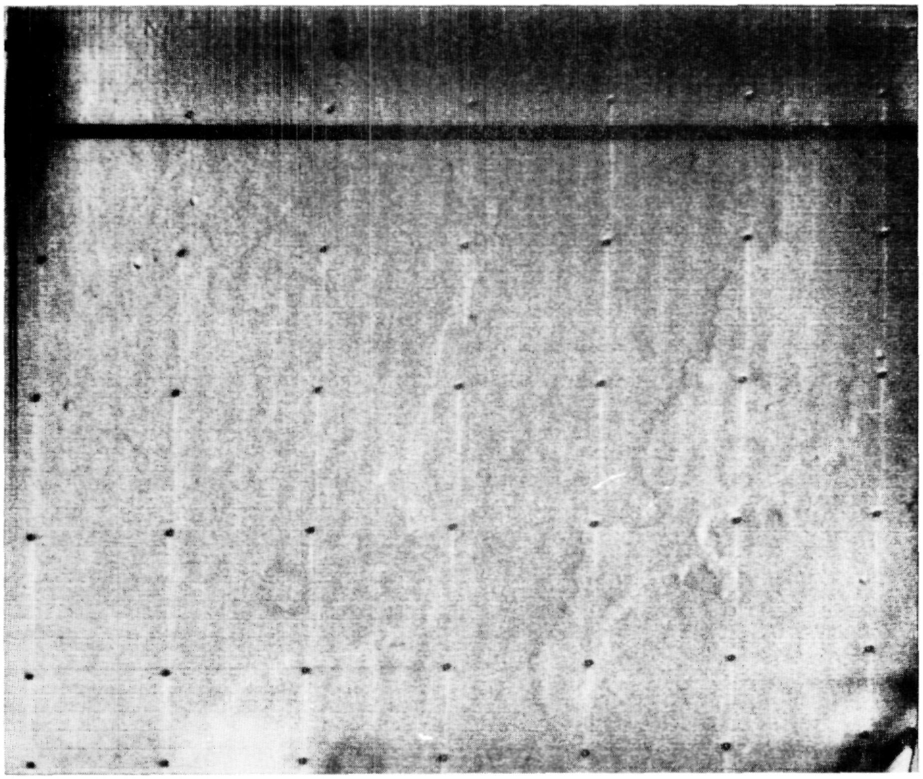

Frame B

Rev. 152

DAS 7039343

Center Point
12.7° 116°

MC 9

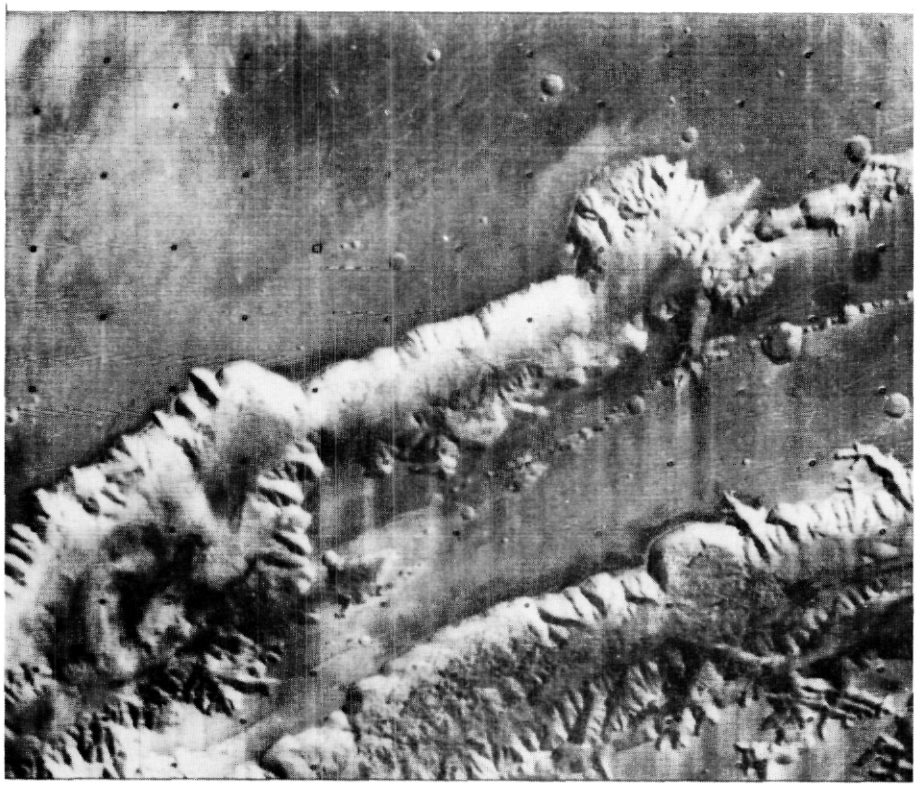

Frame A

Rev. 160

DAS 732798

Center Point
4.8° 86.2°

MC 18

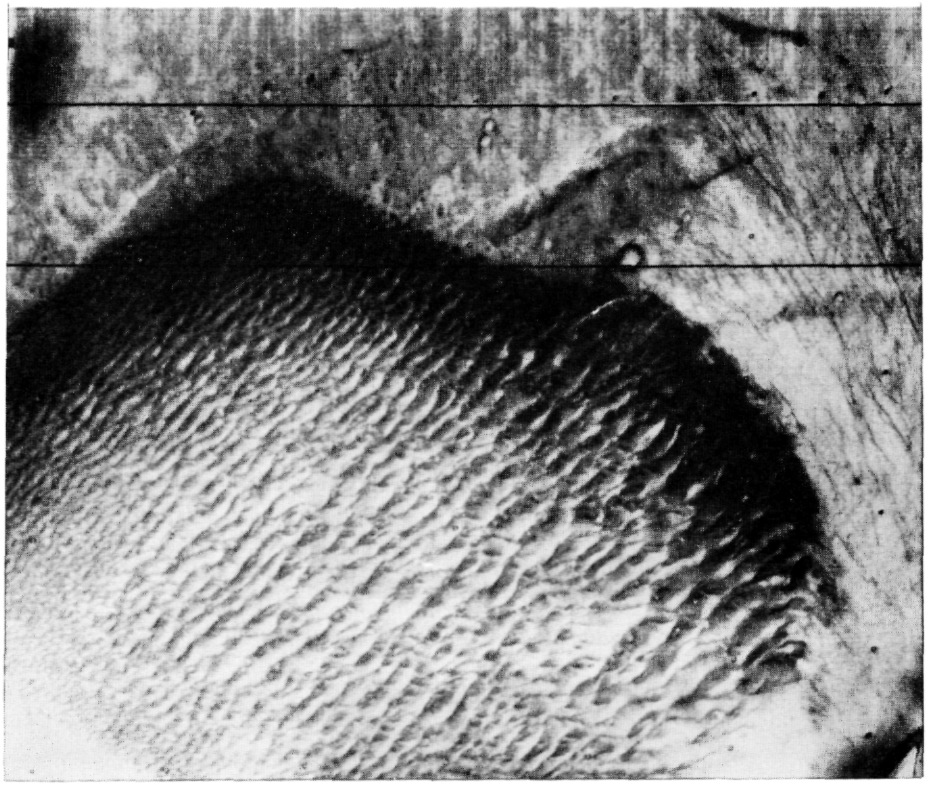

Frame B

Rev. 229

DAS 09807429

Center Point
47.6° 329.8°

MC 27

10 km

Figure 3-62. Sand dune structures in floor of a crater

3.2.2.2 Conclusions

Inasmuch as the present VDAT mapping exercise concerns itself with defining accessible regions for Viking landing sites and establishing a comprehensive understanding of the terrain features and their implications in assessing engineering and science criteria, a brief summary of the relative merit of the data products and their subsequent interpretation is warranted.

3.2.2.2.1 Mariner Photographic Resolutions and Viking Requirements

During a joint meeting of VDAT/LSWG (Landing Site Working Group), some discussions as to the utility of Mariner pictures for Viking site certification were presented. Concern arises because the best resolution capability of the Mariner system is only 100 meters and the Viking need for terrain evaluation on the scale of the Viking Lander, is 2 - 4 meters.

Several answers to this concern are possible. First, it should be noted that B-frames reveal a great deal of slope information not contained in A-frames. One can calculate mean slopes for the several accessible slope lengths and then extrapolate this information to slope lengths of Viking interest. Essentially, Mariner 9 data allows one to refine the data of Figure III-C-8 in the Mars Engineering Model.

Secondly, one can apply inferential arguments. B-frames reveal certain features with morphology reminiscent of certain terrestrial features: lava flows, ejecta deposits, sand dunes, etc. If one accepts these analogs, then he can predict the appearance and behavior of these terrains at Viking scales, arguing from his experience with terrestrial counterparts.

3.2.2.2.2 The Use of Maps

It should be understood that a 1:25,000,000 terrain map cannot be automatically converted to the scales that interest Viking without additional analysis. For example, it would be a mistake to assume that all "Cratered Terrain" is prohibitively hazardous, or that all "Smooth Plains" fall within acceptable limits. The mapped provinces have dimensions of hundreds or thousands of kilometers and, necessarily, include many subunits with greater and lesser topographic hazard.

3.2.2.2.3 Craters

Because of lunar experience, a great deal of interest centers on craters. Intuitively, any Viking landing ellipse that includes craters is considered unacceptable or--at the very least--to represent a high engineering risk. This proposition is worth examining in slightly more detail.

Large Martian craters differ from their lunar counterparts in more commonly having flat floors and lacking recognizable ejecta deposits. If, as seems likely, the interiors are filled with aeolian deposits, then they might be exceptionally smooth. If the ejecta deposits have been modified and removed by some combination of physical weathering and aeolian transport, then these regions will also be smooth. Larry Soderblom (personal communication) has estimated that median slopes (slope length several hundred meters) in large, flat-floored craters are 10° to 11° and that slopes in smaller cup-shaped craters are about 10°. At Viking scales, any crater wall should be considered hazardous, although landing on the wall of subdued, flat-floored craters might not involve as much risk as intuition suggests.

Assume that a landing ellipse intersects several flat-floored craters 100 km in diameter. These craters would be impressive features. Nonetheless, the amount of wall area (i.e., demonstrably hazardous terrain) would probably comprise no more than 1-5% of the total ellipse. Should this make the landing site unacceptable, especially if the site has other desirable properties, i.e., absence of wind activity, optimum elevation, etc. ?

Considerable discussion has been presented as to the many ramifications of terrain analysis by photointerpretation. It would be an error to quickly assume that only sites that are smooth at B-frame resolution should be further considered. Subsequent analysis might reveal some exceedingly undesirable properties for these smooth regions (e.g., unacceptably low dielectric constant, evidence of wind activity, etc.) in which case one might wish to give serious consideration to a site previously ranked low, solely on a qualitative photographic analysis.

3.2.2.2.4 Major Terrain Considerations

On a very gross scale, the Viking Zone can be divided into two regions: cratered terrain and smooth plains. Almost without exception, the cratered terrain is rougher than the plains at B-frame resolution. This is true for intercrater areas which appear relatively smooth at A-frame resolution.

There is no reason to think that roughness differences apparent in B-frames are reversed at more detailed scales. Accordingly, it is valid to generalize that the cratered terrain is less hospitable for a Viking lander than are the smooth plains.

3.2.2.2.5 Viking Lander Site Selection

Preliminary evaluations, furnished to the Landing Site Working Group meeting of April 20, 1972, reveal many significant problems that Mars presents to the Viking Lander. Namely, its surface is highly variable. Parts of the Martian surface are too rough for a landing, probably too hard or cohesive to sample, and probably too porous for landing. Thus, the areas accessible to the Viking Lander are undoubtedly very restricted.

It is abundantly clear that the judicious selection of candidate sites will have to evolve through a continuing and comprehensive analysis of all data sources, both spacecraft and Earth-based, so that our knowledge of the Martian surface and processes do not conflict with Viking mission constraints and objectives.

3.2.3 Terrain Mapping and Analysis at a Scale of 1:5, 000, 000

3.2.3.1 Preparation

Terrain maps were prepared at a scale of 1:5, 000, 000 with the hope that additional terrain units could be defined and that the terrain units could readily be characterized, using the existing plots of data on dielectric constants and rms slopes furnished by the Haystack Observatory. This was partly successful in that terrain units could be, and were, easily compared with the radar data. However, it is clear that ample time was not available for satisfactory completion of these maps. Additionally, the terrain mappers were located at different points across the country and close coordination of the effort was not possible.

To prepare the terrain maps, footprint outlines furnished by Steve Saunders of JPL were used as control and the terrain units were mapped, frame by frame, with the footprint outlines. Photomosaics prepared by the USGS were not used directly since up to 4° of Mars were locally lost at the quadrangle boundaries. The mosaics were very valuable, however, in obtaining overviews and estimating sizes of features.

Quadrangle maps were assigned to the following individuals:

MC-8	H. J. Moore	Menlo Park	USGS
9	C. A. Hodges	Menlo Park	USGS
10	C. A. Hodges	Menlo Park	USGS
11	M. Grolier	Washington, D. C.	USGS
12	M. Grolier	Washington, D. C.	USGS
13	T. A. Mutch	Brown University	
14	T. A. Mutch	Brown University	
15	H. J. Moore	Menlo Park	USGS
16	T. A. Mutch	Brown University	
17	A. Olsen	Washington, D. C.	USGS
18	A. Olsen	Washington, D. C.	USGS
19	A. Olsen	Washington, D. C.	USGS
20	A. Olsen	Washington, D. C.	USGS
21	R. Arvidson	Brown University	
22	K. Jones	Brown University	
23	T. A. Mutch	Brown University	

Each mapper had a relatively short period of time to prepare maps without time for adequate coordination of their efforts with others. In addition, final data products were not available and it was found that any given feature shown on different frames from different revolutions could be up to several degrees off in location. These maps are good "working copies", adequate for early mission planning, but additional terrain mapping is required.

Results of the terrain maps are available along with explanations. Some of the broader units had to be modified from those of the mapper and are the responsibility of H. J. Moore. The details included in each were those of the mapper indicated above.

3.2.3.2 Analysis and interpretation: Correlation with Radar

Results of detailed correlation of Haystack Radar data on rms slopes and dielectric constants with the imagery is, in some cases, very satisfying and, in others, unsatisfying. Between 40°W and 63°W along 15°S, estimates of rms slopes are consistently very high (10.5°) and in agreement with visual impressions of the imagery. Indeed, it is possible to delineate the Canyonlands here with the radar. Locally, low rms slopes (0.7-2.0°) appear, that are inconsistent (such as at 14°S, 72°W). These inconsistencies may be related to ephemeris (location) errors. Good agreement with the imagery is found for the Smooth Tablelands, to the west, where the average rms slopes are near 2.7° and average dielectric constants are near 3.0. Some features, which appear rough, do not appear in the radar (such as the faulted area near 15°S, 80°W and the Canyonlands at 17°S, 48°W). High rms slopes are also recorded for the Canyonlands to the north from 15° to 50°W, and between 4° to 17°N. Here, the resolution is not sufficiently fine to consistently separate Smooth Tablelands from Canyonlands, so that large values of rms slope occur along with small ones. Sometimes extreme values occur side by side, such as at 11.5°N and 34.5°W where rms slope values of 2.0° and 8.1° are found within 1/4° of one another. The smaller value probably represents Smooth Tablelands and the larger one Canyonlands. Thus the location of the sampling area is in question. Othere detailed inconsistencies occur. At 15°S, 262°W an area, mapped as CTr, 360 km on an edge appears very rough to the radar (rms slopes 10.5°). Indeed the area is visually rougher than surrounding areas and the radar also indicates the area is rough. Other areas such as 18°S and 231°W, appear equally rough in the imagery. Yet, relatively low rms slopes are indicated. Here again, data points are found side by side with substantially different indications of roughness and dielectric constant. Such discrepancies are not the case everywhere and good agreement can be found for some superposed points.

Thus, the Haystack data on rms slope and dielectric constants should be viewed with caution at this time. The location of points may be in error and the area sampled by nearly coincident points may be different. Additionally, dielectric constants of very rough surfaces cannot be estimated and may be a function of the roughness of the surface.

Unusually large dielectric constants are obtained from the Haystack radar in the region of 320°W to 360°W and 14°S to 22°S where there is a significant amount of Patterned Cratered Terrain, Cratered Terrain, and Flat Cratered Terrain. Some of the values are so large (48.9, 20.8, 13.2) that the possibility of water should be considered and additional data sought (such as IRIS data, Russian Microwave Radiometer data, and IRR data). If there is water here, some of the Viking Site selection criteria can be met. In particular, it may be a low wet area with a (probably) permeable substrate (nearby dielectric constants of 3.0), and smooth rms slopes 2.3° ± 1.5°).

The Results of Attempting a General Correlation of terrain units raises additional questions about the validity of the Haystack estimates of dielectric constants and rms slopes. Plots comparing averaged rms slopes and dielectric constants for selected terrain units from various quadrangles show mixed results. For example, terrain units which are principally cratered terrain (Figure 3-63, Table 3-2) show an inverse relationship between averaged dielectric constants and averaged rms slopes. Although this is the reverse of results reported by R. E. Hutton, G. Pettengill reported the same kind of relationship for some of his data at the COSPAR meeting in May 1972. No such relationship is found for the smooth terrain units. Comparison of the smooth terrains (Figure 3-64, Table 3-2) show the cratered terrains are generally displaced upward and to the right of smooth terrains. Figure 3-65 makes a general comparison of the radar rms slope values and dielectric constant values for both cratered and smooth terrain. Does this mean rms slopes and dielectric constants cannot be separated in their analyses?

3.2.4 Topographic Mapping

An item of major interest (for Viking) arising from the Mariner 9 experiments, is the determination of topographic effects on the atmospheric surface pressure and the subsequent construction of a global map of the surface pressures and their corresponding elevations. Such determinations on an absolute basis are intimately connected with the specification of a mean surface level and its mean corresponding atmospheric surface pressure, and the relation of this mean surface level to the shape of the planet. Surface pressure mapping, on a relative scale, is more readily attainable, but the utility of such determinations would be of limited value for Viking.

An outstanding problem in the analysis of Mariner 9 data concerns the construction of a global map of the surface pressure/elevation based on both the IRIS and UVS data which have been anchored in some meaningful fashion to the grid of occultation values, and which is consistent with the best earth-based radar measurements. To date, only a partial and somewhat unsatisfactory solution to this

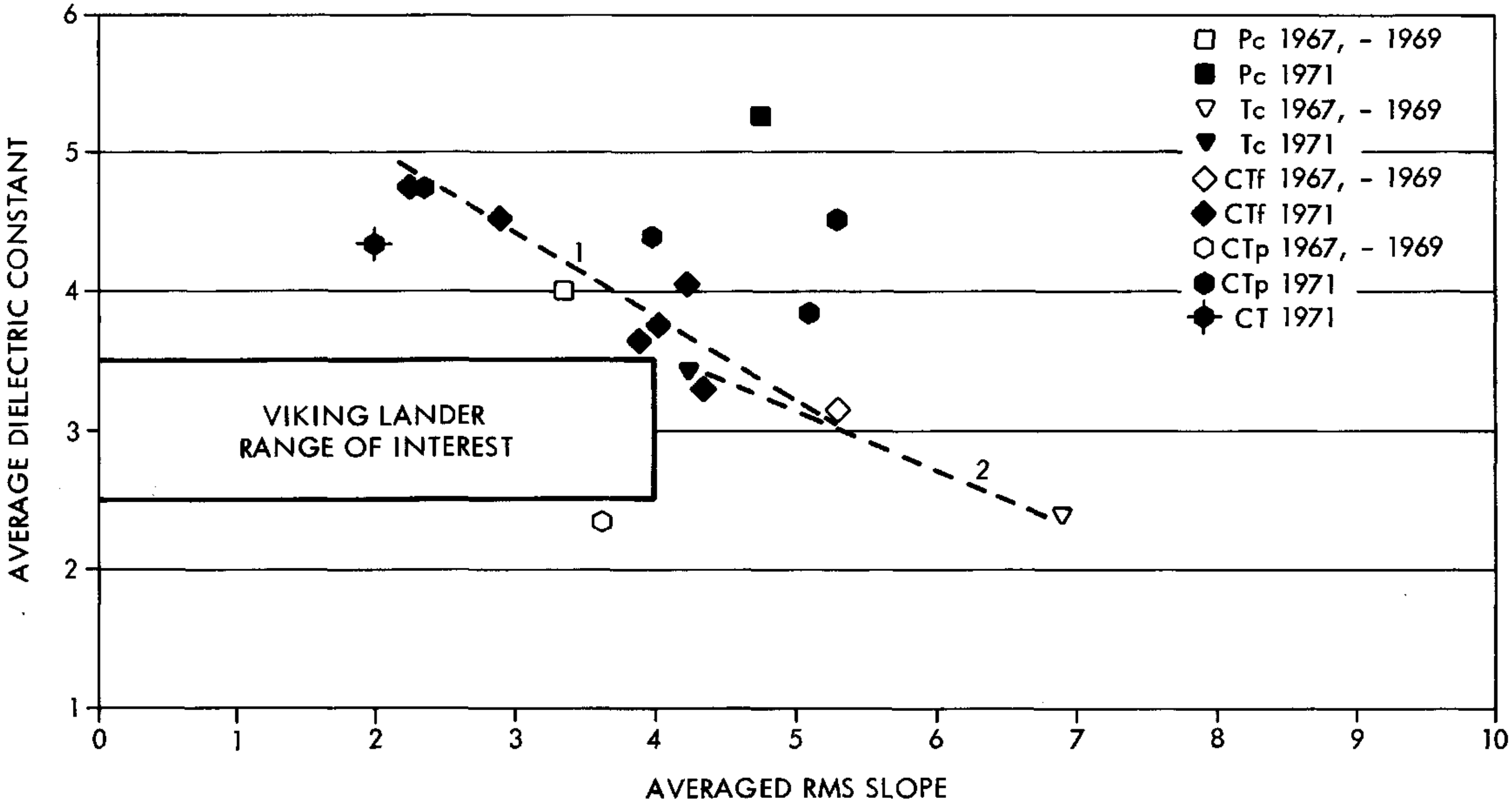

Figure 3-63. Comparison of averaged rms slope and dielectric constant for Cratered Terrain. Line 1 is for Cratered Terrain; Line 2 for Cratered Tablelands. The symbols designate the terrain unit and the year the radar measurements were obtained.

Mars Chart No. / Terrain Unit	MC 8	MC 9	MC 10	MC 11	MC 12	MC 13	MC 14
Ps Smooth Plains	2.0 ± 0.4 4.6 ± 2.8	2.2 ± 0.6 5.0 ± 2.7	2.1 ± 0.6 4.9 ± 2.8	1.8 5.6	2.2 4.0	3.3 ± 0.8 3.9 ± 2.0	3.0 ± 0.9 5.2 ± 2.7
Pp Patterned Plains	1.4 6.2 ± 2.8	2.5 4.0					
Pl Lineated Plains		2.1 3.5					
Ph Hummocky Plains							
Pr Ridged Plains							
Pc Cratered Plains						4.0 ± 1.2 3.4 ± 1.8	
Ts Smooth Tablelands			2.9 ± 0.9 4.1 ± 2.0				
Tp Patterned Tablelands							
Tl Lineated Tablelands							
Tr Ridged Tablelands							
Tc Cratered Tablelands			2.4 6.9 ± 2.2	2.3 ± 0.6 6.3 ± 2.7			
CT Cratered Terrain							8.1
CTp Patterned Cratered Terrain						2.9 4.5	
CTr Ridged Cratered Terrain							
CTf Flat Cratered Terrain			2.8	7.1 ± 2.0	3.2 ± 1.0 5.3 ± 2.4	1.7 3.0	
Cr Crater and Crater Rim			8.1	2.3 5.4	3.0 4.4 ± 3.0		
CL Canyon Lands				2.3 7.8 ± 1.4			
Ir Irregular Terrain	2.6 6.8	1.6 4.5	8.1				1.8 7.5 ± 1.9
Ir Irregular Terrain	1.3 6.3						
Dc Domes		1.6 6.2					

FOLD-OUT #1

Table 3-2. Averaged dielectric constants/ rms slopes for 1/500,000 Terrain Map units. (±) indicates standard deviation when number of samples is larger than 10.

MC 15	MC 16	MC 17	MC 18	MC 19	MC 20	MC 21	MC 22	MC 23
3.0 ± 1.0 3.4 ± 2.7	2.0 ± 0.6 2.3 ± 2.4	2.7 ± 1.2 2.5 ± 2.4				3.3 ± 1.6 3.9 ± 3.0	3.1 ± 0.9 4.7 ± 3.5	
								2.1 4.1
							3.7 4.8	
							5.5 ± 2.2 4.7 ± 2.4	
		4.0 ± 1.5 1.2 ± 0.5	3.0 ± 1.3 2.6 ± 2.6					
		5.8 4.0						
		3.1 2.1	2.7 ± 0.9 2.1 ± 1.9					
		3.7 ± 1.8 1.9 ± 0.8						
			5.1 5.4	3.4 ± 1.8 4.3 ± 3.0				
					4.3 ± 2.0 2.0 ± 1.0	3.7 5.8		
				3.2 7.4 ± 3.8	5.5 ± 2.0 2.3 ± 1.4	3.8 ± 1.8 5.1 ± 3.1	4.5 ± 2.0 5.3 ± 2.8	4.4 ± 1.7 4.0 ± 1.2
							5.7 8.7 ± 2.5	
	3.6 ± 2.2 3.9 ± 2.7			4.5 ± 1.6 2.9 ± 1.9	4.7 ± 1.9 2.2 ± 1.4	3.3 ± 1.6 4.3 ± 2.8	4.0 ± 1.7 4.2 ± 2.3	3.8 ± 1.8 4.0 ± 2.7
4.2 6.5	2.8 7.7 ± 3.5			10.5	10.5			1.9 4.8
			2.3 ± 1.0 7.9 ± 3.3	1.7 5.9				
2.4 5.7	3.6			9.0		2.1 6.0		
2.3 5.5								

FOLD-OUT #2

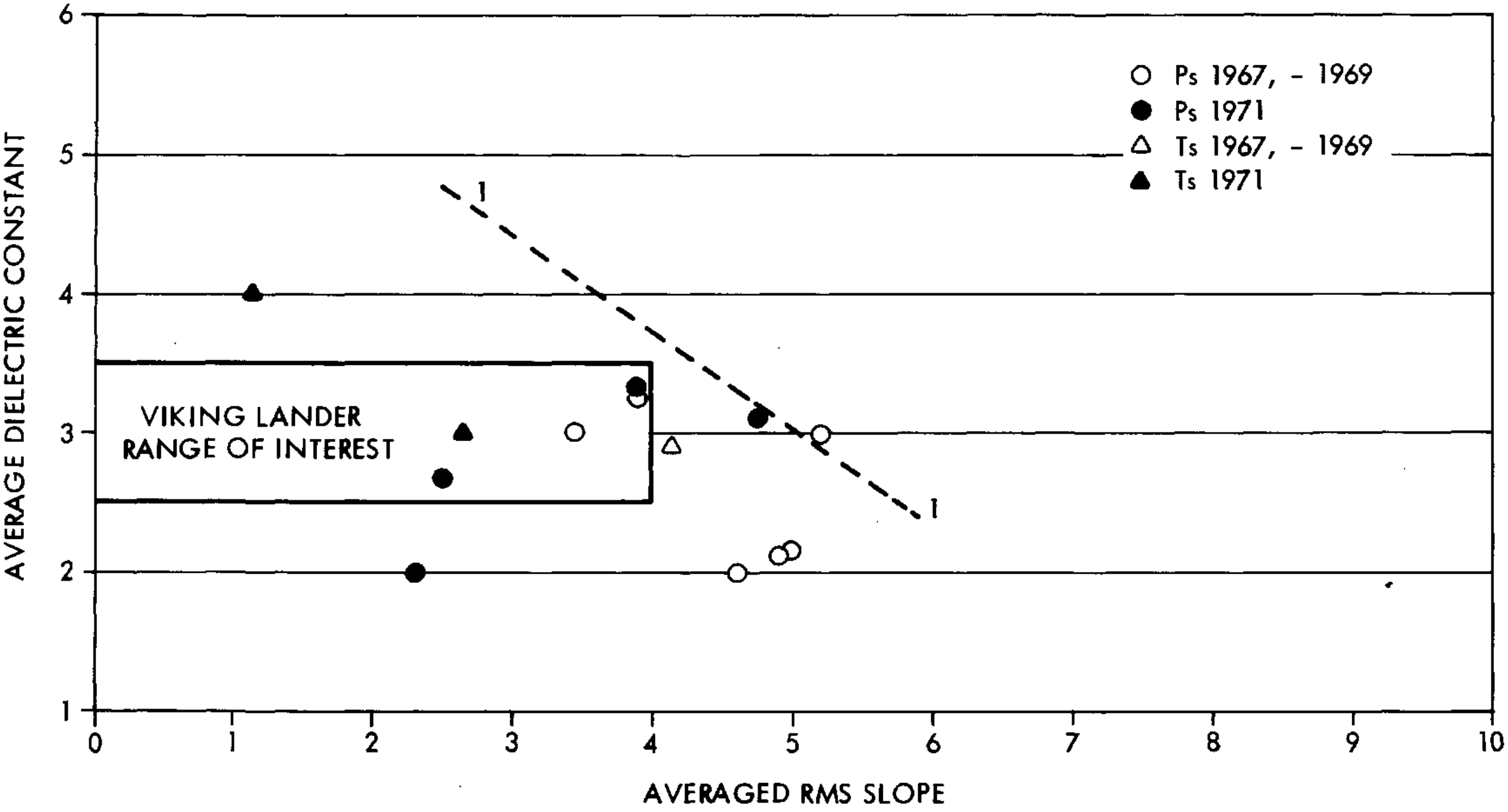

Figure 3-64. Comparison between Smooth Terrain and Cratered Terrains (Line 1). The symbols designate the terrain unit and the year the radar measurements were obtained

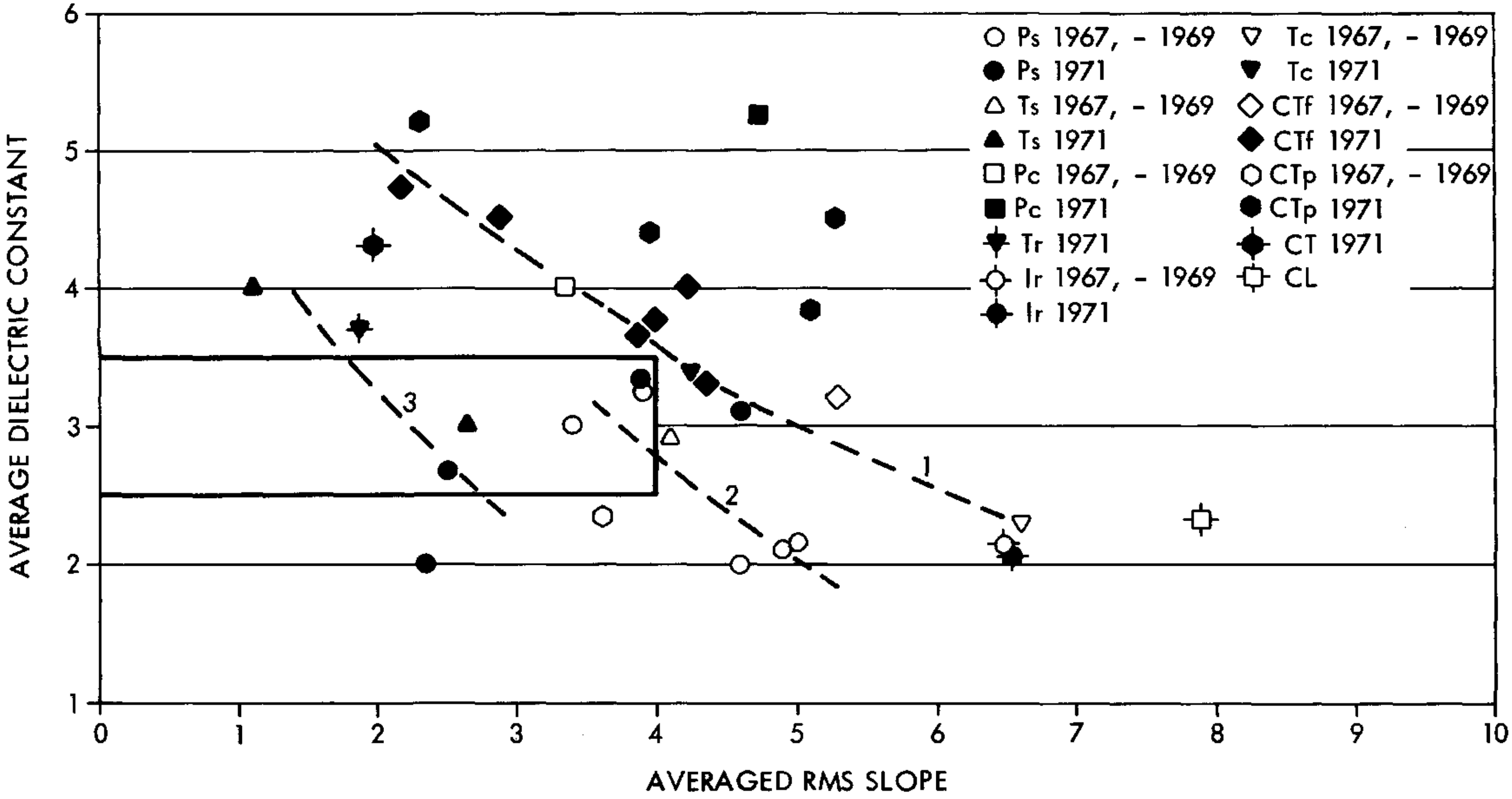

Figure 3-65. Comparison between averaged dielectric constant and rms slopes for various terrain units. Line 1 faired through Cratered Terrains; Line 2 faired through northern smooth appearing units; Line 3 faired through southern smooth units. The symbols designate the terrain unit and the year the radar measurements were obtained.

3

problem has been attained. A limited map constructed from UVS reflectance data, which has been anchored to the S-Band occultation surface pressures is available on a 1:25,000,000 scale. A similar map, based on IRIS data, is imminent. A preliminary elevation contour map, based on radar data, has been assembled. To date, no systematic effort has been attempted to compare these results with each other and with other independent data.

In the discussion below, the analysis concerned with the construction of an elevation contour map from earth-based radar data, in conjunction with the Mariner 9 S-Band occultation results are presented first. The UVS and IRIS pressure/elevation mapping available to date, follows.

3.2.4.1 Radar and S-Band Occultation Results

The S-Band occultation data, with the earth-based radar data, have been strongly considered in defining the elevation and surface pressure of Mars. Several topography maps have been prepared by VDAT utilizing this data; the following is a discussion of the procedures used in preparing these maps.

A preliminary elevation map was prepared using the Haystack radar data and the early occultation results. Fifteen entry occultation measurements available from the first 9 days in orbit (Ref. 15) were used with the radar data to produce Map-4, Preliminary Elevation Contour Map dated January 5, 1972. Since the occultation data were incomplete, it was not possible to use them to tie the Haystack data together (the various latitude bands measured during 1967, 1969, and 1971) and a good north-south control on this map was not achievable. The basis for the tie at that time was the assumption that the mean equatorial radius was 3394 km. With this assumption and the incomplete occultation data, the zero km level was defined to be at the mean equatorial radius, 3394 km, with a corresponding pressure of 6.2 mb.

In May 1972, 149 of the 160 entry and exit occultation measurements obtained from Mariner 9 were reduced and analyzed (Ref. 16) and pressure and radii measurements from these more complete results were then used with the Haystack radar data to produce a revised elevation map (Map-5, Preliminary Contour Elevation Map dated June 28, 1972). The zero km level of the map is defined to be the mean equatorial radius of the planet. From the analysis by Cain, (Ref. 2) the surface of Mars is best represented by a triaxial ellipsoid whose constants are: a = 3400.8 km, b = 3394.7 km, and c = 3372.5 km with an rms fit of 2.2 km. The Viking zone is generally defined as the area bound by the latitudes 30°N to 30°S. Considering the radii measurements in this zone, the best value for the mean equatorial radius is defined to be 3396.8 km.

For Viking purposes, the contours should follow contours of equipotential along which the atmospheric pressure is nearly constant. Thus, occultation radii were converted into elevations (E) above or below the reference level by the equation:

$$E = R_o - 3396.8 \text{ km} (1 - \frac{1}{190} \sin^2 L)$$

where 1/190 is the observed dynamical flattening, L is the latitude at the occultation point, and R_o is the observed radius at that point. The quantity subtracted from R_o on the right hand side of the equation is the dynamical shape of Mars or the aeroid. In reality, the aeroid is also triaxial, but the difference between the a and b axes of the areoid is only about 0.8 km and thus, the longitudinal dependence of the equation can, and has been, neglected.

Elevation profiles were derived which crossed the Haystack radar profiles located at +22°, +3° and -14° to -22°, at two longitudes (see Figure 3-66. In this way the absolute occultation data could be used to accurately tie all 3 sets of Haystack data to the 0 reference level. This was done by simply force fitting each of the Haystack profiles to the occultation profile at the crossover points. This fitting is estimated to be internally accurate to 1 to 2 km, but there exists a strong possibility of systematic errors of up to 3 km in the tie. Thus, the north-south control of the map, along the radar swaths, is about 2 km. The east-west control is 1 km or better in the south (-15°), 1 km to 1 1/2 km near the equator (+10°) and about 2 km in the north (+22°). The east-west control between the 1967, 1969, and 1971 radar sets is, of course, slightly poorer since the contours in these strips are interpolated (see Figure 3-66).

The pressure at 0 km was defined using the entry pressures plotted vs. elevation above an arbitrary equipotential surface. From these data, the pressure at the equator for a radius of 3396.8 km is 4.8 mb and hence is the pressure at 0 km. Figure 3-67 gives the entry data in this form with a theoretical pressure vs. altitude curve for an isothermal atmosphere with T = 250°K, the scale height equal to 12 km, and with $P_o = 4.8$ mb at 0 km.

At present, the greatest uncertainty in the map is the north-south tie. As a result, it is extremely important to get an independent check on the tie. This should be accomplished by utilizing the new Mars ephemeris based on the Mariner 9 tracking results to reduce the Haystack and JPL data to absolute radii. When this is done, the relative north-south accuracy should be 1 km or perhaps better.

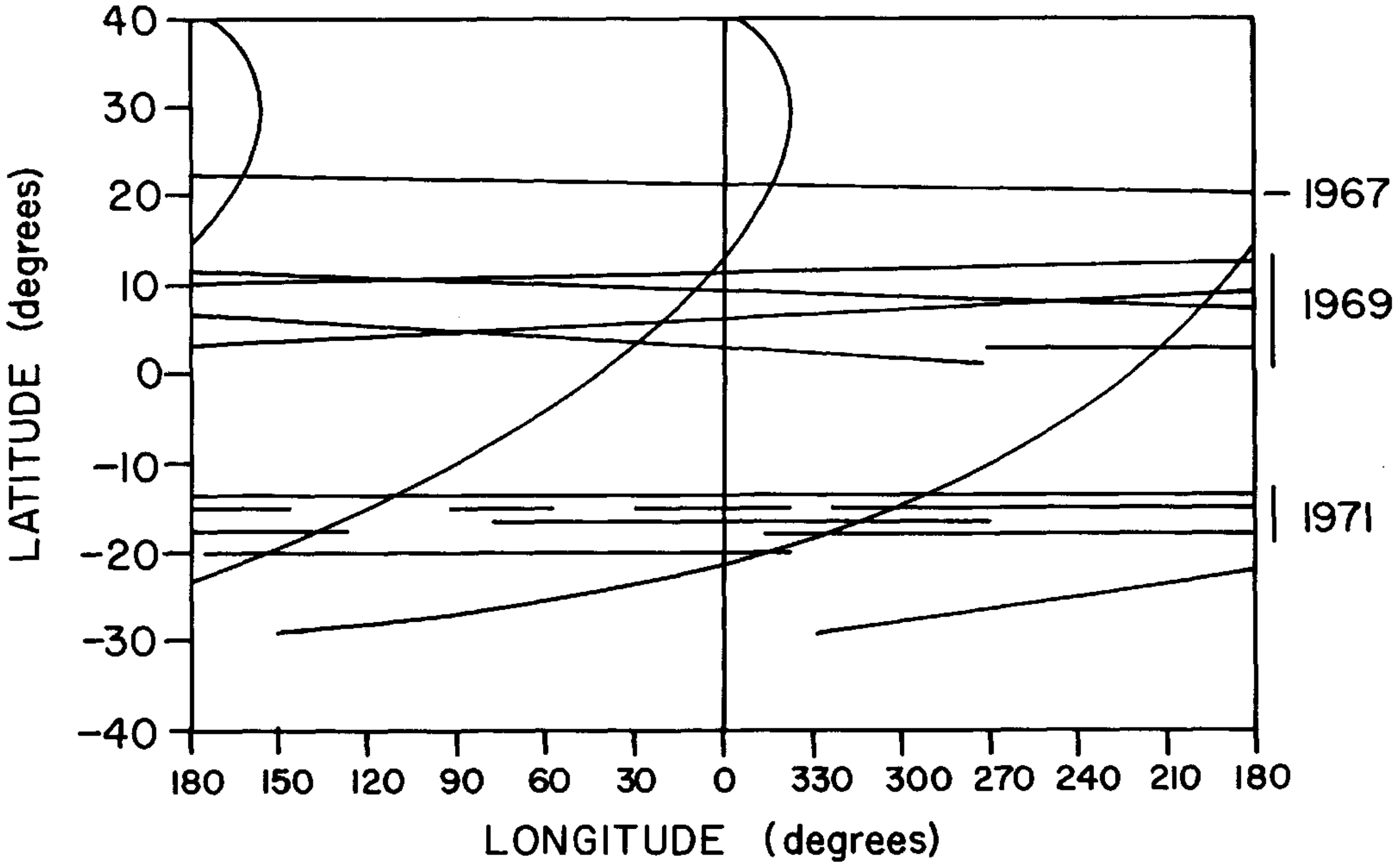

Figure 3-66. Locations of the occultation elevation profiles (curved lines) and the 1967, 1969 and 1971 Haystack radar elevation profiles

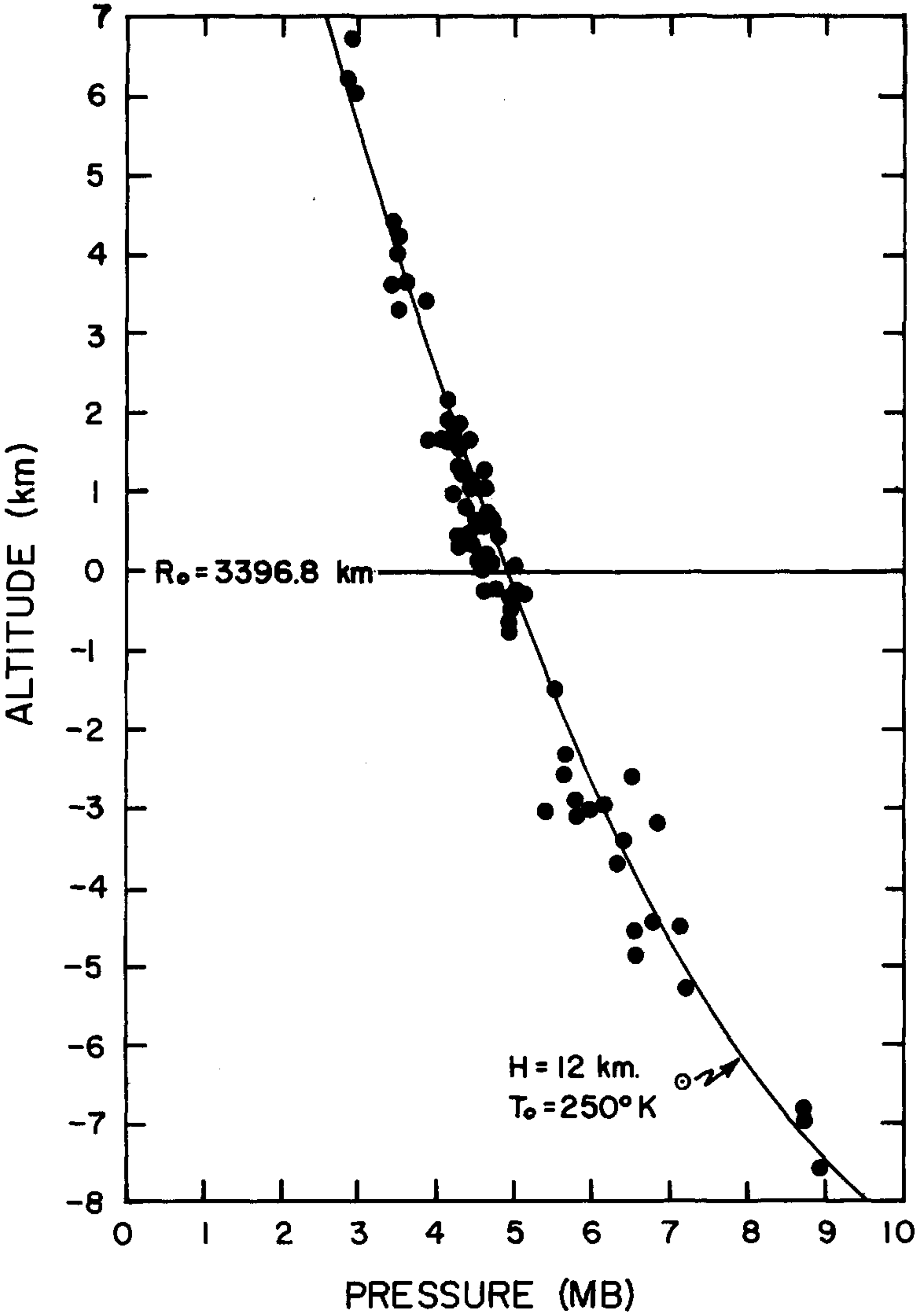

Figure 3-67. Pressure vs. altitude as derived from the occultation data

3.2.4.2 Spectroscopic Results

In the UVS experiment, surface pressures are determined from measured reflectances at 3050Å, which have been fit to a four-parameter analytical reflectance model. This model incorporates the geometry of the measurement (angle of emission and solar incidence referred to the local normal), the UV surface albedo, the atmospheric slant path optical thickness and the scattering phase function. Several assumptions are required that concern the surface UV albedo and the homogeneity of the area observed. The field of view of the instrument is such that a much smaller surface area, relative to the IRIS and TV instruments, is viewed. These differences as well as other differences in technique and analysis, should be borne in mind when making comparisons of common results.

The IRIS experiment requires an analysis of the measured radiances within the wings of the 15μ CO_2 band to infer surface atmospheric pressures. Known transmission functions for the 15μ band of CO_2 are required and depend on the CO_2 abundance, atmospheric temperature and atmospheric pressure. Within the wings of this band, the transmission varies with the pressure primarily, allowing inferences of the surface pressure from the measured radiances and known transmission functions.

The larger field of view of the IRIS instrument averages the surface pressures over relatively large areas on the planet. As such, systematic terrain differences may substantially influence the IRIS results, and likewise rugged or chaotic terrain may influence the UVS results, thus rendering a comparison somewhat difficult.

The measured IRIS spectral radiances also depend on the thermal structure of the atmosphere. In those situations when unusual thermal structures exist, either vertically or globally, systematic effects may arise in the inferred results and in some cases may require special analytical techniques for pressure determinations. The influence of significant amounts of dust may also affect the atmospheric opacity in this part of the spectrum. In such cases, new analytical models incorporating the radiative effects of dust would be required for proper inference of pressure.

As indicated earlier, only preliminary and partial data for surface pressure mapping are available from IRIS and UVS to date. Limited regions exist where coverage by both UVS and IRIS are available and these may be examined for external consistency. The common available regions are the Hellas area and the Amazonis-Tharsis areas; both were chosen by the IRIS group for analysis since they represent regions of generally high and low pressures respectively, and would represent suitable test sites for their analyses.

The preliminary elevation maps for these areas have been published from IRIS data and are shown in Figures 3-68 and 3-69 for the mentioned test areas. The altitudes are referred to an adopted

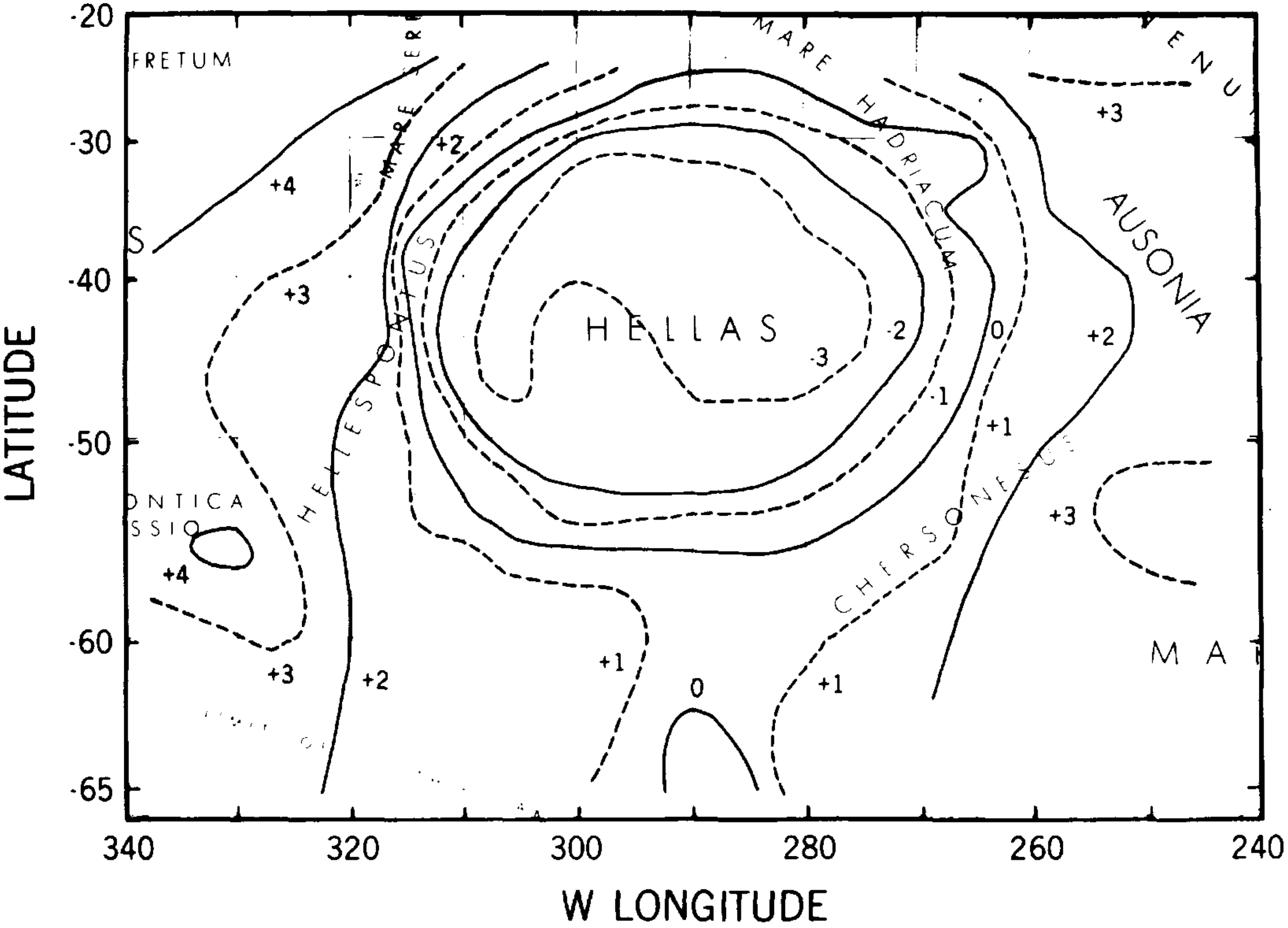

LATITUDE
-20
-30
-40
-50
-60
-65
W LONGITUDE
340
320
300
280
260
240
FRETUM
MARE SER
MARE HADRIACUM
VENU
S
AUSONIA
HELLAS
HELLESPONTUS
NTICA
SSIO
CHERSONESUS
MA
+4
+3
+2
+1
0
-1
-2
-3
+4
+3
+3
+2
+1
+1
0
+1
+2
+3
+3
+2

Figure 3-68. IRIS topography of Hellas area

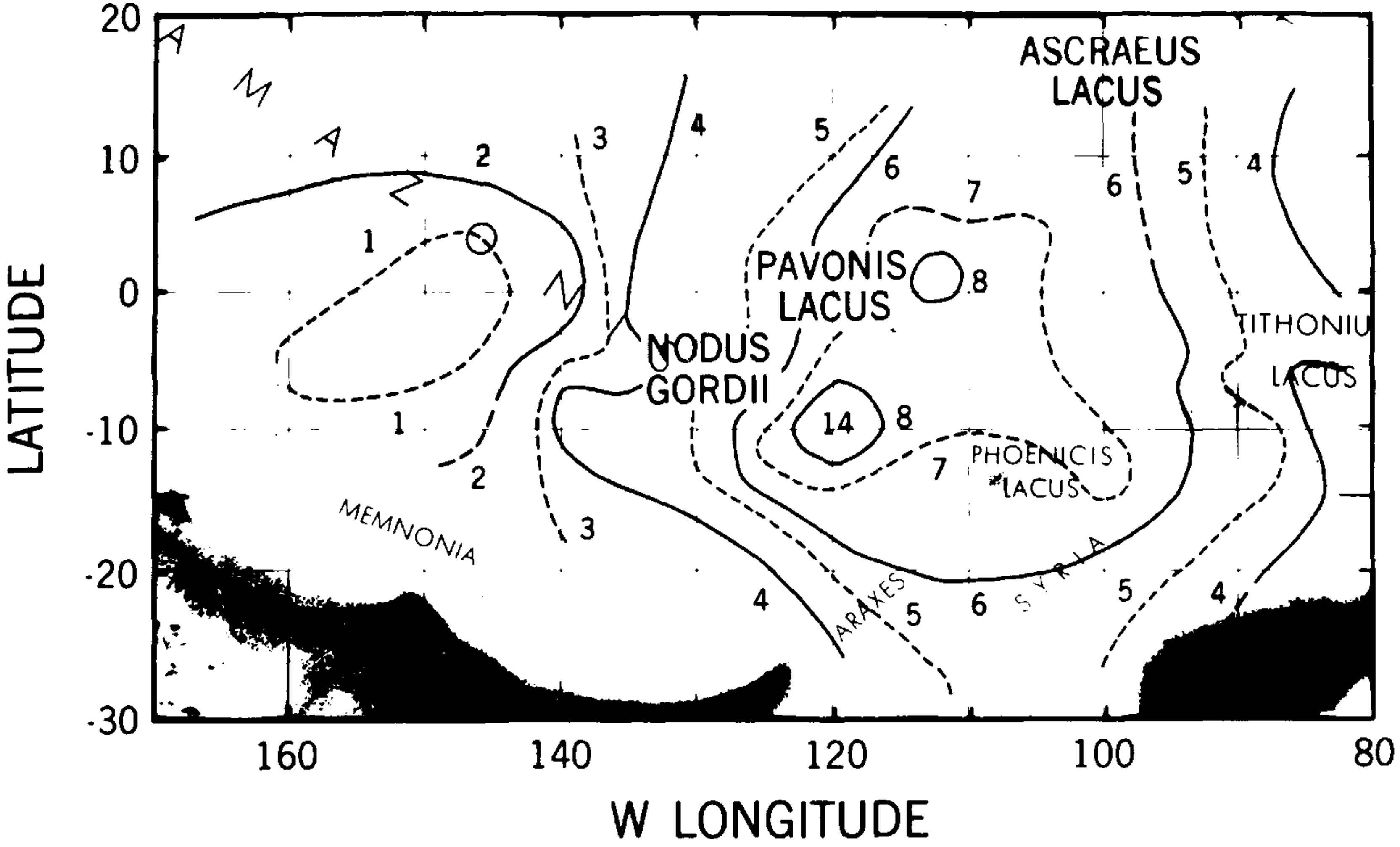

20
10
0
-10
-20
-30
LATITUDE
160
140
120
100
80
W LONGITUDE
AMAZONIS
ASCRAEUS LACUS
PAVONIS LACUS
NODUS GORDII
PHOENICIS LACUS
TITHONIU
LACUS
MEMNONIA
ARAXES
SYRIA
1
1
1
2
2
3
3
4
4
4
4
5
5
5
5
6
6
6
7
7
8
8
14

Figure 3-69. IRIS topography of Amazonis-Tharsis region

mean surface level of 6.1 mb. The contouring illustrated here seems to be in fair agreement with earth-based radar data and previous data from earlier Mariner experiments.

The recent UVS surface elevation map has been made available by the UVS team on a one to twenty-five million scale. The data have been contoured from the many ground swaths available from the later revolutions of the mission, although gaps exist which exceed the field of view of the instrument, requiring some interpolation for contouring. The UVS elevation map is shown in Figure 3-70 for the mid-latitudes and in Figure 3-71 for the south polar area.

An attempt has been made to compare the UVS and IRIS with each other and with radar and occultation results in their common areas (the Amazonis-Tharsis region and a portion of the Hellas area). The elevation contours from each experiment have been superimposed for direct comparison in Figures 3-72 and 3-73. Bearing in mind the differences in analysis, technique and instrumental properties mentioned earlier, the following points may be noted from this comparison.

1. For the Hellas region, there appears to be reasonable agreement in the contouring and the elevation values. The UVS data appear to be systematically higher in elevation (by 1-2 km) than the IRIS values. Such differences could be reconciled on the basis of a continuous supply of atmospheric dust in this area, which would preferentially offset the UVS reflectances. In this region, the UVS data also seems to display an asymmetry in the elevations (better seen in Figure 3-74), systematically displaced to the east. The general agreement in this area may be fortuitous, however, due to the regular shape of the Hellas basin.

2. In the Amazonis-Tharsis region the agreement is somewhat poorer. Again, the UVS data ranges from 1-5 km higher, systematically, than the IRIS results. On the average, the mean difference is approximately 2-3 km. A UVS asymmetry is again evident, but the sense of the asymmetry is opposite to that of the Hellas area. A disconcerting feature in this region, however, is the frequent intersection of contours from each of the experiments. In addition, there appears to be a 14-km feature that has not been recognized by UVS.

3. The cross section of elevation contours incorporating radar and occultation data from the recently revised Map-5 are also included in Figure 3-74. Large systematic difference are indicated between the spectroscopic and the radar analysis. Although the shape of the elevation contours is in agreement, the systematic displacement of several kilometers is disconcerting. Map-5 incorporates Haystack radar elevation data which have been tied to the Mariner S-band occultation data. This experiment provides values for the mean equatorial

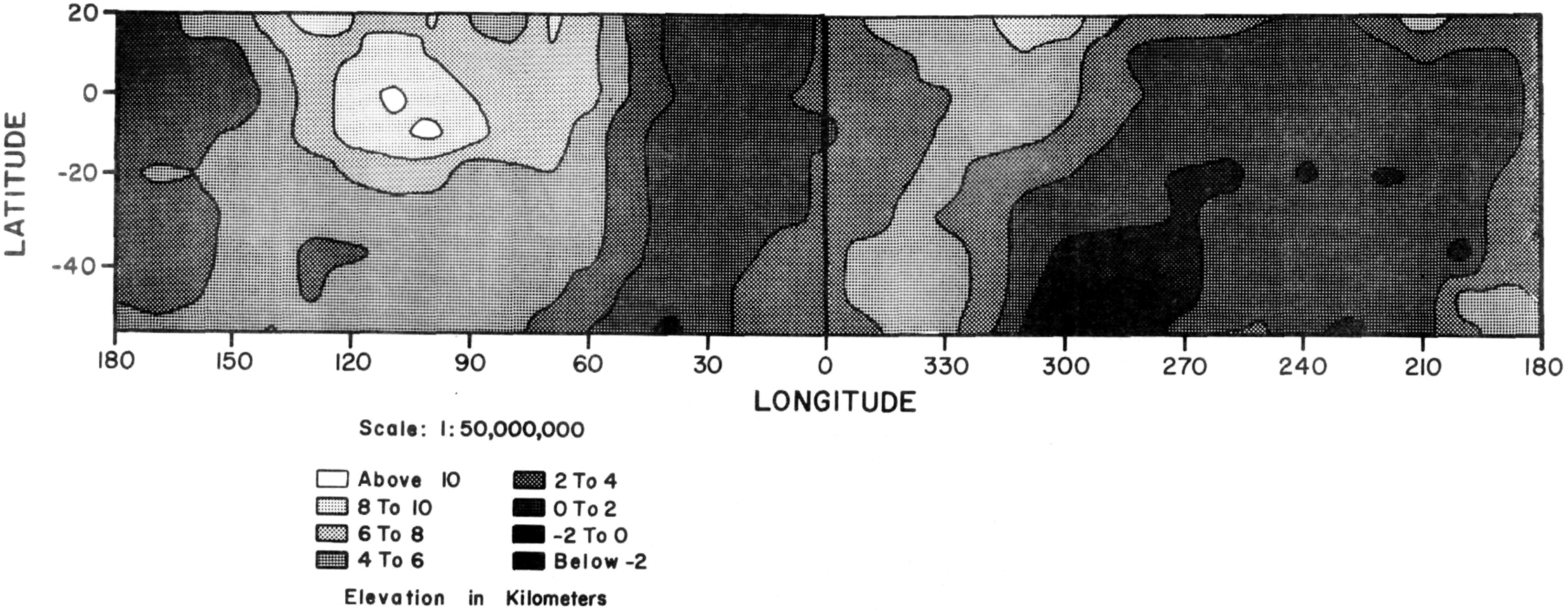
20
0
-20
-40
LATITUDE
180
150
120
90
60
30
0
330
300
270
240
210
180
LONGITUDE
Scale: 1:50,000,000
Above 10
8 To 10
6 To 8
4 To 6
2 To 4
0 To 2
-2 To 0
Below -2
Elevation in Kilometers

Figure 3-70. UVS elevation map of mid-latitudes

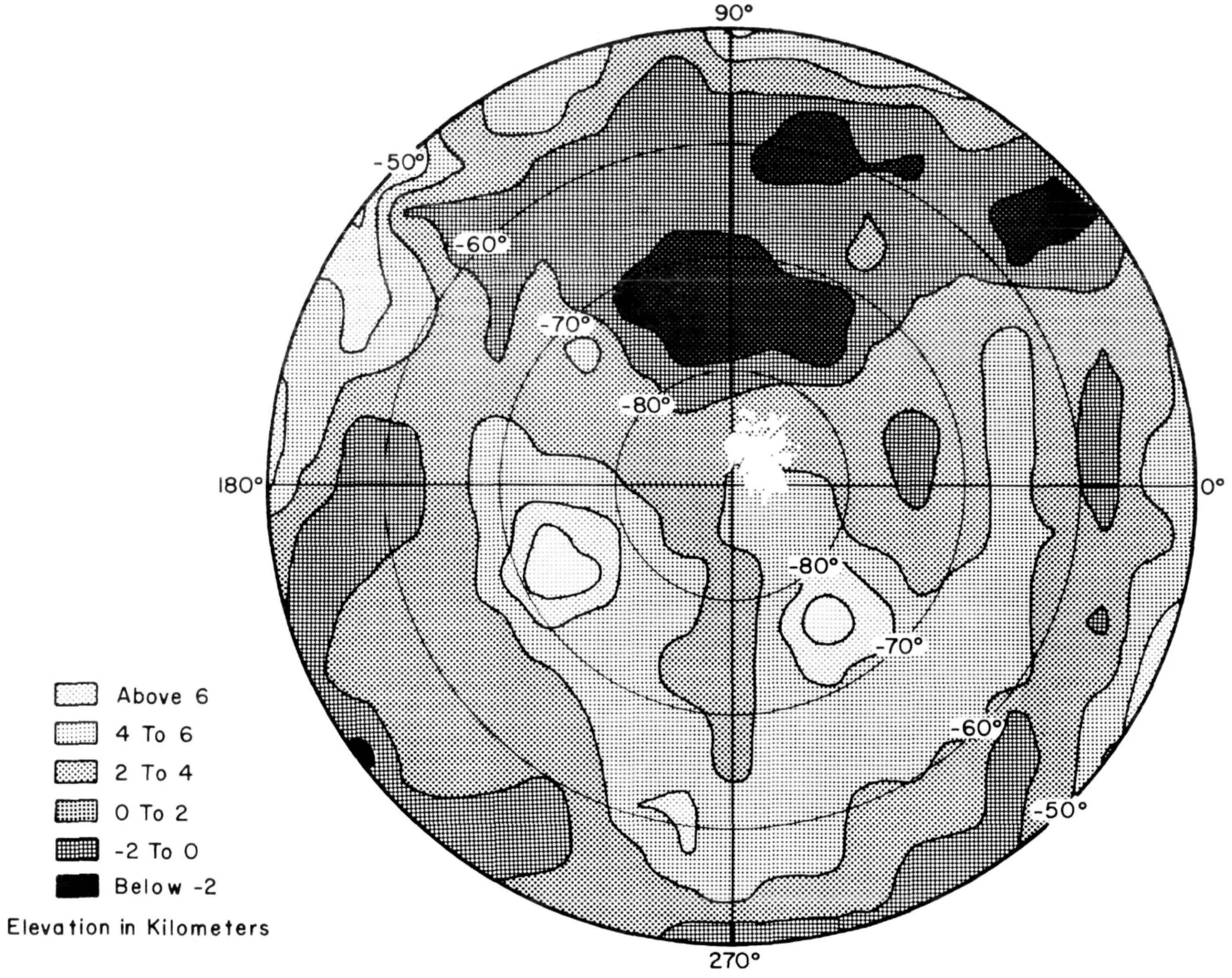
90°
-50°
-60°
-70°
-80°
180°
0°
-80°
-70°
-60°
-50°
270°
Above 6
4 To 6
2 To 4
0 To 2
-2 To 0
Below -2
Elevation in Kilometers

Figure 3-71. UVS elevation map of south polar region

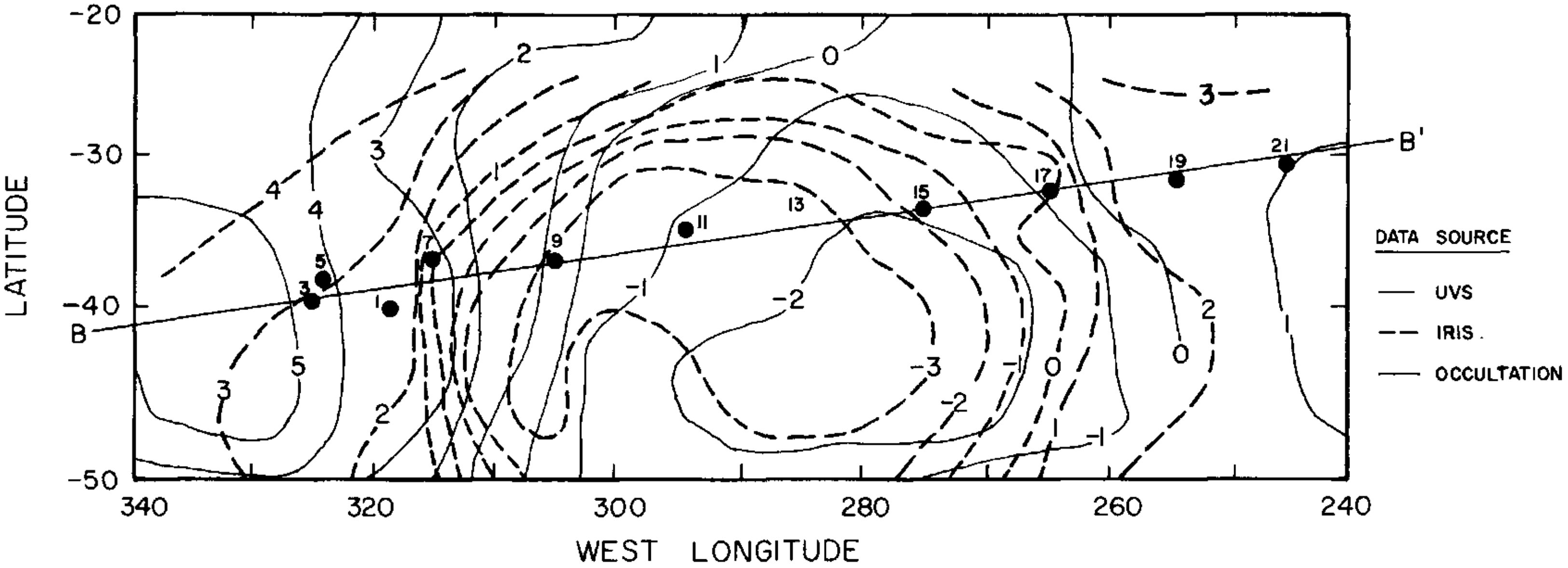
-20
-30
-40
-50
LATITUDE
340
320
300
280
260
240
WEST LONGITUDE
B
B'
1
3
5
7
9
11
13
15
17
19
21
DATA SOURCE
UVS
IRIS
OCCULTATION

Figure 3-72. Comparison of UVS and IRIS elevation contours in Hellas

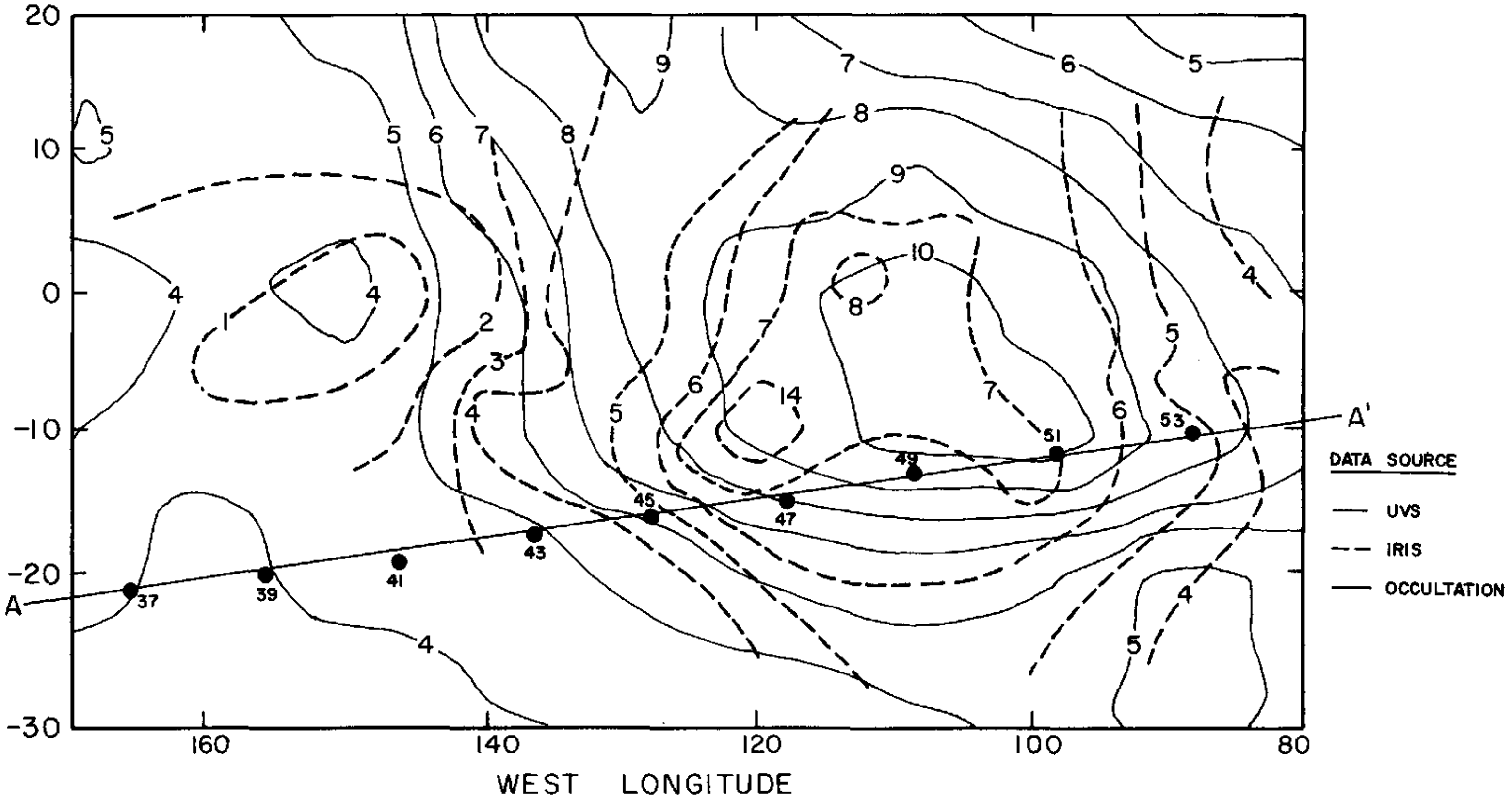
20
10
0
-10
-20
-30
LATITUDE
160
140
120
100
80
WEST LONGITUDE
A
A'
37
39
41
43
45
47
49
51
53
DATA SOURCE
UVS
IRIS
OCCULTATION
1
2
3
4
5
6
7
8
9
10
14

Figure 3-73. Comparison of UVS and IRIS elevation contours in Amazonis-Tharsis

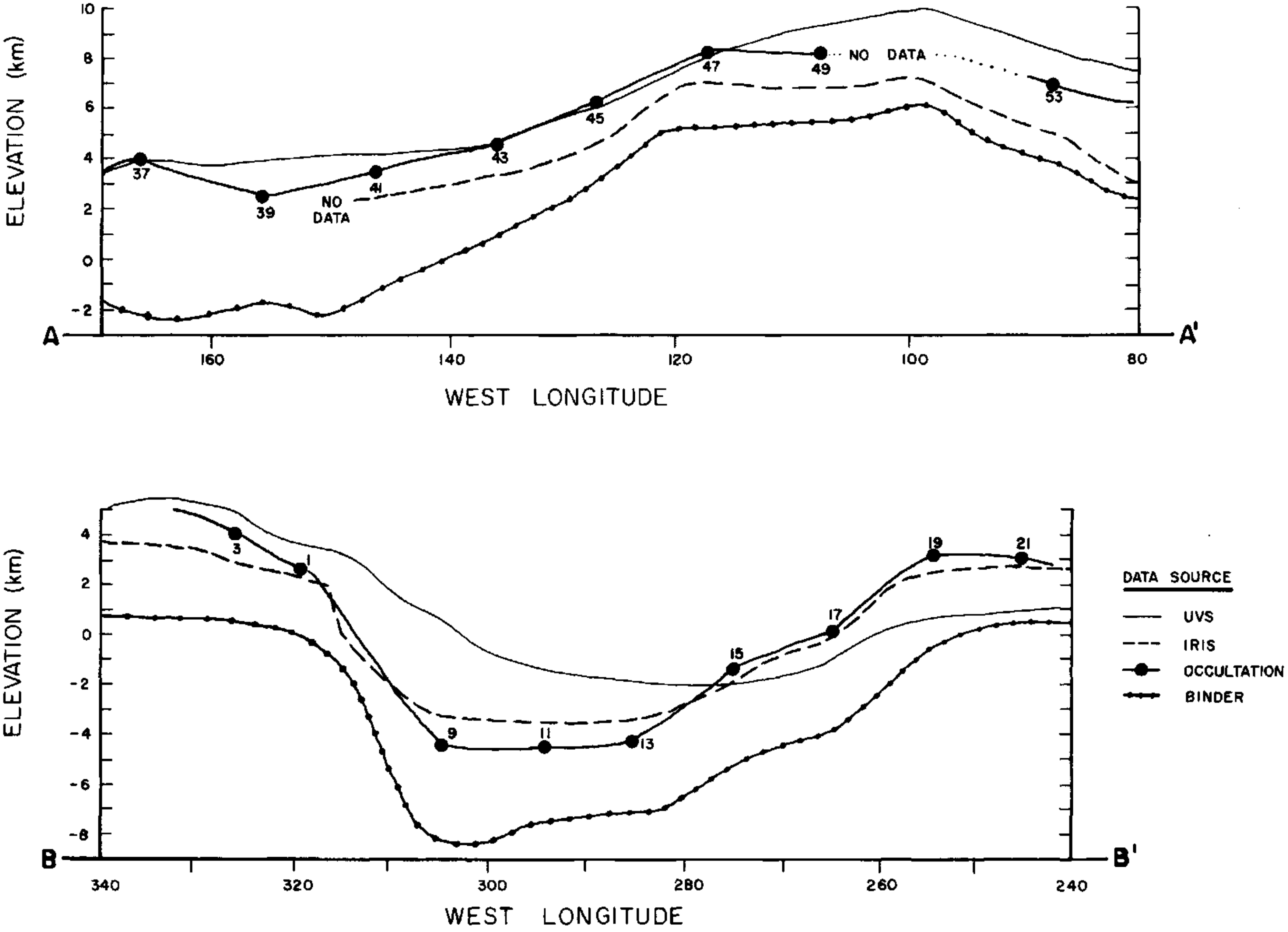

Figure 3-74. Comparison of elevation profiles in Hellas and Amazonis-Tharsis from UVS, IRIS, radar and occultations

radius of the planet, which is taken as the mean reference or 0 km level for the planet. The experiment also provides independent data on the relation of altitude to surface pressure. Using the newly derived value of 3396.8 km as the mean surface reference level, the mean atmospheric surface pressure becomes 4.8 mb. The spectroscopic experiments have arbitrarily adopted the triple point pressure of water of 6.1 mb as the mean reference level surface atmospheric pressure. The differences in these pressures yield corresponding elevation differences of about 4 km. Hence the systematic differences shown in Figure 3-74 may be removed by adoption of a common mean reference surface level. Since the occultation data are not arbitrary, it is recommended that the UVS and IRIS reductions incorporate the mean levels found from analysis. However, since the Haystack radar results will apparently be reduced with the improved Mariner 9 ephemeris, the adoption of a common reference level should await its definitive determination.

4. On the whole, one may conclude from this comparison that, at best, the agreement in the UVS and IRIS topographic mapping is only limited and qualitative. Instrumental differences as well as differences of analyses may account for some of the discrepancies noted. However, transient effects due to either diurnal variations, possible cyclonic disturbances, local dust storms, or the presence of a thin general residual dust layer in the atmosphere may account for some of the variations noted. An alternative possibility concerns the vertical distribution of residual entrained dust particles. The UVS data shows systematically higher elevations or lower pressures in both the Hellas area and the Amazonis-Tharsis region. Moreover, the difference appears to be even greater for the higher elevation area (Amazonis-Tharsis) suggesting that the ratio of atmospheric dust to gas is larger at higher elevations than lower regions. This, in turn, suggests that the vertical scale height of the residual dust may be somewhat larger than the pressure scale height, or distributed in a thin high stratified layer, thus perferentially affecting the UVS reflectance values in the sense indicated.

3.2.5 Surface Physical Properties

The principal sources of Mariner 9 data for the surface properties of Mars come from the IRIS and IRR thermal mapping and from the IRIS restrahlen analysis regarding surface composition. However, only a limited amount of data has been available for analysis so far, so that follow-up investigations should concentrate heavily in these areas.

3.2.5.1 Composition

As mentioned previously in the atmospheric section, the only published data concerning the chemical nature of the surface is that reported on the suspended dust particles. This data is based on the analysis of SiO_2 content from the restrahlen structure appearing in IRIS spectra. Laboratory studies by the IRIS Team on powdered silicate samples have indicated that present determinations may be uncertain, based on unknown particle size effects, and may be subject to revision. Some general conclusions, however, about the surface composition may be made at this time:

1. The dust particles represent a rock type of intermediate silicate composition, 55 - 65% SiO_2.
2. The polar regions together with the volcanic calderas (Nix Olympica, North, Middle, and South Spot) represent a more basic composition than the surrounding terrain.
3. The surface is compositionally heterogeneous.
4. As inferred from the SiO_2 content, the planet is apparently differentiated, perhaps even to the same extent as the Earth.

3.2.5.2 Thermal Properties

Thermal mapping by IRIS and the IRR are available for determinations of the surface thermal inertia parameter and its global variations. The IRR is perhaps more suitable for this purpose due to its higher spatial resolution. Recent examples of diurnal temperature mapping as a function of latitude by IRIS are shown in Figure 3-75. The effects of the entrained atmospheric dust on the surface temperatures are evident from the differences in the measurements obtained early in the Mission (Revs. 1-85) from those obtained later (Revs. 161-186).

Large temperature differences in the thermal scans obtained by IRR have been correlated with TV imagery. Figures 3-76 and 3-77 show observed tmperature variations within the neighborhood of a volcanic crater and in the vicinity of a dark irregular terrain region, respectively.

Most of the observed deviations of IRR Thermal scans from the mean thermal model fall in three categories. The deviations may apparently be accounted for on the basis of surface albedo variations, as illustrated in Figure 3-78. Secondly, topographic effects related to slopes and solar illumination, may result in differential heating. This type is shown in Figure 3-79, for a typical slope variation, and constant albedo and thermal inertia. Thirdly, variations in the thermal inertia parameter, arising from either compositional or density differences have also been observed and are indicated in Figure 3-80 and in the Novus Mons area (Figure 3-77), where irregular terrain exists.

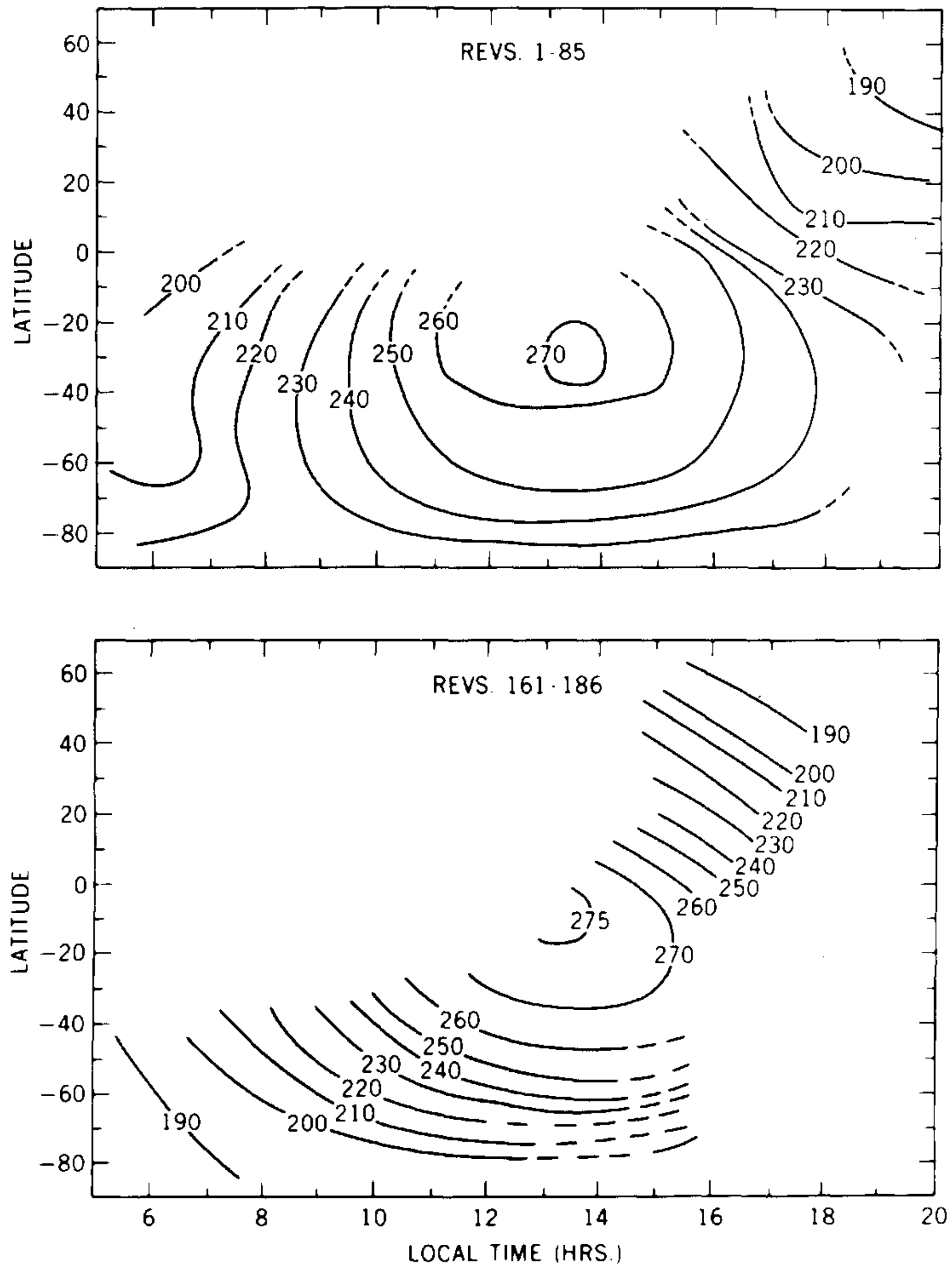

Figure 3-75. Surface diurnal temperature map by IRIS

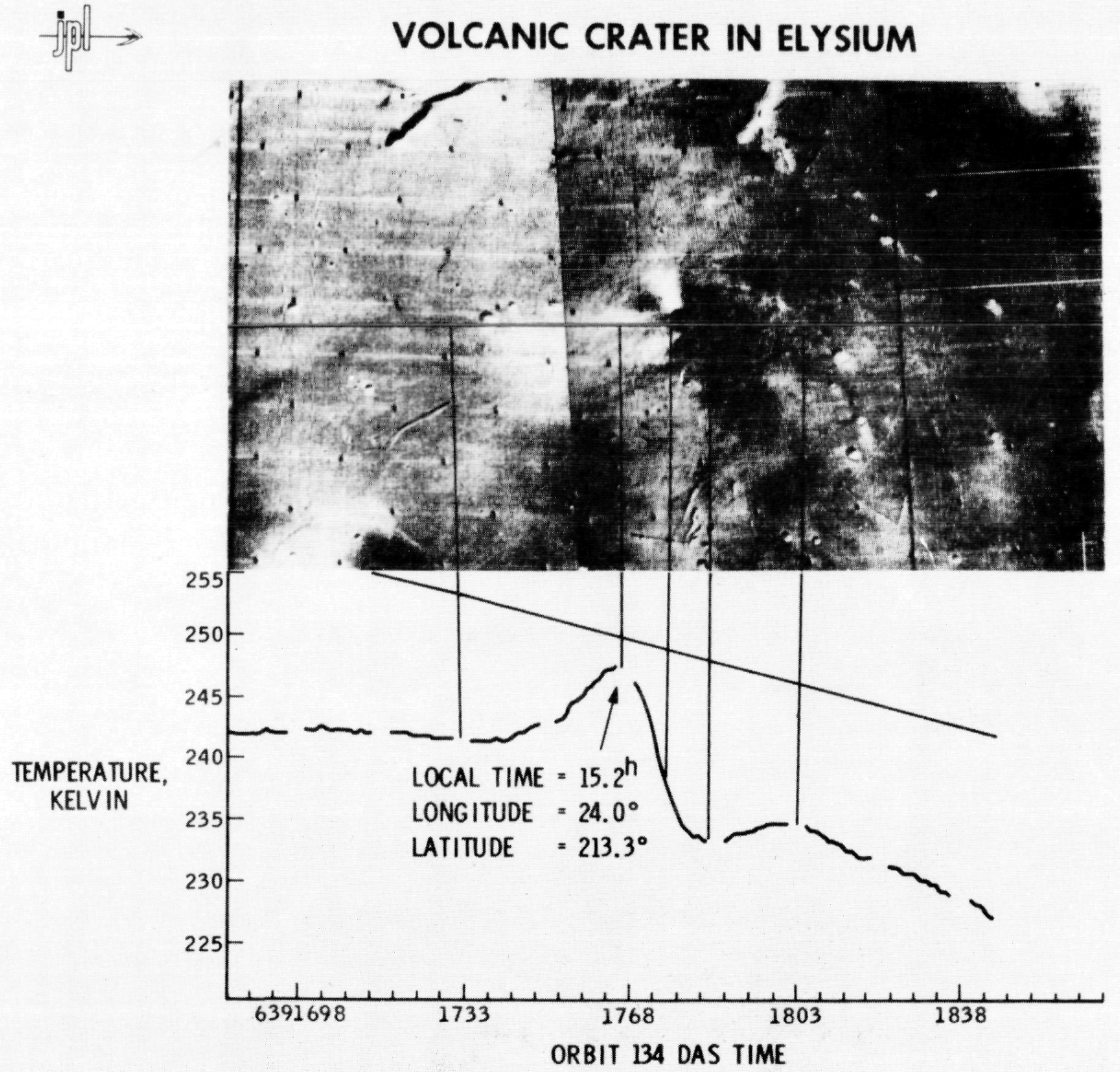

Figure 3-76. IRR thermal scan of volcanic crater in Elysium

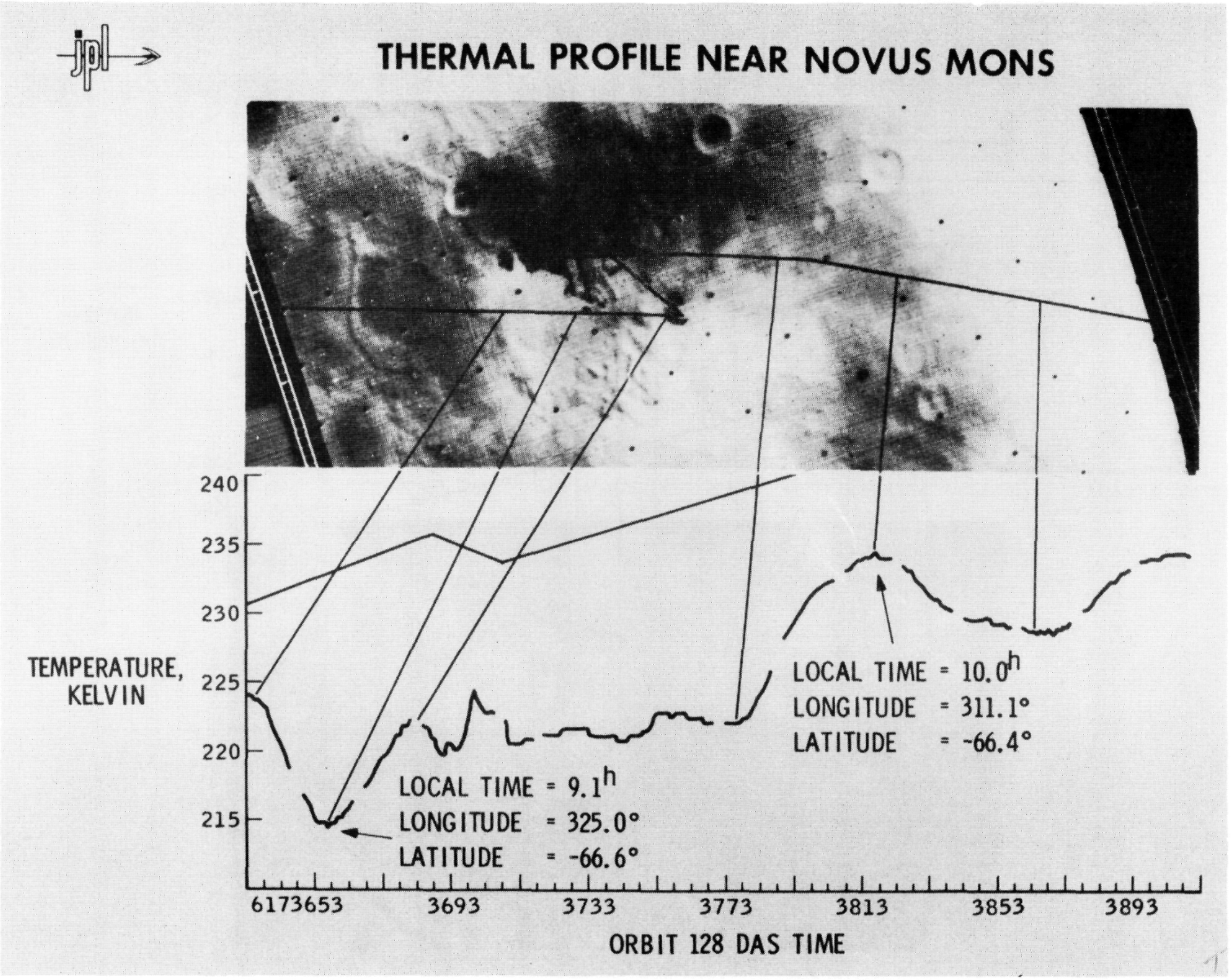

Figure 3-77. IRR thermal scan near Novus Mons

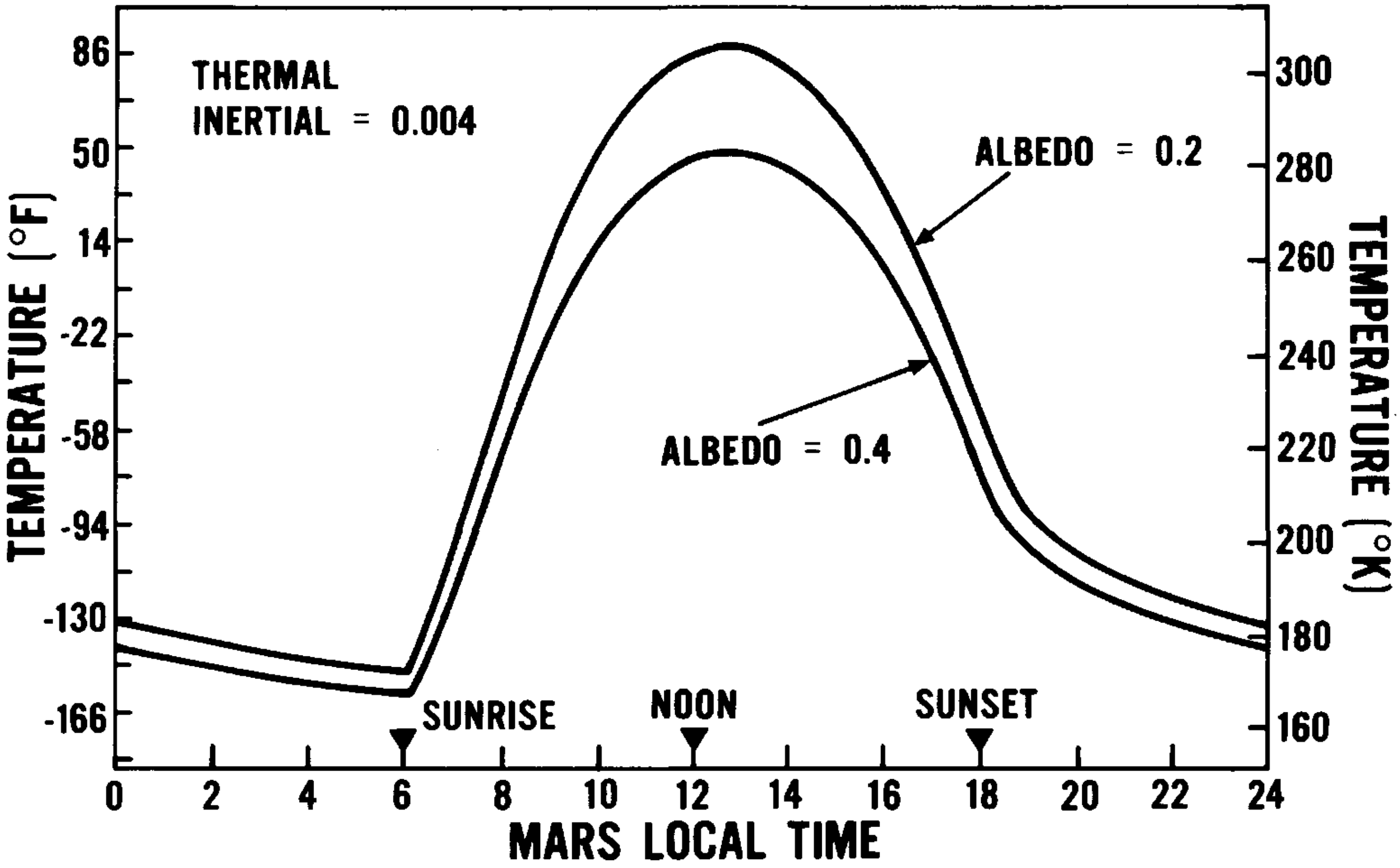

Figure 3-78. IRR thermal scans showing albedo variations

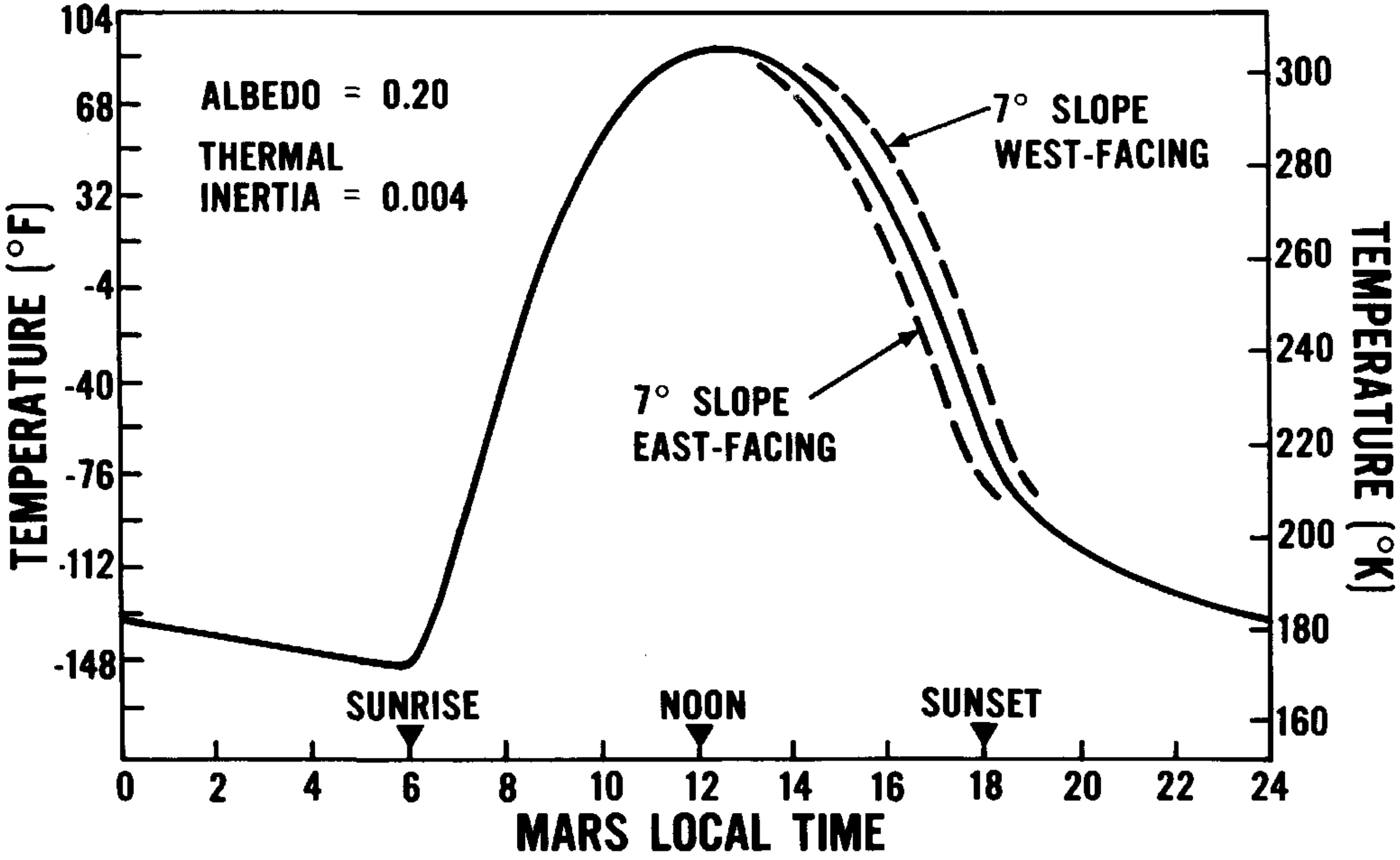

Figure 3-79. IRR thermal scans showing slope variations

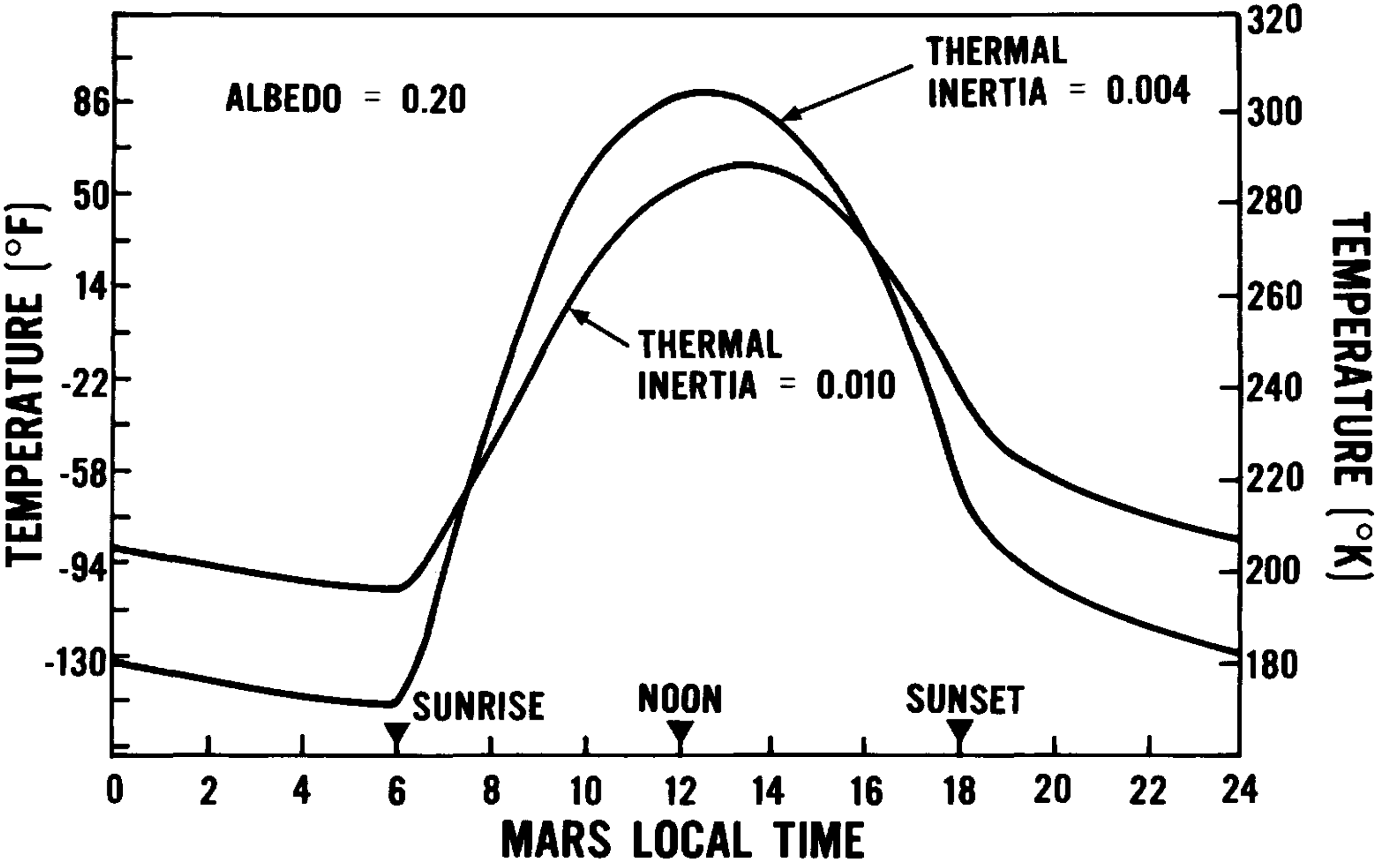

Figure 3-80. IRR thermal scans illustrating possible compositional variations

3.2.5.3 Soil Models

The presence of all soil models described in the Mars Engineering Model have been directly or indirectly verified by Mariner 9 and Earth-based radar results. The TV experiment has identified and transported models, both by suspension and saltation; i.e., so-called comet tails and sand dunes. Radar results based on dielectric constant values indicate hard rock and loess models. Combination interferences regarding soil models and composition must await more definitive investigations by the Mariner 9 IRIS, IRR, and TV Teams.

3.3 ATMOSPHERIC STUDIES

3.3.1 Visual Phenomenon

The array of scientific instruments on Mariner 9 permits extensive and detailed correlations of atmospheric characteristics and phenomenon. The powerful analytical capability of the spectroscopic instruments, in conjunction with the extensive mapping capability of the TV subsystem, should provide a sound understanding of the basic Martian atmospheric characteristics.

Several atmospheric phenomena may be studied directly with visual imaging systems. A representative collection is included in this report with a brief description. The complex vertical structure of the entrained atmospheric dust in the early mission is shown in Figure 3-81. The gradual decline in brightness from the limb suggests a scale of about 10 km. An elevated haze layer, possibly consisting of condensates, is also apparent in these limb photographs.

Figure 3-82, illustrates an example of a localized dust storm. The sequence of photos shows a small dust storm in the center picture, not present in the adjacent photos taken at an earlier and a subsequent time. Also, clearing of the central area into a dark region is believed to be due to the wind transport of the light cover material away from the area, exposing the dark underlying region.

Numerous cases of transient white cloud appearances have also been found, primarily in association with calderas. Two examples are illustrated in Figures 3-83 and 3-84. From estimated altitudes, these clouds are believed to consist of water ice. These are diffuse in appearance and may be created by the motion of warm air up the flanks of the calderas, causing cooling and condensation. The estimated altitudes appear to be too low for CO_2 condensation to occur.

Atmospheric wave phenomena have been observed frequently. Early terminator photographs showed apparent wave structure with wavelengths of about 40 km. It is believed that this structure exists in the thin high, bright clouds common to the terminator regions. Other wave structures have been seen in the north polarhood. Wave patterns and discrete clouds are evident in Figures 3-85 and 3-86.

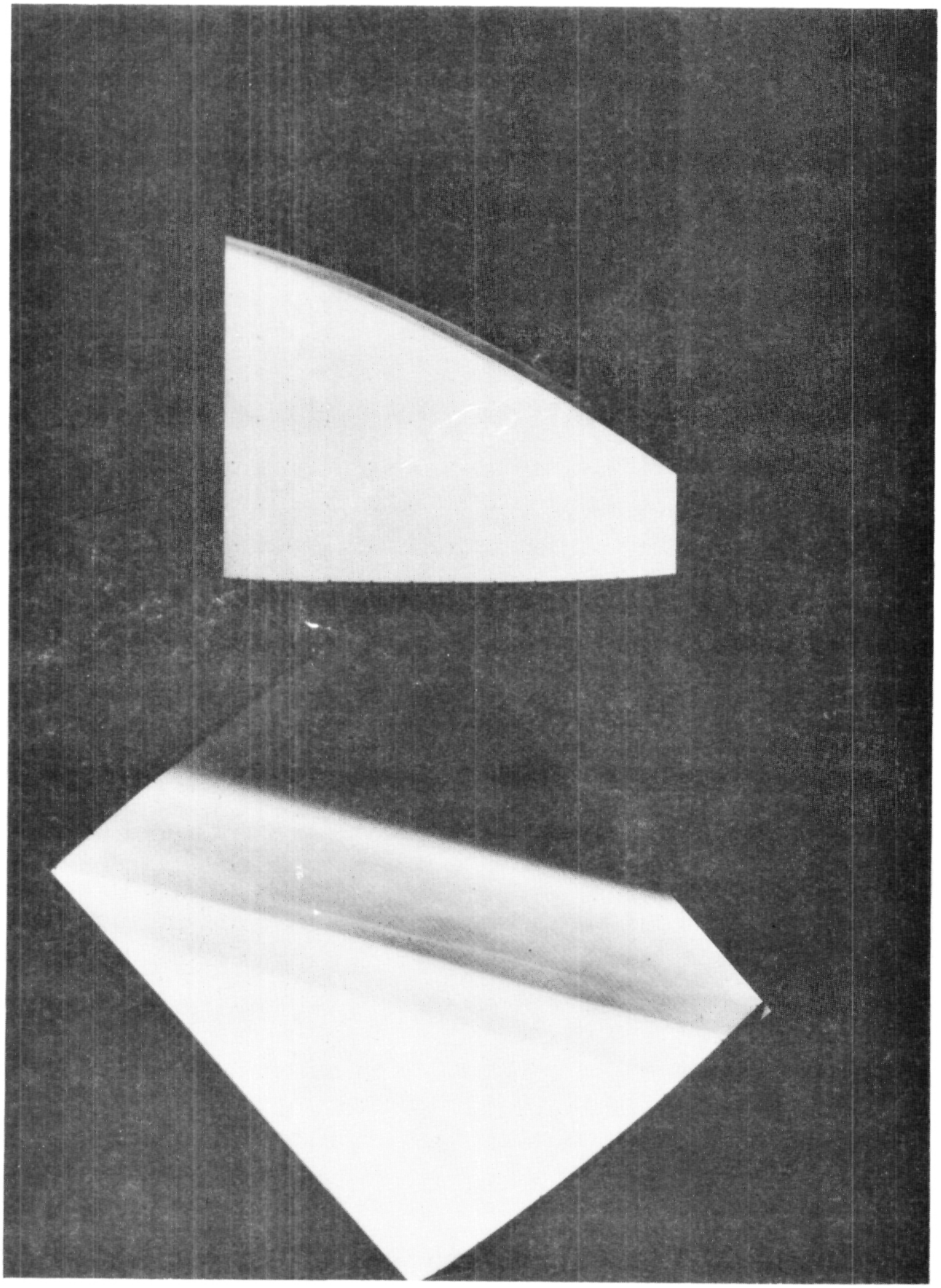

Figure 3-81. TV limb photo showing haze structure

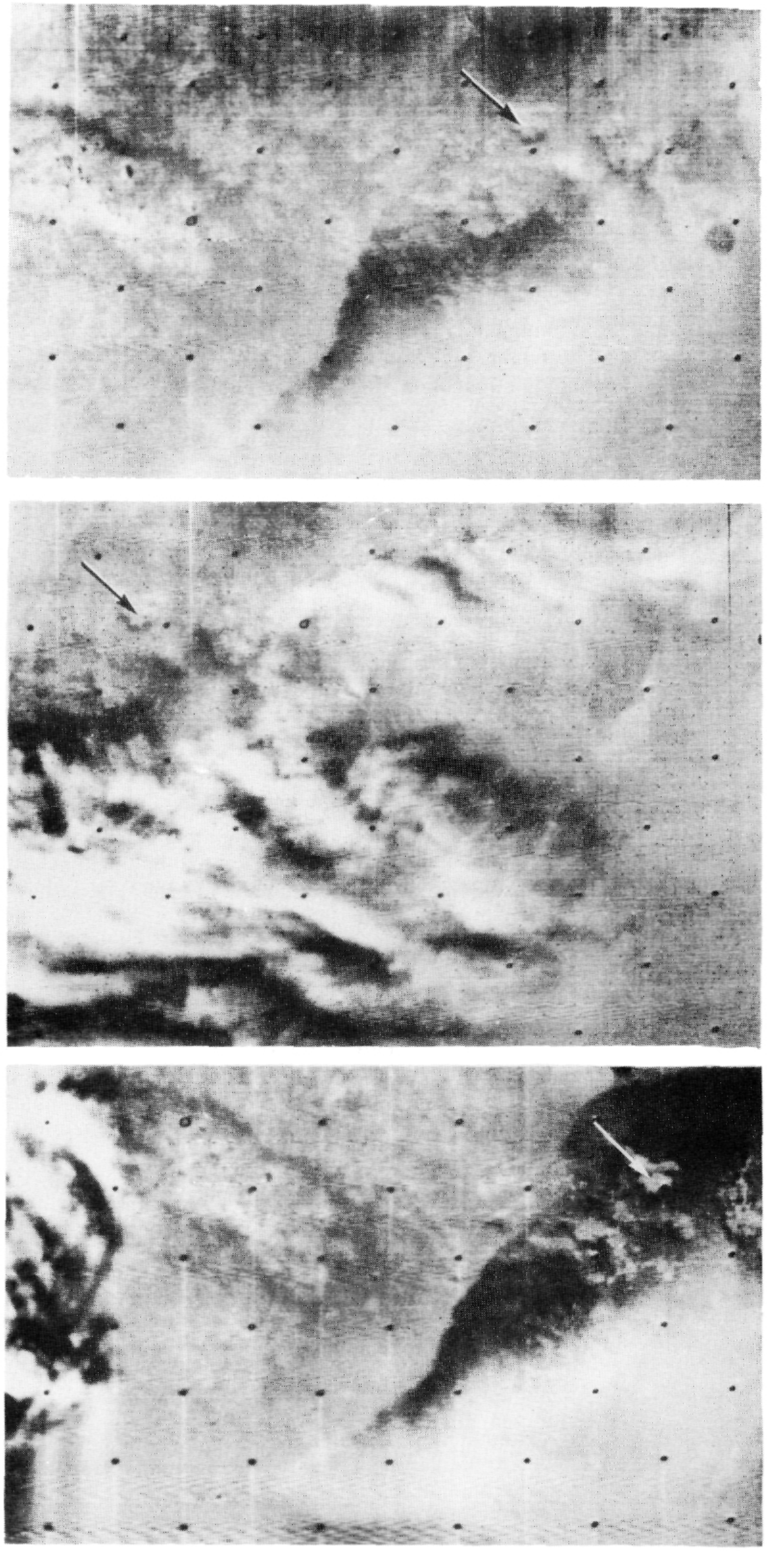

Figure 3-82. Localized dust storm

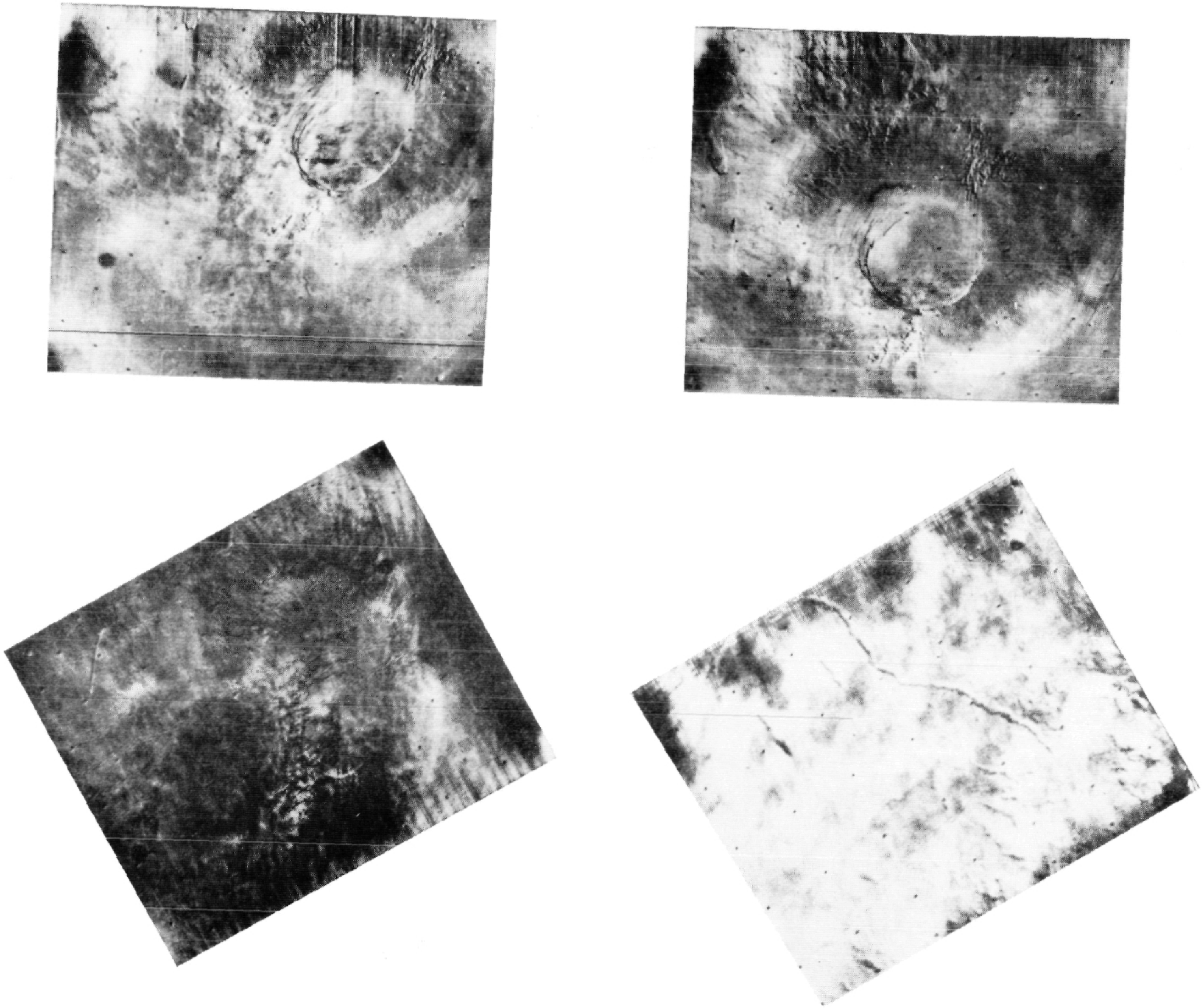

Figure 3-83. White cloud occurrence near calderas

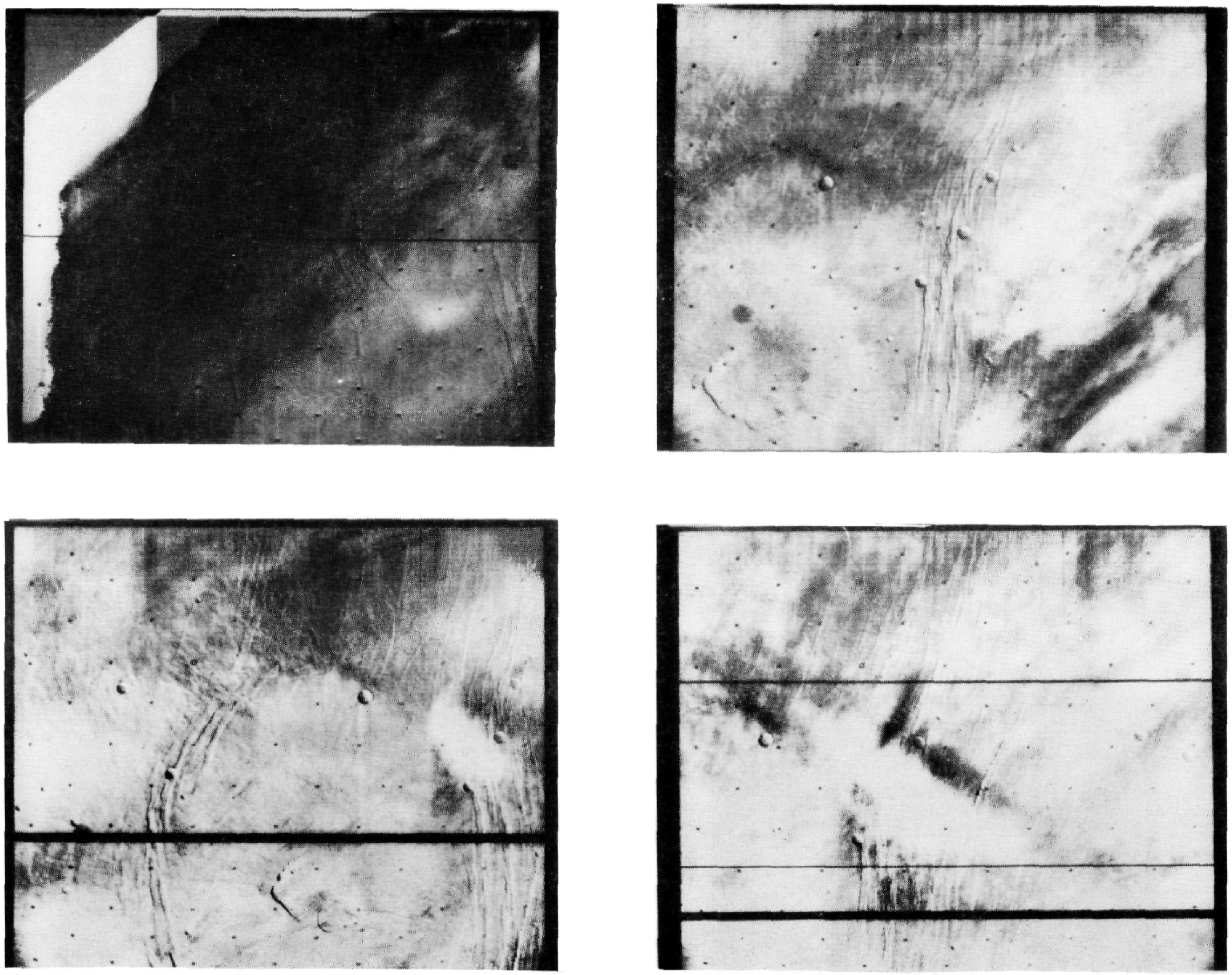

Figure 3-84. White cloud occurrence near calderas

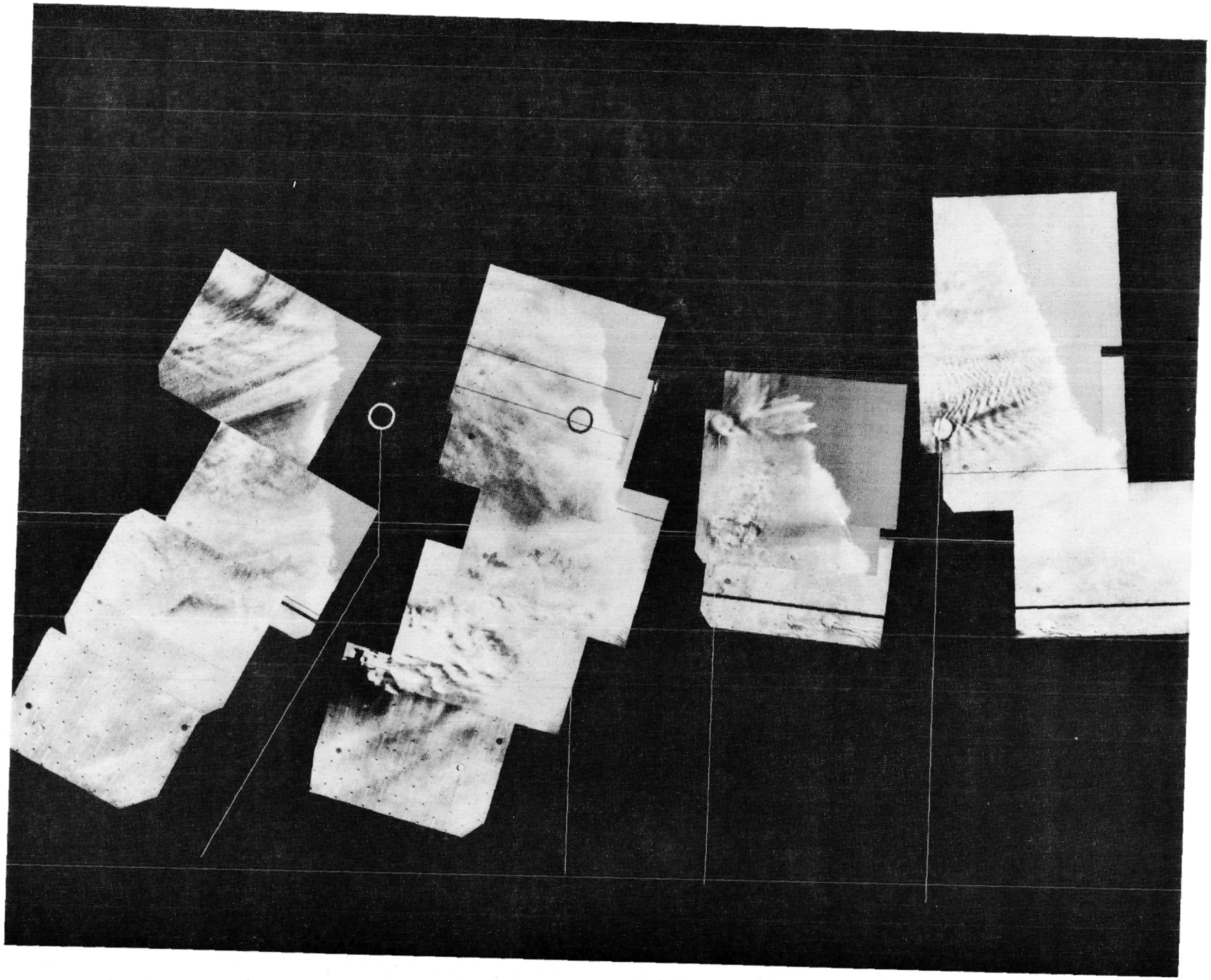

Figure 3-85. Wave pattern and discrete clouds

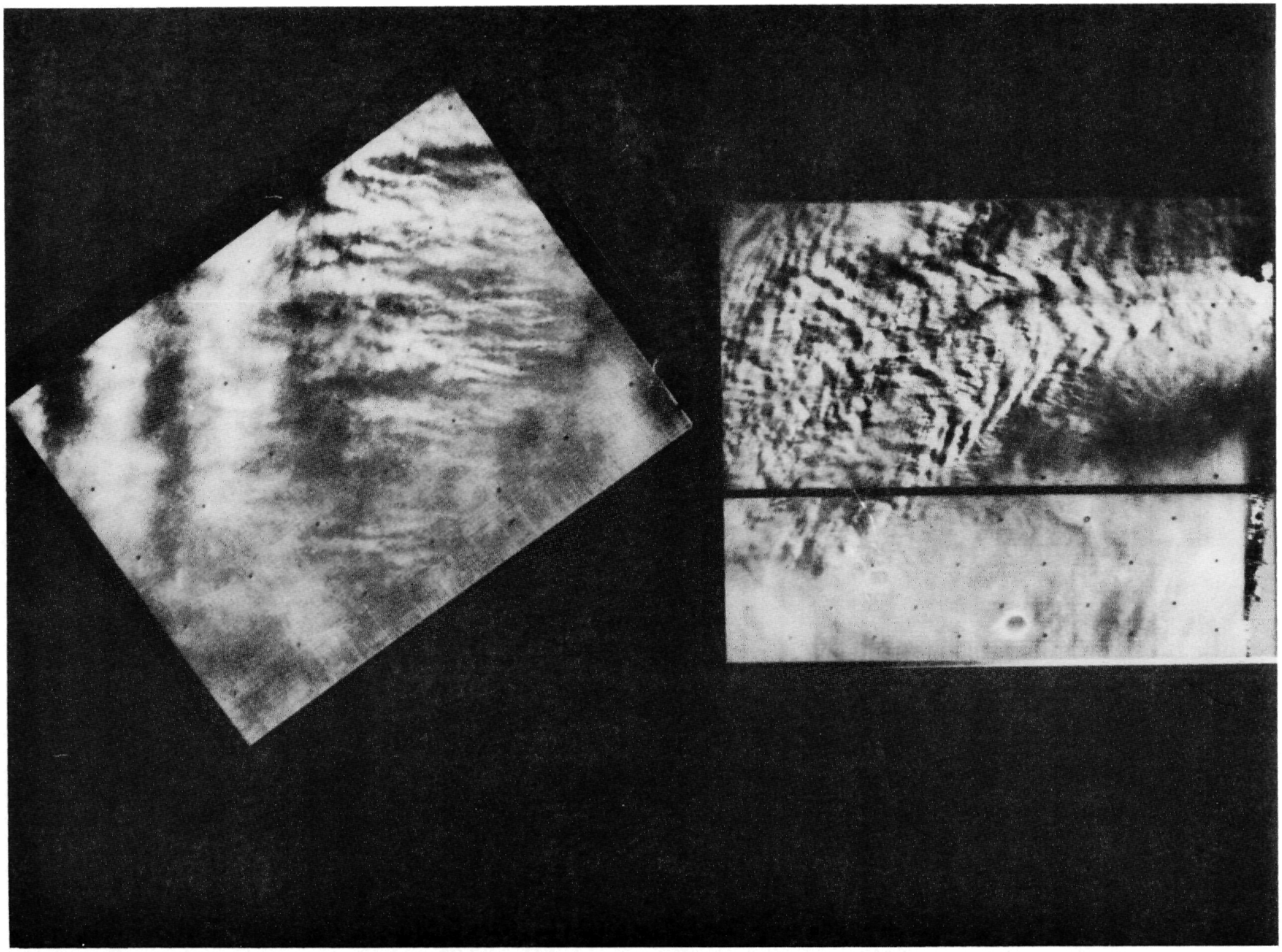

Figure 3-86. Wave pattern and discrete clouds

Evidence for convective motions is also suggested. Finally, wave fronts have apparently been observed and an example is shown in Figure 3-87.

These and other atmospheric phenomena are under investigation by the Mariner TV team and should provide vital data on the motion and dynamics of the Martian atmosphere.

3.3.2 Spectroscopic Investigations - Mariner 9

The IRIS and UVS have provided data for investigations of the physical, chemical and dynamical properties of the lower atmosphere. The S-band occultation experiment has also provided relevant data, but only over selected regions of the surface. Nevertheless, these locations serve vitally for use as calibration points for synthesizing, anchoring and comparing common results of other measurements.

The atmospheric properties deduced by the UVS and IRIS experiments discussed here are the atmospheric composition and its variations, and the vertical atmospheric structure. A summary of the major results and conclusions of the IRIS and UVS experiments to date, are discussed in the following paragraphs.

3.3.2.1 Lower Atmosphere

There are no results obtained so far by either Earth-based or Mariner 9 experiments regarding atmospheric composition that are inconsistent with a virtually pure CO_2 atmosphere. Primary interest regarding atmospheric composition lies principally with the identification and abundance determinations of minor constituents.

Ground-based measures have shown the presence of carbon monoxide and oxygen. Some results from OAO-II indicate the possible presence of either ozone or C_3O_2. Both oxygen and carbon monoxide are not accessible to IRIS and UVS (lower neutral atmosphere). Ozone, however, shows absorption features within the range of both the IRIS and UVS instruments.

Of these minor constituents, the most important from a radiative and biological point of view is water vapor. Estimates of water vapor abundances by IRIS are limited to date. Values of water vapor amounts have been made on the basis of best visual qualitative fits of computed and measured IRIS spectra in the rotational band of water vapor. An example is shown in Figure 3-88.

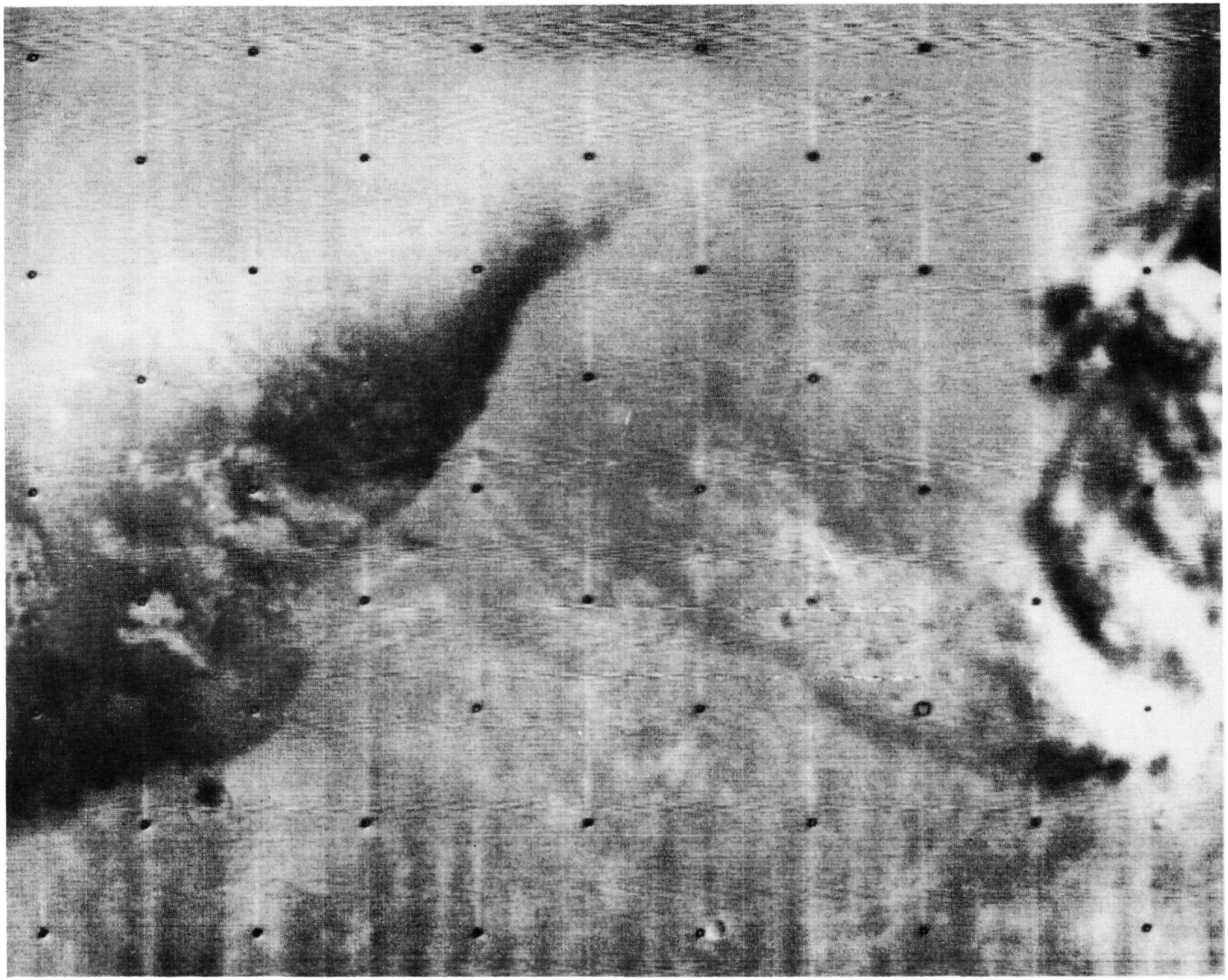

Figure 3-87. Wave front

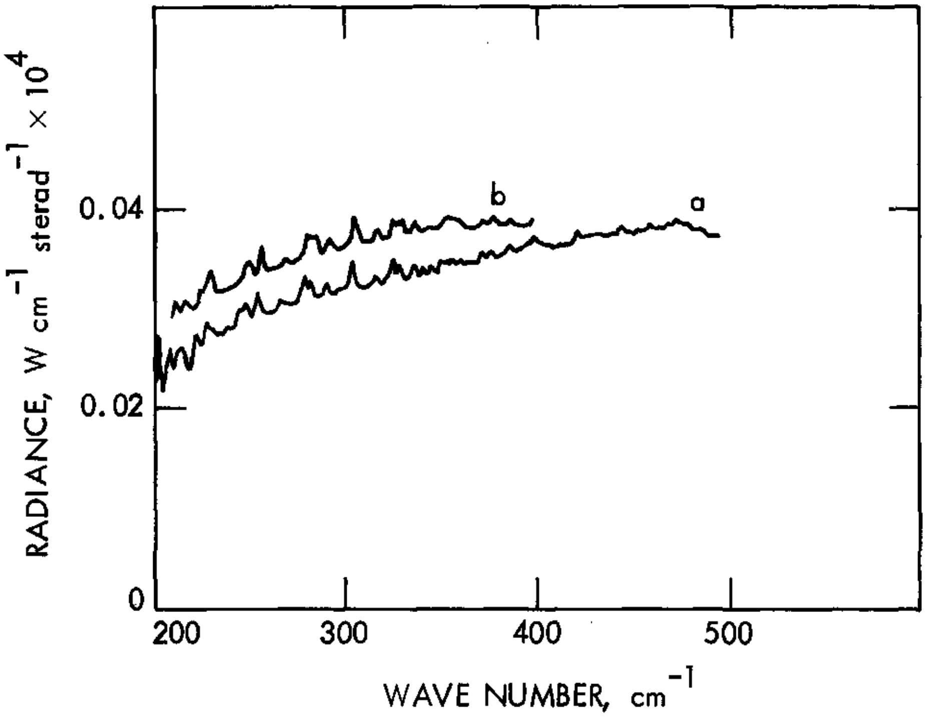

Figure 3-88. IRIS water vapor spectrum

Measured amounts, so far, are in the range 5-20μ of precipitable water and appear to vary with latitude. Early results show spectra suggesting an increase in intensity and corresponding water vapor amounts in going from northerly latitudes to the south polar region. Whether these apparent spectral changes are due to actual variations of water amounts or to variations in the thermal structure of the atmosphere, or some combination of both is not established yet. However, groundbased measured do suggest a seasonal transport of water from one hemisphere to another, showing a real variation of abundance with latitude and time.

Figure 3-89, a polar spectrum, shows the rotational lines of water vapor in the region between 200 and 350 cm^{-1}. Consistent with atmospheric temperatures warmer than surface temperatures, the water vapor lines appear in emission. Also shown in this figure is a synthetic slant path spectrum composed using a two-surface temperature model for the polar cap. The excellent spectral correspondence verifies the existence of atmospheric water vapor in the south polar region.

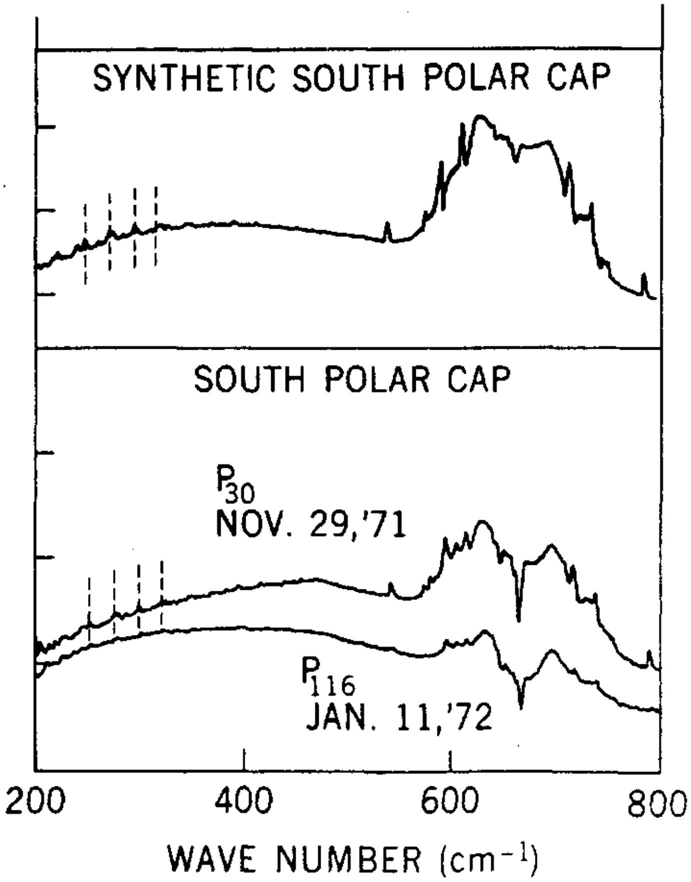

Figure 3-89. IRIS south polar region water vapor spectrum

Further studies regarding water amounts and their systematic variation with time, season, latitude and its vertical distribution are required to study the global water vapor transport and its physical connection with the polar hoods, caps and other condensate clouds. These are anticipated from the IRIS analysis in the relatively near future.

Ozone has been apparently detected in the Hartley-band region by the UVS spectrometer, although the amounts available so far do not appear to be sufficiently great to become apparent in the 9.6μ band of ozone in the IRIS data. A UVS spectrum indicating the presence of ozone is shown in Figure 3-90. The ratio of a north latitude scan to one in the equatorial region is compared with a laboratory spectrum of ozone. The evidence appears convincing, although a very close check with IRIS spectra in the 9.6μ region is warranted. The data obtained so far indicate that ozone was first seen in the north polar hood region well after subsidence of the dust storm. There appear to be diurnal as well as sizeable seasonal variations of ozone abundance, a strong association with the polar hood and cap material, and perhaps an intimate relation with water.

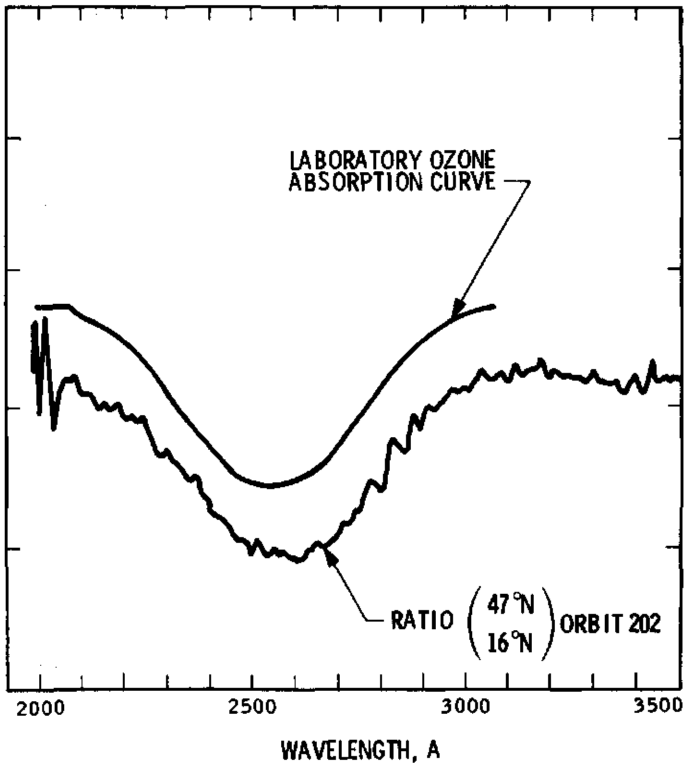

Figure 3-90. UVS ozone absorption spectrum

Further studies by both the UVS and IRIS groups are indicated in establishing the actual abundances, their spatial and temporal dependence and the explicit nature of the relationship of ozone, water vapor and the polar hood and cap materials.

Other compositional studies of great importance and interest concern the isotopic abundances of carbon and oxygen. Due to the presence of an essentially pure CO_2 atmosphere, isotopic band features arising from C^{13} and O^{18} are evident in the IRIS spectra in the carbon dioxide band region. Preliminary analyses indicate that the ratio of C^{12}/C^{13} and O^{16}/O^{18} are in essential agreement with earth-based determinations and are consistent with terrestrial isotopic abundance ratios. Additional studies are required to assess these values definitively.

Other gaseous constituents may be detectable by both the IRIS and UVS instruments. The presence of N_2O by IRIS and N_2 by UVS may be possible and should be carefully studied. A systematic search for these, and other possible minor constituents, should be undertaken by these teams.

An important temporary component resident in the atmosphere during the first few months of the Mariner 9 mission was the particulate matter arising from the global dust storm. The effects of the dust on all aspects of the mission were profound. Aside from visually masking the surface of the planet, significant changes in the thermal structure of the atmosphere resulted, which were readily apparent in the IRIS spectra. During the early mission phases, two broad restrahlen features associated with the dust appeared at approximately 470 and 1075 wavenumbers, in emission over the south polar region and in absorption in the mid-latitude and equatorial regions. Preliminary analyses of this data indicated a composition approximately 60% SiO_2 content. Particle sizes have been estimated to be on the order of several microns in diameter, and the vertical distribution of the particles appeared to be fairly uniform throughout the lower scale height of the atmosphere. The visual and photometric properties were judged to be similar to the light regions on the surface of Mars.

Analyses of thermal scans obtained by IRR early in the mission indicated that the dust could be adequately represented by a single layer with an albedo of 0.3, a solar absorption coefficient of 0.2, and an infrared opacity of 0.5. If the dust composition is representative of silicate particles, as indicated by IRIS, then approximately one milligram of dust in a square centimeter column would suffice to yield the necessary effects.

Although the major portion of the entrained atmospheric dust appeared to have settled out by the end of January 1972, localized concentrations over certain regions still seem to be indicated.

Recent studies regarding the inference of dust particle composition indicate that particle sizes play an important role in the characteristic appearance of restrahlen patterns. Thus, the early estimate of 60% SiO_2 content must be tempered by the effect of particle size on the restrahlen patterns which is presently being studied by the IRIS team. Laboratory studies have indicated that the restrahlen structure from which the compositional results are based is dependent on the particle size distribution from the suspended dust in the atmosphere.

When the particle size problem is resolved, the IRIS data will be presented in a map of emissivity ratios which will display the surface heterogeneity in terms of SiO_2 content. Lately, derived spectra of volcanic calderas (Nix Olympica, north, middle, and south spot) indicate that these features are composed of more basic material than the surrounding terrain.

3.3.2.2 Atmospheric Structure

3.3.2.2.1 Vertical Temperature Structure

The vertical structure of the lower atmosphere is most commonly discussed in terms of its thermal and hydrostatic structure. Radiative and convective energy transfer studies are required to calculate the vertical temperature profiles, surface temperature and their latitudinal or global variations. Studies of hydrostatic balance of the atmosphere are required to deduce the pressure or density distribution, and corresponding scale heights. IRIS data may be analyzed to yield the vertical temperature profiles, while S-band occultation data can be studied to yield both temperature and pressure distributions. The basic analytical inversion techniques required for these analyses are well established and discussed in the literature.

Several estimates by IRIS of the vertical temperature structure of the Martian atmosphere have been obtained from measurements in the 667 cm^{-1} CO_2 absorption band by inversion of the integral equation of radiative transfer. If the atmospheric transmittance is known, the temperature as a function of atmospheric pressure level can be derived. Preliminary retrievals of temperature profiles were made assuming a pure CO_2 atmosphere and neglecting possible additional opacity due to dust. A knowledge of surface pressure is also required for an accurate specification of temperature in the lower atmospheric levels.

Some typical examples of retrieved profiles are shown in Figure 3-91 and the corresponding spectra from which they were derived. These profiles were located over the south polar cap region. The most outstanding feature is the pronounced temperature inversion which is responsible for the CO_2 bands appearing partly in emission. Surface pressure estimates were not available in this region, but the profile was essentially unaffected as the surface pressure was varied. A composite of several such profiles has been used to construct a vertical cross section through the atmosphere along a single scan pass over the south polar cap (Figure 3-92). The lower part of the diagram is uncertain due to the neglect of dust in the analysis and the uncertainty of the surface pressure. The cross section shows a highly localized region of warm air at approximately 1 to 2 mb in the vicinity of the cap.

Additional early examples of retrieved profiles are shown in Figure 3-93. The profiles over Hellas (b) and Sinai (a) are typical of those obtained from spectra corresponding to non-polar cases, while (c) is a polar example. Surface pressure was estimated for Hellas from Mariner 7 ultraviolet spectrometer measurements and for Sinai from Earth-based radar measurements which were normalized at coincident points to Mariner 6 UVS pressure estimates. The near surface profiles may be real but depend on the optical depth of the dust at 15μ. As the optical and radiative properties of the dust

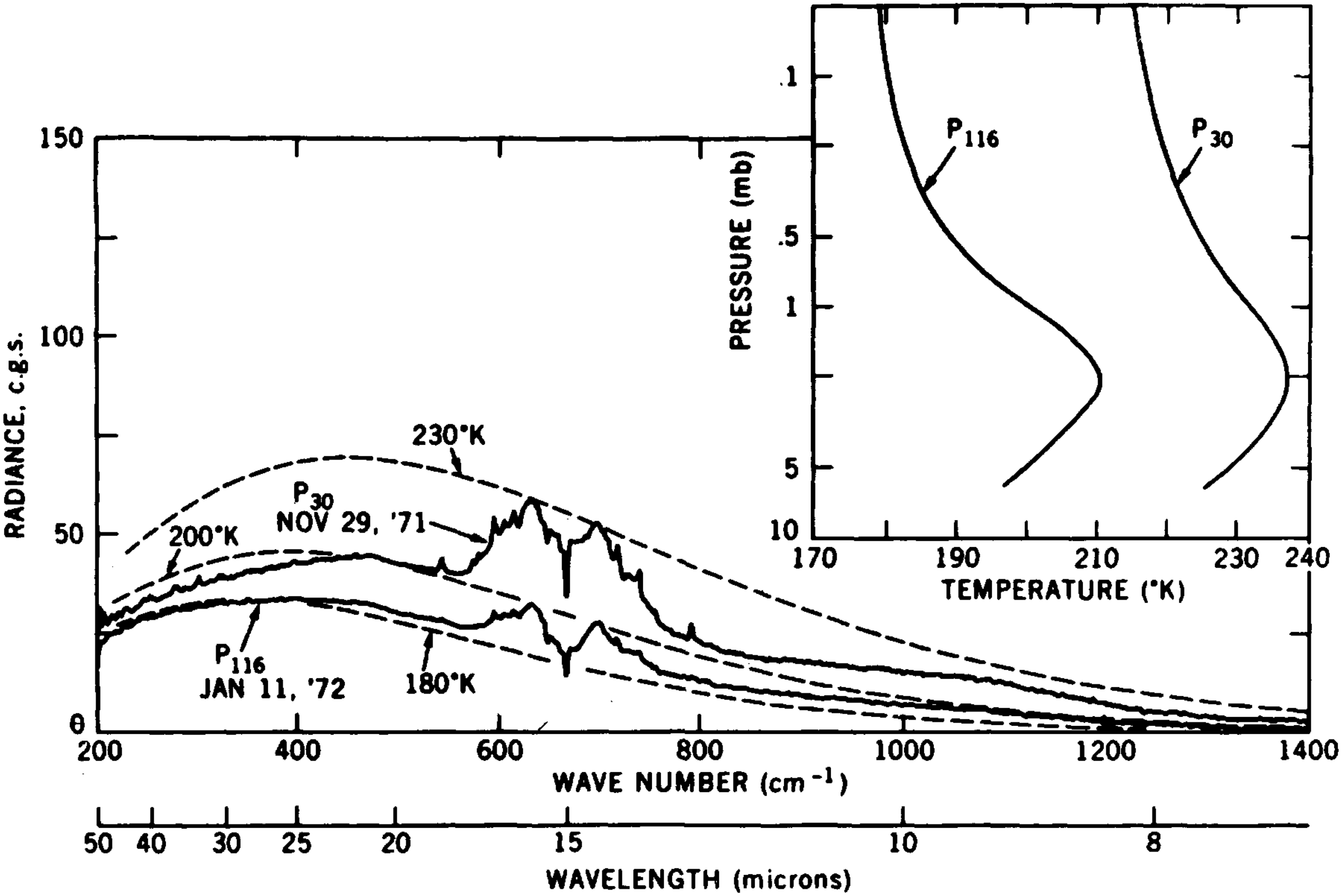

Figure 3-91. IRIS temperature profiles in south polar region

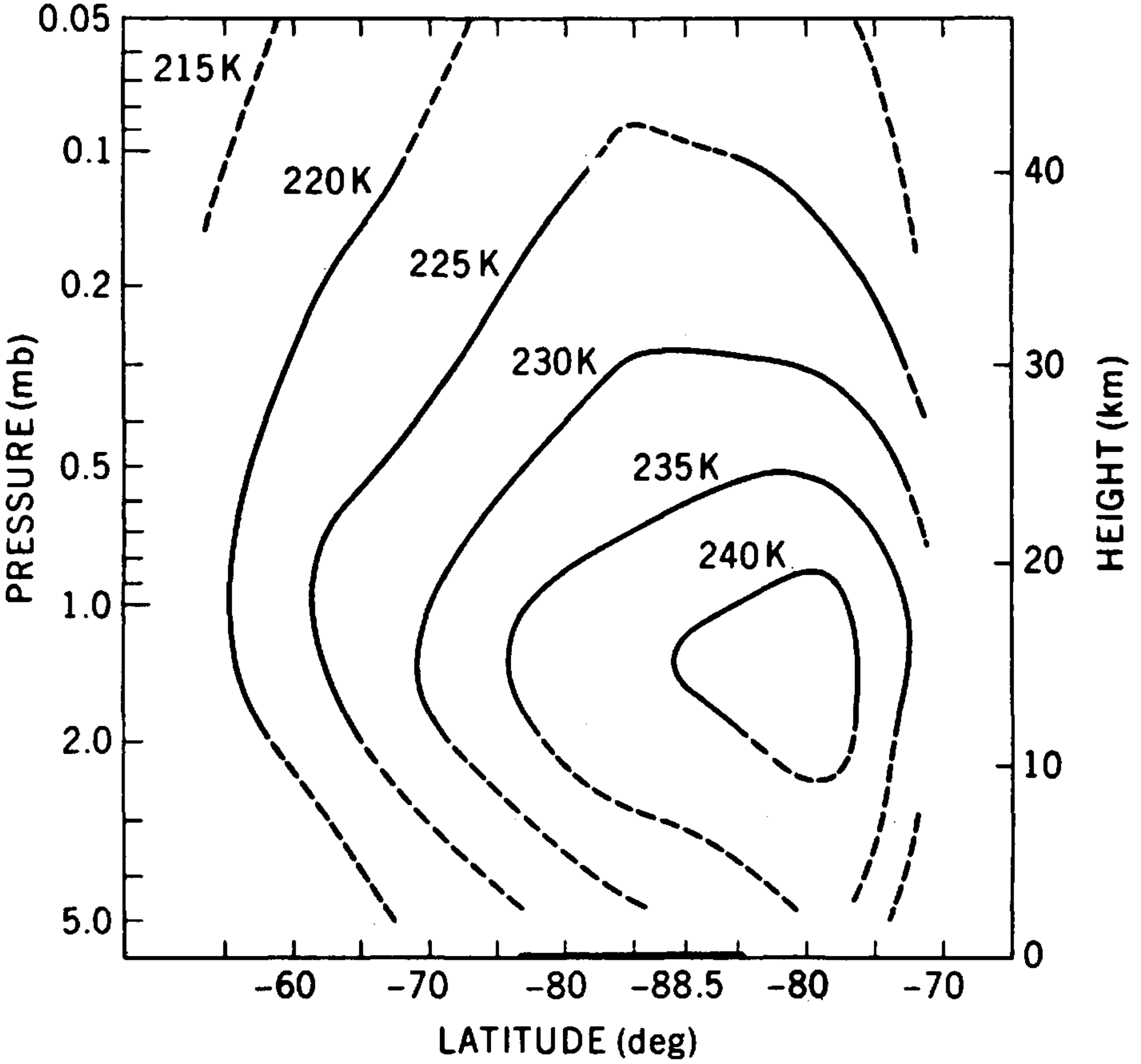

Figure 3-92. IRIS thermal cross section over south polar area

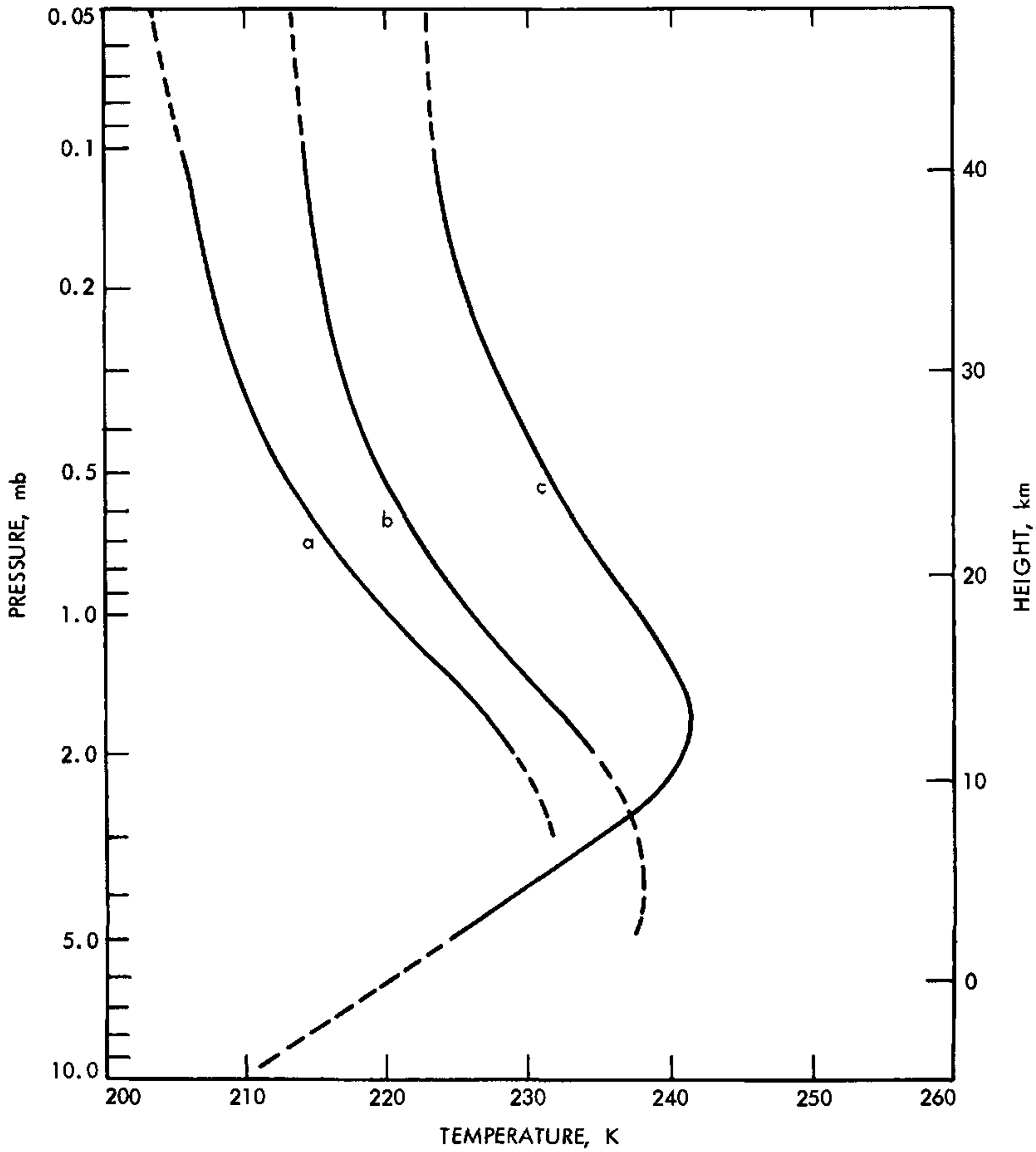

Figure 3-93. Additional IRIS temperature profiles

become better understood, the lower portions of the profiles may be subject to revision. It may be noted that the temperatures above 2 mb are generally warmer than those predicted theoretically for a dust-free atmosphere or those obtained from the Mariner 6 and 7 occultation experiments. Recent calculations (Ref. 8) indicate that the effect of entrained dust in the atmosphere can reasonably well explain the near-isothermal and sub-adiabatic profiles observed early in the mission.

Further analyses throughout the course of the Mariner mission have been concerned with the time and spatial dependence of the temperature field of the atmosphere, particularly as it was influenced by the presence of dust and its subsequent clearing. Such temporal effects of dust settling are illustrated dramatically in Figure 3-94. Retrieved profiles from revolutions 5, 62 and 114 are compared. Although the latitude and longitudes vary somewhat (the local times are very similar), a marked change from a nearly isothermal profile to one approaching near adiabatic conditions is demonstrated. As the dust settling proceeds with time, the atmosphere cools substantially, achieving near adiabatic conditions during later revolutions.

Other studies of atmospheric temperature structure have been concerned with diurnal variations, arising from solar and surface heating. Examples of atmospheric thermal cross sections compiled as a function of local time, both during and after the dust storm, are shown in Figure 3-95. Again the very substantial influence of the dust in the atmosphere is evident. In addition to the influence of the dust on the temperature structure, the effects on the response time of the atmosphere by the dust to heating or cooling are apparent.

Further analyses of the IRIS spectra and inferred temperature structure are proceeding with regard to additional studies of spatial and seasonal dependence, and to the inference of atmospheric winds which are a consequence of the deduced thermal structures. An example of a preliminary analysis (Conrath and Piraglia, 1972) is shown in Figure 3-96. These studies are of vital importance to the Viking mission.

Additional data regarding the atmospheric temperature and pressure distributions are available from the S-band occultation experiment, and provide a valuable check on the overall consistency of the IRIS temperature determinations. Although the occultation experiment results rest on their own merit, their utility relative to IRIS results is limited due to the inherent limitations on the spatial and temporal coverage available. As a result, the IRIS data should play an essential role in global and temporal studies of the temperature field of the atmosphere, yet retaining the additional security of having reliable checks on its internal and external consistency with the occultation results.

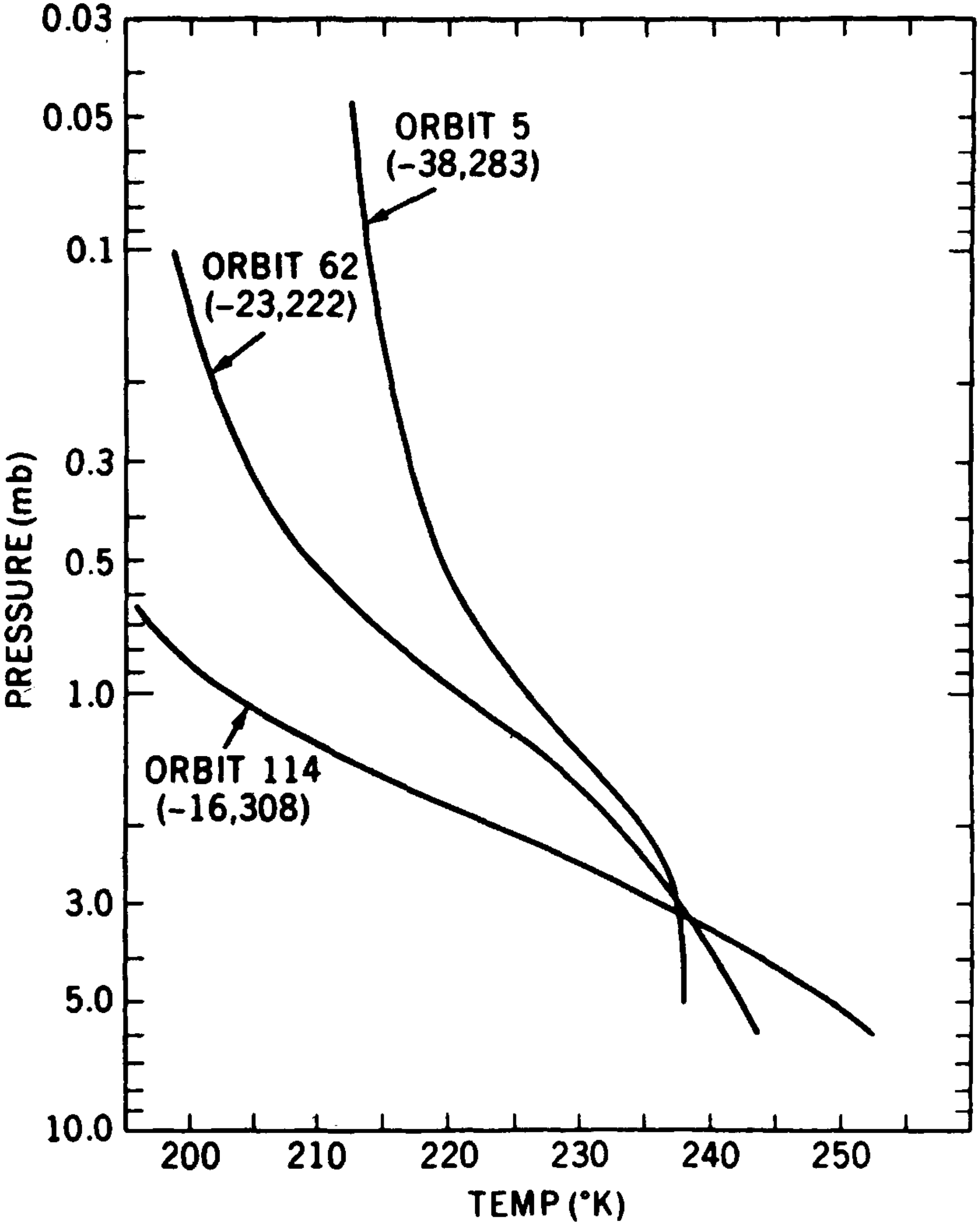

Figure 3-94. Effects of dust settling on IRIS retrieved temperature profiles

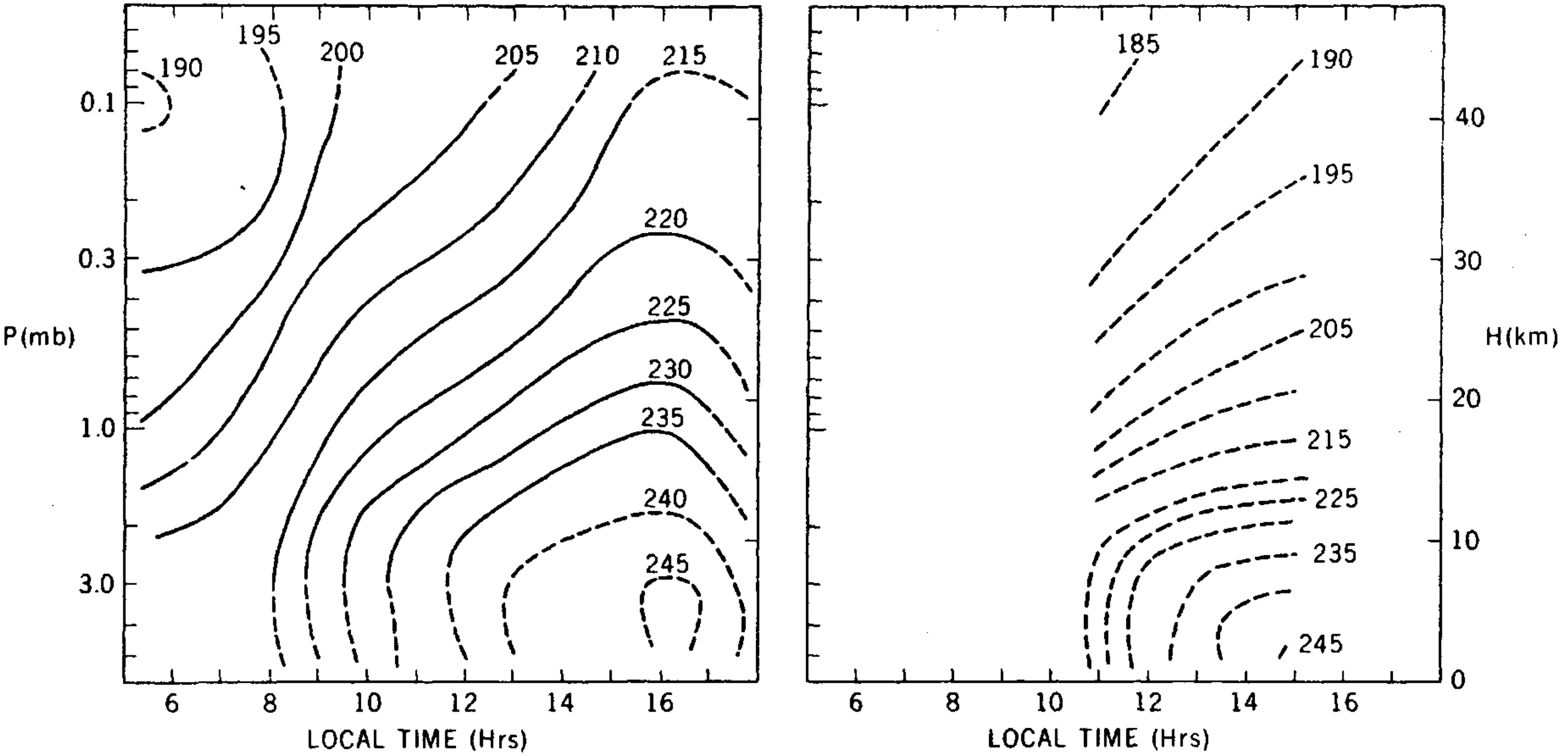

ORBITS 17-30 (DURING DUST STORM)

ORBITS 106-118 (AFTER DUST STORM)

M75-144-0

Figure 3-95. Diurnal atmospheric heating in Noachis

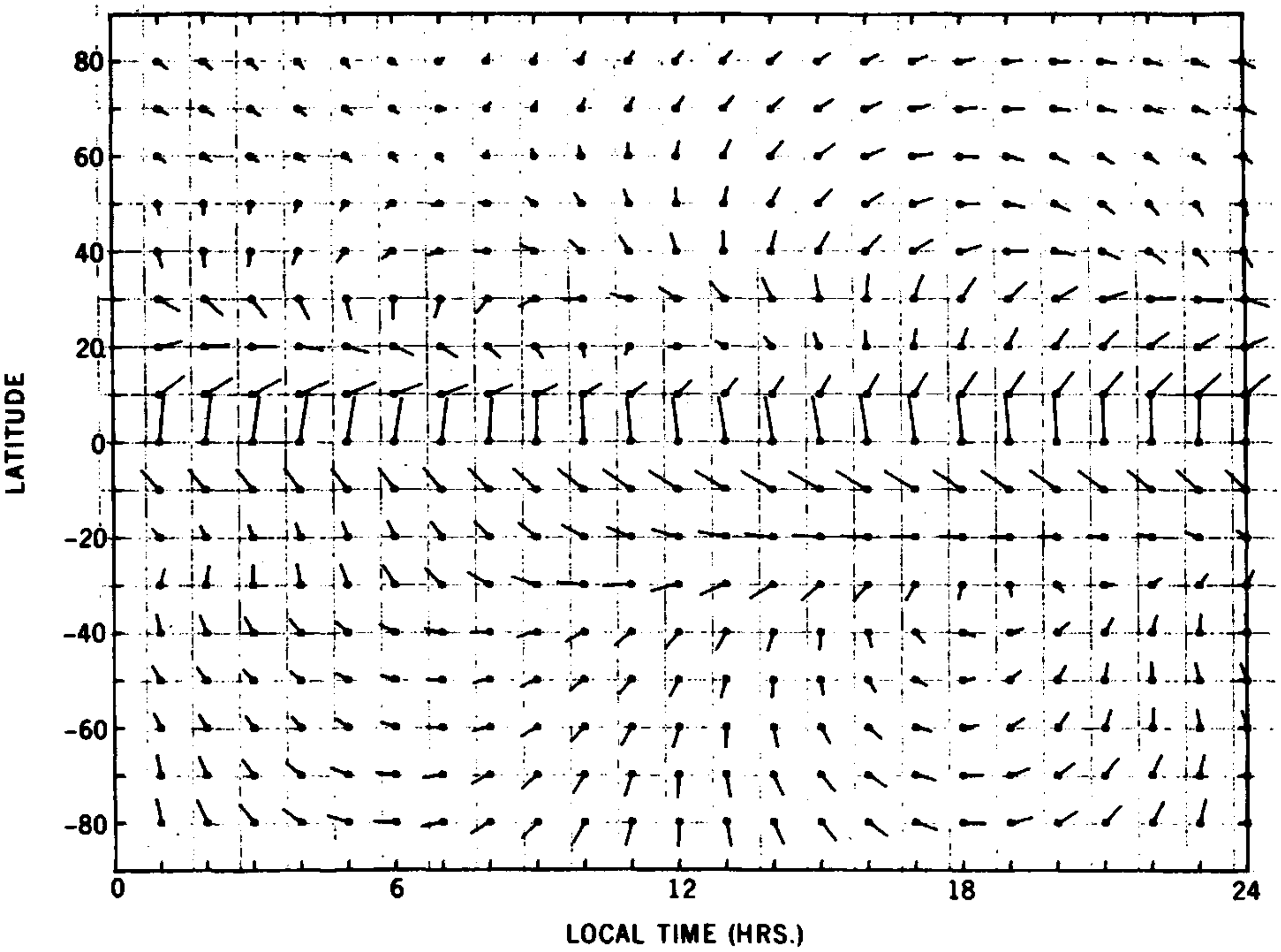

Figure 3-96. Preliminary wind fields deduced by IRIS

Several temperature profiles from S-band data are shown here, for a time in the early mission phases, and for a time subsequent to the subsidence of the global dust storm. Figure 3-97 displays profiles for Revs. 1 through 9. The profiles for even revolutions are shown dashed, and those for odd revolutions are shown as solid curves. Most of the profiles are nearly isothermal for about 10 to 15 km above the surface, lapsing somewhat with height above those altitudes. As indicated earlier, the isothermal effect is caused by solar radiation absorbed by fine dust suspended in the atmosphere, thus raising the temperature of the dust particles and in turn heating the atmosphere. The mean temperatures at all tropospheric levels also are higher than expected, and likewise appear to be due to the solar energy deposition in the first 1 or 2 scale heights due to absorption by the entrained dust. The near isothermal nature of the lower atmosphere had apparently been observed during the entry of Mariner 4 into occultation. Other comparisons of Mariner 9 measurements with Mariner 6 and 7 data, obtained for similar solar zenith angles and local times, have also indicated a significant difference in the thermal state of the atmosphere. The 1969 data yielded temperature profiles with approximately adiabatic lapse rates in agreement with theory for a clear atmosphere.

Later profiles (Figures 3-98 and 3-99) display a somewhat increasing temperature gradient towards the later revolutions. The gradual increase in the magnitude of the temperature gradient along with an increase in the temperature near the surface is consistent with the gradual clearing of dust in the Martian atmosphere as indicated earlier by IRIS results.

The temperature profiles found from the results of the S-Band occultation experiment and those deduced from the IRIS experiment appear to be in good qualitative and quantitative agreement. In addition, the trends in atmospheric temperatures with the gradual clearing of the dust clearly shown by IRIS results, also seem to be apparent in the most recently reduced occultation data. Further analyses are required for a more systematic and definitive comparison. Since some regions of the planet are inaccessible to either the IRIS (North Polar region) or the S-Band occultation experiment, mutual investigations are required to obtain more complete global coverage.

3.3.2.2.2 Pressure Scale Height Measurements

Additional data of importance for atmospheric studies, from the S-band occultation results, include the surface atmospheric pressure and the pressure scale height. The surface pressure data is of vital importance in topographic mapping of the surface over limited regions and in providing absolute data for calibration or testing of the spectroscopic results. The scale height data is important in estimating the vertical pressure distribution, in conjunction with the surface pressure data. Under the assumption of hydrostatic equilibrium, with an isothermal atmosphere, the pressure distribution follows the barometric law. An example of a resulting profile

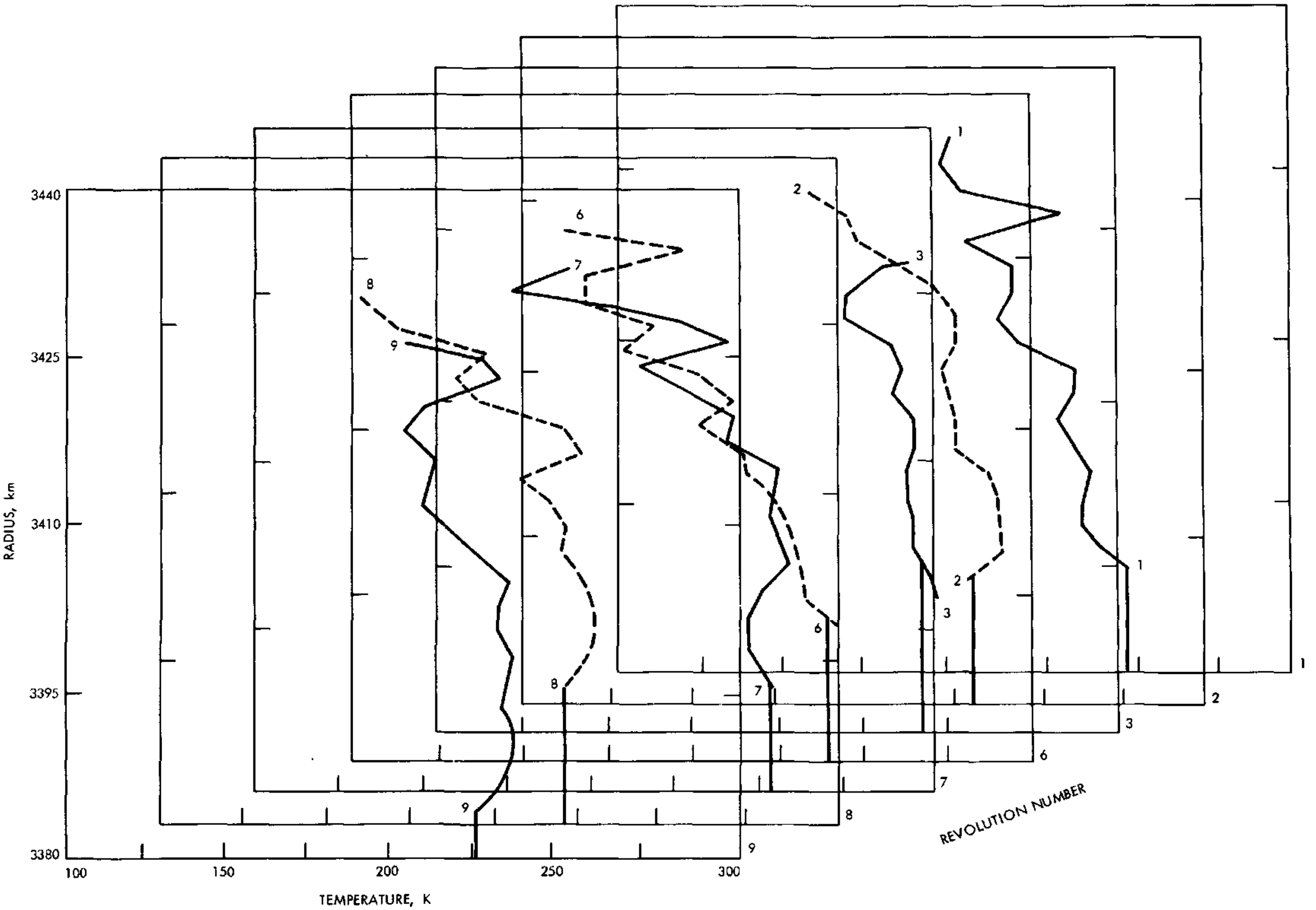

Figure 3-97. Early S-band occultation temperature profiles

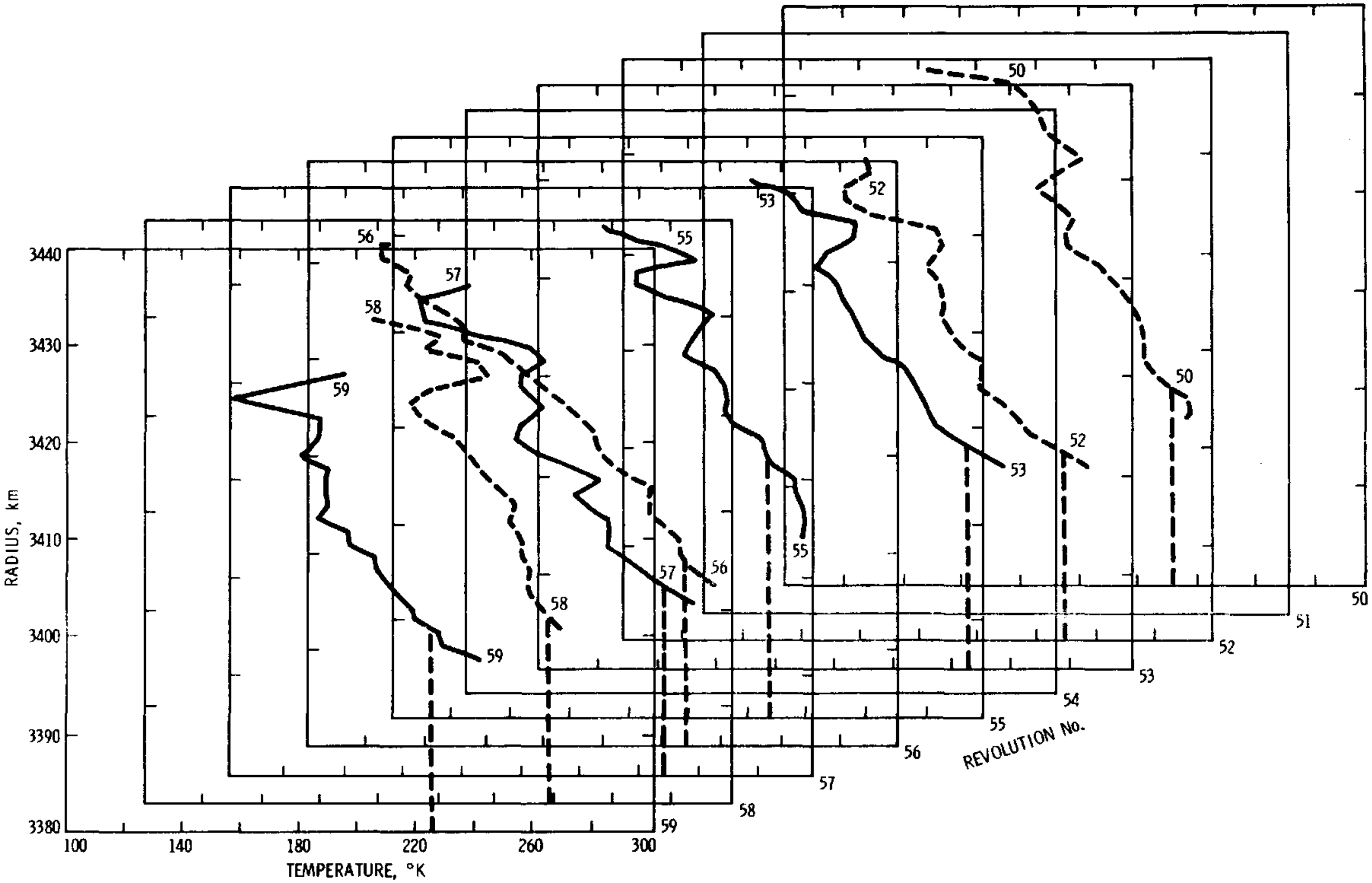

Figure 3-98. Later S-band occultation temperature profiles

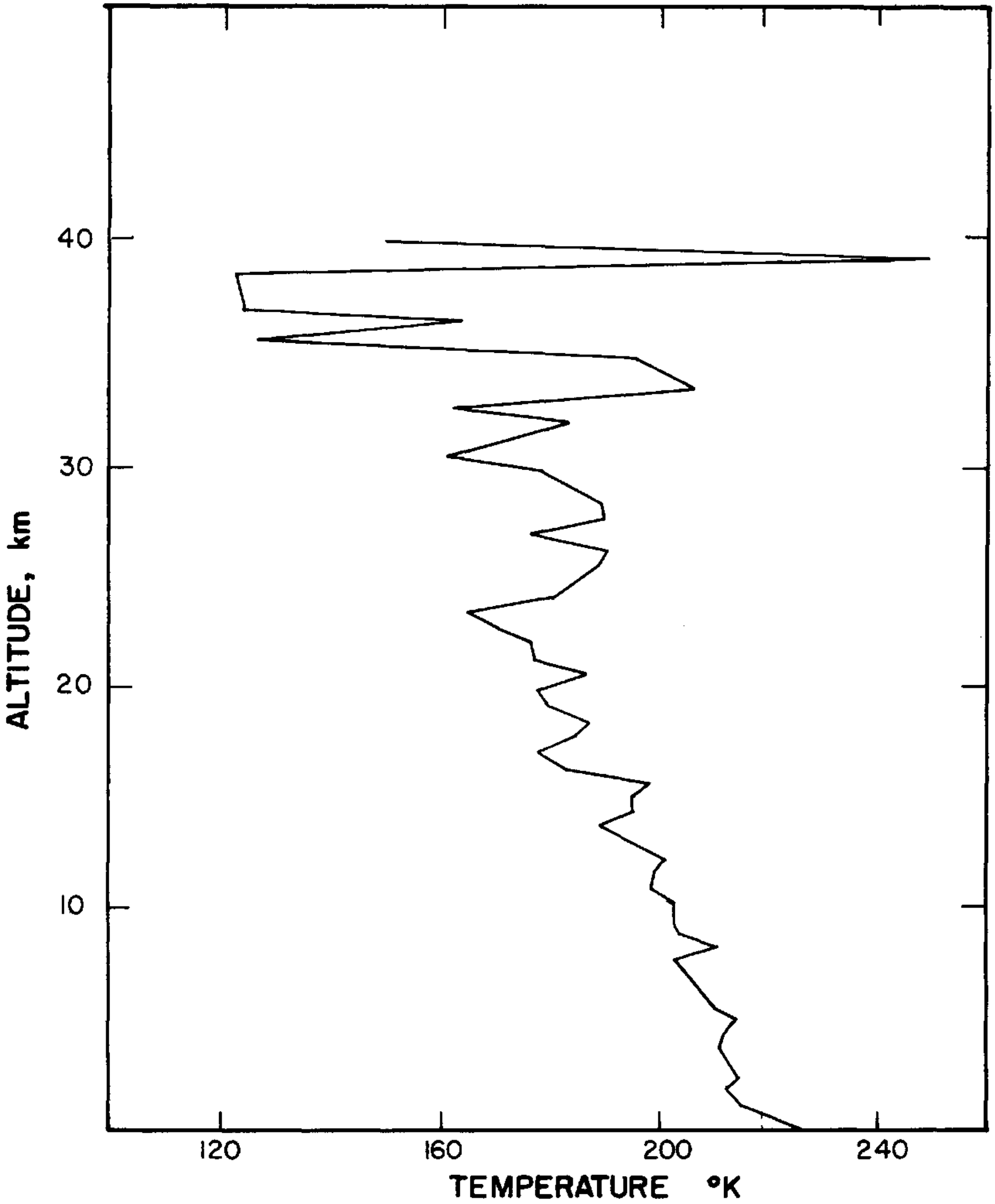

Figure 3-99. Additional, later occultation temperature profiles

deduced from the occultation data under the above conditions is shown in Figure 3-100. Typical resulting scale heights fall in the range 10 - 12 km. Comparisons of the pressure scale height, with other data inferred on vertical distributions of dust or water vapor, are important in assessing the degree of mixing within the atmosphere.

3.3.2.2.3 Upper Atmosphere

The UVS and S-band occultation experiments are important sources of data for investigations of the structure of the upper atmosphere of Mars. The UVS results are obtained by analyses of spectrometric airglow observations of the bright limb. These limb scans provide good altitude profiles of the emission rates of important ions resident in the upper atmospheric regions. The principal spectral emissions identified during these limb crossings were those first measured in 1969 by the ultraviolet spectrometers on Mariner 6 and 7: the atomic hydrogen 1216Å Lyman-alpha line; the atomic oxygen 1304, 1356, and 2972Å lines; the atomic carbon 1561 and 1657Å lines, the carbon monoxide A-X fourth positive and a-X Cameron bands, the ionized carbon monoxide B-X first negative bands, and the ionized carbon dioxide B-X and A-X bands. This airglow is the result of solar ultraviolet radiation incident on the upper atmosphere of Mars.

The airglow spectrum of Mars in the 1910 to 2460Å range contains the intense CO a-X bands and the weaker CO^+ B-X bands and are used to infer their altitude emission profiles. The CO A-X bands appear to contribute most of the intensity in the 1420 to 1760Å region, with the atomic carbon lines making a substantial contribution. Previous analysis of the Mariner 6 and 7 data showed that the most probable source of excitation of the carbon monoxide A-X and a-X bands results from electron and photon impact-induced dissociative excitation of carbon dioxide. The intensity of these bands as a function of altitude may be used to determine the density distribution of carbon dioxide in the upper Martian atmosphere. In turn, the scale height of these emissions can be used to deduce the temperature of the upper atmosphere. Typical emission rates of these two CO band systems as a function of altitude are presented in Figure 3-101 for a limb observation made early in the mission. Resulting values for the CO scale heights are in the range 17 - 26 km, for altitudes between 160 - 220 km.

The 1304Å resonance line of atomic oxygen which appears in the air glow is an indicator of atomic oxygen abundance. The apparent emission rate of this line on a typical pass is plotted in Figure 3-102. This emission line is optically thick in the Mars atmosphere. As a result, multiple scattering occurs and a radiative transfer analysis must be performed to determine the actual atomic oxygen density.

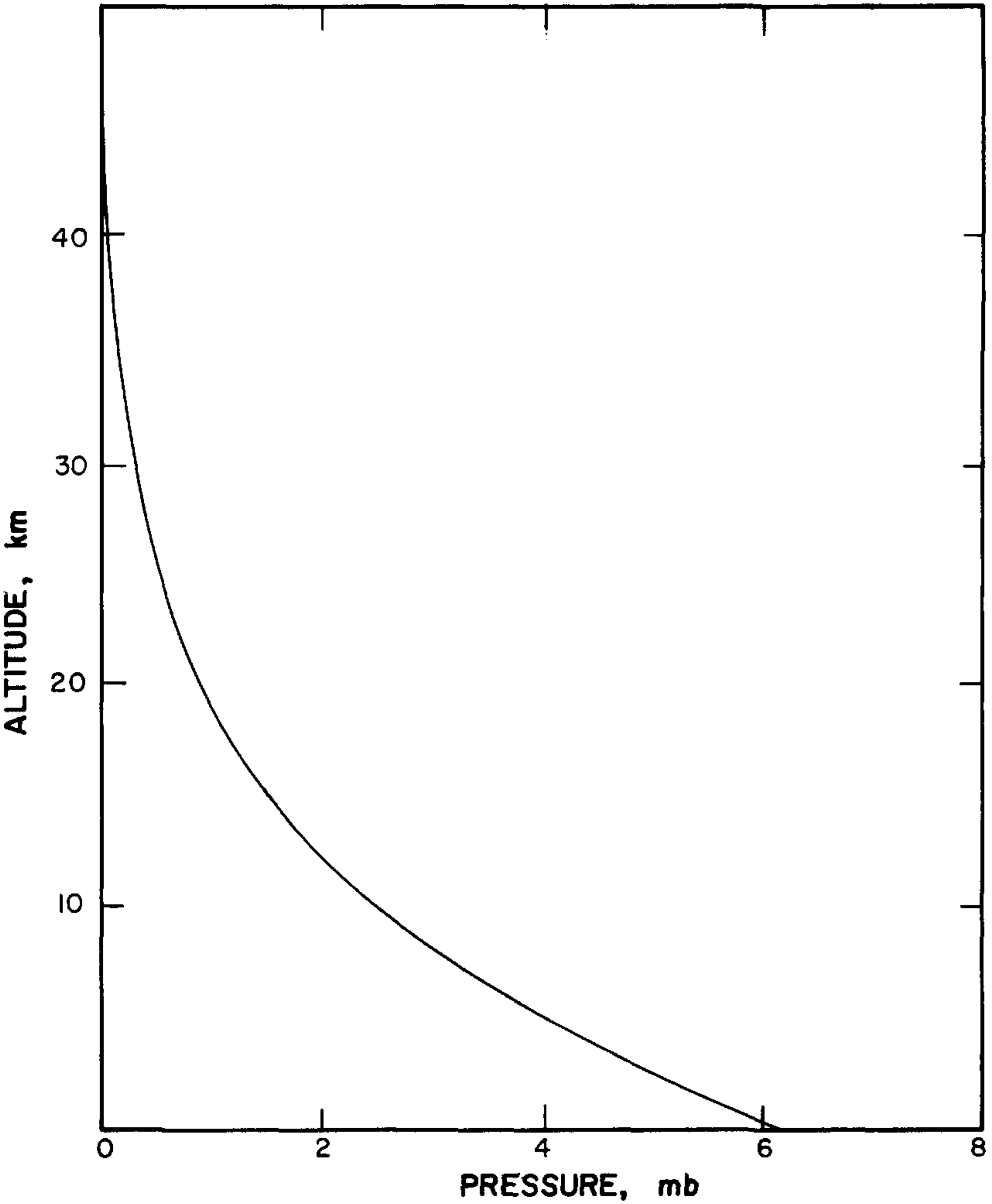

Figure 3-100. S-band occultation pressure profile

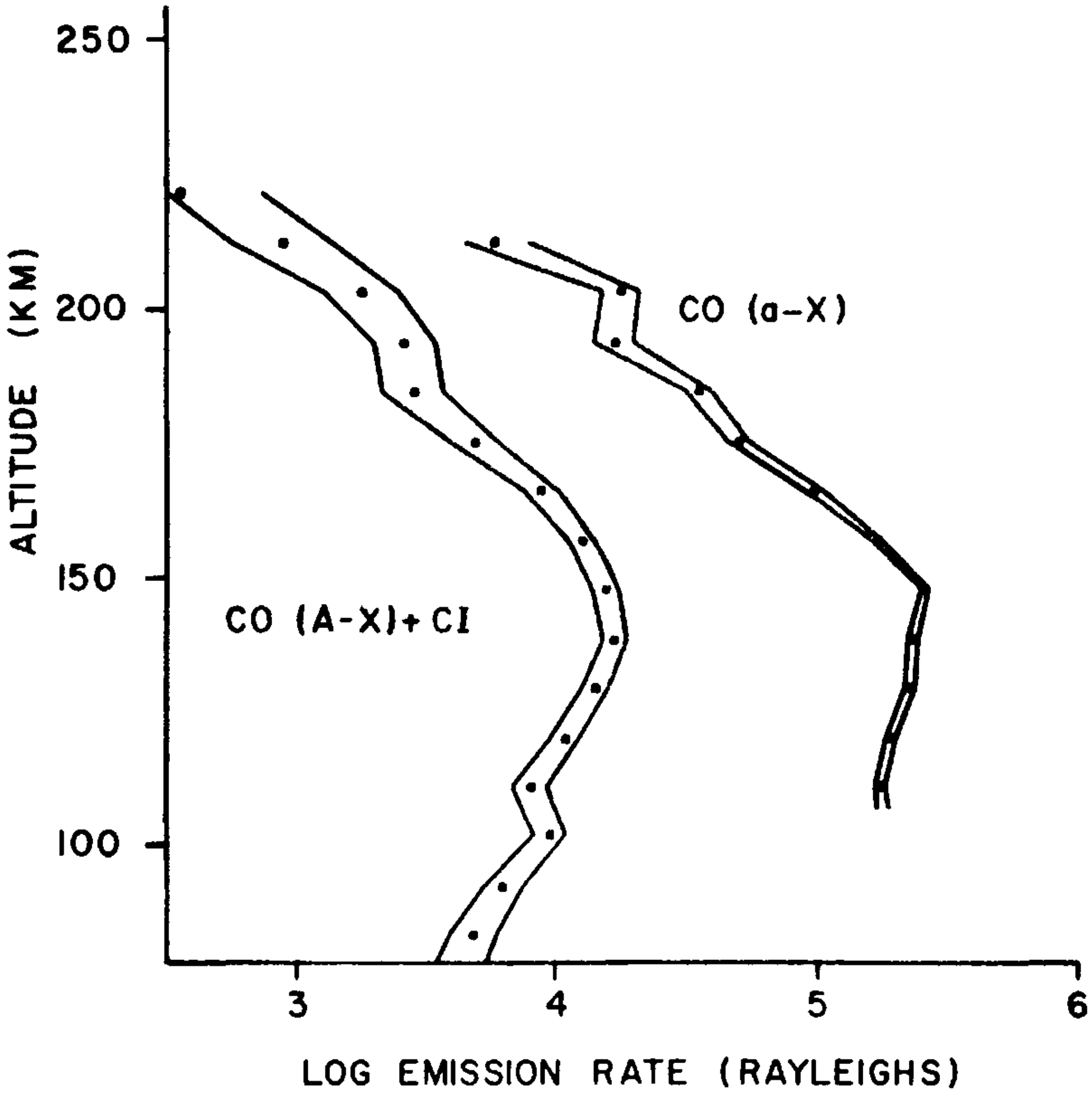

Figure 3-101. UVS CO emission profile

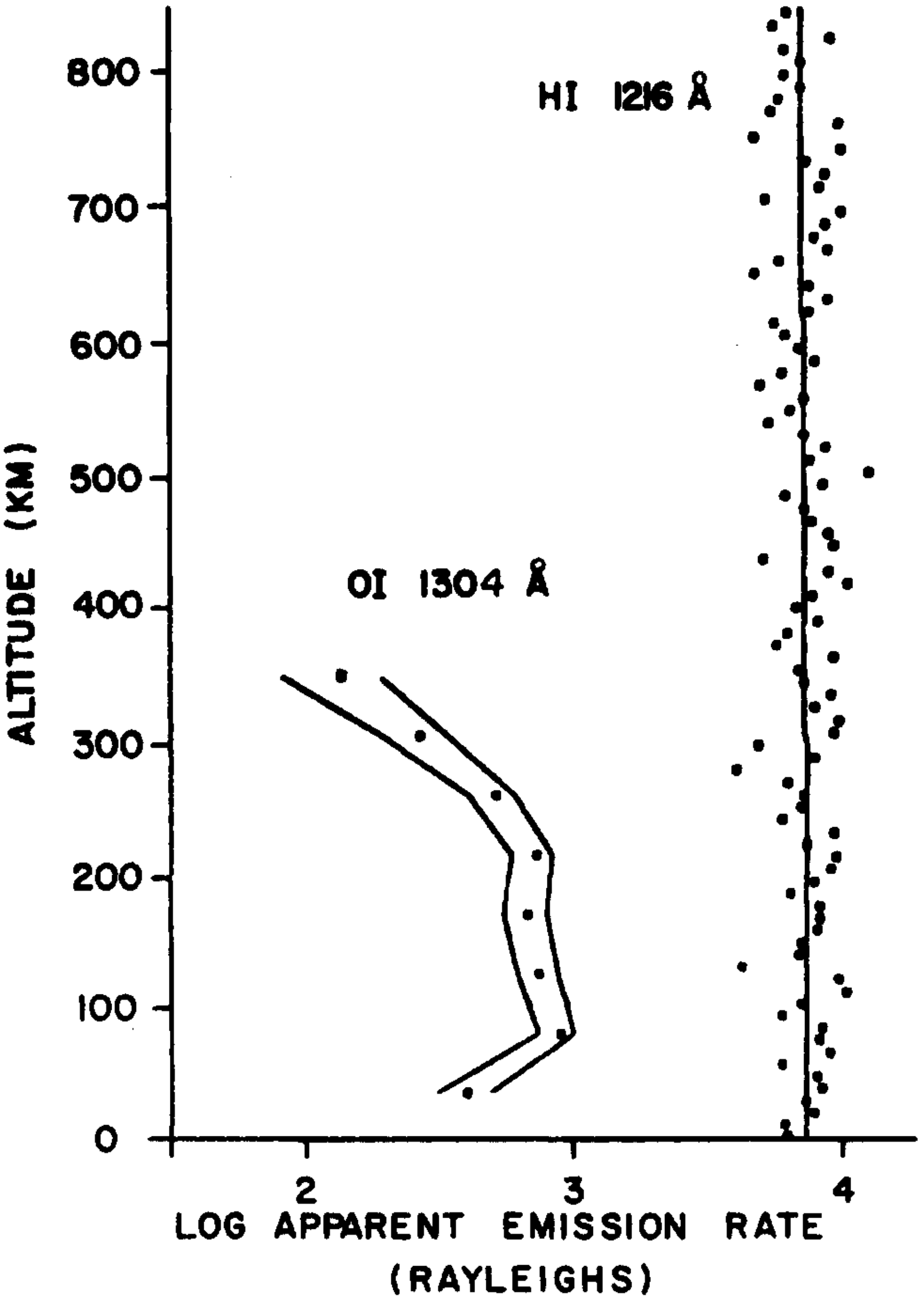

Figure 3-102. UVS O and H emission profiles

The Lyman-alpha airglow at 1216Å is a measure of the atomic hydrogen density and extends to great altitudes above the planet. A sample of an apparent emission profile is also plotted in Figure 3-102. This emission line is also optically thick, and to determine the exospheric temperature and density distribution of atomic hydrogen, an analysis of this emission along the entire orbit is necessary.

Variations in the scale height appear to be of sufficient magnitude to be statistically significant and are correlated with changes in the solar 10.7 cm flux. This solar flux is an indicator of the intensity of the incident UV solar radiation which ionizes and heats the upper atmosphere. Apparently the upper atmosphere of Mars responds to changes in solar activity similar to Earth's. However, it is apparently affected by atmospheric processes not related to changes on the Sun. Significant variations in the scale height of the CO Cameron band airglow have been observed during a period of variable solar activity, although the atomic oxygen and hydrogen lines are present during all the observations. The measured Lyman-alpha intensities seem to be correlated with the Zurich sunspot number, which is an indicator of the intensity of the incident solar Lyman alpha radiation. However, the variation in these intensities may reflect actual changes in atomic hydrogen densities in the Martian atmosphere.

These observations have also demonstrated the result that the Martian atmosphere responds to changes in solar activity, and the Mariner 9 UVS senses the Martian atmosphere response to solar activity 3 days before the effects of the changes are felt in Earth's atmosphere.

The S-band occultation experiment provides data on the spatial electron density distribution. Figure 3-103 shows a typical electron density profile. The solar zenith angle was approximately 55° and the electron density shows a maximum of about 1.6×10^5 electrons/cm^3 near 140 km altitude. The topside plasma scale height is about 38 km.

Investigation of a sizeable number of early revolutions yield peak electron densities and topside scale heights which differ by less than 5%. The altitude of the ionization peak changes somewhat from one pass to another, and this effect appears related to elevation differences on the surface. The mean scale height is approximately 38 km, and additional studies have shown that there does not appear to be any systematic change in the scale height with changing solar zenith angle, solar activity, or local time.

Some of these data may be compared with scale height values determined from the UVS measured CO a-X emissions. The mean scale height value obtained from these measurements was 20.4 km with a standard deviation from the mean of 2.6 km, a value about one-half the topside plasma scale height.

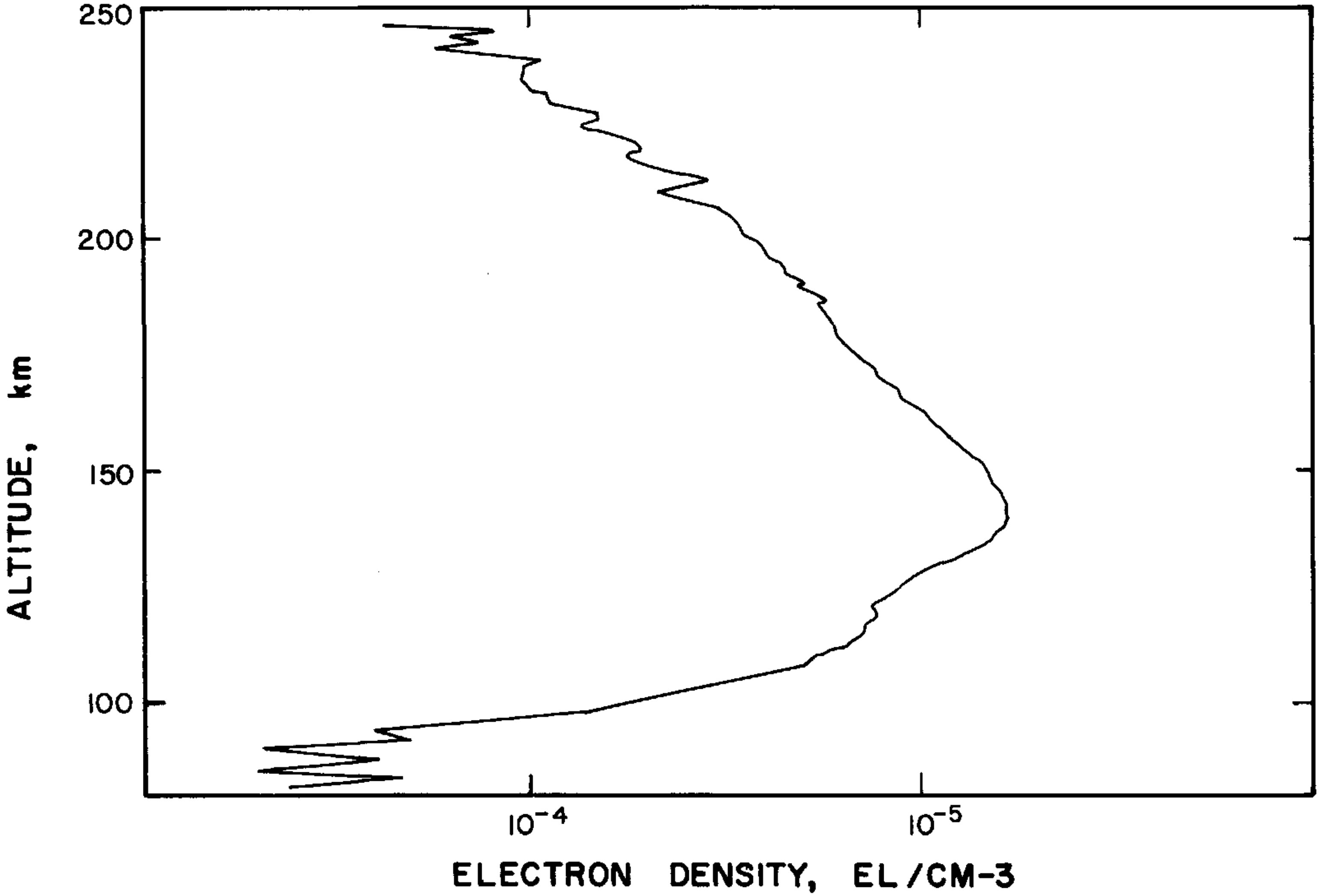

Figure 3-103. S-band occultation electron density distribution

M75-144-0

The general results recorded to date show that the density and temperature of the Martian ionosphere have been reduced since 1969, but are higher than during the quiet solar conditions prevailing at the time of the Mariner 4 mission to Mars in 1965. However, the most notable difference between measurements from Mariner 9 and those from earlier spacecraft is the increased altitude of the inoization peak, which shows that the atmospheric region below 145 km is warmer than before. This observation is consistent with the measured temperatures in the lower atmosphere, as influenced by the great global dust storm.

Continuing studies of peak electron densities are summarized in Figure 3-104. The measured data are compared with the results of theoretical calculations of ionizations produced in an F_1 type ionosphere, in which a variable incident solar UV flux is included. The results show excellent agreement, and hence indicate an excellent representation of the Martian upper atmosphere.

3.4 SYNOPSIS OF RESULTS

The scientific results of the Mariner 9 Experiments have already dramatically increased our knowledge of the planet Mars. Results of the TV imaging experiment, of course, with its mapping of the surface, the study of transient atmospheric and surface phenomena, and photometric investigations, transcends all other previous data. Both the UVS and IRIS experiments have contributed a very important body of basic data leading to a better knowledge and understanding of the Martian atmosphere and surface.

The composition of the atmosphere is basically understood, but better determinations of the minor constituents, their vertical and latitudinal dependence, their relation to the polar caps and their pole-ward transport characteristics will result from further analyses of the UVS and IRIS data.

New and more complete coverage of the lower and upper atmospheric structure is also available as a result of the UVS and IRIS measurements. In this regard, the effects of the global dust storm were readily apparent from the IRIS and IRR studies and some effects in the upper atmosphere have been noted by UVS.

Topographic effects appear very important, in discussions of surface atmospheric pressure, the spatial and temporal scales of the wind field, and in the gravity field of the planet. Continued analyses of IRIS data in conjunction with results of certain wind related features is especially important for Viking and should better clarify the nature and characteristics of the Martian atmospheric winds.

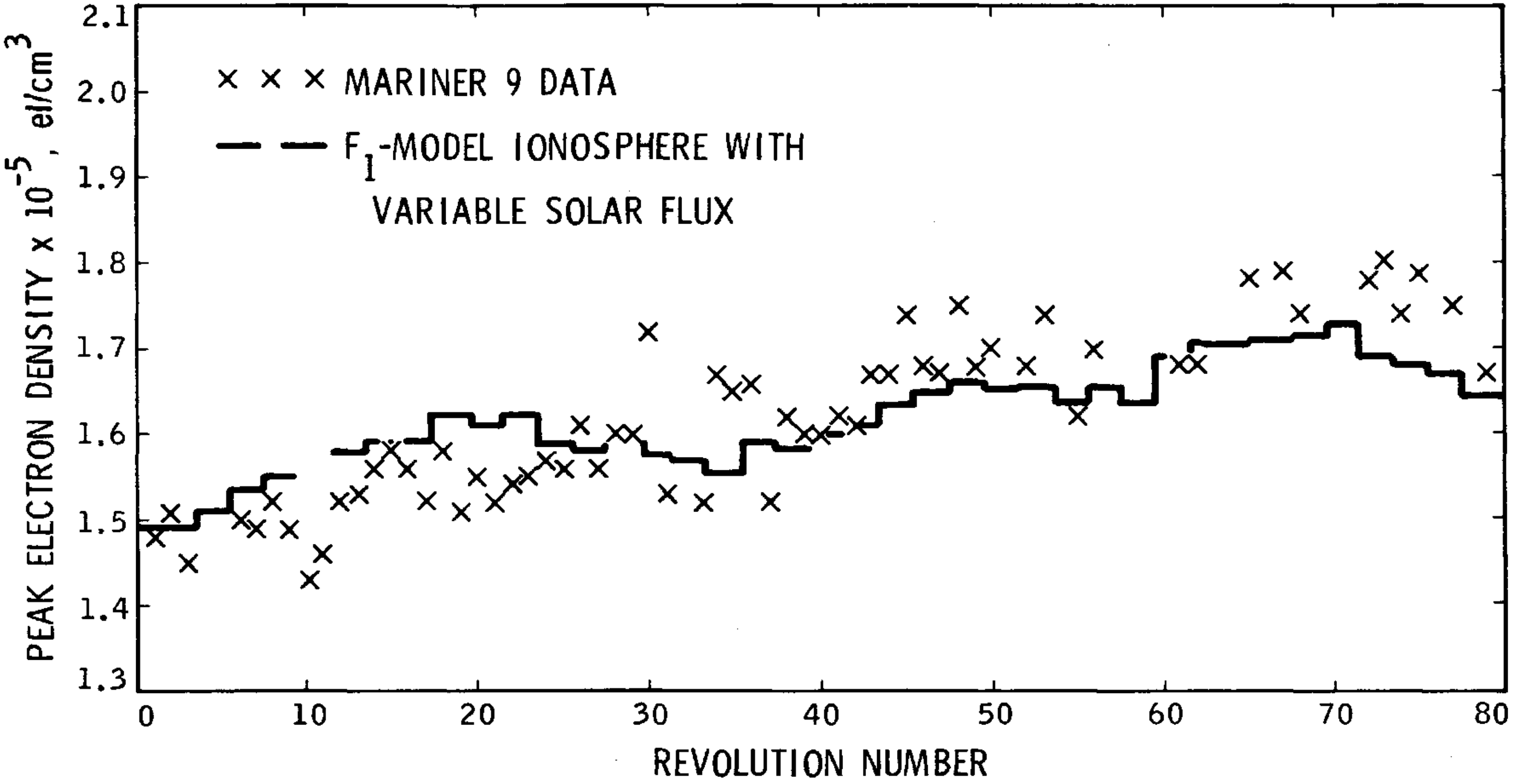

Figure 3-104. Variation of S-band peak electron density with time

An important characteristic that has emerged from results of preliminary analyses of the Mariner 9 experiments is that the thin Martian atmosphere is extremely sensitive and responsive in a radiative and dynamical manner, to temporal and spatial variations of energy inputs. The great global dust storm that emerged during the initial Mariner 9 mission phases is perhaps the best example of this characteristic. In this regard, its physical or dynamical behavior for future Martian missions will be extremely complex and may be uncomfortably unpredictable.

Additional results from current and forthcoming studies regarding the physical and chemical properties of the Martian surface are anticipated. The deduction by the IRIS team regarding the dust composition (approximately 60% SiO_2) and its inferences concerning the possible high degree of differentiation of the Martian crust are of considerable importance. The verification of this result, by continued analysis of IRIS and IRR data as well as determination of the global distribution of surface composition, are important to Viking.

On a planetary basis, considerable improvements have resulted from Mariner 9 navigational tracking and occultation data. These include better determinations of the physical and dynamical figure of Mars, improved spin-axis orientation determinations, improvements in the mass of Mars and the Earth/Moon mass ratio, and detailed mapping of irregularities in the gravity field of Mars. This improved data should allow much more precise planning of the Viking mission.

Clearly, the Mariner 9 experiments have provided a wealth of new scientific data of tremendous value to planetary scientists. The impact of the results on subsequent investigations will be great, particularly for Viking.

However, the needs for the Viking mission have not been met as yet. Numerous detailed investigations involving the correlations of Mariner 9 results and earth-based data are required to better establish and define the Viking environment. Within the time scale of the mission, however, and the rate of availability and publication of additional Mariner 9 results, it is apparent that much vital data will not be available for Viking planning.

3.5 REFERENCES

1. Barth, C. A., Hord, C. W., Stewart, A. I., and Lane, A. L., (1972), Mariner 9 Ultraviolet Spectrometer Experiment: Initial Results, Science, 175, 309-312.
2. Bartko, F., VDAT Memorandum, 1972.
3. Cain, D. L., Kliore, A. J., Seidel, B. L., Sykes, M. J. The Shape of Mars from Mariner 9 Occultations.
4. Chase, S., Miner, E., Munch, G., and Neugebauer, G., Icarus, 12, 46 (1970).
5. Conrath, B. J., Hanel, R. A., Kunde, V. G., and Prabhakara, C., J. Geophys. Res., 75, 5831 (1970).
6. Fjeldbo, G. and Esheleman, V. R., (1968), The Atmosphere of Mars Analyzed by Integral Inversion of the Mariner 4 Occultation Data, Planet. Space Sci., 16, 1035-1059.
7. Bierasch, P. and Goody, R., (1968), The Study of the Thermal and Dynamical Structure of the Martian Lower Atmosphere, Planet. Space Science, 615-646.
8. Gierasch, P. and Goody, R. M., (1972), The Effect of Dust on the Temperature of the Martian Atmosphere, J. Atmos. Sci., 29, 400-402.
9. Hanel, R. A., Conrath, B. J., Hovis, W. A., Kunde, V., Lowman, P. D., Prabhakara, C., Schlachman, B., and Levin, G. V., Icarus, 12, 48 (1970).
10. Hanel, R. A , Conrath, B. J., Hovis, W. A., Kunde, V. G., Lowman, P. D., Pearl, J. C., Prabhakara, C., Schlachman, B., and Levin, G. V., Infrared Spectroscopy Experiment on Mariner 9: Preliminary Results, Science, 175, 305-308, 1972.
11. Havel, R. A., et al., Private Communication, 1972.
12. Hord, C. W., Barth, C. A., Pearce, J. B., Icarus, 12, 63, (1970).
13. Hord, C., et al, Private Communication, 1972.
14. Hovis, W. A., Appl. Opt., 5, 245 (1966).
15. Kliore, A. J., Fjeldbo, G. and Seidel, B. L., (1971), Summary of Mariner 6 and 7 Radio Occultation Results on the Atmosphere of Mars, in Space Research XI, Academic Verlag, Berlin, 165-175.

16. Kliore, A. J., Cain, D. L., Fjeldbo, G., Seidel, B. L., and Rasool, S. I., (1972) Mariner 9 S-Band Martian Occultation Experiment: Initial Results on the Topography and Atmosphere of Mars, Science, 175, 313-317.

17. Kliore, A. J., Cain, D. L., Fjeldbo, G., Seidel, B. L., and Rasool, S. I., S-Band Occultation Experiment, Atmosphere, Ionosphere, and Topography of Mars, JPL TR 32-1550 dated February 1, 1972.

18. Kliore, A. J., et al. The Atmosphere of Mars from Mariner 9 Occultation Measurements, Presented at the IAU/URSI/COSPAR Symposium on Planetary Atmospheres and Surfaces, Madrid, Spain, May 10-14, 1972.

19. Lane, A. L., Barth, C. A., Hord, C. W., and Stewart, A. I., Mariner 9 Ultraviolet Spectrometer Experiment: Observations of Ozone on Mars. To be Published.

20. Lincoln Laboratory, 1970, Radar Studies of Mars - Final Report: Lincoln Lab., MIT, prepared under NASA contract NAS 9-7839, 79 p.

21. Lyon, R. J. P., Technical Note D-1871 (NASA, 1964).

22. Masursky, H., Batson, R., Borgeson, W., Carr, M., McCauley, J., Milton, D., Wildey, R., Wilhelms, D., Murray, B., Horowitz, N., Leighton, R., Sharp, R., Thompson, W., Briggs, G., Chandeysson, P., Shipley, E., Sagan, C., Pollack, J., Lederberg, J., Levinthal, E., Hartmann, W., McCord, T., Smith, B., Davies, M., de Vaucouleurs, G., and Loevy, C., Icarus 12, 10-45 (1970).

23. Masursky, H., et al, (1972), Mariner 9 TV Reconnaissance of Mars and Its Satellites, Preliminary Results, Science, 175, 294-304.

24. Neugebauer, G., Munch, G., Kieffer, H., Chase, S. C., and Miner, E., Astron. J., 76, 719 (1971).

25. Pearce, J. B., Gause, K. A., Mackey, E. F., Kelly, K. K. Fastie, W. G., and Barth, C. A., Appl. Optics, 10, 805 (1971).

26. Radar Data 1967, 1969, 1971.

27. Rasool, S. I. and Stewart, R. W., J. Atm. Sci., 28, 869 (1971).

28. Sagan, C., Veverka, J., Gierasch, P. (1971), Observational Consequences of Martian Wind Regimes, Icarus, 15, 253-278, (1967).

29. Thomas, Paul D., 1952, Conformal Projections in Geodesy and Cartography: U. S. Dept. of Commerce Coast and Geodetic Survey Special Publ. 251.

4.0 EARTH-BASED DATA ANALYSIS

This section of the report discusses the analysis of earth-based observations. In particular, the radar data have been prepared for correlation with the Mariner 9 experimental results. In addition, there is a brief discussion of some of the observations considered in selecting areas of interest to Viking for observations by Mariner 9 in the extended portion of the mission.

4.1 TERRESTRIAL RADAR DATA

Terrestrial radar observations at the Haystack Observatory of MIT (Refs. 5 and 6) and JPL's Goldstone Tracking Station (Ref. 2) yield three types of data that are useful to Viking: (1) estimates of surface roughness at a slope length comparable to the base length of the spacecraft; (2) estimates of the dielectric constant of the surface and; (3) surface elevations. The first two are estimated from the spectral width of the echo and radar cross-section and the last from time delay measurements.

Estimates of surface roughness yield root mean square (rms) slopes which represent one standard deviation for a slope frequency distribution at a slope length 10 to 100 times the wave length of the radar. For Haystack observations, this is a slope length near 0.38 to 3.80 m. Some experimental data suggests the slope length may be larger and possible 225 wavelengths (8.55 m).

Dielectric constants are a function of the reflecting material. Laboratory studies show that dielectric constants of cohesive rocks may vary from 2.5 (porous pumice) to about 9 (dense basalt). Powdered rocks with densities of 1.0 g/cm^3 have dielectric constants between 1.8 and 2.2 and rock powders with 40% porosities have dielectric constants between 2.5 and 3.5. The presence of ice and water (dielectric constant 80) in pores of granular materials can profoundly affect the bulk dielectric constant.

Elevations obtained by time delay measurements provide data on topography and slope frequency distributions at slope lengths down to about 7.15 km.

In the discussion below, it is assumed that the radar data (Refs. 3, 5 and 6) are valid, that the rms slopes and dielectric constants are, in fact, correct, and that the elevations are accurately determined points. Much of the discussion is at the 1:25,000,000 scale, whereas the appropriate level of generalization for interpretation of radar data for Viking is 1:5,000,000-scale.

The importance of these estimates to the Viking project is clear. Estimates of surface roughness at the spacecraft scale can be used to define areas accessible to the Lander by virtue of slope. As will be shown below, some areas of Mars are less favorable (or even prohibitive) than others. Estimates of dielectric constants affect the spacecraft and landing site choice in three ways. First, areas with low dielectric constants (<2.5) may be cohesionless and thus too porous to land on. Areas with high dielectric constants (>3.5) may be cohesive rocks which prohibit sampling and comminution, or, alternatively, the dielectric constants may be high because of pore water in soils -- thereby satisfying the site selection criterion of a "moist permeable substrate." Finally, elevations may provide data affecting the radar altimeter design as well as elevation data that may be correlated with surface pressure, for defining accessible areas of the planet for the Viking Lander.

4.1.1 Root Mean Square (rms) Slopes on Mars and Lunar Comparison

Average values of terrestrial based radar estimates of rms slopes for Mars (3.3°) are less than those for the central disk of the Moon, 7° to 9° (Ref. 9). Thus Mars is smoother than the Moon on the average. However, the roughness of the surface of Mars is heterogeneous. For example, averaged values for the rms slopes obtained from Haystack, 1967, 1969, and 1971 data are 2.364, 3.162, and 2.659 and one concludes there may be a significant difference for the various latitudes sampled by the radar. Comparison with the Generalized Terrain Map (Map 2) indicates this may be the case because of the difference is distribution and amounts of the various terrain units in the northern and southern hemispheres. To further illustrate the heterogeneous nature of Mars' roughness, Haystack estimates of rms slopes were averaged along the radar traces in steps of 5° longitude (Map 6). Values for the rms slopes range from about 0.7° to 10.5°. Good correlation with visually determined terrain units at a scale of 1:25,000,000 appears in some cases, but not in others. For example, the band near 5° to 10° N (1969 data) indicates large rms slopes near Rugged Terrain (Ir) where rms slopes vary from about 5.4° to 8.1°. Generally small values (1.6° to 4.9°) are found in the Cratered Plains (Cp). Large values of rms slopes are found near the Canyonlands (CL) and Cratered Tablelands (Tc). General agreement between the 1969 data and 1967 data at about 22° N is not found. Some of the lowest values (0.8°) are found over Rugged Terrain (Ir). Cratered Tablelands (Tc) do appear rough (8.1°), however. Haystack data for 1971 (10° to 25° S) show remarkable correlations with the imagery. For example, the Smooth and Ridged Tablelands (Ts and Tr) appear smooth to both the radar (1.0° to 3.3°) and visual impressions of the imagery. When the Canyonlands (CL) at about 14° S are reached, average rms slopes promptly increase to values of 4.8° to 7.6°. Inspection of 1:5,000,000 plots show many values are 10.5°. Additional areas appear smooth to the 1971 radar, such as the bands between 110° W and 310° W to 360° W. Domes (Dc), where sampled by radar, are rough (6.3° to 8.1°). Puzzling disagreement is found for the Smooth Tablelands (Ts) unit since both the 1967 and 1971 data indicate it is smooth, but the 1969 data indicate it is fairly rough (4.1° to 6.5°).

Because terrestrial radar determinations of lunar rms slopes are confined to the central disk of the Moon, where the Moon is relatively rough, a better intuitive appraisal of Martian roughness at small slope lengths can be obtained by comparing standard deviations of lunar slope frequency distributions at slope lengths of 1 and 10 meters, obtained using photoclinometric methods with radar rms slopes. Lunar values are tabulated below:

Table 4-1. Algebraic standard deviation of slope angles for four gross lunar terrain types

	Slope length 1 m			Slope length 10 m		
	Mean	Low	High	Mean	Low	High
Smooth Mare	3.6	1.5	5.0	2.5	1.3	3.5
Rough Mare	6.6	4.4	9.7	4.7	3.1	7.0
Hummocky Upland	10.2	5.8	12.4	7.2	4.4	8.7
Rough Upland	13.7	10.0	18.6	9.6	7.7	13.7

Inspection of Table 4-1 shows that Mars, on the average, is somewhat like smooth mare on the Moon. Comparison of the numbers on Map 6 with those of the table show a large part of the Martian surface has a surface comparable to, or smoother than average lunar maria. Other Martian surfaces are as rough as Hummocky Lunar Uplands.

4.1.2 Dielectric Constants

Average values of terrestrial based radar estimates of dielectric constants for Mars (3.5) are larger than those for the central disk of the Moon (2.8). Thus, Mars may have more rock, moisture, or high dielectric constant material than the Moon. Although the average Martian value is more or less consistent with powdered basalt with 40% porosity, values for Mars vary widely. Averaged dielectric constants obtained using Haystack Observatory estimates are 2.074, 2.767, and 3.654 for their 1967, 1969, and 1971 data, and one concludes there may be significant differences for the various latitudes sampled by the radar. Judging from the Generalized Terrain Map (Map 2), this is entirely possible since the 1967 data has the lowest average dielectric constant, and samples more of the Smooth Plains Ps) unit which appears to be partly obscured by dust than either the 1969 or 1971 data. The 1971 data has the highest average dielectric constant and samples the least amount of the Smooth Plains unit. Additionally, as shown in Map 7, wherever the 1971 data crosses the Smooth Plains unit, estimated dielectric constants are generally lower than the average 1971 dielectric constant. This occurs for the 1971 data over longitudes of 110° to 145° W where the averaged numbers are almost always less than 3.4 and commonly near 2.0. In one area the 1971 Haystack estimates are particularly large ($\approx$14° S, 320° to 360° W), where averaged values range between 4.9

and 7.5, and local values are as high as 20 to 49. Additionally, an empirical comparison of the 1971 Haystack dielectric constant data with the 14° South latitude radar topographic profile exhibits a distinct correlation. The distribution of low dielectric constant values (1.0 to 2.0) is very sensitive to local topography with the low values residing in topographic depressions. This correlation is not elevation dependent, since low dielectric values occur equally in regions of high and low topographic relief.

4.1.2.1 Experimental Dielectric Constants

Laboratory determinations of dielectric constants (permittivity) of natural materials have been reported by Cambell and Ulrichs (Ref. 1) for frequencies of 450 MHz (67 cm wavelength) and 35 GHz (0.86 cm wavelength). In general, cohesive dense rocks have large dielectric constants although porous cohesive rocks may have small constants. Silica-rich rocks tend to have smaller constants than silica-poor mafic rocks. Rock powders have low constants when the powders are relatively free of fragments comparable in size to a wavelength and the powder is dry. Additionally, the constants are not strongly dependent on wavelength or temperature. Mafic pore-free, dense rocks such as basalt have dielectric constants in the range of 7 to 9.6 and more silicic ones, such as granite and andesite have constants in the range of 5.5 to 6.5. Porous cohesive rocks such as pumice, semi-welded tuff, shale, volcanic ash, and rhyolitic tuffs have constants in the range of 2.4 to 3.6. Thus, both the composition and porosity of dry rocks affect the dielectric constant. Dielectric properties of powders and porous fine-grained materials are a function of porosity and pore fillings such as water. For dry powders with bulk densities near 1.0 g/cm^3, dielectric constants are between 1.8 and 2.2. When the porosity is 40%, they range between 2.5 to 3.5. Thus, it is clear that some cohesive rocks have dielectric constants equal to those of dry cohesionless powders and dielectric constants from a planetary surface will not estimate cohesion. Very large dielectric constants in the range of 9.0 to 80 can result from large amounts of water in porous granular media, some meteorites, and iron-rich materials.

4.1.2.2 Dielectric Constants and Viking

Data on the mechanical properties of the Martian surface are important to the Viking Lander because it must land without penetrating too far and must collect a sample for the Biology, GCMS and X-Ray Fluorescence experiments. Dielectric constants estimated by the Haystack Observatory are, at this time, the best estimate of the surface properties of Mars and they vary widely. In the southern hemisphere at about 14° S and between 320° and 360° W very large values are reported (up to about 48) and many of these are larger then 9.6. Does this mean there is water or ice in granular surface materials, or possibly iron-rich soils, or rock? Haystack reports a significant number of values above 4.0 which may be interpreted as rock. On the other extreme there are a large number of values of dielectric constants less than 2.5 and near 1.5 to 2.0. Are these due to low density loess unsuitable for landing or moving dispersed granular materials?

If the estimates of dielectric constants of Haystack are correct and the surface materials are dry, then there are few areas suitable for the Viking Lander (that is, areas with granular soils with 40% porosity and dielectric constants of 2.5 to 3.5. Additionally, the Mariner '71 IRIS experiment confounds the problem with their reports of a large range in silica content from place to place. Thus, further examination of the data needs to be made.

Preliminary estimates of dielectric constants obtained by the microwave radiometer aboard Russia's Mars 3 indicate a wide range of dielectric constants for the surface of Mars. They report values between 2.0 and 5.0. The lower number might represent porus, underdense loess while the higher one might represent rock.

The combined radar, radiometric, and visual interpretation of the imagery show that the surface of Mars is heterogeneous. Blowing fine micron-sized dust implies the presence of underdense dust, imaged sand dunes imply granular materials with 40% porosity are present, and both imply removal of material elsewhere to produce rocky lag gravels and bare rock surfaces.

4.1.3 Preliminary Slope-Frequency Distributions on Mars

Frequency distributions of slopes along a topographic profile (slopes computed over a constant base length, or L) and statistics reflecting central tendency and dispersion characteristics of these distributions are useful descriptors of planetary surface geometry. The procedures have been previously on both lunar and terrestrial terrains, and are extended to Mars in this report. The data presented here describe a sample of the whole planet; a more detailed areal breakdown can be prepared when required. This analysis has been done by R. J. Pike of the U. S. Geological Survey.

The Martian slope information discussed herein was generated from topographic elevations obtained by the Goldstone, California radar facility during the 1971 Martian opposition. The 9946 elevations furnished by Goldstone occupy a nearly continuous, approximately 0.75 km-wide belt around the planet; the data band is centered at about 15° south of the Martian equator. Thus, the information samples only about 0.6 of one percent of the Martian surface area. Generalizations from this small sample should of course be treated with the appropriate cautions.

The horizontal (east-west) distance separating the elevations is variable. The best resolution possible for the data is about 5.0 km. The mean distance between all contiguous elevations spaced less than 0.2° (11.8 km) apart is 7.15 km. Thus the largest-scale slope information can be obtained at a resolution of about 7 km.

For comparative purposes, Martian slope-frequency distributions were derived at three base lengths: 7.15 km, 23.69 km, and 94.8 km; the 7.15 km information being reduced by programmed calculations, and the remainder being obtained by hand calculations from elevation points printed out on 1:5,000,000 charts supplied by Goldstone. To assure a representative average slope length for the computer (7.15 km) data, slopes more than 11.8 km long were omitted; this procedure eliminated only about 200 slopes from the study. The remaining 8665 slopes were divided into those facing east (+) and those facing west (-), and an algebraic frequency distribution computed on 100 slope angle categories. The numbers of slopes in each slope angle class were accumulated and them divided by the total N. These procedures yielded the data in Figures 4-1 and 4-2, the histogram and the probability plot of algebraic slope. Similar calculations were run on the 7.15 km data without the algebraic constraint, resulting in Figures 4-3 and 4-4, the absolute slope histogram and the cumulative curve of the absolute slope-frequency distribution. Figures 4-5 through 4-8 and 4-9 through 4-12 are, respectively, similar results of manual calculations on the 23.69 km and the 94.8 km slope data. Table 4-2 summarizes some descriptive statistics for each of the three sets of Martian slope data. Figure 4-13 shows some of the Martian results together with roughly comparable lunar and terrestrial data.

Table 4-2. Martian terrain slope statistics

Slope Statistics (Degrees)	Slope Length (ΔL), km/Sample Size, N		
	7.15/8665	23.69/2052	94.8/363
Absolute Mean	0.38	0.20	0.15
Absolute Median (Est.)	0.29	0.28	0.14
Absolute Mode (Est.)	0.20	0.12	0.03
Maximum Slope	11.20 ?	3.50	0.78
Algebraic Standard Deviation (Est.)	0.38	0.36	0.21

Curves and histograms of the Martian slope data resemble results obtained for lunar and terrestrial data, save that the Martian surface may be somewhat smoother than that of the other two bodies. The algebraic slope data are, as expected, highly symmetric. The two 11° Martian slopes shown in Figure 4-1 may be real, although they are very steep for this base length. All three sets of Martian data are highly leptokurtic, i.e., they are peaked strongly at low slope values. This fact supports the common-sense hypothesis that steep slopes become increasingly scarce with increasing slope length. The low skewness and high kurtosis of the Martian data are

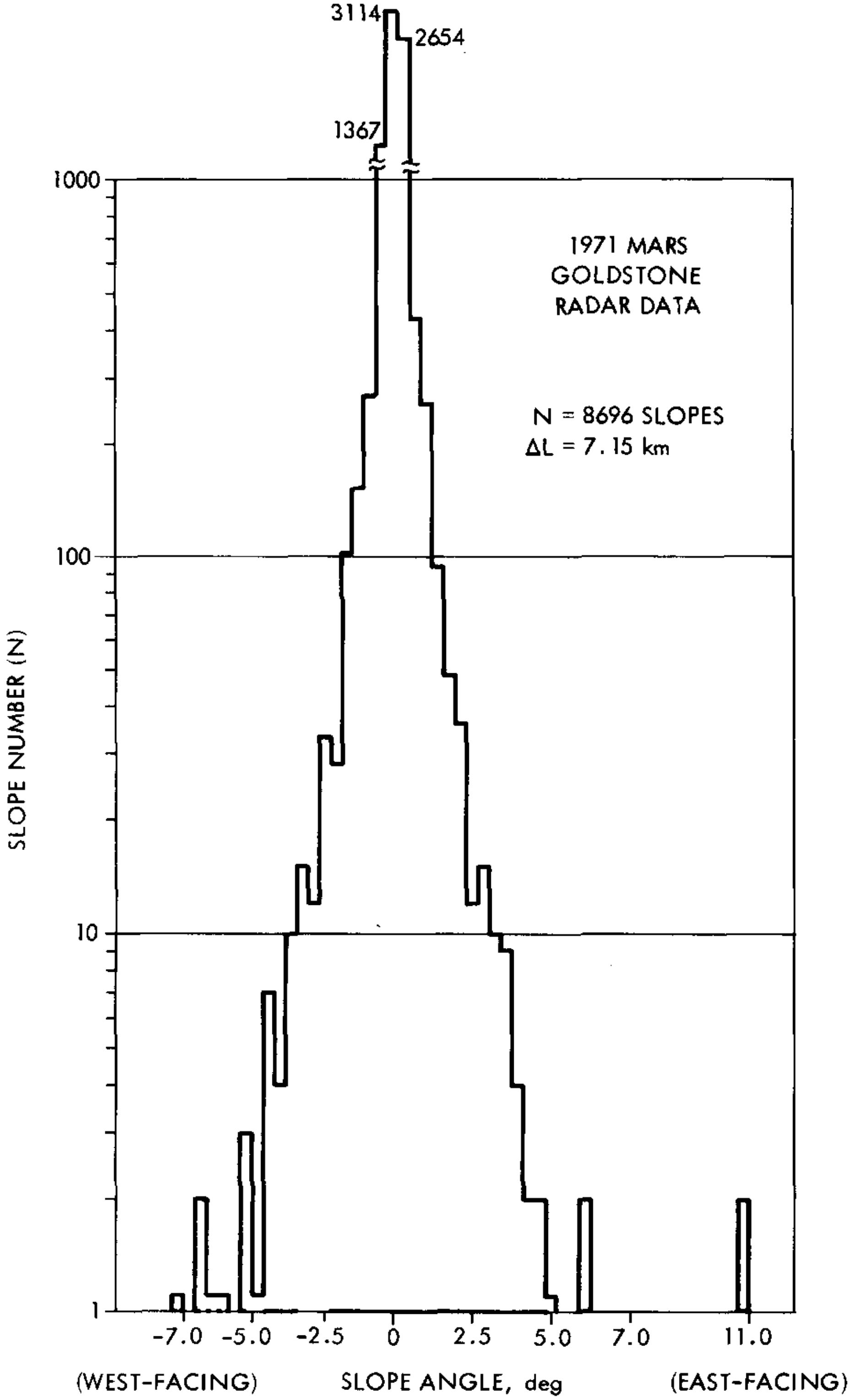

Figure 4-1. Histogram of algebraic slope angles (7.15 km baselength)

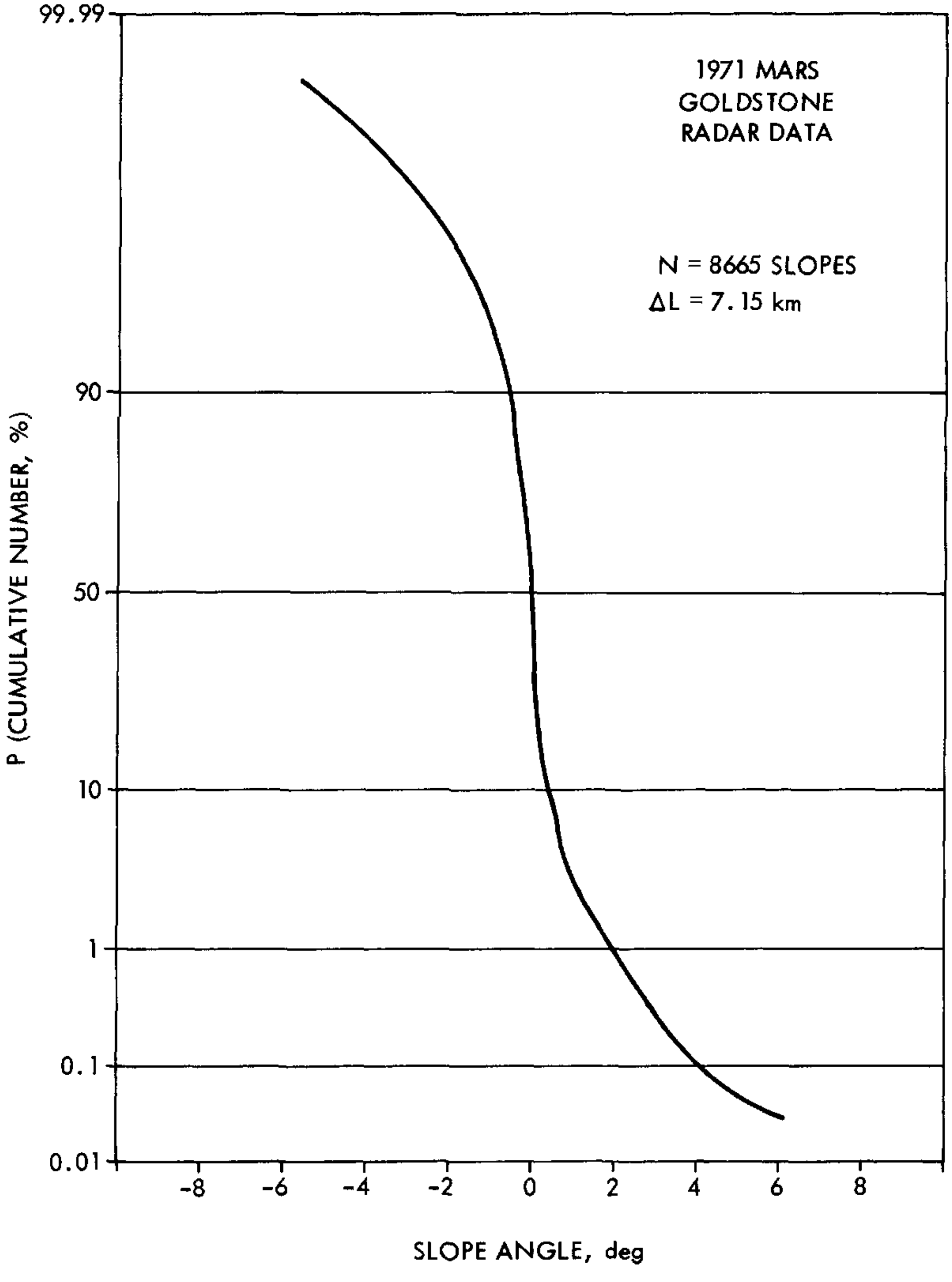

Figure 4-2. Probability distribution of algebraic slope angles (7.15 km baselength)

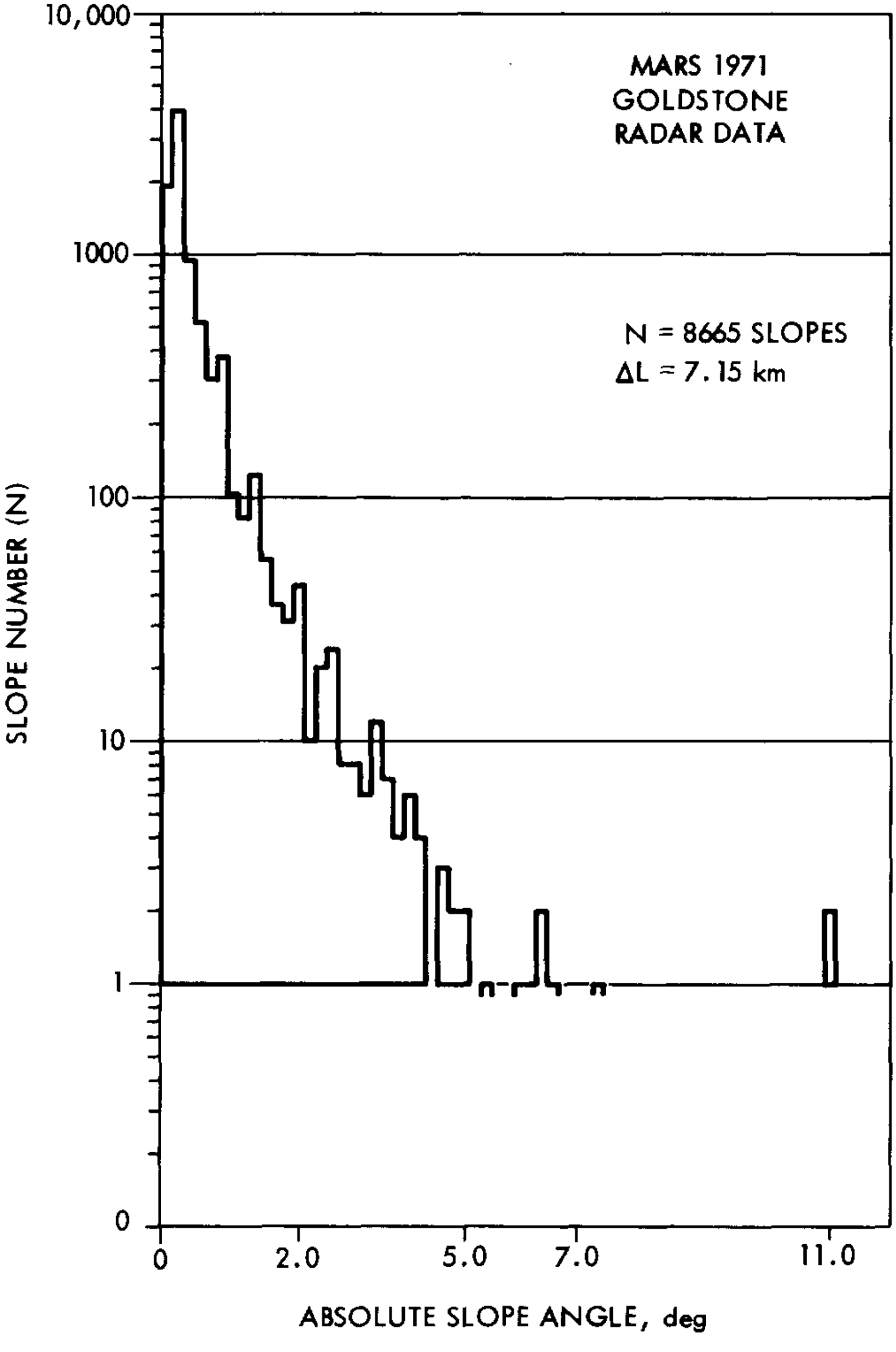

Figure 4-3. Histogram of absolute slope angles (7.15 km baselength)

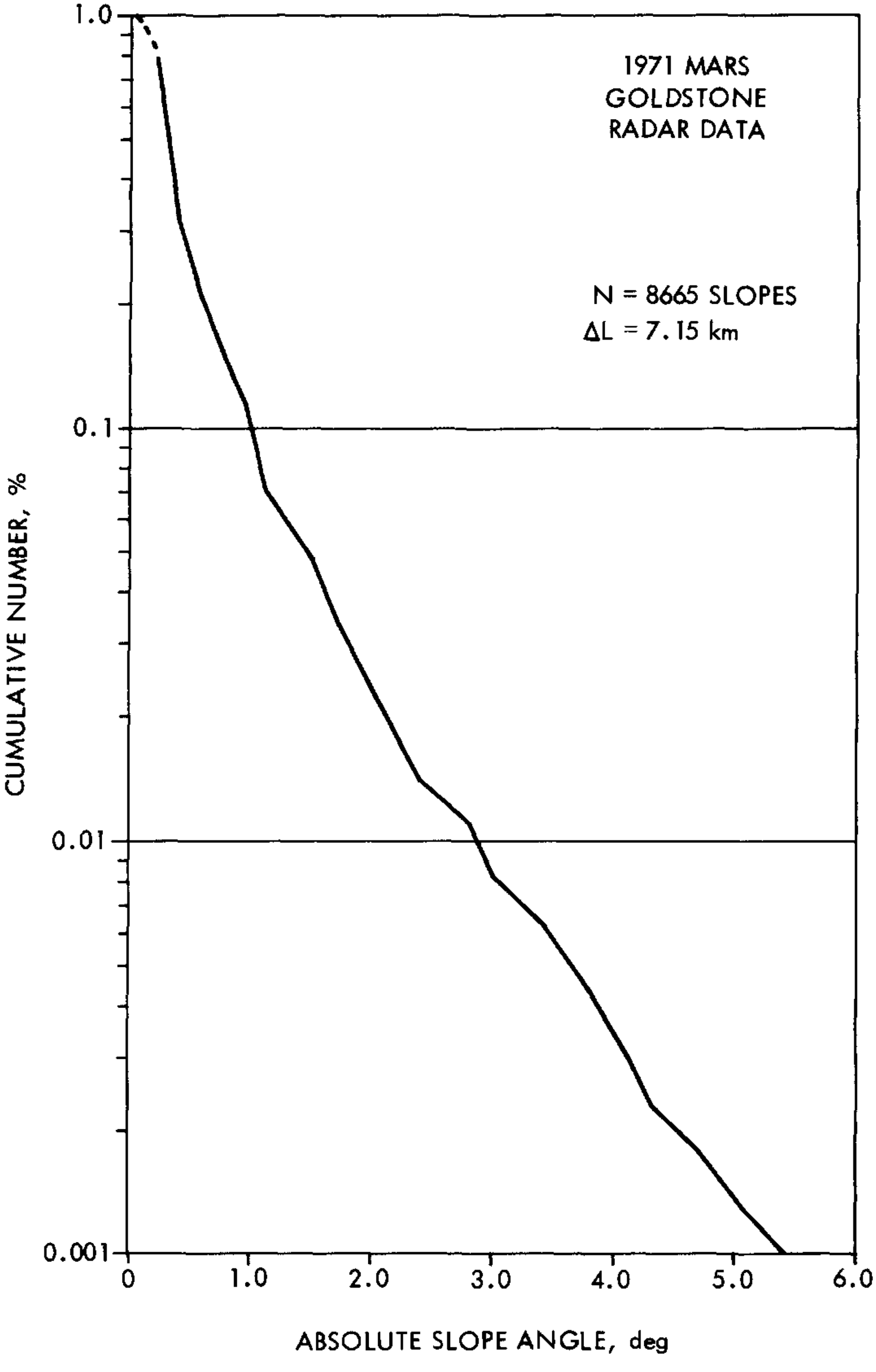

Figure 4-4. Probability distribution of absolute slope angles (7.15 km baselength)

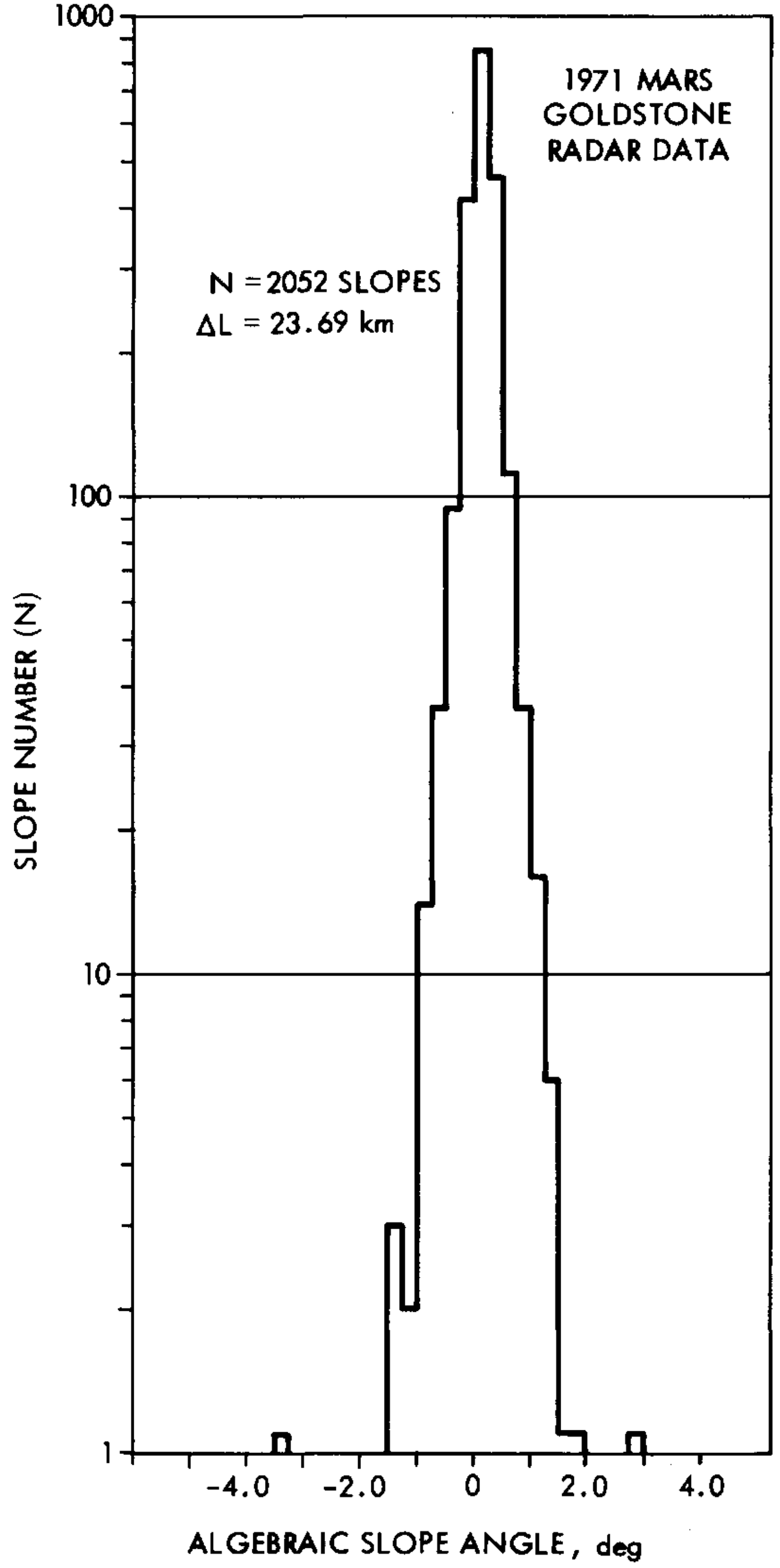

Figure 4-5. Histogram of algebraic slope angles (23.69 km baselength)

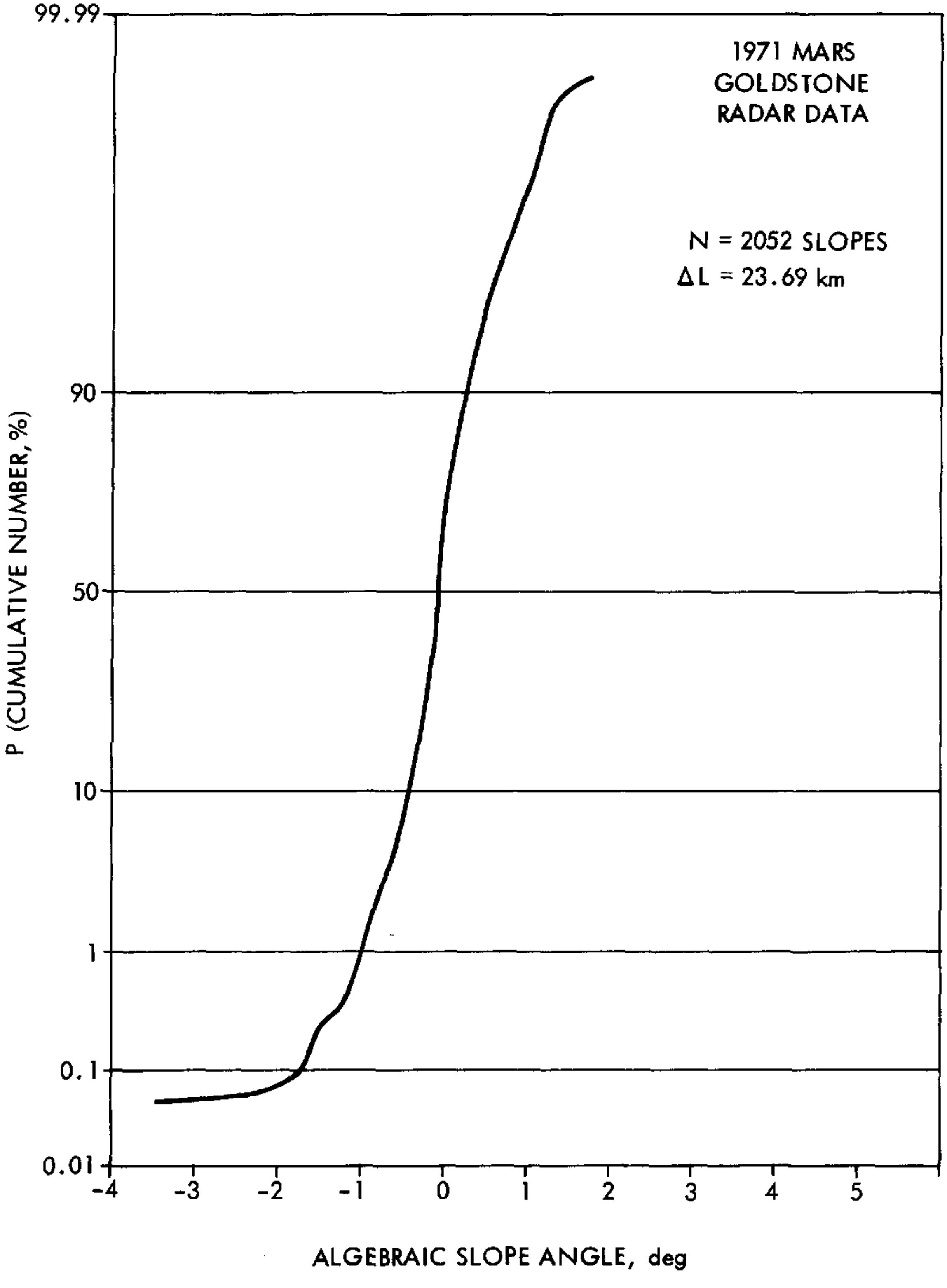

Figure 4-6. Probability distribution of algebraic slope angles (23.69 km baselength)

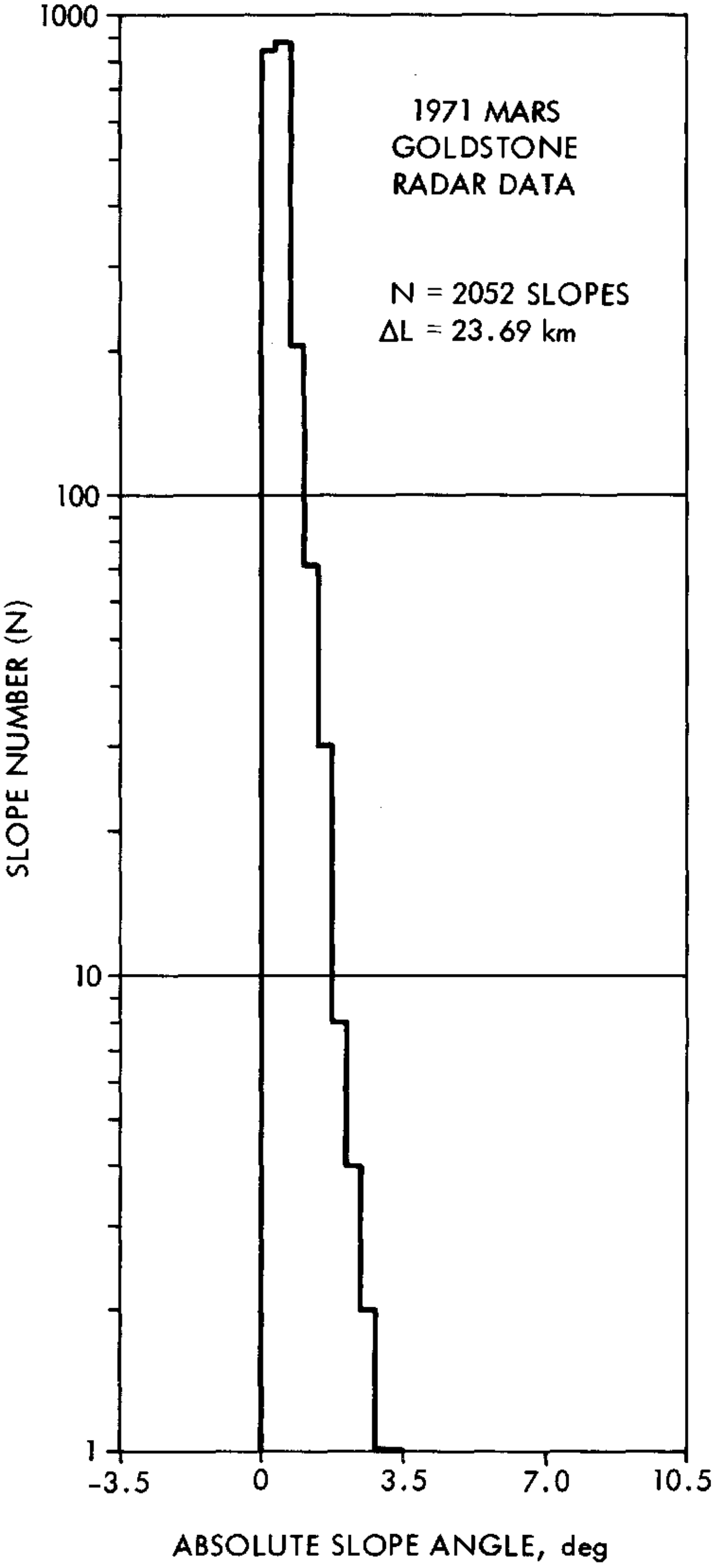

Figure 4-7. Histogram of absolute slope angles (23.69 km baselength)

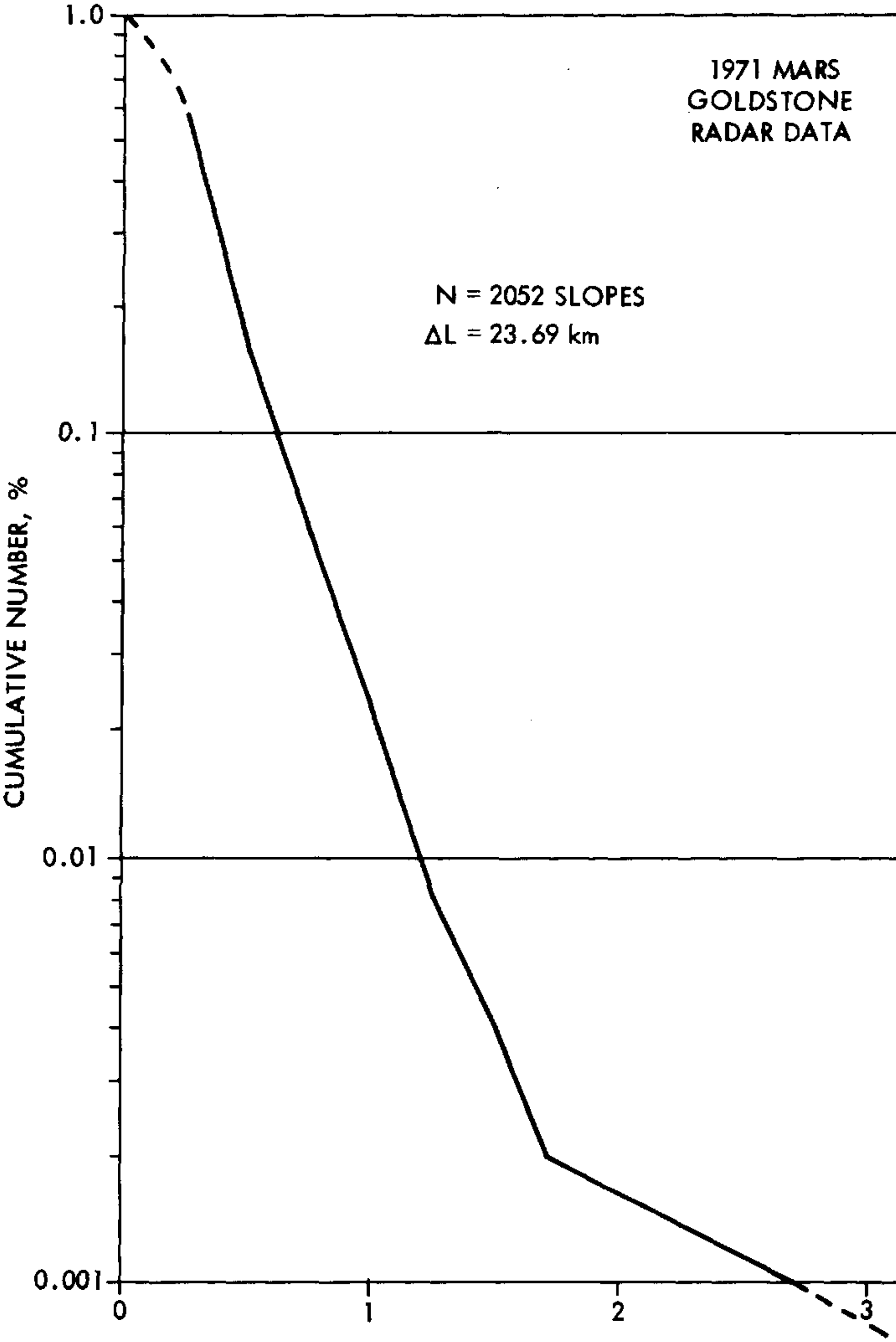

Figure 4-8. Probability distribution of absolute slope angles (23.69 km baselength)

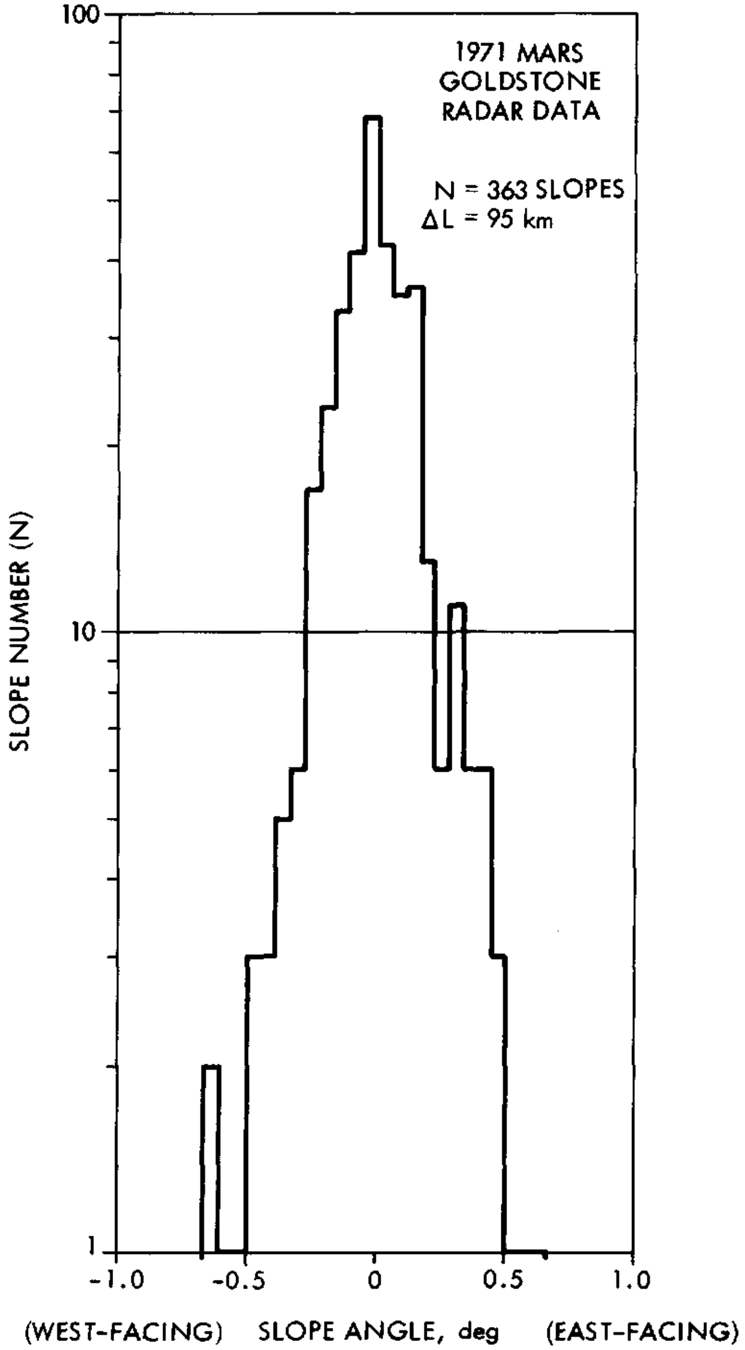

Figure 4-9. Histogram of algebraic slope angles (94.8 km baselength)

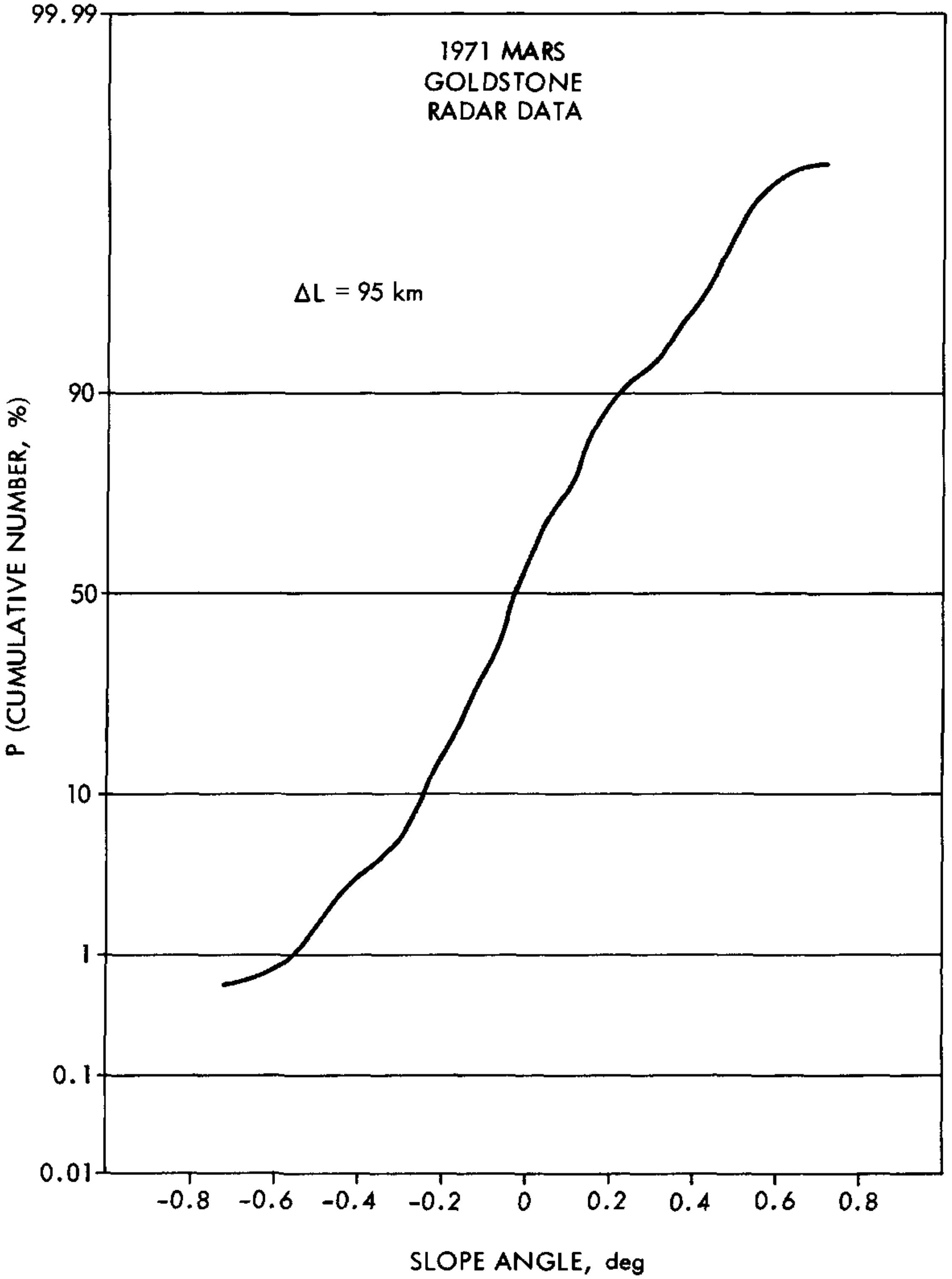

Figure 4-10. Probability distribution of algebraic slope angles (94.8 km baselength)

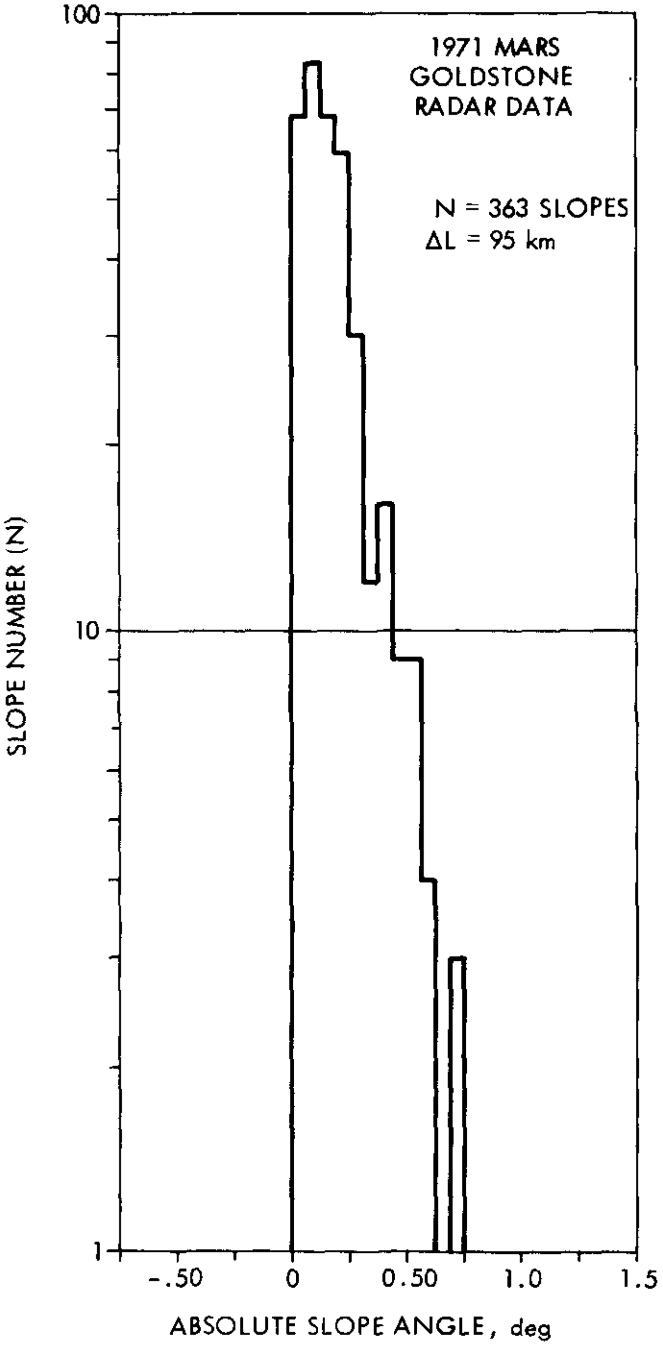

Figure 4-11. Histogram of absolute slope angles (94.8 km baselength)

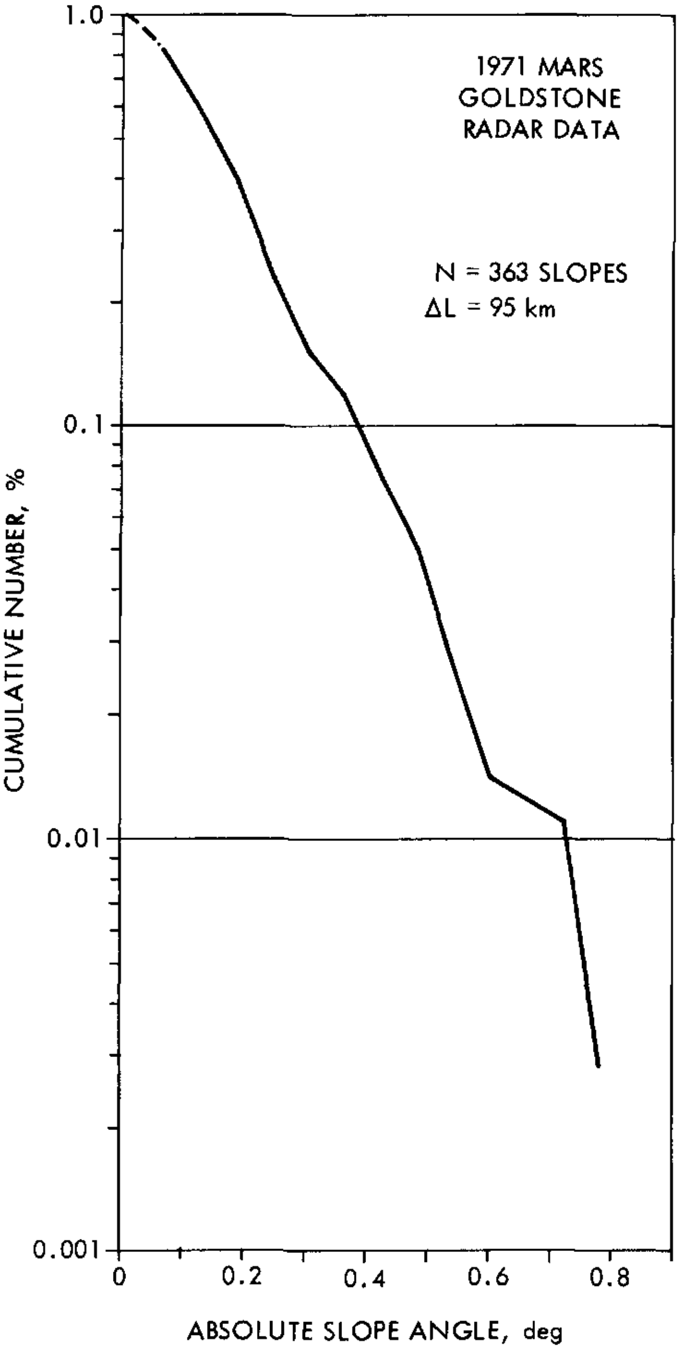

Figure 4-12. Probability distribution of absolute slope angles (94.8 km baselength)

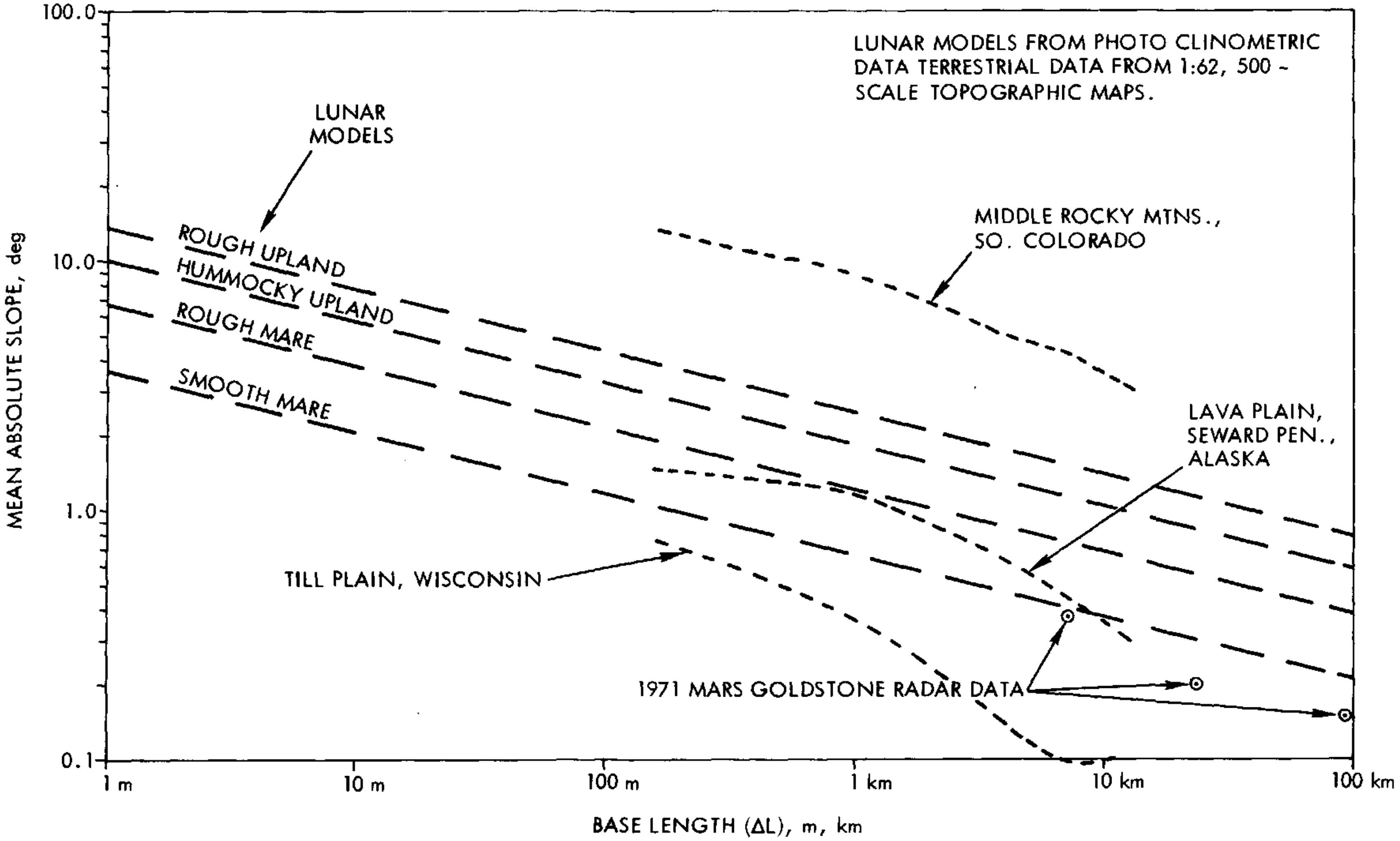

Figure 4-13. Comparison of lunar, terrestrial and Martian absolute slope angles as a function of baselength

obvious and statistics measuring these properties are not really necessary.

Table 4-2 and Figure 4-13 show the expected orderly decrease of Martian terrain roughness with increasing slope length. The data in Figure 4-13 also show that the Martian sample is smooth compared to possibly representative lunar and terrestrial terrains. The gentler Martian slopes could reflect data smoothing inherent in the radar scanning procedure; it could also be real. Projection of the Martian mean slope data to smaller slope lengths probably is not a simple linear extrapolation, as shown by the four lunar slope length models, but rather is a more complex, convex-upward trend such as represented by the three samples of real terrestrial data. Other lunar data (not shown) at smaller base lengths also exhibit a convex-upward trend.

4.2 TERRESTRIAL PHOTOGRAPHIC AND SPECTROSCOPIC OBSERVATIONS

Observable indicators of the atmospheric environment include water and other minor constituents, white cloud data, atmospheric motions, and various manifestations of dust. Much of our knowledge about these indicators still rests on Earth-based observations, but Mariner 9 results have been helpful in understanding atmospheric motions and dust, and additional analyses of the Mariner 9 data is expected to provide more knowledge of the atmospheric environment. Ideas concerning local wind velocities presently rest mainly on theory, although analyses of IRIS data should put such information on a firmer basis. In this section, a brief discussion of the results of some relevant earth-based photography and spectroscopic studies is presented.

4.2.1 Cloud Phenomena

From an analysis of Earth-based photographs, the distribution of white clouds on Mars has been studied in detail by Martin and Baum at the Planetary Research Center of Lowell Observatory. Martian white clouds large enough to be detected from the Earth were found to favor certain locations, to develop during the Martian afternoon, and to have a distribution that depends on season.

The initial survey of white cloud histories for the interval from 1907 to 1958 revealed some degree of correlation with west-facing slopes at high elevation, suggesting that they result from adiabatic cooling. In other words, the white clouds are evidently a condensate. Their daily motion was found to be slow, averaging no more than a few meters per second, as might be expected from the theoretical model of Leovy and Mintz. Local wind speeds, however, can be many times greater. Sagan, Veverka, and Gierasch have predicted local surface winds exceeding 80 meters per second.

A more recent Lowell study of the white cloud distribution for a particular season is represented in Figure 4-14. From a comparison of this diagram with the elevation map (Map 5), one can see that

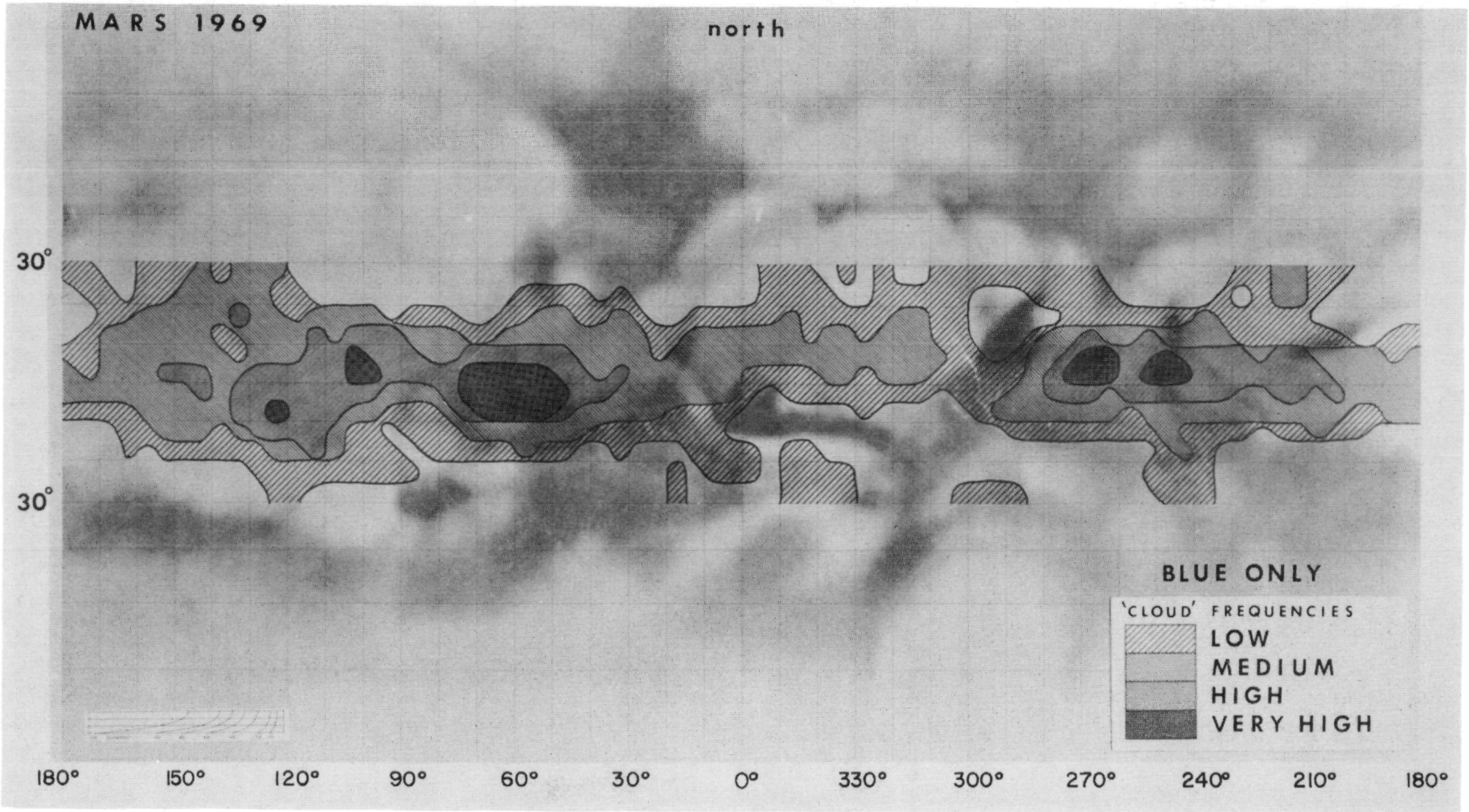

MARS 1969
north
30°
30°
BLUE ONLY
'CLOUD' FREQUENCIES
LOW
MEDIUM
HIGH
VERY HIGH
180°
150°
120°
90°
60°
30°
0°
330°
300°
270°
240°
210°
180°

Figure 4-14. White cloud frequency distribution on Mars (1969) Earth-based observations

some of the regions of medium or high cloud frequency do occur at relatively low elevation, i.e., white clouds are not exclusively associated with high regional elevations. It is therefore possible to find candidate landing sites that have white cloud occurrences as well as a high value of water vapor content. In this diagram the lowest to highest frequency categories span a factor of 10. "Very high" frequency means that afternoon clouds were detected in those regions on at least half of the days during the season (Martian "September") that was studied in 1969. The fact that these white clouds invariably build up during the Martian afternoon hints at the recondensation of water that was evaporated during the middle of the day.

Although global or semi-global dust storms tend to be associated with the season when Mars is near perihelion (just oppostie to the Viking season), there is evidence that the Martian atmosphere is somewhat dusty all the time. Mariner images require a lot more contrast enhancement to reveal surface features than similar images of Phobos do. Oblique images, like the one reproduced in Figure 4-15, show dramatically that murkiness of the atmosphere is responsible for this. Figure 4-15 was obtained after the dust storm had ended and mapping sequences were in progress; the camera was aimed at South Spot through several air masses, and no trace of the surface can be detected at all. This picture is significant, because enhanced vertical imaging of the same prominent surface feature gives the misleading impression that the view of the surface is relatively unobstructed by the atmosphere.

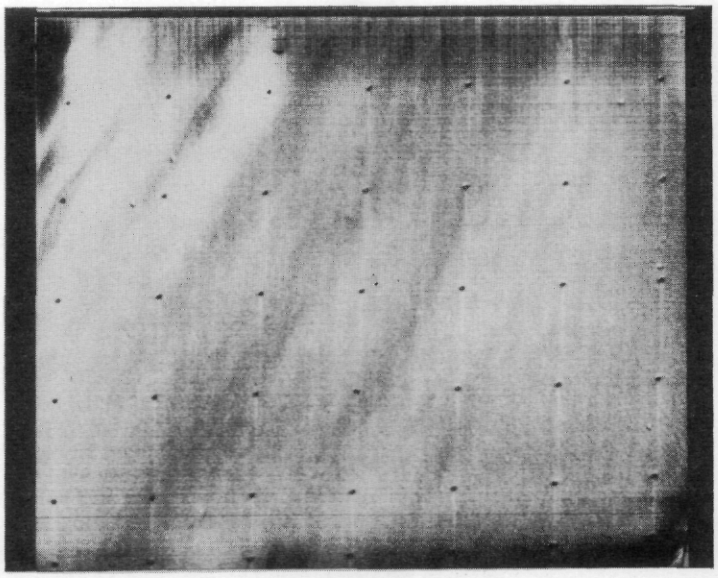

Rev. 154
Frame B
DAS 7109693
Center Point:
-11.9, 121.0

Figure 4-15. Oblique view of south spot through several air masses. This photo was obtained after the dust storm ended during the mapping sequences, and shows that surface features are still not distinguishable in oblique images because of remaining dust in the atmosphere.

What do we know about the regional and temporal distribution of this dust? Ordinary albedos may be a general clue. From Earth-based photometry, Boyce found that some light-colored areas tended to be variable in brightness, while darker areas were relatively non-variable. This result strongly hints that the light-colored areas may be characterized by the chronic stirring of dust near the surface, and it is not limited to the season of perihelion. More pronounced brightenings, identified as "yellow clouds," also occur regionally (but not globally) at scattered times in the Martian year. A survey of yellow cloud sightings was compiled by Wells.

Some of the particles, especially those raised during a global dust storm, may be relatively large (10 to 100 microns diameter) and short fallout times. From O'Leary's photometry of the opposition effect, however, Mead has shown that the principal scattering is probably due to smaller particles (on the order of 1-micron diameter). The existence of a continuous veil with long fallout times can thus be understood.

The vertical distribution of Martian dust is not yet directly known, but it is of importance to the Viking lander because it may limit the useful range of the lander camera. We have no assurance that all of the veil in Figure 4-15 is high above the surface. One clue concerning the amount of suspended dust near the surface can be inferred from the data in Figure 4-16. This shows a systematic diurnal increase in contrast between adjacent light and dark areas found at Lowell Observatory by Thompson. Since Boyce's data imply that the

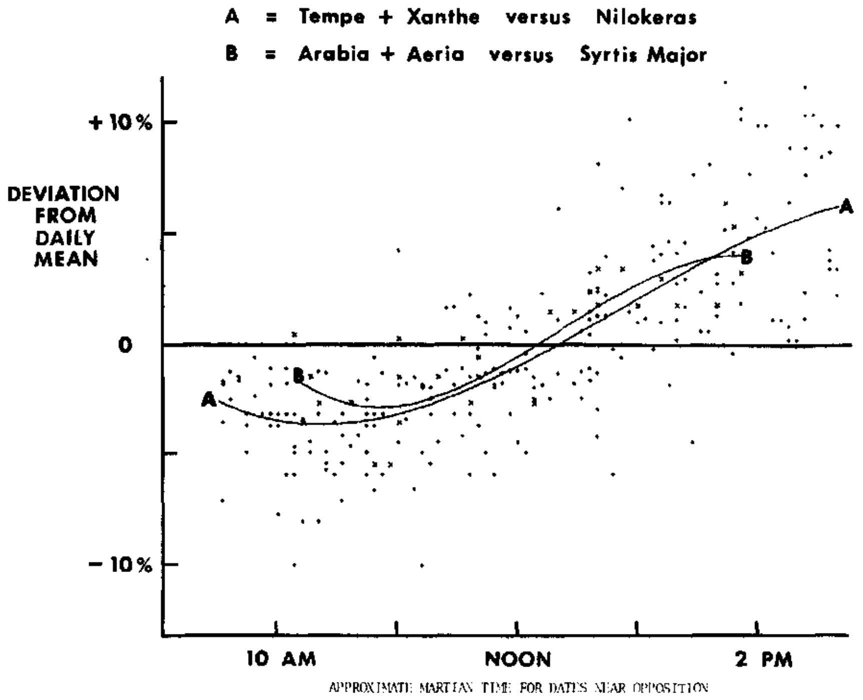

Figure 4-16. Diurnal increase in blue contrast (1969)

light areas are more variable than the dark, Figure 4-16 can be read approximately as a diurnal brightening of the light areas. If this is due to a midday raising of dust, then approximately an equal amount must settle each night so that the cycle can continue. Using scattering theory and fallout times, Baum has estimated the maximum horizontal visibility range to be only a few kilometers near the surface. This would be comparable with a very smoggy day in Pasadena when Mount Wilson is invisible.

4.2.2 Spectroscopic Studies

Earth-based spectroscopic studies and some recent OAO-II investigations have provided new data regarding the composition of the Martian atmosphere. Evidence for CO has been presented by Connes, as well as determinations of isotopic ratios of carbon and oxygen. OAO-II observations have indicated the presence of a broad absorption feature near 2600 Å that may be due to either ozone or carbon suboxide. The presence of oxygen by Barker and by Traub and Carlton has also been established recently.

Much attention has been placed on water vapor determinations with respect to abundance estimates, and to its latitudinal and seasonal dependence. Numerous studies have been attempted notably by Tull at McDonald Observatory.

More recent spectroscopic observations by Farmer's group at JPL indicated that the latitude distribution of water vapor in the Martian atmosphere depends on season. During the first few months after the Viking spacecraft arrives, about 40 micrometers of precipitable water above a site at an arbitrary elevation (6 millibars) may be expected in the latitude range between 10° and 30° north. This is the zone that receives maximum solar flux at that time. Elsewhere the amount of water vapor is evidently much less. The observed distribution of Martian water vapor with season is diagrammed in Figure 4-17.

As on Earth, the amount of water vapor per cubic centimeter in the Martian atmosphere probably decreases more steeply with elevation than the rest of the atmosphere does. This situation is diagrammed in Figure 4-18. The saturation line represents the maximum amount of water that the Martian atmosphere should theoretically be able to hold at various elevations during the daytime. It falls off steeply with height because of the dependence on air temperature. The observed amount of summertime water vapor corresponds to about 3 percent relative humidity at mean elevation. As on Earth, the relative humidity should not be greatly different at other elevations; therefore, one would expect the absolute amount of water vapor per cubic centimeter to follow the line marked "observed" in Figure 4-18. This means that one might expect as much as 400 micrometers of precipitable water above a landing site that lies four kilometers below mean elevation. Moreover, much of this 400 micrometers of water would be in the bottom kilometer and would be available for nighttime condensation at points where the temperature drops lowest. This may be favorable for biological organisms.

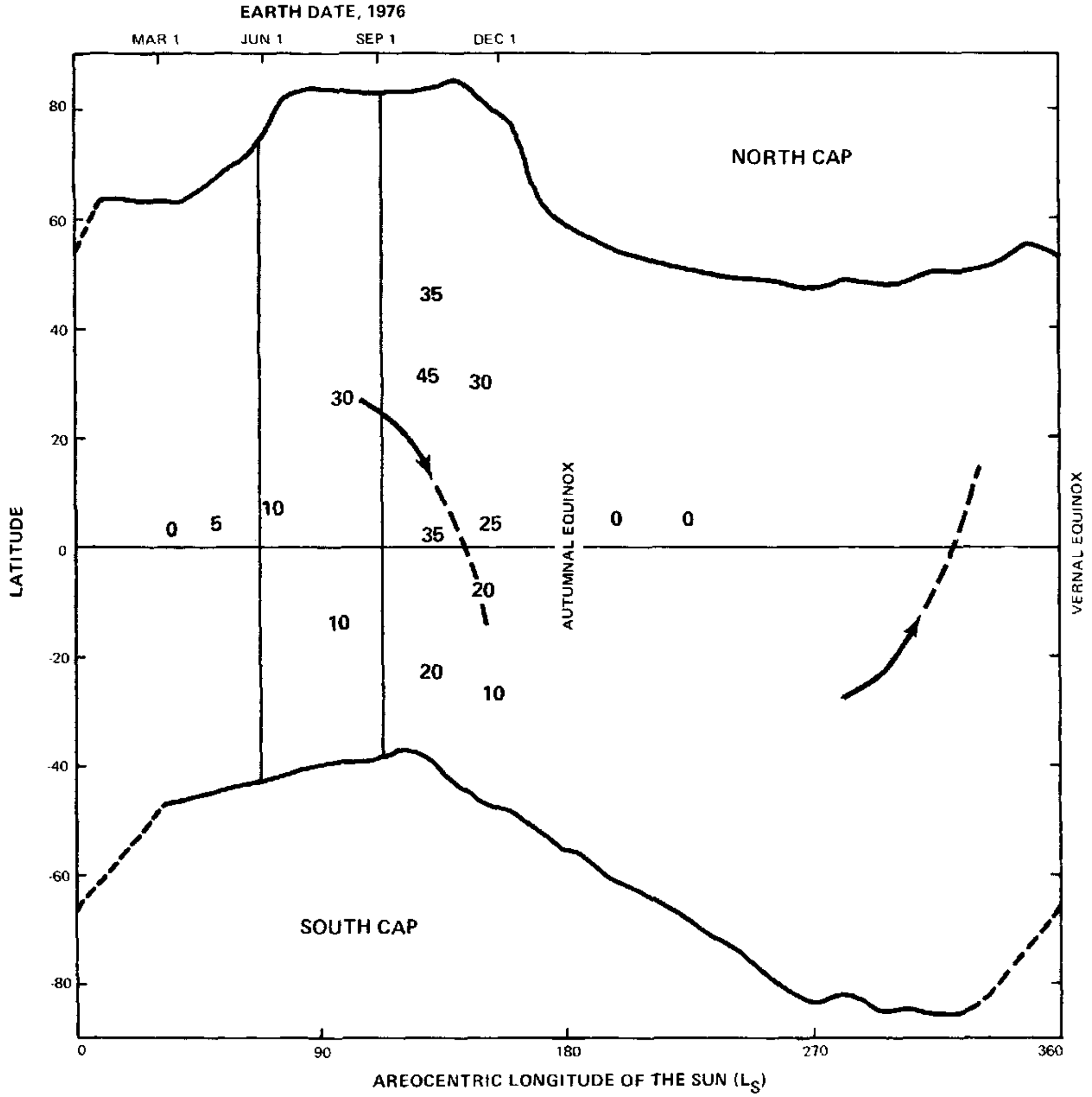

Figure 4-17. Earth-based observed seasonal distribution of Martian water vapor

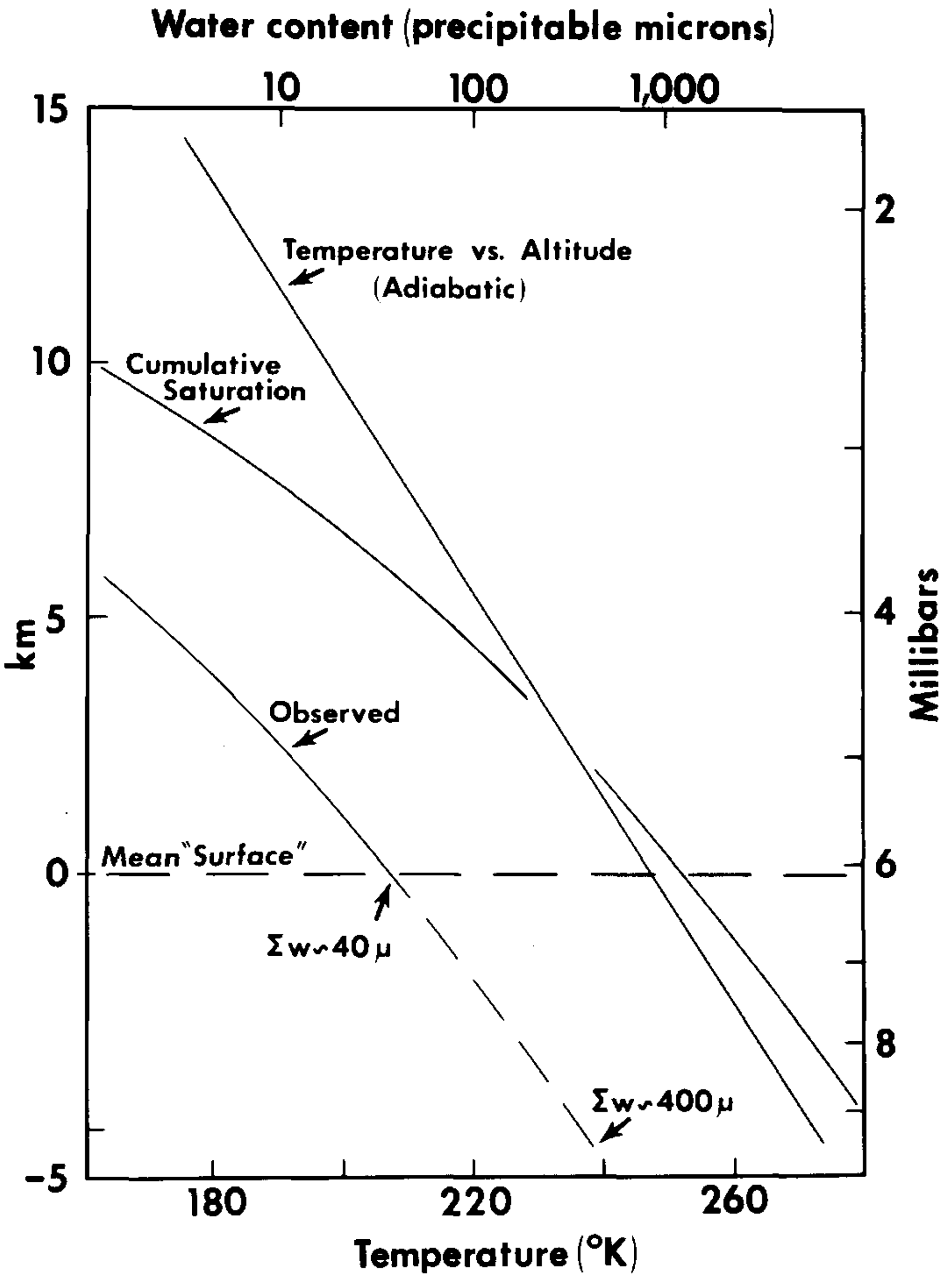

Figure 4-18. Suggested vertical distribution of Martian atmospheric water vapor

All of the above atmospheric constituents are of interest to Viking, and since some of them are not measureable with Mariner 9 experiments, further ground-based studies should be pursued to better establish their abundances in the Martian atmosphere.

4.3 REFERENCES

1. Cambell, M. J. and Ulrich, J., 1969, Electrical properties of rocks and their significance for lunar radar observations: Jour. Geophys. Res., v. 74, no. 25, p. 5867-5881.
2. Downs, G. S., Goldstein, R. M., Green, R. R., Morris, G. A., 1971, Mars radar observations, a preliminary report: Science, v. 174, no. 4016, p. 1324-1327.
3. Goldstein, R. M., 1972, unpublished data.
4. O'Handley, D., 1971, unpublished data.
5. Pettengill, G. H., 1972, unpublished data.
6. Pettengill, G. H., Rogers, A. E. E., Shapiro, I. I., 1972, Martian Craters and a scarp as seen by radar: Science, v. 174, no. 4016, p. 1321-1324.
7. Pike, R. J., 1969, unpublished data.
8. Pike, R. J., 1972, unpublished data.
9. Rogers, A. E., Pettengill, G. H., Shapiro, I. I., Ash, M. E., and Counselman, C. C., Radar Studies of Mars. Final Report, Lincoln Laboratory, MIT, January 15, 1970, Contract NAS9-7830.

5.0 MARINER 9 COVERAGE OF VIKING AREAS OF INTEREST

5.1 INTRODUCTION

During the extended phase of the Mariner 9 Mission beginning in the first week of June 1972, there was an opportunity to obtain specific coverage of areas of interest to Viking as potential landing sites. A compromise data budget was agreed upon to satisfy the Viking requirements and the various science disciplines of the Mariner 9 Mission. Initially, thirty-five targets were identified for coverage. R. Schmitz met daily in the SRT meetings to represent Viking to obtain the measurements of the targets. At the time of this report, planning for the first five weeks of the extended mission had been completed and data was to be acquired on nineteen of the initial set of targets. Mission constraints, viewing conditions and target priorities were considered in planning each week's data taking sequences and the net result was coverage of fewer Viking targets. In addition, the number of high-gain antenna (HGA) maneuvers for data acquisition were restricted, to assure the achievement of the Relativity experiment, and this resulted in approximately one-half the number of data taking opportunities that were considered in the initial planning. Control gas required for maintaining the spacecraft attitude was limited and initial estimates of gas usage allowed two HGA maneuvers per week for the first nine weeks. Later, estimates of the gas usage reduced these maneuvers to less than half the number considered in initial planning. At this time, it is marginal if any additional science data will be acquired after the fifth week of the extended mission, to assure that one gas bottle remains to control the spacecraft through superior conjunction.

5.2 DEFINITION OF ACCESSIBLE AREAS

To support the site selection planning for Viking targeting in the extended Mariner 9 Mission, areas accessible for Viking were identified. The area considered was the Viking Zone within the latitude band of ±30 degrees and the primary constraints used in identifying the accessible areas were elevation (pressure) and terrain (roughness). The elevation contour map prepared by A. Binder dated January 15, 1972 was used to identify the elevation limits. This map (Map 4) was prepared using primarily the earth-based radar data and the early occultation results. Section 3.2.4 discusses this map preparation in more detail. Using the atmospheric models defined in the Mars Engineering Model (MEM) dated April, 1972 the spacecraft entry and terminal descent constraints dictate that the landing areas must be within the elevation range of +3 km to -8 km. Because of the uncertainty in the data and correlation of the atmosphere models and the elevation data, the elevation limits were established at 0 km and -5 km. At the time the targets were being identified, a revision to the MEM atmosphere models was proposed. If the revised models are adopted, additional areas become accessible as shown in Map 8, a composite map identifying the accessible areas and Viking targets. Areas have been excluded because either the surface terrain is considered generally too rough or the elevation is either too high or too low. The unshaded areas are accessible. The areas shaded with horizontal lines never become accessible because of terrain or elevation constraints. The solid and dashed contour lines identify the elevation constraint limits. The solid line is the limit using the existing MEM (April 1972) atmosphere models. The dashed line identifies the elevation limit if the proposed changes to the MEM atmospheres are adopted, and the area shaded with dots then becomes accessible.

The Generalized Terrain Map (Map 2) was used to identify the terrain units that are accessible. The terrain units were correlated with the rms slopes and dielectric constant values to better define the terrain "roughness." This correlation by H. Moore is shown on Figures 5-1 and 5-2. The terrain units generally identified as too rough are Tablelands (Tc), Cratered Plains (PC), Irregular Hummocky (IR), Canyonlands (CL) and Domes (Dc). Optimum dielectric constants (considering soil properties for landing and surface sampling) are between 2.5 to 3.5 and rms slopes should generally be less than 5 degrees.

5.3 DEFINITIONS OF TARGET AREAS

A group consisting of some members of the Landing Site Working Group (LSWG) and Viking Data Analysis Team (VDAT) met at JPL on April 14, 1972 to identify areas of interest in the Viking Zone. The terrain and elevation maps discussed above were used in selecting the sites, along with the USGS photo-mosaics. In addition, when available, radar data on dielectric constant values and rms slopes were considered in selecting the targets. The science criteria, as presently defined, were also considered in selecting the targets and relevant areas were identified according to the (1) highest probability of water; (2) varied terrain and geology; (3) terrain "contact" areas; (4) regions of high white cloud frequency; (5) areas where fluid or fluidized erosion seems to have occurred. Thirty-five areas were identified as targets, and additional data on these areas were compiled for the LSWG meeting on April 25, 1972. The data and target areas were reviewed at the LSWG meeting. A spacecraft sun occultation constraint was identified which effected targets above 25°N latitude and targets above this latitude were relocated to meet this constraint. The targets were then reviewed and prioritized; this is discussed in more detail in the minutes of the April 25th LSWG meeting. The targets were subsequently reviewed considering additional information and constraints, and thirty-three targets were finally identified for coverage. Table 5-1 lists the thirty-three targets. They are located on a composite terrain and elevation map (Map 8). Table 5-1 also lists some of the criteria used in selecting the targets. As the data from Mariner 9 for each of these targets becomes available, more detailed analysis is required to better identify the characteristics of the areas.

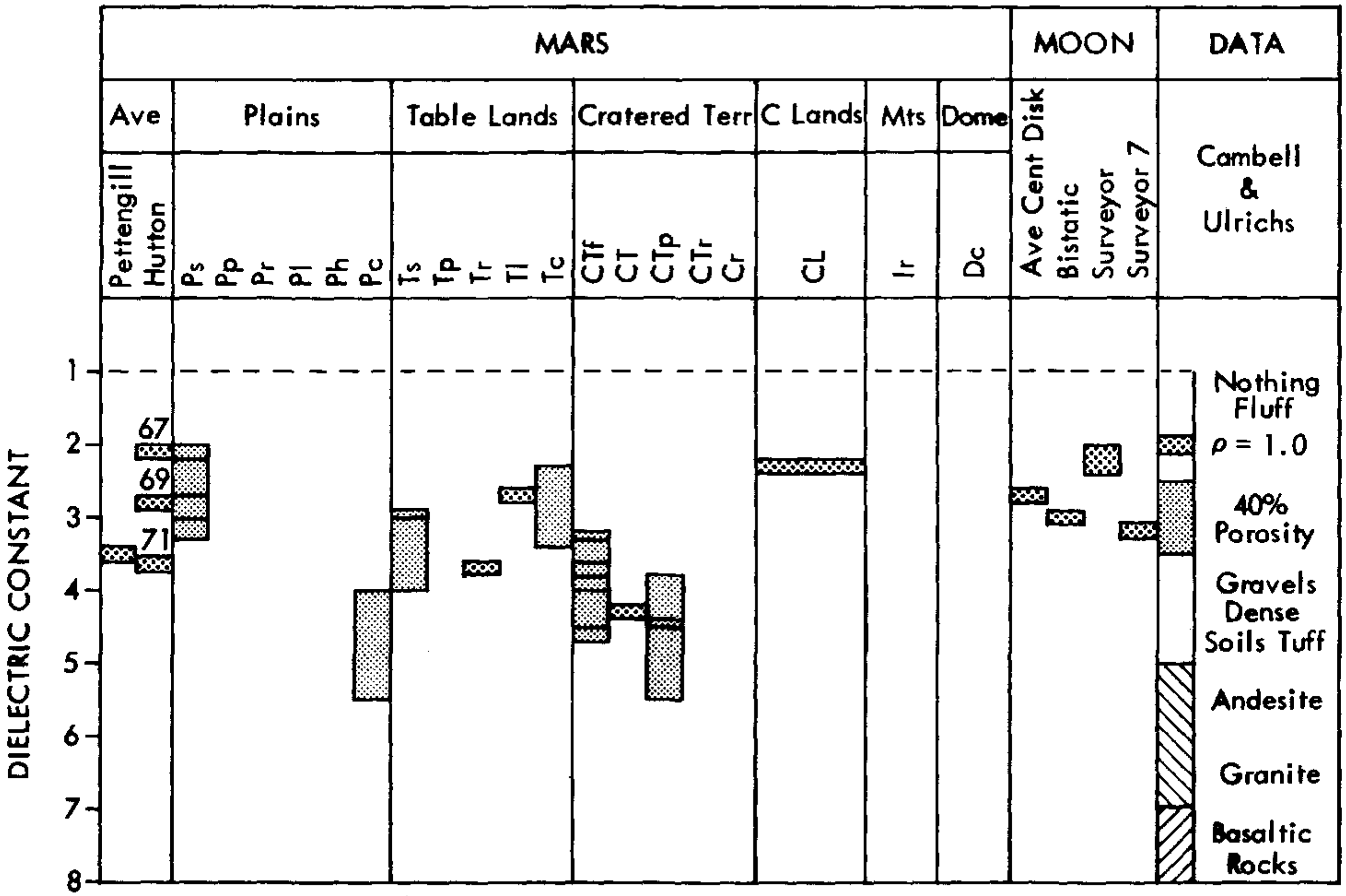

No Values Shown Where Number Of Samples Are Limited

Figure 5-1. Correlation of Mars radar dielectric constant values with the various Martian terrain units

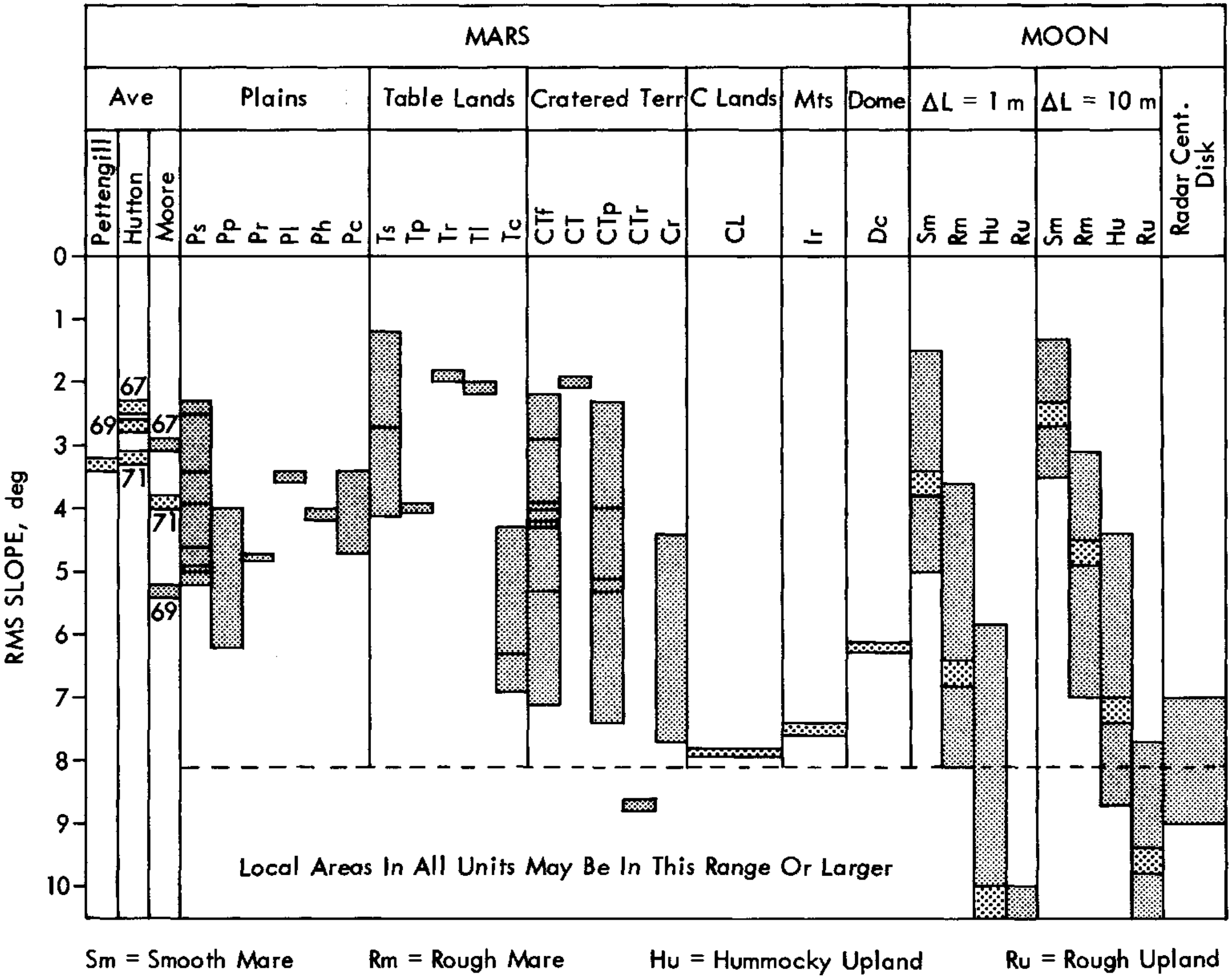

Figure 5-2. Correlation of Mars radar rms slope with the various Martian terrain units

Table 5-1. Summary of Viking target sites

Site No	Lat. (Deg)	Long. (Deg)	Elevation (KM)	Dielectric Constant	RMS Slope (Deg)	Albedo*	Cloud Frequency*	Wind Pattern	Terrain	Identifying Characteristics
T-1	-15.0	5.9	$-5 < h < -4$	2.5 - 3.5	2.0 - 5.0	Medium	Low		CTf adjoined by CTp	Optimum dielectric constant
T-2	+22.0	27.0	$-3 < h < -2$	(2.0 - 4.0)	(2.5 - 6.0)	Dark	Very Low		Ps adjoined by Tc & Ph	Smooth area adjacent to prominent Scarp and cratered plateau
T-3	+21.6	40.0	$-3 < h < -2$	(2.0 - 4.0)	(2.5 - 6.0)	Dark	Very Low		Ps	High water vapor according to ground-based spectra
T-4	+18.6	34.0	$-2 < h < -1$	(2.0 - 4.0)	(2.5 - 6.0)	Medium	Low		Ps adjoined by Tc, CL, Ts	Plains region near plateau
T-5	-21.4	44.5	$-3 < h < -2$	(2.0 - 4.0)	(2.5 - 6.0)	Dark	Very Low		Ps and CTf adjoined by Ts	Plateau near Red River
T-6	- 2.0	63.7	$0 < h < 1$	(2.8 - 3.9)	(1.1 - 4.0)	Light/Dark	Very High		Ts adjoined by CL, Tc	High frequency of white cloud occurrence according to ground-based data
T-7	-18.2	76.3	$-1 < h < 0$	2.5 - 3.5	1.8 - 2.3	Medium	Low		Tr adjoined by Ts	Optimum dielectric constant
T-8	+21.5	75.5	$1 < h < 2$	2.0 - 4.0	2.5 - 6.0	Light	Very Low		Ps adjoined by Ts and CL	Plains near mount of large channel
T-9	-20.5	142.5	$-2 < h < -1$	(2.0 - 4.3)	(2.5 - 6.0)	Light	Very Low		Ps and CT	Plains near normal faults
T-10	- 2.5	147.0	$-3 < h < -2$	(2.0 - 4.0)	(2.5 - 6.0)	Light	Medium		Ps adjoined by CT	Plains at mouth of braided channel
T-11	+ 4.0	152.0	$-3 < h < -2$	2.0 - 4.0	2.5 - 6.0	Light	High		Ps adjoined by CT	High frequency of white cloud occurrence according to ground-based data
T-12	+23.0	153.0	$-1 < h < 0$	2.0 - 4.0	2.5 - 6.0	Light	Low		Ps adjoined by Ir	High water vapor according to ground-based spectra
T-13	+ 5.5	164.3	$-4 < h < -3$	(2.0 - 4.0)	(2.5 - 6.0)	Light	Medium		Ps adjoined by CT	Plains near mesas and channels
T-14	-11.3	169.0	$-4 < h < -3$	2.5 - 3.5	2.5 - 4.6	Light	Very Low		CT adjoined by Ps	Optimum dielectric constant
T-15	(Deleted)									
T-16	- 7.0	187.0	$-5 < h < -4$	(2.0 - 4.0)	(2.5 - 6.0)	Light	Medium		Ps adjoined by Dc, Ph, CT, Pp	Caldera flank
T-17	- 3.0	191.0	$-5 < h < -4$	(2.0 - 4.0)	(2.5 - 6.0)	Light	Medium		Ps adjoined by Pp, Pc	Plains
T-18	- 2.0	203.0	$-5 < h < -4$	(2.0 - 4.0)	(2.5 - 6.0)	Light	Medium		Ps and Pc adjoined by Ir	Plains
T-19	+ 8.0	207.0	$-2 < h < 0$	2.5 - 3.5	2.5 - 6.0	Light/Dark	Medium	V. Feature	Ps	Optimum dielectric constant
T-20	+ 8.0	215.0	$-2 < h < 0$	2.0 - 4.0	2.5 - 6.0	Medium	High	V. Feature	Ps	High water vapor according to ground-based spectra
T-21	+ 1.3	221.4	$-3 < h < -1$	2.0 - 4.5	2.5 - 6.0	Light	Medium		Ps adjoined by Tl, Ts	Smooth plains adjoining hummocky terrain
T-22	-14.0	230.0	$-2 < h < -1$	2.5 - 3.5	2.5 - 4.6	Dark	Very Low		CT adjoined by CTp	Optimum dielectric constant

NOTES:

(1) Parentheses ( ) indicate generalization; data not available.

(2) *Source of data are ground-based observations
*Albedo values are for Viking Season

Table 5-1. Summary of Viking target sites (Contd)

Site No	Lat. (Deg)	Long. (Deg)	Elevation (KM)	Dielectric Constant	RMS Slope (Deg)	Albedo*	Cloud Frequency*	Wind Pattern	Terrain	Identifying Characteristics
T-23	+21.5	232.5	0 < h < 1	(2.0 - 4.0)	(2.5 - 6.0)	Light	Very Low		Ps adjoined by Pp	Channel with "islands" in plains
T-24	+21.0	245.0	-1 < h < 0	2.0 - 4.0	1.8 - 6.0	Light	Very Low		Ps	High water vapor according to ground-based spectra
T-25	+16.0	250.0	-1 < h < 0	(2.0 - 4.0)	(2.5 - 6.0)	Light	Very Low		Ps adjoined by Pp	High water vapor according to ground-based spectra
T-26	-22.0	251.0	-2 < h < -1	------	(3.8 - 4.3)	Dark	Low		Pr adjoined by CTp, Dc	Dandelion crater - volcanic caldera
T-27	+21.0	251.0	-2< h < -1	(2.0 - 4.0)	(2.5 - 6.0)	Medium	Very Low		Ps	High water vapor according to ground-based spectra
T-28	+ 1.9	253.4	-1 < h < 0	(2.1 - 4.5)	(2.0 - 5.0)	Medium	Very High		CTf adjoined by CTp and Ir	High frequency of white cloud occurrence according to ground-based data
T-29	+22.0	264.0	-1 < h < 0	(2.0 - 4.0)	(2.5 - 6.0)	Dark	Very Low		Ps	High water vapor according to ground-based spectra
T-30	+ 6.2	268.8	-2 < h < 0	2.0 - 4.0	2.5 - 6.0	Dark	Very High		Ps adjoined by Ir	High frequency of white cloud occurrence according to ground-based data
T-31	+10.0	275.0	-2 < h < -1	2.5 - 3.5	2.5 - 6.0	Dark	Med/High	Near V. Feature	Ps adjoined by Ir, Pc	Optimum dielectric constant
T-32	-17.5	288.3	-4 < h < -2	2.4 - 4.6	4.0 - 5.3	Dark	Very Low		CTp adjoined by Ir	Upland, smooth intercrater area
T-33	(Deleted)									
T-34	-16.0	331.8	-1 < h < 0	2.1 - 4.5	2.0 - 5.0	Light	Very Low		CTf and CT adjoined by CTp	Smooth area with high dielectric constant
T-35	-17.4	350.2	-3 < h < -2	2.1 - 4.5	2.0 - 5.0	Light	Very Low	Near V. Feature	CTf adjoined by CTp and Ps	Smooth area with high dielectric constant

NOTES:

(1) Parentheses ( ) indicate generalization; data not available.

(2) *Source of data are ground-based observations
*Albedo values are for Viking Season

5.4 TYPE AND EXTENT OF COVERAGE

The type and extent of coverage for each target was identified by the LSWG. High resolution photographic coverage (with 3 to 4 B-frames per target) along with a low-resolution A-frame was defined as the desired photographic coverage. In obtaining the photo-coverage, low emission angles are desired, preferable 0° to 20°, with 35° as an acceptable upper limit. When possible, both ultraviolet and infrared spectral data is to accompany the photographic coverage. Stereo coverage, although desired, was not obtainable because of the mission constraints, target problems, and limited photo budget. Separate B-frames were initially targeted to cover the lander ellipse (240 km by 45 km) and the coverage was subsequently revised to provide contiguous photographing of the center of the ellipse.

6.0 CONCLUSIONS AND RECOMMENDATIONS

6.1 SUMMARY AND IMPLICATIONS FOR VIKING

In the previous sections, a summary of some of the impressive conclusions and scientific highlights of the Mariner 9 mission to date has been presented. While significant gains have been indicated in many areas of Martian data, significant gaps and inconsistencies still exist. In this section some of these gaps and inconsistencies will be indicated, some implications of Mariner 9 results for Viking and the MEM summarized, and a list of recommended follow-on studies presented.

Some implications for the Viking lander regarding terrain analysis of Mariner 9 TV data may be enumerated here. Large portions of the Martian surface appear to be particularly inhospitable to landers. The surface is heterogeneous at all scales, exhibiting a wide range of topographic and geological features. Some surfaces appear too rough or too porous for landing, or too hard or cohesive for sampling of the soil. Three terrain types have been identified which represent excessive engineering risks for a lander. These are the Irregular Terrain, the Canyonlands, and the Domes. Most of the cratered terrain occurs in the southern hemisphere while the smooth plains appear in the north. Locally, the plains appear to be at lower elevations.

Other implications for Viking are concerned with potential revisions of the Viking MEM. Significant revisions in the MEM should most likely occur, for example, in the following areas:

1. Higher and more frequent winds, including topographic and diurnal effects, and the extensive transport of particulate material.
2. Physical properties of the surface, especially regarding the composition and thermal characteristics.
3. Extensive terrain analyses available, especially for site selection work.
4. Topographic effects on surface atmospheric pressure, cloud occurrence, wind fields and the gravity field of the planet appear to be more significant than in the MEM data.
5. Improved tracking and orbital data obtained by Mariner 9, especially the improved pole determinations, dynamical figure and astronomical unit.
6. Improved atmospheric models capable of including the severe disturbances due to the presence of atmospheric dust.

As mentioned earlier, some inconsistencies, both internal and external to various Mariner 9 experiments have been noted. It is important to resolve these discrepancies by intensive analysis as quickly as possible.

The physical shape of the planet is not accurately determined as yet. Although the S-Band occultation and the Celestial Mechanics results appear in substantial agreement, discrepancies between terrestrial radar data and location of Martian surface features exist. Furthermore, sizeable targeting errors have resulted from the lack of an accurate grid during acquisition of the regular mission sequences and in the attempts to construct 1:5, 000, 000 terrain maps.

The topographic mapping is presently in an unsatisfactory state. Large differences between the UVS and IRIS data have been indicated. Furthermore, large and small scale asymmetries appear in UVS topographic scans. All data need to be adjusted or normalized to the same mean reference level. Radar elevations also appear to be systematically displaced, but this could be due to radar reductions based on old ephemeris data.

Recent analyses by UVS have indicated the presence of ozone in the polar regions, confirming the detection by Mariner '69. Recent ground-based observations have indicated the presence of oxygen in amounts which appear to be inconsistent with the inferred UVS ozone amounts. The resolution of this problem, by either improved photochemical studies, or by repeated and more accurate abundance estimates, should be closely pursued by Viking.

6.2 RECOMMENDED FOLLOW-ON STUDIES AND ANALYSES

As a result of reported results to date and VDAT involvement with some of the Mariner 9 data and results, some recommendations for future analyses or follow-on studies are offered here. Some of these suggestions may already be incorporated in the overall analysis plan of the Mariner 9 team investigators, but some may be feasible for undertaking by other groups, and may assist in resolving some of the current inconsistencies and discrepancies. We would like to propose the following list of studies, which may be periodically updated:

1. A continuing effort should be effected to reduce the tolerances on all Martian environmental properties. In this regard, a comprehensive survey and analysis of the UVS and IRIS data should be undertaken to yield the best lower and upper atmospheric models. This is essential for improving and updating the atmospheric models in the MEM.

2. A brief comparison of some elevation and pressure mapping has been discussed above from preliminary and limited data. These clearly indicate problems that must be resolved to provide the best, most reliable and most consistent mapping

possible. We strongly suggest that a complete and careful analysis of all of the various data available for topographic and surface pressure mapping be vigorously pursued.

3. A comprehensive study of surface temperature mapping, which includes the dependence on diurnal, seasonal, latitudinal, and surface albedo effects is required. Analysis of data from IRIS and IRR should provide definitive determinations of the surface thermal properties such as the thermal inertia parameter and emissivity. Furthermore, the relation and inference of these quantities to surface composition, to the compositions inferred from IRIS restrahlen analysis, and their relation to soil models can be exploited, particularly with reference to the global surface composition distribution. These items are of particular importance to Viking site selections.

4. A thorough analysis of earth-based radar data for determination of surface properties such as bulk density, block distributions, slope distributions, dielectric constants and their relation to other surface thermal and physical properties, as well as terrain types should be done. Although much effort has been directed at the radar data, the full effectiveness of the results and their impact on the knowledge and understanding of the Martian surface have not yet been felt.

   Specifically, terrestrial radar estimates of surface dielectric constants should continue to be acquired along with the Russian dielectric constant data obtained from Mars 2 and 3. Each of these should be checked for internal and external consistency.

   Evidence for near surface water or soil moisture should be investigated, especially at the locations indicating very large dielectric constants obtained by Haystack Observatory. Other areas exhibiting frosted crater rims or terrain features characteristic of permafrost, should be carefully examined.

   Furthermore a test of the very low values of dielectric constants obtained by Haystack in the smooth plains regions for moving dust may be possible.

   Finally, additional radar estimates of slope frequency distributions and their relation to terrain types are also recommended. These may be compared with other values of slopes estimated by possible photogrammetry, IRR thermal measurements or possibly UVS determinations.

5. The evidence, to date, indicates that the mechanical properties of the surface of Mars vary in time and location. Blowing dust seen early in the MM'71 mission, wind tails around craters and other obstacles, sand dunes seen in the imagery, Haystack and Russian data on dielectric constants indicate extreme variations in physical properties of the Martian surface. If the surface materials are dry, then rock, lag gravel, sand,

and low density loess are clearly present. The distribution of such materials is important to Viking because of spacecraft limitations. The spacecraft cannot land successfully on low density loess or coarse lag gravels. Additionally, it cannot sample rock and coarse lag gravels, so that extremely careful analyses of data indicative of soil mechanical properties should be pursued. Furthermore, it is suggested that a provision be made for a photographic analysis of the initial soil sample obtained by the Viking Lander by the Physical Properties Team, theLander Imaging Team, and the Biology and GCMS Teams, to assess the suitability of the sample before internal processing is initiated.

6. An accurate geodetic grid indicating surface features in precise planetary coordinates and elevations remain to be completed by the Mariner 9 TV team. The resolution of this gap by the cartographic team should be carefully followed.

7. More extensive and detailed terrain maps should be constructed with special emphasis on previous lunar and terrestrial experience to delineate and characterize rough areas. More extensive use of high resolution B-frames should be attempted.

8. Upon completion of the Mariner TV coverage of the 33 Viking target sites, a detailed photo-interpretation is recommended. In particular, crater distributions may be established on a regional scale and extrapolation attempted to the scale of the Viking lander. Also, the regional slope distributions could be attempted photometrically. The feasability of stereographic mapping of Viking sites should be studied with the Mariner 9 data.

9. A study of the IRIS data on the atmospheric temperature structure and its dependence on diurnal, seasonaly and global effects may be used to determine the atmospheric wind fields. The relation of the resulting winds to diurnal effects and their possible relation to topographic or terrain features should be carefully examined. Comparison with certain data available from TV photographic analysis regarding the crater tails and their relation to the strength and frequency of wind fields should be made. Such analyses may allow the possible use of such visible features as quantitative wind indicators.

10. The atmospheric surface pressure determinations by IRIS and UVS should be carefully examined for transient effects such as cyclonic disturbances, tidal phenomena, local storms and condensation cloud phenomena. Upper atmospheric tidal effects (solar and/or planetary) may possibly be apparent in both the UVS data and the results of the celestial mechanics experiment.

11. IRIS water vapor determinations, indicating regions of higher concentrations, and data on its vertical distribution and diurnal and seasonal variations, and the relation of the white cloud occurrence to the water measures are important, particularly for biologists in site selection investigations.

APPENDIX A

PRODUCTS PRESENTLY AVAILABLE FROM MARINER MARS '71 AND VDAT ACTIVITIES

PLOTS AT 1:5,000,000

Data	Source	Preparation
Elevations (radar)	Haystack 1967-1969, 1971	VDAT & MM'71
Elevations (radar)	Goldstone 1969-1971 (Generalized)	VDAT & MM'71
Elevations (radar)	Goldstone 1971 (Detailed)	VDAT
RMS Slope (radar)	Haystack 1967-1969, 1971	VDAT
Dielectric Constant (radar)	Haystack 1967-1969, 1971	VDAT
Elevations (UVS)	MM'71 UVS	VDAT & MM'71
Elevations (UVS)	MM'69 UVS	VDAT & MM'71

PLOTS AT 1:25,000,000

Elevations (radar)	Haystack 1967, 1969, 1971	VDAT
RMS Slope (radar)	Haystack 1967, 1969, 1971	VDAT
Dielectric Constant	Haystack 1967, 1969, 1971	VDAT
Elevation contours	Haystack radar & MM'71 occultation data	VDAT
Elevation contours (UVS)	MM'71 UVS	VDAT & MM'71

MAP PRODUCTS

1. Mercator photomosaics (from unrectified pictures) of the sixteen 1:5,000,000 charts that cover the Viking zone. Both Cronapaques and Ozalid available through USGS, Flagstaff, Arizona.
2. Same as (1) above, with footprints of B-frames included. Ozalids only.
3. 1:25,000,000 air-brush drawing of Viking zone. Cronapaques and Ozalids available through USGS.
4. 1:25,000,000 "Mini-Terrain" map produced by VDAT; part of this report.

5. 1:25,000,000 Generalized Terrain Map prepared by VDAT and part of this report.

6. Sixteen 1:5,000,000 terrain maps of Viking zone. These products were prepared by VDAT and are available with this report. An explanation of each map is included in Appendix B.

7. 1:15,000,000 "geologic" map of Viking zone compiled by Mariner investigators for COSPAR meetings.

8. Preliminary geologic province map of Mars prepared by R.S. Saunders, of JPL.

9. Photocopies of near-real time mosaics assembled by VDAT; sixteen mosaics.

APPENDIX B NOT FILMED

(contains large maps) see original document.

APPENDIX B

MAPS PREPARED BY THE VIKING DATA ANALYSIS TEAM

Maps MC-8 through MC-23 (16 Maps): Terrain maps at a scale of 1:5,000,000 prepared for the sixteen quadrangles in the Viking zone. Maps not included in this version of this report are being distributed under separate cover.

Map-1: Mini-Terrain at a scale of 1:25,000,000 defining surface features identified from Mariner 9 imagery.

Map-2: Generalized terrain map at a scale of 1:25,000,000 prepared from Mini-Terrain Map and Mariner 9 imagery to identify the major types of terrain.

Map-3: USGS Preliminary Mars Chart prepared from Mariner 9 data with footprints identifying the location of photos used to characterize the various terrain units. (See Figures 3-24 through 3-62.)

Map-4: Preliminary Elevation Contour Map at a scale of 1:25,000,000, dated January 15, 1972, prepared from Haystack Radar Data (1967-1969, 1971) and limited S-Band Occultation Data at a scale of 1:25,000,000.

Map-5: Preliminary Elevation Contour Map (Revised) dated June 28, 1972, prepared from Haystack Radar Data (1967-1969, 1971) and all available S-Band Occultation Data.

Map-6: Plots of RMS Slope at a scale of 1:25,000,000 from Haystack Radar Data (1967-1969, 1971).

Map-7: Plot of Dielectric Constant at a scale of 1:25,000,000 from Haystack Radar Data (1967-1969, 1971).

Map-8: Map identifying location of Viking targets for Mariner 9 Extended Mission. This composite map identifies the accessible areas of elevation and terrain with the Viking target locations.

AL76-108

BORROWERS NAME & MAIL STOP	DATE
Ken [illegible]	6/9/76
2455	

North
South
West
East
180°
170°
160°
150°
140°
130°
120°
110°
100°
90°
80°
70°
60°
50°
40°
30°
20°
10°
0°
350°
340°
330°
320°
310°
300°
290°
280°
270°
260°
250°
240°
230°
220°
210°
200°
190°
65°
60°
50°
40°
30°
20°
10°
0°
-10°
-20°
-30°
-40°
-50°
-60°
-65°
3-40
3-42
3-24
3-25
3-27
3-47
3-48
3-34
3-52
3-53
3-60
3-58
3-59
3-28
3-36
3-35
3-33
3-41
3-69
3-61
3-45
3-26
3-55
3-54
3-30
3-29
3-57
3-56
3-37
3-38
3-31
3-32
3-43
3-44
3-46
3-50
3-49
3-51
3-62

Prepared under JPL contract WO-8122

This chart was made from Mariner 9 television image data. The positions of topographic features were taken from a series of uncontrolled photo mosaic charts prepared by the U.S. Geological Survey from unrectified Mariner 9 pictures. The pictures in these mosaics were positioned primarily for consistancy with spacecraft tracking data with some adjustment to minimize the mismatch between pictures. Positional inaccuracies as large as 60 km exist throughout the chart. It is intended to portray topography only. A later version will show both topographic and albedo variations

SCALE 1:25 000 000 AT 0° LATITUDE
MERCATOR PROJECTION

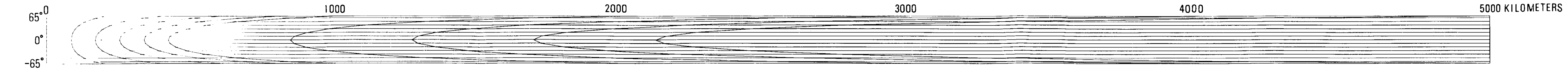
0
1000
2000
3000
4000
5000 KILOMETERS
65°
0°
-65°

PRELIMINARY MARS CHART

Footprints of Fig. 3-3 through 3-41

JUNE 1972

MAP-3

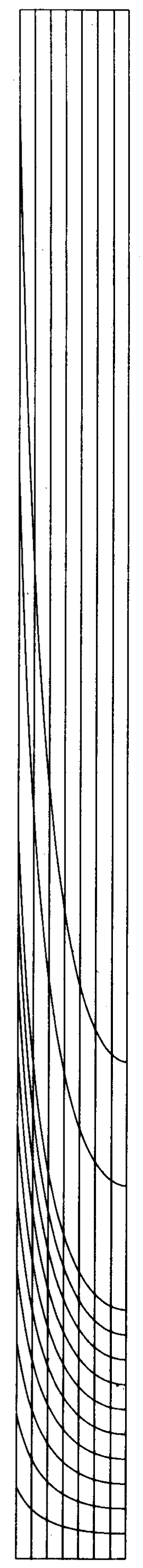

60N
50N
40N
30N
20N
10N
0
10S
20S
30S
40S
50S
60S
1967
3.6/3 5.1/2 8.1/1 3.2/3 4.0/1 4.5/2 0.8/2 4.5/2 0.8/1 3.4/2 1.9/3 2.5/4 2.5/3 2.8/2 6.1/2 2.9/3 2.4/2 2.7/1 3.4/2 2.9/3 3.0/2 3.0/2 3.4/2 1.4/2 4.0/1 6.7/3 4.7/2 8.1/1 8.1/1 8.1/1 8.1/1 8.1/1 2.7/1 4.0/1 4.0/1 2.7/1 4.0/1 1.2/1 4.0/2 8.1/1 1.6/2 4.0/1 1.8/2 8.1/1 0.8/1 2.0/1 2.7/1 2.0/1 6.1/3 3.3/3 3.4/2 2.7/2 5.4/2 4.0/2 2.4/2 0.8/1 1.2/1 1.5/1 5.4/2 1.2/2 0.9/3 1.0/3 2.5/3 3.0/2 2.3/3
1969
6.5/4 6.6/5 2.4/2 8.1/2 8.1/3 3.6/3 6.6/5 3.4/2 5.6/6 4.0/4 5.8/3 3.1/3 3.1/3 4.7/6 6.3/4 8.1/3 6.5/5 8.1/4 5.1/4 5.2/5 5.3/5 6.5/5 5.4/6 4.8/5 4.7/6 7.2/6 8.1/4 5.8/5 8.1/6 6.9/5 6.7/7 7.2/6 6.7/6 7.6/8 8.1/7 6.9/7 4.7/9 6.1/7 5.9/7 7.4/6 3.8/5 1.8/5 4.0/5 4.0/2 4.0/2 5.4/4 4.9/4 4.4/4 2.6/5 2.0/5 2.7/7 3.7/5 3.1/6 5.2/5 6.9/7 8.1/5 7.5/7 6.9/6 8.1/3 8.1/4 7.1/4 6.3/7 4.6/5 4.7/6 5.8/7 2.4/7 4.4/7 6.5/5 6.7/3 8.1/4
6.1/2 5.4/3 8.1/1 5.8/3 5.9/3 5.3/4 8.1/3 5.9/3 3.4/3 6.8/4 7.3/5 4.0/3 5.3/5 6.2/5 6.6/8 4.6/5 4.5/4 5.3/6 6.8/4 6.3/4 2.7/7 4.1/6 5.0/7 6.7/6 6.8/4 7.1/7 6.1/6 5.7/6 8.1/6 8.1/7 6.6/5 7.1/7 8.1/3 6.8/4 6.2/8 6.1/4 4.4/5 5.4/2 5.4/3 6.1/2 6.1/2 4.0/2 4.3/3 5.3/3 3.7/4 5.3/3 2.7/2 2.4/2 2.7/2 5.7/6 6.2/5
0.8/2 4.0/1 0.8/2 1.0/1 4.3/3 2.7/1 1.6/1 2.7/1 4.0/1 8.1/1
1971
0.7/1 4.0/2 10.5/1 4.7/1 10.5/1 0.7/1 5.7/1 10.5/1 0.7/1 5.7/1 4.1/1 2.0/1 2.0/1 8.1/1 2.0/1 4.1/1 4.6/3 6.3/2 0.7/1 8.5/2
3.5/16 2.4/18 6.2/24 5.0/21 5.3/16 6.0/17 2.6/17 1.7/18 4.1/9 1.8/8 3.7/9 4.4/2 3.9/14 1.6/12 1.0/10 1.2/19 1.1/17 1.3/16 1.3/18 1.3/19 2.0/18 3.3/21 2.1/19 4.8/20 5.8/14 7.6/13 7.4/9 5.9/8 5.7/18 5.8/18 5.5/22 3.7/23 6.9/33 2.5/37 3.4/33 2.2/33 2.0/34 2.1/28 2.3/33 2.1/28 2.2/30 2.0/22 1.9/23 2.1/26 2.7/20 2.7/24 4.3/24 3.5/24 5.6/25 6.1/30 6.0/29 6.4/23 4.2/25 5.6/21 5.5/17 8.8/18 4.8/16 4.9/19 4.7/20 4.5/25 3.5/22 5.5/24 4.6/31 4.1/30 3.0/34 4.2/28 3.9/28 4.9/25 4.3/27 4.0/20 3.2/20 4.8/19
3.4/6 2.7/7 4.0/7 3.4/8 4.5/6 2.3/10 2.8/4 1.6/3 2.3/3 1.7/3 1.8/6 1.3/4 1.2/3 0.8/4 0.9/3 2.0/4 5.3/3 3.0/7 3.0/7 3.4/7 1.8/7 1.7/5 2.9/6 4.1/2 3.8/2 9.7/3 4.3/2 3.5/2 10.5/2 5.7/1 1.0/2 0.7/1 7.6/3 4.0/2 5.3/6 3.2/8 3.8/5 2.7/9 1.3/7 1.8/6 1.5/8 2.4/7 4.8/7 2.2/7 3.1/5 5.0/6 5.3/5 5.0/6 4.6/10 3.1/11 6.1/12 5.4/10 5.9/14 5.5/9 5.8/11 5.3/11 6.3/8 4.1/8 4.7/9 5.7/9 3.8/9 7.0/9 4.3/13 4.0/12 6.9/11 3.2/10 3.6/8 3.9/8 2.6/9 3.6/8 3.6/4
1.0/1 0.7/1 10.5/1 2.9/1 4.1/1 2.0/1 2.7/2 1.0/1 4.1/1 6.3/2 4.1/1 5.7/1 2.9/1 10.5/1 7.6/2 1.0/2 4.4/2 0.7/1
180 170 160 150 140 130 120 110 100 90 80 70 60 50 40 30 20 10 0 350 340 330 320 310 300 290 280 270 260 250 240 230 220 210 200 190 180

HAYSTACK MARS DATA 1967,69 & 71
RMS Slope in Degrees
Scale 1:25,000,000

Average Value/Number of Values per 5°

MAP-6

WEST LONGITUDE
180 170 160 150 140 130 120 110 100 90 80 70 60 50 40 30 20 10 0 350 340 330 320 310 300 290 280 270 260 250 240 230 220 210 200 190 180
60N 50N 40N 30N 20N 10N 0 10S 20S 30S 40S 50S 60S
REGION OBSCURED BY NORTH POLAR HOOD
Ts-Smooth tablelands
Tl-Lineated "
Tc-Cratered "
Ridged "
Patterned "
Ps-Smooth plains
Ph-Hummocky "
Pl-Lineated "
Pp-Patterned "
Pc-Cratered "
Pr-Ridged "
CT-Cratered terrain
CTf-Flat " "
CTp-Patterned " "
Ir-Irregular terrain-rugged
CL-Canyonlands
Dc-Domes with caldera-like craters

MARS

GENERALIZED TERRAIN MAP—2

SCALE 1/25,000,000 at Equator

Mercator Projection

This map is preliminary and may be revised at a later date.
Prepared by the U.S. Geological Survey for internal use only by Viking Project.
April 1972

January 15, 1972

Preliminary Elevation Contour Map

Po = 6.2 mb
Re = 3394 km
30
10
0
-10
-20
-30
180
120
60
0
310
250
180

MAP-4

60N
50N
40N
30N
20N
10N
0
10S
20S
30S
40S
50S
60S
180
170
160
150
140
130
120
110
100
90
80
70
60
50
40
30
20
10
0
350
340
330
320
310
300
290
280
270
260
250
240
230
220
210
200
190
180
1967
2.1/3 1.5/1 1.6/2 2.1/1 1.6/1 1.3/1 1.3/1 1.3/1 2.1/2 1.8/3 2.0/3 1.9/3 1.9/2 1.9/1 1.7/3 1.6/2 1.5/1 1.7/2 2.0/3 1.9/2 2.0/2 2.0/2 1.6/2 1.8/1 1.9/1 1.7/1 2.3/1 3.0/1 2.1/1 1.9/1 2.3/1 1.8/1 2.5/2 1.6/2 2.0/1 1.7/2 1.5/1 1.6/1 2.6/1 2.2/1 2.3/1 1.9/2 2.7/2 2.8/2 3.1/1 2.8/2 3.0/2 1.5/2 2.0/1 2.3/2 1.8/1 1.9/2 2.4/3 3.0/3 2.6/3 2.3/2 2.4/3
1969
4.0/2 1.3/1 3.2/1 3.4/1 3.5/1
1.9/1 1.5/1 2.4/2 2.3/3 1.2/1 1.8/2 2.0/3 2.2/3 1.7/1 2.3/3 2.7/3 3.1/5 1.3/1 2.1/1 1.9/1 2.5/2 2.4/3 1.5/2 3.7/3 3.6/3 3.3/4 2.6/4 2.0/1 1.8/1 2.2/1 1.8/1 2.4/2 1.9/1 3.1/2 2.4/1 2.7/2 4.2/7 4.4/4 3.0/2 3.4/1 2.2/4 2.0/6 2.1/3 3.1/2 3.0/3 2.5/1 2.3/2 2.5/3 4.1/5 3.3/5 4.2/6 5.8/4 3.7/5 2.9/3
4.2/1 2.4/2 1.7/1 2.0/1 1.3/1 1.3/1 1.2/2 1.6/1 2.2/1 1.9/3 1.5/2 2.1/4 2.7/1 2.7/4 3.1/3 2.4/3 2.9/1 1.5/1 3.1/8 3.4/4 3.2/5 3.2/2 1.8/1 1.5/1 3.1/3 1.6/2 1.8/1 1.7/1 2.2/2 4.1/1 4.4/2 4.0/4 3.3/2 2.9/2 1.9/3 3.1/2 2.3/4 2.1/3 2.6/5 3.4/3 3.1/3 3.1/3 4.8/2 4.5/3 4.4/1 5.3/2 3.1/1 2.4/1 3.9/3 3.8/4 4.6/4 3.8/3 3.1/7 3.7/6 2.7/2 1.9/1 2.7/3 2.3/2
1971
3.4/8 6.8/8 8.1/6 6.3/6 6.7/10 5.0/8 3.6/8 3.5/15 6.6/7 4.5/16 3.1/14 4.3/14 2.9/11 3.0/11 4.2/8 2.1/11 1.7/5
2.7/15 3.6/20 2.9/13 3.2/15 2.7/11 2.0/10 2.2/16 1.8/18 1.6/7 1.9/8 1.9/7 1.2/1 2.3/12 3.1/12 4.3/10 4.0/18 3.3/18 3.8/15 3.4/19 2.5/17 2.7/18 2.5/18 2.4/18 2.6/13 2.6/9 3.2/5 1.5/3 1.7/2 2.6/11 2.7/12 2.7/15 3.3/21 4.5/15 4.6/39 4.9/29 7.0/34 5.4/34 6.4/28 6.3/33 6.1/27 6.0/29 7.5/23 5.6/22 6.3/26 4.9/20 4.0/23 4.7/19 2.5/22 4.2/17 4.4/17 4.7/18 3.6/12 4.2/20 6.1/12
3.8/8 4.5/11 5.5/16 5.7/14 4.7/16 8.5/18 4.8/21 3.9/17 3.4/14 4.1/32 4.2/28 4.6/15 4.2/22 5.1/19 3.1/18 4.2/17 4.0/14 4.1/11
4.9/5 4.4/7 7.7/7 4.6/8 4.8/5 3.7/10 3.2/4 2.2/3 2.6/3 2.4/3 3.4/6 2.6/4 2.8/2 5.2/5 4.7/3 6.3/4 6.5/2 5.7/6 11.7/7 12.0/6 6.6/7 3.2/5 5.3/6 7.1/2 5.1/2 6.9/2 5.1/2 5.3/1 1.6/2 1.7/1 4.5/1 2.3/1 11.3/4 4.7/7 4.3/4 3.8/8 2.4/7 3.4/7 3.5/7 5.3/7 4.1/6 2.9/7 3.4/5 4.3/5 1.8/3 2.0/3 3.2/9 2.8/10 2.7/6 4.9/7 4.9/9
4.5/2 3.1/2 4.3/2 2.0/1 5.7/1 2.2/1 4.1/1 11.4/1 2.7/1 8.0/1 1.7/1 4.8/2 2.2/1

HAYSTACK MARS DATA 1967,69 & 71
Dielectric Constant (R)
Scale 1:25,000,000

Average Value/Number of Values per 5°

MAP—7

LOCATION OF VIKING TARGETS MARINER 9 EXTENDED MISSION

WEST LONGITUDE
180 170 160 150 140 130 120 110 100 90 80 70 60 50 40 30 20 10 0 350 340 330 320 310 300 290 280 270 260 250 240 230 220 210 200 190 180
60N
50N
40N
30N
20N
10N
0
10S
20S
30S
40S
50S
60S
1
2
3
4
5
6
7
8
9
10
11
12
13
14
16
17
18
19
20
21
22
23
24
25
26
27
28
29
30
31
32
34
35
Ps
Pp
Pl
Ph
Pc
Pr
Ir
Dc
Tc
Tp
Ts
Tl
Tr
CL
CT
CTf
CTp
+2
0

MARS
GENERALIZED TERRAIN MAP
SCALE 1/25,000,000 at Equator
Mercator Projection

MAP-8

This map is preliminary and may be revised at a later date.
Prepared by the U.S.Geological Survey for internal use only by Viking Project.
April 1972

JUNE 28, 1972

Preliminary Elevation Contour Map (BASED ON HAYSTACK RADAR & MM '71 OCCULTATION DATA)

$P_o = 4.8$ mb
$\bar{R}e = 3396.8$ km.
30
20
10
0
-10
-20
-30
180°
120°
60°
0°
310°
250°
180°
-3 -4 -4 -3 -2 -1 0 1 2 3 4 4 3 2 1 0
-5 -6 -6 -5 -4 -3 -2 -1 -4 -3 -2 -1 0 0 -1 -2 -3 -4 -4 -3 -2 -1 0 1 2 -3 -4
1 2 3 3 3 4 5 6 6 5 4 3 2 1 0
9 8 7 7 8 3 2 -1 -2 -1 0 -3 -2 -1 0 1 2 2
-7 -6 -5 -4 -3 -2 -1 0 1 -3 -2 -1 0 1 2 1 1

MAP – 5

FOLD-OUT #1

FOLD-OUT #2

FOLD-OUT #3

REGION OBSCURRED BY NORTH POLAR HOOD
60N
50N
40N
30N
20N
10N
0
10S
20S
30S
40S
50S
60S
180
170
160
150
140
130
120
110
100
90
80
70
60
50
40
30
20
10
0
350
340
330
320
310
300
290
280
270
260
250
240
230
220
210
200
190
180
Ridge
Scarp-barb points downslope
Crater rim crest
Crater with central peak
Depression
Linear depression (graben, rill, or river-like feature)

This map is preliminary and may be revised at a later date.
Prepared by the U.S. Geological Survey for internal use only by Viking Project.
April 1972

FOLD-OUT #4

FOLD-OUT #5

MARS

MINI-TERRAIN MAP-1

SCALE 1/25,000,000 at equator

Mercator Projection

FOLD-OUT #6